Probing the role of magnetic fields in star-forming filaments and protostellar cores Observations with NIKA2-Pol

Hamza Ajeddig

To cite this version:

Hamza Ajeddig. Probing the role of magnetic fields in star-forming filaments and protostellar cores Observations with NIKA2-Pol. Instrumentation and Methods for Astrophysic [astro-ph.IM]. Université Paris-Saclay, 2022. English. NNT : 2022UPASP014 . tel-04078332

HAL Id: tel-04078332
https://theses.hal.science/tel-04078332v1

Submitted on 23 Apr 2023

Probing the role of magnetic fields in star-forming filaments and protostellar cores: Observations with NIKA2-Pol

Champ magnétique et formation stellaire le long des filaments interstellaires : Observations avec NIKA2-Pol

Thèse de doctorat de l'université Paris-Saclay

École doctorale n° 127 : astronomie et astrophysique d'Île-de-France (AAIF)
Spécialité de doctorat : Astronomie et Astrophysique
Graduate School : Physique. Référent : Faculté des sciences d'Orsay

Thèse préparée dans l'unité **Astrophysique, Instrumentation et Modélisation de Paris-Saclay (Université Paris-Saclay, CNRS, CEA)**, sous la direction de **Philippe ANDRÉ**, Directeur de recherche, CEA Université Paris-Saclay.

Thèse soutenue à Paris-Saclay, le 31 Janvier 2022, par

Hamza AJEDDIG

Composition du jury

Alain ABERGEL Professeur, Université Paris - Saclay	Président
Dan CLEMENS Professeur, Université de Boston	Rapporteur & Examinateur
Isabelle RISTORCELLI Directrice de recherche, CNRS, Université Paul Sabatier	Rapportrice & Examinatrice
Helmut WIESEMEYER Astronome, Max-Planck-Institut für Radioastronomie	Rapporteur & Examinateur
Francois-Xavier DÉSERT Astronome, Université Grenoble-Alpes	Examinateur
Carsten KRAMER Astronome, IRAM, Université Grenoble-Alpes	Examinateur
Annie ZAVAGNO Professeure, Aix Marseille Université	Examinatrice
Jean Philippe BERNARD Directeur de recherche, CNRS, Université Paul Sabatier	Invité
Philippe ANDRÉ Directeur de recherche, CEA Université Paris-Saclay.	Directeur de thèse

THESE DE DOCTORAT

NNT : 2022UPASP014

Dedication
To my father Ahmed AJEDDIG (1926 - 2016)
To my mother Aicha KNIOUI

Acknowledgements

Doing a PhD is not an easy task and one needs strength to continue till the end of the journey. This PhD can not be achieved without a help of certain people which I will explicitly mention in this acknowledge. My passion of astronomy has started at the desert of Morocco in a small village called Askjour in the province of Zagora. As a little child, I was fascinated by the beauty of stars in the sky and I was questioning their distribution and formation. Who can said that after more than 20 years I will get a PhD in astrophysics and especially in star formation. If I learned something about life in this PhD challenge it will be the power of believing on yourself and never give up a dream whatever it is. This achievement is not three years of PhD, it is a journey of discoveries, making friends, and giving a sens to my life.

Thank you Philippe André for accepting me to this adventure and helping me trough these PhD years. I have learned a lot of things from you, especially being precise in everything and encouraging sometimes when I needed it. I hope that B-FUN will shine in coming years and you get very nice data with NIKA2-Pol. Thank you for the scientific discussion everyday (not fun about those during the launch time). I thank all the committee of my PhD defense for their patience and their inputs to improve my PhD manuscript. Thank you Michel Talvard and Rodriguez Jerome for being my monitoring committee.

The support of my familly was one of my great key of this achievement. My father Ahmed AJEDDIG (1927-2016) wanted at least one of his son to get a high degree of education because no one went the school besides me. My PhD is a dream to father and it is for him and my mother AICHA KNIOUI that I dedicate this PhD. Thank you my sisters Touda and Fatima (Fato) for being there and supporting from thousands miles away. My brothers, all of you, Mouha, Said, Salah, Zaid, Daoud, thank you for your help and your support. Thank you Hanane AJEDDIG for your support.

They said, “show me with whom you are I tell you who you are”, more than 10 years of friendship with Idir Benaissa and Ahmed Aitkhouya. You have been here with me and where I go I find you, thank you so much for standing with me and supporting me (sometimes) more than my family. I am thankful to you Hakim Amazigh, Daoud Oulkisane, Omar Talibi, Karam, Chaimae, Asmae ... for your help and your support, and for the parties and afterworks in Toulouse, Nice and in Paris. You have been and you still a great mates and friends, thank you guys. I thank my friend Meriem Elyajouri and Taha Shieseh for being here the first time I came to Paris and helping to pass my interview. I thank the Space-Bus Morocco team for the incredible experience. I am a lucky person because wherever I go I made friends, I thank Omar Ait-khouya, Omar Elmoutaoukil, Hicham Atmani, Belfakir Mohamed, the ”High Energy Physics and Astrophysics Club" especially, Imane Moumne, Abderahmane Soubkiou, Youssef Moulane, Khalid Berkaoui, Abdelkarim Boskri, and all the team. I can not Imagine my life without you and I have enjoyed all moments during our events. You were incredible in all the hundreds events that we organized, thank you for supporting the club and being here with me, I hope that this club continue shining and organizing outreach events in Morocco. I would love to write all names of my friends but it is not possible, because you are thousands and I am happy that you are.

Before moving to France, I had the opportunity to work and learn astrophysics in Morocco. I would like to thank my mentors in Morocco and the High Energy Physics and Astrophysics Laboratory in Marrakesh. Before pursing this PhD I have lived in five countries for internships, I would like to thank all my supervisors.

At last but not least, I thank CEA for hosting me during this PhD. I have made a lot of friends in CEA. I thank first my co-office Micheal Mattern for all our discussions, lot of coffees, drinks and for his support during my defense and before. I thank the CEA after-work team, Sunayna, Boris, Carlos ...Thank you. My thanks to my master MAUCA colleagues at Nice, Alison, Christian, Ahmed ... Thank you.

During this PhD, I have been working with NIKA2 team, I thank them for accepting me to be in the core team of the collaboration and helping getting the NIKA2-Pol commissioning done. I thank Anaëlle Maury for coordinating the commissioning of NIKA2-Pol and all discussions and advises during this PhD. I enjoyed observations with NIKA2-Pol team Alessia, Nicolas, Juan ... Thank you. Thank you Yoshito Shimajiri for your help during my first year of my PhD and all our discussions and your advises... Thank you. I am grateful to my mentors, my family, my friend, colleagues for supporting me along the journey.

Synthèse en français

La formation d'étoiles dans le milieu interstellaire est débattue depuis des décennies. Les observations récentes de la mission spatiale *Herschel* ont montré que les structures filamentaires sont présentes dans tout les nuages moléculaires observés et que ces filaments jouent un rôle crucial dans la formation d'étoiles. Ces observations ont montré que ces filaments ont une largeur commune de 0.1 pc et que la plupart (75 %) des coeurs pre-stellaires détectés sont dans des filaments trans-critiques ou super-critiques pour lesquelles la masse par unité de longueur excède le seuil critique de l'instabilité gravitationnelle d'un filament cylindrique de gaz isotherme avec M$_{line}$ $\gtrsim$ M$_{line}^{crit}$ (M$_{line}^{crit}$ $= 2c_s/G \sim 16M_\odot$ est la masse par unité de longueur). Les résultats d'Herschel favorisent le paradigme de formation d'étoiles dans les filaments dans lequel : (1) la turbulence supersonique magnétohydrodynamique (MHD) à grande échelle comprime la matière pour former des structures filamentaires avec une largeur interne commune $\sim$ 0.1 pc; (2) Les filaments les plus denses se fragmentent et s'effondrent pour former des noyaux préstellaires en raison de leur instabilité gravitationnelle lorsque M $_{line}$ est proche ou dépasse la masse critique par unité de longueur M $^{crit}_{line}$. Cependant, le processus détaillé de comment les filaments fragmentent en noyaux pre-stellaire est activement débattu. Il y a des indices que le champ magnétique peut être l'ingrédient ignoré pour comprendre la formation d'étoiles. De plus, les données obtenues avec *Planck* en émission polarisée des poussières froides suggèrent que la formation et l'évolution des filaments moléculaires sont en grande partie contrôlées par le champ magnétique. Les observations polarisées avec Planck sont incapables de determiner la géométrie du champ magnétique à l'intérieur des filaments aux échelles auxquelles la fragmentation se produit. La compréhension du rôle du champ magnétique dans la formation d'étoiles n'est donc pas encore complete. Explorer la géométrie et l'intensité du champ magnetique dans les filaments moléculaires à différentes longueurs d'onde et à une résolution angulaire élevée aidera à comprendre son rôle dans le processus de formation d'étoiles dans le milieu interstellaire froid.

L'objectif de cette thèse est de clarifier le rôle champ magnétique dans la formation d'étoiles en utilisant des polarimètres sensibles et à haute résolution angulaire. Le grand programme d'observations 300 heures en temps (B-FUN) garanti avec NIKA2-Pol et alloué par l'IRAM 30m va conduire des observations d'imagerie polarimétrique à 1.2 mm pour observer des filaments moléculaires proches formant des étoiles. Durant ma thèse, j'ai contribué aux tests et à la mise en service de l'instrument NIKA2-Pol. Cet instrument a dû faire face à plusieurs problèmes, en particulier l'effet de la polarisation instrumentale ou la fuite de l'intensité totale à la polarisation. J'ai caractérisé la variation de cet effet avec plusieurs paramètres (elevation, foyer et conditions d'observations). J'ai enquêté sur l'origine de cette polarisation instrumentale affectant les données de NIKA2-Pol comme tout autre polarimetre au monde. J'ai présenté un modèle analytique qui permet de reproduire cet effet. J'ai montré comment corriger les données de NIKA2-Pol de la polarisation instrumentale et j'ai exploité ces données pour étudier le filament d'OMC-1 dans le nuage moléculaire d'Orion A. J'ai présenté une comparaison statistique entre les résultats obtenus par les polarimètres SCUBA-POL2 et NIKA2-Pol. Ces résultats ont permis de démontrer la capacité de NIKA2-Pol à fournir des données de polarisation de haute qualités. Par ailleurs, j'ai étudié la géométrie/l'intensité du champ magnétique avec les données obtenues durant les compagnes de tests de l'instrument NIKA2-Pol. J'ai confirmé la présence du champ magnétique se forme d'une "hourglass" (sablier) à grande échelle dans le filament OMC-1 précédemment détecté par d'autre polarimetres. J'ai trouvé des preuves d'un possible nouvel "hourglass" centré à la position d'Orion-KL grâce à la sensibilité et la haute résolution angulaire de NIKA2-Pol. J'ai estimé l'intensité du champ magnétique dans cette région en utilisant la méthode Davis-Chandraskher-Fermi. En parallèle, j'ai utilisé les données de polarisation obtenus par le polarimetre SOFIA/HAWC+ pour étudier la géométrie/intensité du champ magnétique dans le filament B211/B213 du nuage moléculaire Taurus. Enfin, j'ai effectué une analyse du spectre de puissance des fluctuations de vitesse le long d'un échantillon de filaments dans la région de formation d'étoiles d'Aquila pour élucider les conditions initiales de la fragmentation des filaments en chaînes de noyaux denses.

Abstract

Star formation in the interstellar medium has been under debate for decades. The unprecedented high-quality images provided by *Herschel* have shown that filaments are ubiquitous in molecular clouds and play a key role in the star formation (SF) process. These filaments have been shown to exhibit a common inner width of about ~ 0.1 pc, and more than 75 % of the detected prestellar cores are embedded in thermally trans-critical or super-critical filaments with masses per unit length $\mathrm{M}_{line} \gtrsim \mathrm{M}_{line}^{crit}$ (where $\mathrm{M}_{line}^{crit} = 2c_s/G \sim 16M_{\odot}$/pc is the critical mass per unit length of an isothermal filament). *Herschel* findings support a filament paradigm for SF in which : (1) Large-scale magnetohydrodynamic (MHD) supersonic turbulence compresses interstellar material to form a cobweb of filamentary structures with a common inner width of about ~ 0.1 pc; (2) The densest filaments fragment to form prestellar cores due to gravitational instability when M_{line} is close to or exceeds the critical mass per unit length M_{line}^{crit}. However, the detailed process of how filaments fragment into cores remains actively debated. There are hints that the magnetic field may be the ignored ingredient toward understanding SF. *Planck* results suggest that the B-field lines tend to be parallel to low density filaments and perpendicular to the high-density filaments. Due to the low angular resolution of *Planck* polarization data (10 arcmin), these observations are, however, unable to probe the magnetic field inside filaments on scales at which fragmentation occurs. The detailed knowledge of the role of magnetic fields in the SF process has therefore not yet been achieved. Constraining the B-field geometry/strength at different wavelengths and high angular resolution will help understand how magnetic fields may regulate the SF in the cold interstellar medium (ISM).

This thesis aims to clarify the role of magnetic fields in SF using high-angular resolution, sensitive polarimetric instruments. The B-FUN large program with the NIKA2-Pol polarimeter on the IRAM 30m telescope will provide high angular resolution (11.7 arcsec) and sensitive polarization data toward nearby star-forming filaments. During my Ph.D., I contributed to the commissioning of NIKA2-Pol. The commissioning of NIKA2-Pol had to face several challenging issues, in particular, the instrumental polarization (IP) or intensity-to-polarization “leakage” effect. I characterized the variation of the leakage effect with several parameters (elevation, focus position, and observing conditions). I investigated the origin of the IP, and presented an analytical model for the IP leakage. I illustrated how this effect can be corrected for, leading to reliable exploitable data in a structured, extended field such as the OMC-1 filament in the Orion A molecular cloud. I presented a statistical comparison between NIKA2-Pol and SCUBA2-Pol2 results in the OMC-1 region. These results helped to demonstrate the ability of NIKA2-Pol to provide high-quality polarization data. Furthermore, I investigated the geometry/strength of the magnetic field toward the OMC-1 filament using NIKA2-Pol commissioning data. I confirmed the presence of a previously-detected large-scale hourglass pattern in the magnetic field distribution, and I found evidence of a possible new local hourglass centered at the position of Orion-KL detected thanks to the NIKA2-Pol high angular resolution data. I also made estimates of the magnetic field strength in this region using the Davis-Chandraskher-Fermi method. In parallel, I used SOFIA/HAWC+ polarization data to study the magnetic field geometry/strength in the B211/B213 filament of the Taurus molecular cloud. Finally, I performed a power spectrum analysis of velocity fluctuations along a sample of filaments in the Aquila star-forming region to elucidate the initial conditions for the fragmentation of filaments into chains of dense cores.

Contents

Chapter 1

Star formation in interstellar filamentary clouds

1.1 General introduction

Since antiquity, the shiny stars in the sky have aroused questions about their distribution, which was before the Copernicus Revolution in the 16^{th} century related to mythology and religion. The question of how these celestial objects move in the sky and emit light has been a mysterious challenge for humanity. The significant steps toward understanding the stars came after the first observations of a collection of stars crossing the sky, the Milky Way, with a telescope made by Galileo Galilee in 1609. In the same century, Isaac Newton published his book "*Philosophiae Naturalis Principia Mathematica*", where he introduced a mathematical approach of gravity that allowed to explain the motion of planets and celestial objects, which is still used until now. After the 16^{th} and 17^{th} centuries, scientists have been exploring the universe with new instruments at different wavelengths and angular resolutions. For example, Edwin Hubble in 1929 built an optical telescope of 1m in diameter to confirm the theory of the expansion of the Universe (Hubble, 1929). In the 17^{th} century, Herschel (1785) in his paper "*On the Construction of the Heavens*" gave an explanation and first proposal on how stars form where he suggested that they may from individually or in clusters and pointed out the existence of "holes in the sky" where no star had been observed. The development of a new instrument dedicated to astronomy led Barnard (1919) to suggest the existence of dense absorbing regions between the stars. Observations of the sky at radio-wavelengths in the second part of the 20^{th} century allowed to give new interpretations of star formation. The formation of stars in the interstellar medium (ISM) has therefore been debated for several decades. Star formation community has been trying to mimic the observations with simulations to understand where and how stars form in the Universe. The enigma of the physics behind star formation is still unclear.

In this introductory chapter, I present some general information about star formation in the interstellar medium (ISM), the filamentary structures observed in the ISM, especially with the *Herschel* Space Observatory, the role of molecular filaments in the star formation process, and the role of turbulence and magnetic fields in star formation. I also introduce the scientific motivation for this thesis. This chapter will thus help the reader understand the following chapters of the thesis.

1.1.1 Interstellar medium (ISM)

The interstellar medium (ISM) represents all the material between stars, including large-scale structures of gas and dense small-scale structures (e.g, prestellar cores or stars). Understanding the ISM has been given an impulse by high-quality radio observations in recent decades. For example, Ewen & Purcell (1951) detected the atomic hydrogen line at 21 cm wavelength, which proved the existence of diffuse atomic gas in the ISM. Subsequently radio observations at a wide range of millimeter wavelengths led to the detection of several molecular lines in the ISM. The most commonly used observations are the CO(1-0) line emissions discovered by Wilson et al. (1970) at 2.6 mm wavelength.

The ISM is a non-homogeneous, complex, and evolving medium that presents a scientific laboratory to understand the material from which stars form. McKee & Ostriker (1977) proposed a theory of the ISM in which they divided the ISM into different phases depending on their physical conditions. These phases are mainly regulated by the feedback from supernova explosions in the medium.

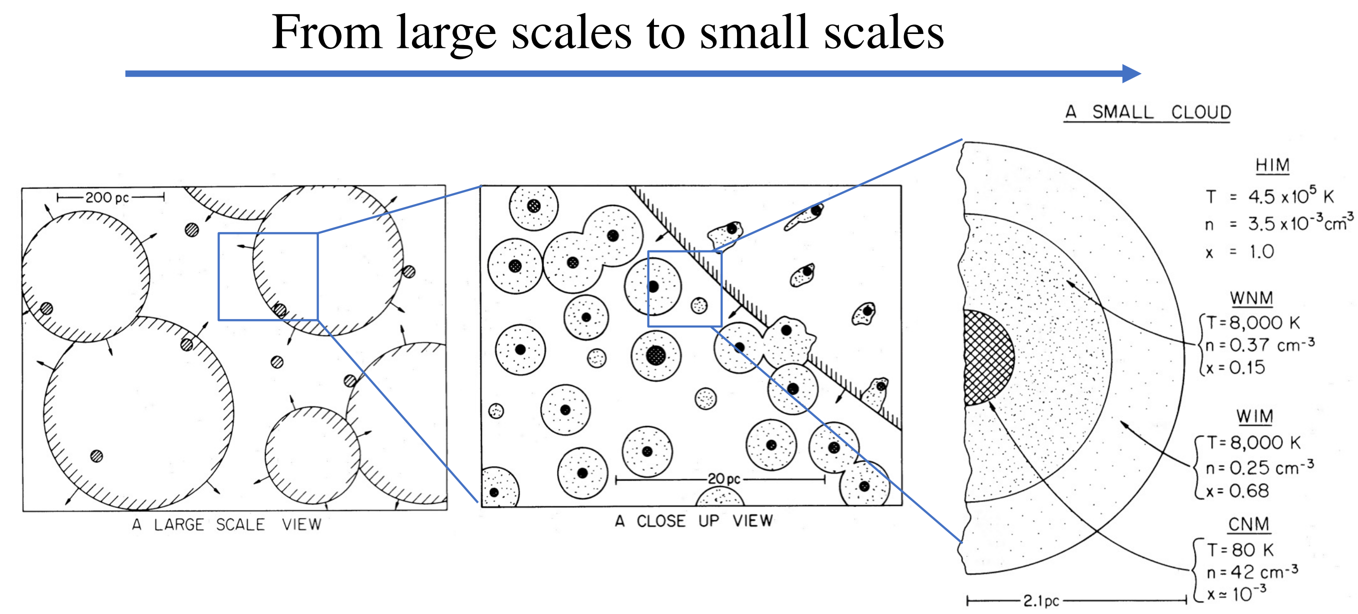

Figure 1.1: The different phases of the ISM as proposed by McKee & Ostriker (1977). From left to right, panels indicate the ISM phases from large-scale bubbles (>100 pc) to cold clumps (<0.1 - 1 pc). McKee & Ostriker (1977) classified different phases by their hydrogen surface density n, temperature of the medium T (K) and ionisation factor $x = n_e/n$. However, this schematic illustration of the ISM does not strictly reflect our modern knowledge of the ISM. The molecular clouds in the ISM are complex, turbulent structures and span scales of hundreds of parsecs.

Draine (2011) reviewed the different phases of the ISM based on the McKee & Ostriker (1977) theory of the ISM as presented in Fig. 1.1 as follows :

1. *Hot Ionized Medium (HIM)* : It is mainly composed of ionized hydrogen with extremely high temperature (10^6K) (Ferrière, 2001). It contains the hot plasma heated by the feedback from the radiation of massive stars and shocks. It is considered the most diffuse gas in the ISM. Its heating timescales vary on a case-by-case basis. The cooling timescales are of the order of 1 Myr or more.

2. *Warm Ionized Medium (WIM)*: It consists of a hot plasma embedded mostly in the HIM and heated by the Lyman continuum radiation coming from nearby hot young stars.

3. *Warm Neutral Medium (WNM)*: Its gas has a low ionization fraction, and 60 % of it is in the form of neutral atomic hydrogen with a temperature of 8000 K.

4. *Cold Neutral Medium (CNM)*: It consists of colder atomic gas (< 100 K) mainly associated with molecular gas and is highly filamentary (eg. Audit & Hennebelle, 2005).

5. *Diffuse H_2*: Known to be extended in the CNM region and denser enough to prevent the photo-dissociation of H_2 molecules by the thermal radiation from nearby stars.

6. *Dense H_2*: Temperature varies between 10 K and 50 K and the density ranges between 10^3-10^6 cm^{-3} which is high enough to form clumps and cores that can be observed using CO line or dust continuum observations.

Each of these environments has different physical conditions, which depend mainly on the medium's heating and cooling. In addition, observations at different wavelengths and/or in different molecular lines can be used to distinguish between the different phases of the ISM.

1.1.2 The star formation process in the ISM

Stars, by definition, are hot self-gravitating gas spheres with extremely high temperatures at their center, sufficient to sustain the thermonuclear fusion reactions of hydrogen. They are fundamental building blocks of galaxies. Understanding the early stages of star formation is crucial to probe the physical conditions and criteria in which embedded gas would form a star. It is commonly known that stars may form in clusters or individually in molecular clouds. Giant molecular clouds are the main birthplaces of stars in galaxies, and their temperature is about ~10 K, their mass about $\sim 10^5 \mathrm{M}_\odot$ and they are close to isothermal equilibrium (Blitz, 1993; Williams et al., 2000; Mac Low & Klessen, 2004).

The condensation/fragmentation of the material in the cloud to form a prestellar dense core is a multi-scales process that involves several physical effects, such as ambipolar diffusion (Mouschovias, 1991), turbulence dissipation (Myers, 1983), and dynamic accretion or outside impulses (Bonnell, 1997). After accumulating enough mass, the prestellar cores within molecular clouds become gravitationally unstable and collapse to form a star. In the present section, I will briefly present the star formation process and widely known process. A detailed presentation of the initial conditions of solar-type protostar formation may be found in André (2002).

1.1.2.1 Gravitational collapse

The collapse of a spherical cloud due to gravitational instability is one of the first scenarios proposed by Jeans (1902) to explain the star formation process in the ISM. This scenario mainly assumes that molecular clouds are regulated by self-gravity and thermal energy. The Jeans (1902) model assumes the hydrostatic equilibrium of the clump and neglects the influence of turbulence and magnetic fields. Therefore it is considered an approximated scenario for protostar formation. Using the equilibrium hydrostatic equation, Jeans (1902) established the minimum mass that a core within a cloud must have to collapse owing to its gravitational instability depending on its temperature and density.

Thus, the Jeans mass can be expressed as follows:

$$M_{Jeans} = \frac{\pi}{6}(\frac{\pi}{G})^{3/2}\rho_0^{-1/2}c_s^3 \tag{1.1}$$

where ρ_0 is the density of the ambient cloud, for isothermal gas $c_s^2 \propto T$ (where T is the temperature of the gas in the cloud and c_s is the sound speed), G is the gravitational constant. Thus, the critical mass $M_{Jeans} \propto \rho_0^{-1/2} T^{3/2}$ and it decreases when the density of the cloud grows or when the temperature T sinks (Mac Low & Klessen, 2004).

An alternative expression for the critical mass of a cloud that can undergo gravitational collapse was developed by Bonnor (1956), which takes into account external pressure. This mass is known as the critical Bonnor-Ebert mass, which can be expressed as follows:

$$M_{BE} = 1.182\frac{\sigma_{th}^4}{(G^3 P_{th,0})^{1/2}} = 1.182\frac{\sigma_{th}^3}{(G^3\rho_0)^{1/2}} \tag{1.2}$$

where $\sigma_{th} \propto (P_{th}/\rho_0)^{1/2}$ is 1D thermal speed (where ρ_0 is the density and P_{th} is the thermal pressure) (e.g, McKee & Ostriker, 2007). The Jeans mass and critical Bonnor-Ebert mass are related by $M_{Jeans} = 2.47 M_{BE}$ (for more information, see McKee & Ostriker, 2007 and reference therein).

1.1.2.2 Gravo-turbulent process

The pioneering work of Larson (1969) using numerical calculations of a collapsing protostar starting from a uniform density cloud, found that the collapse process is non-homologous. He found that the central part of the cloud collapses faster than the outer parts. In the same year, Penston (1969b,a), using a different approach than Larson (1969), found that the collapse of a proto-star is mainly stopped by the rise in optical depth in the center when the surface density reaches 10^{-15} g.cm^{-3}. Their simulations assumed that only hydrodynamic turbulence and gravity governed the collapse process of a cloud core. These 1D numerical models considered neither the angular momentum of the cloud (due to the rotation of the cloud around its barycentric axis) nor magnetic field effects. In 1977, Shu (1977) introduced *the classical theory* of isolated star formation in which he argued that the initial physical conditions adopted by Larson and Penston (1969) were artificial (because out of equilibrium) and highlighted the need of involving the magnetic fields in the star formation process (Shu et al., 1987). In the gravo-turbulent scenario, supersonic turbulence provides global support and produces density enhancements that allow local collapse of cores, thus, this process relies only on turbulence and gravity (Mac Low & Klessen, 2004).

1.1.2.3 Magnetic support and mass-to-magnetic flux ratio

Knowing the magnetic field strength is important to derive two physical parameters that allow to quantify the physical importance of the magnetic field and for instance determine whether the magnetic pressure is strong enough to prevent gravitational collapse. The first parameter is the index κ in the $B_{POS} - n$ relationship ($B_{POS} \propto n^{\kappa}$) (Crutcher, 2012) that gives the variation of the field strength as a function of the cloud volume density. The second and most important parameter is the mass to magnetic flux ratio M/Φ which can be introduced by considering the equation for virial equilibrium between gravitational and magnetic energies as follows:

$$\frac{3GM^2}{5R} = \frac{B^2R^3}{3} \tag{1.3}$$

The magnetic flux Φ can be expressed as follows:

$$\Phi = \pi R^2 B \tag{1.4}$$

From Eq. 1.3 and Eq. 1.4, the critical mass-to-magnetic flux ratio is :

$$\left(\frac{M}{\Phi}\right)_{crit} = \frac{1}{3\pi}\sqrt{\frac{5}{G}} \tag{1.5}$$

The mass-to-flux ratio has been widely used to quantify the magnetic state of a cloud. The normalized mass-to-flux ratio can be expressed as follows :

$$\mu_\Phi = (M/\Phi)_{cloud}/(M/\Phi)_{crit} \tag{1.6}$$

If the cloud is magnetically super-critical, $\mu_\Phi >> 1$, the magnetic field is too weak to prevent gravitational collapse (cF. weak field model presented in Sect. 1.4.2 at the end of this chapter). If the cloud is magnetically sub-critical, i.e, $\mu_\Phi < 1$, the magnetic field is strong enough to prevent cloud collapse. The (column) density at which interstellar clouds change from being magnetically sub-critical to becoming magnetically super-critical is still under debate. Crutcher & Kemball (2019) suggested that for a column density (N_H) below $N_H \sim 10^{21}$ cm^{-2}, interstellar clouds are mostly magnetically subcritical, and those above $N_H \sim 10^{22}$ cm^{-2} are magnetically super-critical. They suggested that the transition from sub-critical to super-critical occurs at a column density of about $N_H \sim 10^{22}$ cm^{-2}. The normalized mass-to-flux ratio μ_Φ varies from the large scales of the parent cloud to dense core scales, and it appears to increase from cloud envelopes to dense cores (<0.1 pc) (Crutcher, 2004).

1.1.2.4 Formation of a magnetically super-critical core by ambipolar diffusion

In low-density molecular clouds, the ionization degree is relatively large, and ions and neutrals are well coupled. However, the ionization degree decreases when going to the denser molecular cores and ions and neutrals progressively decouple. Furthermore, the neutrals can then stream through the ions accelerated by gravity, leading to a drift velocity between ions and neutrals. In this process, the magnetic field is sufficiently strong to prevent the gravitational collapse of a clump if $\mu_\phi < 1$. Nakano & Nakamura (1978) introduced the strong magnetic field theory in which the magnetic field regulates the formation of the cloud. Neutrals stream through the ions accelerated by gravity. There is a drag force between ions and neutrals from collisions. The Lorentz force acts directly on ions. Large ions and neutrals are strongly collisionally coupled. In denser molecular cores, the ionization degree decreases, and neutrals and ions can easier decouple. During the ambipolar diffusion process, the mass of cloud increases faster than the magnetic field strength, so that a magnetically super-critical core eventually forms. Since $\mu_\phi > 1$ in the center, the central super-critical core is gravitationally unstable and collapses (for more information, see Shu et al., 1987; Mouschovias, 1991).

1.1.2.5 From prestellar cores to protostars and young stars

Observations of different phases of star formation from embedded prestellar cores of gas and dust to protostars and more advanced young stars can give insights into the star formation process. The evolution from dense core to the formation of an early prestellar core, to a protostar, then pre-main-sequence stars, and finally main-sequence stars can be summarized in the following different stages (Lada, 1987; André, 2002).

1. Prestellar phase: Core grows and the temperature ranges between 10 and 20 K, and $M_* = 0$.

2. Class 0 protostars: Young protostars embedded in early envelope clouds. Observationally, Class 0 objects are envelope dominated protostars ($M_* << M_{env}$), which exhibit a collimated CO outflow and present a high sub-millimeter to bolometric luminosity ratio (see Andre et al., 1993, 2000 for more detailed information).

3. Class I protostars: Represent a more advanced phase of protostellar evolution with $M_* > M_{env}$ in which the central stellar radiation heats the surrounding dust and gas. The observation of these objects can be made at sub-millimeter, and infrared, and sometimes at optical wavelengths (André, 2002 and references therein).

4. Class II or T Tauri pre-main-sequence stars: These objects correspond to classical T Tauri stars, surrounded by optically thick circumstellar disks and only residual envelopes (see Fig. 1.2.

5. Class III pre-main-sequence stars: These objects correspond to “Weak” T Tauri stars whose spectral energy distribution (SED) resemble a stellar blackbody. The PMS star is surrounded by an optically thin debris disk, presumably hosting planets.

While this evolutionary sequence for young low-mass stars is relatively well constrained, the initial conditions of protostellar collapse and the early steps of the accretion process are still, however unclear. The manner in which a molecular cloud is organized from large scales ($>$ pc) to small scales (AU) can provide information about star formation in the ISM. Furthermore, studying the role of magnetic fields at different stages of the star formation process and different scales in a molecular cloud and at different wavelengths will give key insight into the star formation process. Whether gravity, turbulence, magnetic fields, or angular momentum, is the dominant factor regulating star formation in the ISM, is still under debate. In the next sections, I introduce the role of molecular filamentary structures, turbulence, and magnetic fields in star formation.

1.2 Filamentary structures in the cold ISM

Molecular clouds (MCs) in the ISM made mostly of H_2 are usually classified by their mass and size (e.g., Miville-Deschênes et al., 2017). Molecular clouds are highly filamentary, and the filamentary structure can be detected in high dynamic range observations of both CO lines and dust emission (e.g., André et al., 2014 and references therein). Observations of star-forming clouds at high angular resolution and different wavelengths allowed the detection of elongated structures in MCs. For example, CO line and dust continuum observations have been used to study MCs for a few decades.

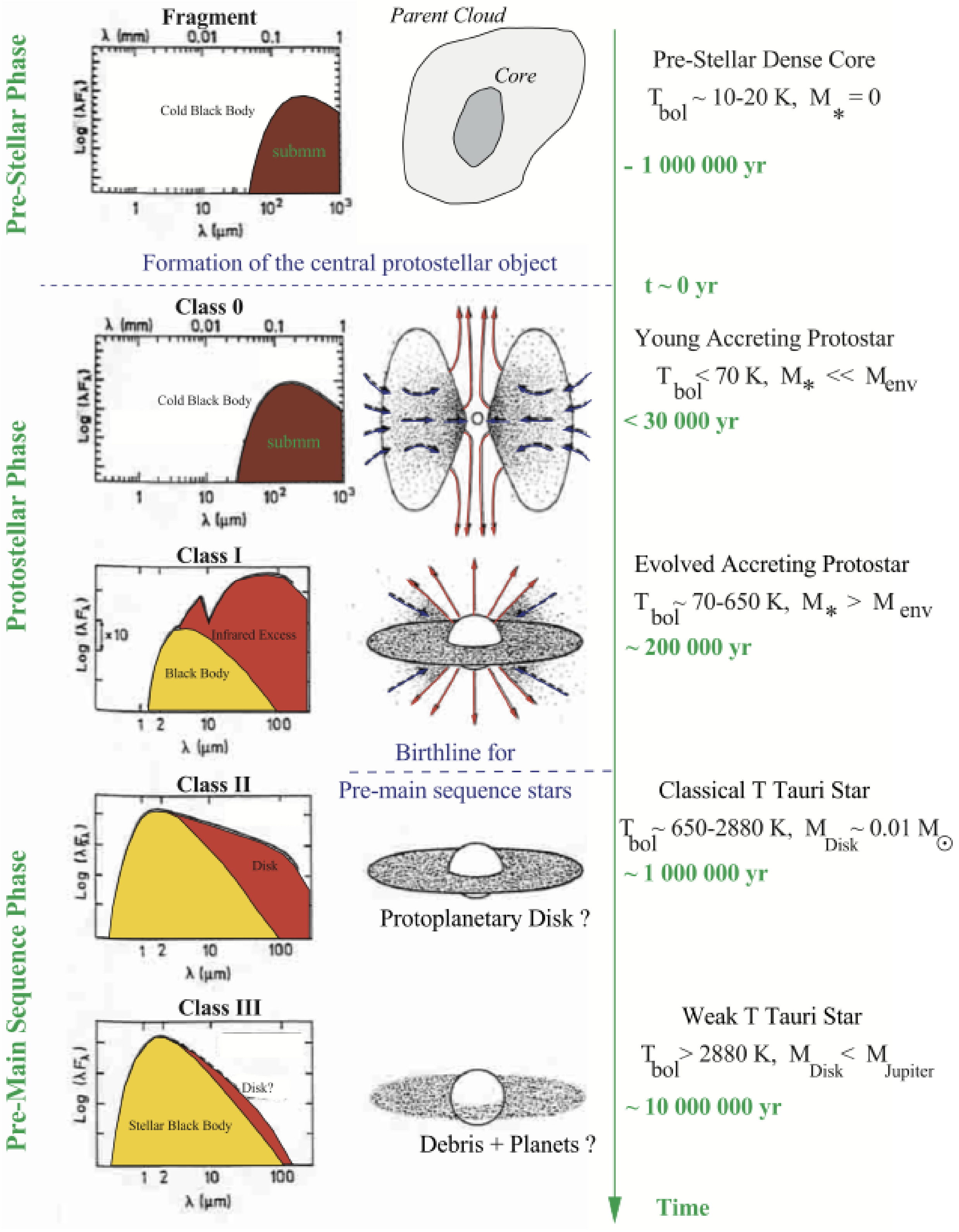

Figure 1.2: Schematic illustration of the evolutionary sequence from a prestellar core to Class 0, I, II III Young Stellar Objects (YSOs). *Left* : Evolutionary stage of the star formation process from the fragmentation phase (first case on the top) to the Pre-Main Sequence Phase (the bottom case). *Left* : Temperature, circumstellar masses, and timescales for each evolutionary stage (figure from André, 2002).

Bally et al. (1987) observed the Orion A region and found the well-structured Integral Shape Filament (ISF). They pointed out the importance of these filaments in the evolution of MCs. Later on, Chini et al. (1997) observed the same region and found the presence of protostellar condensations along the OMC-2 and OMC-3 portions of the ISF. Sub-millimeter observations at 450 μm and 850 μm of the Orion A cloud with SCUBA on JCMT revealed a high structured filament in this region (Johnstone & Bally, 1999). Other CO observations toward different MCs have revealed their filamentary structure, such as Taurus cloud, Musca-Chamaeleon, and Perseus (see André et al., 2014 for more details).

Over the last decade, detailed observations of MCs in both dust continuum with *Herschel* and CO lines have suggested that the filamentary structured molecular clouds are a key to understand the star formation process (e.g, see for example, the CO mapping studies of the Taurus cloud by Goldsmith et al., 2008; Hacar & Tafalla, 2011; Hacar et al., 2013).

It is only with the *Herschel* Space Observatory (Pilbratt et al., 2010) that these filaments have been well characterized and studied in detail (André et al., 2010, 2014). *Herschel* imaging of star-forming regions in the ISM with high angular resolution at 70 μm - 500 μm wavelengths revealed the crucial role played by interstellar filaments in the star formation process (André, 2017). The *Herschel* results emphasized the universality of interstellar filaments in which for star formation occurs. These results provided new insights into the origin of the stellar initial mass function, e.g, using the census of prestellar cores extracted from *Herschel* observations (e.g, Könyves et al., 2015).

In the present section, I present the main results of the *Herschel* observations of nearby molecular clouds and the importance of filaments in star formation (see the example of the Aquila cloud complex in Fig. 1.3).

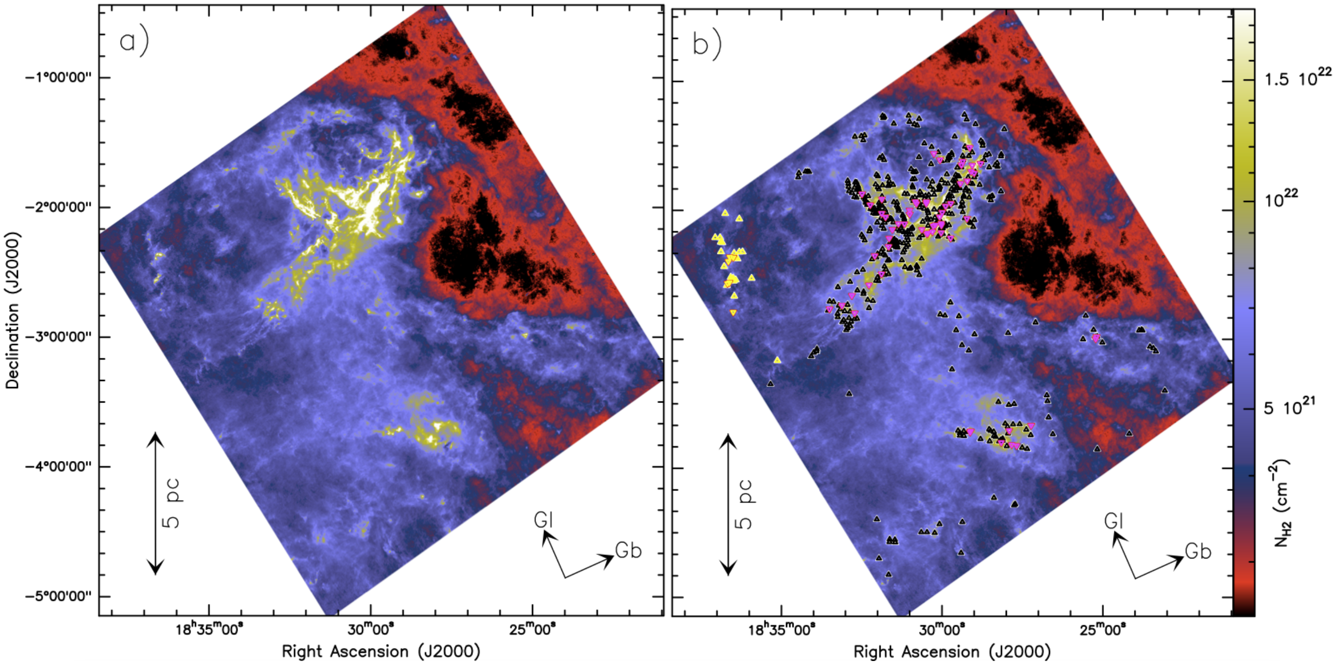

Figure 1.3: *Herschel* observations of the star-forming cloud Aquila (André et al., 2010; Könyves et al., 2015). a) : Column density map (H_2) from the *Herschel* Gould Belt Survey of Aquila region at 18″ angular resolution. b) Similar to a) but with the 446 detected prestellar cores and 58 protostars identified using getsources from *Herschel* data shown as black and magenta triangles (Men'shchikov et al., 2012) overlaid on the column density image. This figure is taken from Könyves et al. (2015).

1.2.1 Molecular filamentary structures revealed by the *Herschel* Space Observatory

Four main large surveys of Galactic molecular clouds were carried out with *Herschel*, (1); The *Herschel* Gould Belt Survey (HGBS) (André et al., 2010), (2); The *Herschel* Infrared Galactic Plane Survey (HIGAL) (Molinari et al., 2010), (3); The *Herschel* imaging survey of OB young stellar objects (HOBYS) (Motte et al., 2010), (4); The Galactic cold cores (or clumps) survey (Juvela et al., 2010). Molecular filaments proved to be omnipresent in all observed regions. Observations of the cold ISM with *Herschel* have already helped to understand the filamentary structures in the ISM and have provided clues to the star formation process (André et al., 2014). Panels (a) and (b) of Fig. 1.3 show the column density map of the Aquila region as observed in the *Herschel* Gould Belt survey (HGBS) overlaid with the detected prestellar and protostar cores (Könyves et al., 2015). The spatial distribution of filaments varies from one cloud to the other, and some contain very complex filamentary networks with low-density sub-filaments (Arzoumanian et al., 2019). Some of the clouds observed with *Herschel* are organized in hub-filamentary systems, for example, the Mon R2 hub-filament system (Didelon et al., 2015).

1.2.2 The common inner width of molecular filaments

Detailed analysis of the radial column density profiles of HGBS filaments suggests a quasi-universality of filament inner widths with a typical half power value of ∼0.1 pc at least in nearby star-forming regions (Arzoumanian et al., 2011, 2019; Palmeirim et al., 2013; André et al., 2014; Koch & Rosolowsky, 2015; Schuller et al., 2021). The radial column density profiles of molecular filaments can be described using a Plummer-like function and can generally be well expressed as :

$$\rho_p(r) = \frac{\rho_c}{[1+(r/R_{flat})^2]^{\frac{p}{2}}} \rightarrow \Sigma_p(r) = A_p \frac{\rho_c R_{flat}}{[1+(r/R_{flat})^2]^{\frac{p-1}{2}}} \tag{1.7}$$

Where ρ_c is the density at the center of the filament, R_{flat} is the radius of the flat inner region, p is the power-law exponent of the density profile at large radii, $p \approx 2$ at large radii (r>> R_{flat}). A$_p$ is a constant factor that takes into account the inclination effect of the filament in the plane of the sky.

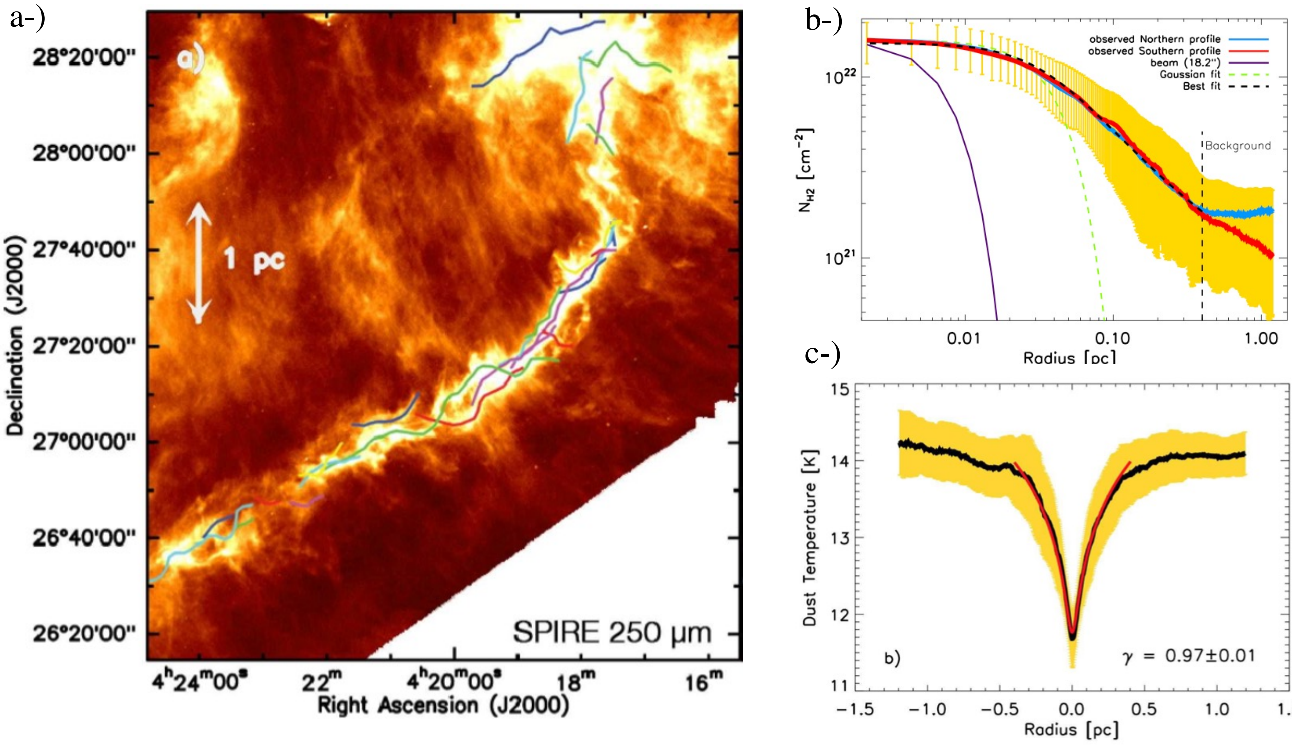

Figure 1.4: Column density radial profile of the B211/B213 filament in Taurus based on *Herschel* Gould Belt Survey data. *a-)* : *Herschel* dust continuum image at 250 μm of the B211/B213 filament in the Taurus region (Palmeirim et al., 2013), with the fiber-like structures detected in C^{18}O(1-0) molecular line observations by Hacar et al. (2013) overlaid. *b-)*: The radial column density profile of B211/B213 region for the Northern and the Southern part of the filament in blue and red color, respectively. The yellow bars show the 1σ dispersion of the radial profile along the filament. The purple and the black curves indicate the effective resolution and the best fit using the Plummer-like function, respectively (Palmeirim et al., 2013; André, 2017). *c-)*: The dust temperature profile measured perpendicularly to the B211/B213 filament and fitted by the Plummer-like model (for more details, e.g., Palmeirim et al. (2013)).

For example, Palmeirim et al. (2013) investigated the width and radial profile of the B211/B213 filament in the Taurus cloud from the *Herschel* GBS observations using the mean radial column density profile and found an inner width of ∼ 0.1 pc as plotted in panel b of Fig. 1.4. Arzoumanian et al. (2019) conducted the same analysis of the radial column density profile of 600 filaments in 8 nearby molecular clouds observed with *Herschel* and found that the distribution of filament widths has a narrow histogram shape with a median of 0.09 pc and a standard deviation of about 0.04 pc.

The universality of the filament widths suggested by the *Herschel* results has been confirmed by other dust continuum instruments, such as SCUBA at 850 μm where Salji et al. (2015) found a similar width for most of the filaments detected in the Orion A cloud. The omnipresence of filamentary structures with a typical inner width ∼ 0.1 pc in nearby star-forming regions has raised many questions about the origin of the filaments themselves and the physical interpretation of their typical transverse scale. A possible explanation of this from *Herschel* result is that the intersection of two shock waves forms the filaments as possibly already observed in some regions (for example, OMC-1 in the Orion A cloud observed by Smith, 1991 using H_2 spectrum) due to the supersonic turbulence in the ISM (Federrath, 2016; André, 2017). On the other hand, others claim that magneto-hydrodynamic turbulence is the origin of this universal width of molecular filaments (i.g, see André et al., 2014; André, 2017 and references therein).

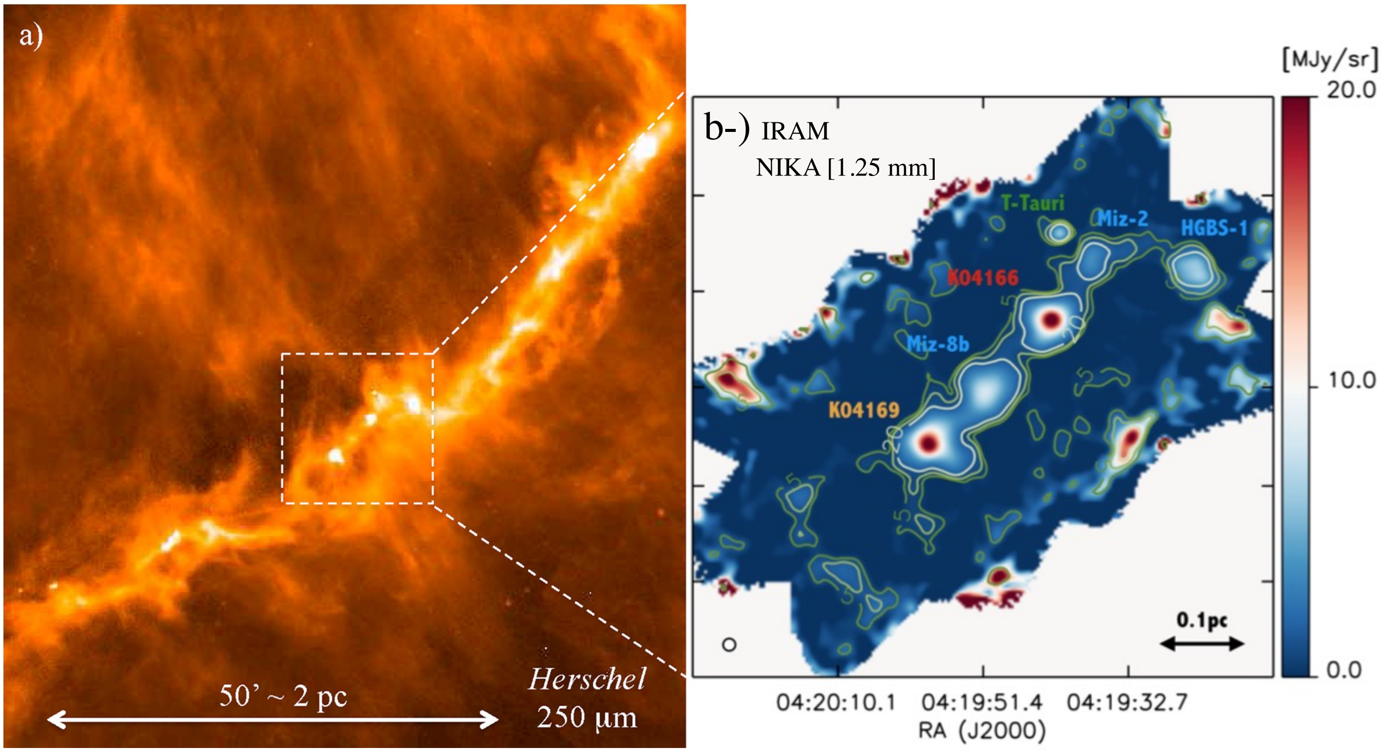

Figure 1.5: The Taurus B211/B213 filament as seen by the HGB Survey. *a-)* : *Herschel*/SPIRE dust continuum map of B211/B213 at 250 μm (Palmeirim et al., 2013; Marsh et al., 2016). *b-)* Intensity map zooming sub-region of B211/B213 with NIKA/IRAM at 1.25 mm showing six detected cores in this region (Bracco et al., 2017). Figure taken from André (2017).

1.2.3 From filaments to star-forming cores

A challenging question is how filaments structures in molecular clouds are involved in the star formation process. A detailed analysis of high-resolution observation of nearby star-forming regions provided by *Herschel* led to another major result which is that most of prestellar cores (> 75%) are found in filaments (André et al., 2010; Könyves et al., 2015). An example of a chain of dense cores along the B211/B213 filament as seen with *Herschel* is shown in Fig. 1.5a and at higher angular resolution with NIKA at the IRAM 30m telescope in Fig. 1.5b. *Herschel* observations in the Aquila region identified 446 prestellar cores and 58 protostars and most of them lie in filaments (cf, Fig. 1.3 from Könyves et al., 2015).

Other *Herschel* GBS observations confirmed that most of prestellar and protostellar cores are identified along filaments (e.g, Marsh et al., 2016; Könyves et al., 2020; Ladjelate et al., 2020; Di Francesco et al., 2020; Pezzuto et al., 2021). SCUBA-2 observations of the Orion A star-forming region also found that most dense cores candidates are located within the filamentary structures in this region (Salji et al., 2015).

1.2.4 A Filament paradigm for star formation ?

The *Herschel* findings in nearby star-forming clouds support a "filament paradigm" for star formation (André et al., 2014; Inutsuka et al., 2015), in which: (1) The large scale MHD turbulence compresses the interstellar material to form a web of filamentary structures of $\sim$ 0.1 pc width in the clouds, (2); Most of these filaments accrete material from their surroundings and the densest ones collapse to form prestellar cores (or protostars) under their gravitational instability after exceeding the critical mass per unit length. This filament paradigm provides clues to the problem of the origin of the IMF, which relies on the fact that most of the cores form in gravitationally unstable cylindrical filaments. The filament paradigm suggests that magnetic fields play a role in controlling the evolution of interstellar filaments and regulating the star formation process. The filament paradigm differs from the gravo-turbulent scenario which relies purely on gravity and turbulence as the main factors regulating star formation in molecular clouds (see Sect. 1.1.2.2).

1.3 Interstellar turbulence

Turbulence in the ISM can be described as a chaotic multi-scale flow of material in the medium. The turbulence can be compressible, supersonic and magnetized turbulence or incompressible turbulence (Mac Low & Klessen, 2004). The mathematical description of incompressible turbulence was first introduced by Kolmogorov (1941). Larson (1981) analyzed 54 molecular clouds and found that most of them did not collapse and suggested that hydrodynamic turbulence would disperse a part of the material and produce substructures in the cloud. He found scaling relation between the density ρ, the velocity dispersion σ and the size R of each cloud, $\rho \propto R^{\alpha}$ and $\sigma \propto R^{\beta}$, where $\alpha \sim 2$ and $\beta \sim 0.5$ are constant scaling exponents (e.g, Mac Low & Klessen, 2004). Turbulence in magnetized turbulent clouds is dominated by the interaction of Alfvén waves which can be described by a Kolmogorov 1D energy spectrum scaling as $k^{-5/3}$, where k denotes the wave number (Mac Low & Klessen, 2004, and references therein). Several attempts to understand the role of turbulence in star formation have been carried out by confronting numerical simulations and observations. The first step to understand the role of turbulence in star formation is to characterize the column density fluctuations at different scales (Ballesteros-Paredes et al., 1999, 2020). The density/velocity fluctuations observed in molecular clouds are typically originated from large-scale turbulence. Observations of velocity fluctuations along filaments provide direct measurements of the variation of turbulence in the medium. The kinematics analysis of the interstellar medium using molecular line observations showed the variation of turbulence in the ISM from a large-scale turbulent cloud down to core scales.

A recent analysis of the column density fluctuations along 80 filaments detected with *Herschel* in nearby star-forming clouds suggests that the power spectrum of these fluctuations is consistent with 1D Kolmogorov spectrum (Roy et al., 2015). The non-thermal velocity dispersion in a cloud depends on cloud size (e.g, Larson, 1981). Thus it provides a piece of information about the turbulent motions in filaments. For example, Arzoumanian et al. (2013) found that thermally sub-critical and trans-critical filaments mostly have a "transonic" velocity dispersions ($c_s \preceq \sigma_{tot} \preceq 2c_s$, where c_s is the sound speed). In contrast, the non-thermal velocity dispersion of super-critical filaments exceeds the sound speed (c_s). However, column density fluctuations do not provide a direct measurement of turbulent motions. Therefore as part of this thesis, I analyzed the velocity power spectrum of a sample of filaments using kinematic observations and centroid velocity information in the Aquila region. A discussion of this power spectrum analysis using velocity fluctuations instead of column density fluctuations is presented in chapter 7 of the present thesis.

1.4 Magnetic fields in the star formation process

The role of magnetic fields in star formation and interstellar clouds has been under debate for several decades. The importance of B-fields in the star formation process has been a subject of several studies that confronted simulations and observations.

In the present section, I discuss the importance of studying magnetic fields to understand the star formation process in magnetized turbulent clouds within the cold ISM. The next chapter will review the techniques used to measure the geometry and strength of magnetic fields.

The gravo-turbulent paradigm (Mac Low & Klessen, 2004) of star formation in which magnetic fields have a negligible importance does not take into account the case of a strong magnetic field present in the clouds. Thus, this scenario is incomplete to understand the star formation process. The applicability to real filaments of the simple model of fragmentation of isothermal cylindrical filaments depending on their mass per unit length as presented in Inutsuka & Miyama (1997) is debatable. One possibly key and ignored ingredient is the magnetic field which may be the missing part to understand the star formation. However, recent simulations and observations have revealed the important role played by the magnetic field in regulating molecular clouds evolution and therefore star formation in the ISM (e.g, for models and simulations ; (Hennebelle & Fromang, 2008; Hennebelle & André, 2013; Hennebelle et al., 2016; Soler & Hennebelle, 2017), for observations (Chapman et al., 2011; Crutcher, 2012; Palmeirim et al., 2013; Planck Collaboration et al., 2016a,b,c; Soler et al., 2016; André et al., 2019)). Knowing the strength and direction of the magnetic field in molecular clouds would help to understand at which stage and at which scale the magnetic field becomes more important. Depending on the strength and geometry, the physical conditions of the medium are different (e.g., Crutcher, 2012). How molecular filaments fragment into cores is not yet well understood, but there are hints that the magnetic field is crucial in this process (André et al., 2014). Investigating how the magnetic field is organized from the large scales of the parent molecular clouds to filament scales and core scales is one of the main motivations for this thesis.

1.4.1 Dominant magnetic fields

The critical mass-to-flux ratio in which a cloud is supported by the magnetic field can be obtained using the virial equilibrium equation $(\mathrm{M}/\Phi)_{crit} \approx (1/3\pi)\sqrt{5/G}$ (where G is the gravitational constant). The normalized mass-to-flux ratio $\mu_\Phi = (M/\Phi)_{cloud}/(M/\Phi)_{crit}$ is mostly used to identify whether the cloud is magnetically super-critical or sub-critical. In case of $\mu_\Phi < 1$, the magnetic field is strong and more important than gravity, and preventing cloud collapse. The magnetic field strength increases and counters the collapse of the cloud and slows down the star formation process. Strong magnetic fields in a turbulent environment mainly delay the gravitational instability. At the same time, the B-field is frozen in the dust and gas, which contracts radially and help to increase the mass inside the core until it becomes magnetically super-critical, the mass increase in the center of the core and the gravity takes over and the clump/core-collapse under gravitational instability (e.g., Crutcher, 2012). This process is called the magnetic flux diffusion, or ambipolar diffusion described already in Sect. 1.1.2.4 (Nakano & Nakamura, 1978).

Another way to examine the importance of magnetic fields versus gravity in the filament is to compute its mass-to-flux ratio (described in Sect. 1.1.2.3), which can be expressed as $\mu_\phi = 7.6 \times 10^{-21}\ N_{H_2}/B$ (Crutcher, 2004), where N_{H_2} is the column density of the filament, B is the measured magnetic field strength in μG. If $\mu_\phi > 1$ (normalized ratio), the filament is magnetically super-critical and the gravo-turbulent model is more likely the dominant scenario in the star formation process. If $\mu_\phi < 1$, the cloud is magnetically sub-critical which favors the ambipolar diffusion scenario. When the $\mu_\phi \simeq 1$, the filament is magnetically transcritical, and magnetic field and gravity forces balance each other (Crutcher, 2012). The B-field lines in the strong-field model are more ordered and tend to be perpendicular to the main filaments in the cloud as shown in the simulations from Li et al. (2015) in panel a-) of Fig. 1.6 and from *Planck* dust polarization observations (Planck Collaboration et al., 2015, 2016a,b,c).

1.4.2 Weak magnetic fields

This model assumes that the magnetic field is very weak $\mu_\Phi >> 1$ and the turbulence is super-Alfvénic. Thus it has relatively little importance compared to gravity and turbulence. Large-scale supersonic MHD turbulence regulates the cloud and forms filaments in it (filament paradigm, e.g., André et al., 2014). When the mass of the cloud exceeds the Jeans or Bonnor-Ebert critical mass, the cloud becomes gravitationally unstable and collapses to form a new protostellar core. In this model, the magnetic field cannot prevent the cloud from collapsing because turbulence and gravity are energetically dominant. However, the magnetic pressure in the filament can be more important in the last stages of gravitational collapse (Crutcher, 2012). The mass-to-flux ratio in this model varies from the large scale of the cloud to the filament scales (∼0.1 pc), and some filaments are magnetically sub-critical, and some others are magnetically super-critical depending on their masses. In the weak field model, the field lines are more perturbed due to strong turbulent motions in the cloud (panel b in Fig. 1.6).

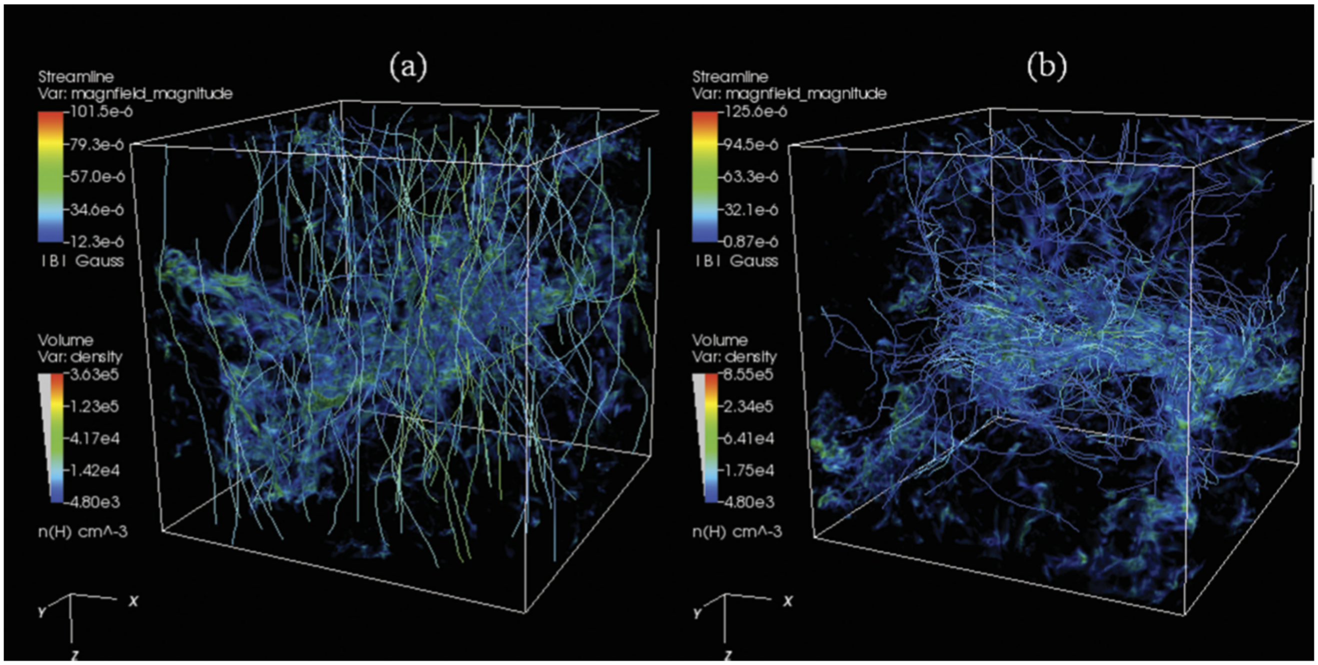

Figure 1.6: Difference in the organization of B-field lines between weak-field and strong-field numerical models (from Li et al., 2015). Organized field lines in the case of the strong-field model where the B-field is dominant (a) compared to highly-perturbed field lines in the case of the weak field model (Li et al., 2015)

.

1.5 Motivation for my thesis

The detailed analysis of the radial contraction and longitudinal fragmentation process of molecular filaments is crucial to understand star formation in molecular clouds. Numerical models predict the fragmentation of isothermal cylindrical filaments when they exceeds their line mass. However, Observational results have shown that even above the $M_{th}^{line,crit}$ threshold (16 $M_\odot$. pc^{-1}) filaments fragment (example of B211/B213 and NGC6334 e.g. Shimajiri et al., 2019; Shimajiri, 2019). Moreover, the standard filament fragmentation model discussed by Inutsuka & Miyama (1997) suggests a characteristic core spacing of 4 times the filament width (i.e, ∼ 0.4 pc) in the case of cylindrical filaments in isothermal equilibrium. However, observational results of super-critical filaments suggest two modes of fragmentation, (1); fragmentation of cylindrical filaments in which cores form in group/clumps spaced by ∼0.4 pc along the filaments, (2); Jeans-type fragmentation of filaments in which cores inside filaments collapse under their gravitational instability to form protostellar cores spaced by ∼0.1 pc (for example, Könyves et al., 2015 found a typical spacing between *Herschel* cores of about 0.08 pc).

The question that remains unanswered is how some filaments contract radially or fragment longitudinally to form cores especially in high mass filament structures, and others are unable to contract/fragment. To answer this question, one needs to explore different physical conditions of the filaments and have more observational constraints on the fragmentation of filaments into cores. For example, the isothermal equilibrium of filaments is not universal, and filaments are also not strictly isothermal, especially in the case of high mass filaments, and most of them accrete material from their surroundings. Depending on its orientation (parallel or perpendicular to the filament), magnetic fields may play a crucial role for both the radial contraction and the fragmentation of filaments. The magnetic field geometry may lead the filament to its gravitational instability and help the fragmentation of the material inside of it, or it can prevent the fragmentation. High-angular resolution, sensitive polarimetric observations are needed to highlight the role of magnetic fields in star-forming filaments.

While detailed knowledge of the distribution of magnetic fields in the ISM is crucial to understand the star formation process, the lack of data at sufficiently high resolution and over a wide range of wavelengths has so far prevented any definitive conclusion about the role of magnetic fields. Nevertheless, recent polarization observations have revealed a multi-scale morphology of magnetic fields in the ISM (Planck Collaboration et al., 2016a,c; Alina et al., 2019; Pattle & Fissel, 2019). Combining the observed morphology and strength information of the magnetic field will peer into the enigma of the star formation process and help to understand the role of B-fields in filament fragmentation/contraction. The main motivation for my thesis has been to probe the magnetic field geometry and strength from filament scales (>> pc) to core scales (<<0.1 pc) and at different wavelengths and different angular resolutions thanks to the B-FUN large program with NIKA2-Pol at the IRAM 30m telescope and to a smaller pilot program with the HAWC+ polarimeter on the SOFIA airborne telescope. I will present promising work toward understanding filament fragmentation into cores in the case of the trans-critical filament B211/B213 in Taurus observed with SOFIA/HAWC+, showing how the magnetic field regulates the star formation process in this region (see Chapter 6).
In this chapter, I gave general information about the ISM and the critical driving parameters of the star formation process. The next chapter will review some recent results on measuring the magnetic field morphology/strength in the cold ISM.

Chapter 2

Magnetic fields in star-forming filamentary molecular clouds

Contents

2.1 Introduction

This chapter introduces the technical methods of measuring magnetic fields in the ISM, especially by observing the polarized thermal emission from dust grains in interstellar clouds. Polarization observations can be used to infer the geometry and strength of magnetic fields in the ISM. Measuring the polarization by observing the thermal radiation of elongated dust grains has been used for decades to scrutinize the role of magnetic fields in star-forming regions. Dust polarimetric mapping of molecular filaments provides a good estimation of the geometry/strength of magnetic fields in star-forming filaments from the large-scale diffuse clouds to core scales. Recent polarization observations of nearby molecular clouds have raised several questions about the role of B-fields in the star formation process. In-depth analysis of polarization observations from cloud scales ($\sim$ 20 pc) to core scales ($<$0.1 pc) will provide key insight into the star formation process. Observing how the B-field geometry changes with column density, and thus the physical conditions of the medium with the high angular resolution and sensitivity of the current and next generations of polarimetric imaging instruments is crucial (André et al., 2019; Pattle & Fissel, 2019).
In section 2.2, I introduce generalities about dust polarization observations. In section 2.3, I show recent results

of the magnetic field geometry/strength in filaments. I present the Davis-Chandrasekhar-Fermi method, which is one of the widely-used methods to estimate the B-field strength from dust polarization observations (Davis, 1951; Chandrasekhar & Fermi, 1953). I briefly introduce the Zeeman effect, which directly measures the line-of-sight magnetic field strength in the ISM. The present chapter aims to help the reader understand state-of-the-art observations of the role of magnetic fields in the star formation process and present some open issues and questions that remain unanswered and to which my thesis attempts to provide answers. This chapter focuses only on observations of magnetic fields in interstellar filaments.

2.2 Observations of linear polarization from dust grains

The polarization of the light emitted by interstellar matter is produced by several mechanisms involving magnetic fields, mainly synchrotron radiation, Zeeman splitting, or dust emission. In this thesis, I will focus only on the thermal emission from elongated dust gains aligned with respect to the magnetic field. Several mechanisms have been proposed to explain the alignment of interstellar dust grains with magnetic fields, such as (1); the Davis-Greenstein mechanism, which is based on the rotation of dust grains and their paramagnetic properties, in which molecules have unpaired electrons allowing them to align with the magnetic field (Davis & Greenstein, 1951), (2); The Radiative alignment torque (RAT) mechanism which is based on the alignment of the dust by a supersonic gaseous flow producing the spin-up of the grains by the radiative torque arising from the anisotropy of the medium and producing a high degree of dust alignment with the magnetic field (Lazarian & Hoang, 2007; Lazarian et al., 2015; Andersson et al., 2015).

2.2.1 Stokes parameters

An electromagnetic wave is a superposition of two orthogonal components of the electric field $\overrightarrow{E}(\vec{r}, t)$ which propagates in a given direction. A wave propagating along Z axis can be described by the D'Alembert equation as follows :

$$\nabla^2 \vec{E}(Z, t) = \frac{1}{c^2} \frac{\partial^2 \vec{E}(\vec{r}, t)}{\partial t^2} \tag{2.1}$$

Monochromatic waves can be polarized circularly, linearly or elliptically and can be represented by their amplitude A and their phase ϕ. In the present work, I am mostly interested in the linear polarization in which the wave is monochromatic and the phase difference of the orthogonal vibrations is $\phi = 0$ (the orthogonal vibrations are in phase). A linearly polarized wave propagating along the Z axis with amplitude (E_{0X},E_{0Y}, E_{0Z}) along the (X, Y, Z) axes, respectively can for instance be linearly polarized along the X axis ($E_{0X} \neq 0$ and $E_{0Y} = 0$), along the Y direction ($E_{0Y} \neq 0$ and $E_{0X} = 0$), or polarized in 45° direction ($E_{0X} = E_{0Y} = E_0$ and $\phi = 0$ or $\phi = \pi$).
The polarization radiation of an electrical field can be described by four Stokes parameters in the case of a fully polarized, partially polarized, or unpolarized wave. The electric field $E = (E_X, E_Y, E_Z)$ for a plane wave propagating along the +Z direction with +X north and +Y east with their phases ϕ_X and ϕ_Y, respectively, can be expressed as follows :

$$\begin{aligned} E_X(Z, t) &= E_{0X} e^{i(kz - 2\pi\nu t - \phi_X)} \\ E_Y(Z, t) &= E_{0Y} e^{i(kz - 2\pi\nu t - \phi_Y)} \end{aligned} \tag{2.2}$$

where k is the wave number $k = \omega/c$, ω is the wave pulsation, c is the light speed, ν is the wave frequency, and ϕ_X and ϕ_Y are the phases of the wave along the X and Y axes, respectively. In each measurement of polarization, receivers typically detect incoming radiation either trough linear or circular polarized feeds. Using Equations 2.2, the Stokes parameters defining the polarization state of an electromagnetic wave are defined as follows :

$$\begin{aligned} I &= \langle E_X E_X^* \rangle + \langle E_Y E_Y^* \rangle \\ Q &= \langle E_X E_X^* \rangle - \langle E_Y E_Y^* \rangle \\ U &= \langle E_X E_Y^* \rangle + \langle E_X^* E_Y \rangle \\ V &= j(\langle E_X E_Y^* \rangle - \langle E_X^* E_Y \rangle) \end{aligned} \tag{2.3}$$

where E_X^* and E_Y^* are the complex conjugates of E_X and E_Y, respectively. A common way to express the Stokes parameters that takes into account directions of linear polarization (vertical, horizontal, or at ± 45°) is given as follows:

$$
\begin{aligned}
I &= |E_{0^\circ}|^2 + |E_{90^\circ}|^2 \\
Q &= |E_{0^\circ}|^2 - |E_{90^\circ}|^2 \\
U &= |E_{45^\circ}|^2 - |E_{-45^\circ}|^2
\end{aligned}
\tag{2.4}
$$

The Stokes parameters Q and U allow to interpret the linear polarization physically, and from them, we can derive other physical parameters, such as the polarized intensity, the polarization fraction, and the polarization angle. A simple way to express the Stokes Q and U as a function of the polarization fraction and polarization angle is given by the following formula:

$$
\begin{aligned}
Q &= I \times P_{frac} \cos 2\psi \\
U &= I \times P_{frac} \sin 2\psi
\end{aligned}
\tag{2.5}
$$

where P_{frac} is the fraction of linear polarization

$$P_{frac} = \frac{\sqrt{Q^2 + U^2}}{I} \tag{2.6}$$

and the polarization angle :

$$\psi = \frac{1}{2} \arctan(\frac{U}{Q}) \tag{2.7}$$

In our definition of the polarization angle, we use the IAU convention of the angle in which $\psi = 0^\circ$ represents the axis in North-South, and the polarization angle is measured East of North.

2.2.2 Polarimetric imaging techniques

To measure the polarization in the plane of the sky, one needs detectors to measure the difference in the power of electrical fields between different directions. Due to the noise coming from the instrument itself or from the background to the sky emission (atmospheric backgound in the case of a ground-based instrument), modulation of the signal is needed to measure the Stokes Q and U parameters properly. Recent ground-based polarimeters have used a fast modulation technique or the measurements of the E-field power difference to provide polarization observations. Technological development have allowed to increase the number of detectors in polarimetric cameras, the scanning speed, the sensitivity, and the angular resolution. Examples of sub-millimeter cameras are SCUBA-POL and SCUBA-POL2 at the James Clerk Maxwell Telescope (JCMT, 15-m) (Ward-Thompson et al., 2000; Bastien et al., 2011), HAWC+ on board SOFIA, and recently the NIKA2-Pol instrument at the IRAM 30m telescope (which is the main subject of this thesis). As Ground-based observations suffer from atmospheric effects, a far-IR/sub-mm space observatory with the ability to measure dust polarization star-forming regions would revolutionize the field [for example, *Planck* observations (Planck Collaboration et al., 2016a,c) and the cancelled SPICA space mission (André et al., 2019)].

In the present section, I will briefly describe polarization measurements using modulation. The classical method for the polarization observations is to measure the difference in E-field power using a grid installed in the light pathway with the detectors installed at the focal plane position, allowing the measurement of the parallel and perpendicular field simultaneously. In this section, I refer to Pattle & Fissel (2019) for a review of recent and forthcoming polarimetric imaging techniques.

2.2.2.1 Modulation of the polarized signal by a Half Wave Plate

The noise due to the thermal emission fluctuations from the atmosphere and the telescope can be reduced by using a rotating birefringent half-wave-plate (HWP). Such a HWP rotates the incident polarized wave by an angle of 2θ, where θ is the angle of the HWP rotation. The HWP can be used to measure the Stokes parameters in different directions, allowing proper measurement of polarized signal from the source. Modulation by a HWP has been widely used in recent years on ground-based polarimeters (e.g, SCUBA2-POL2, TolTEC, NIKA2-Pol). Thus, it is considered as one of the powerful techniques for polarization observations by modulation. However, this observing method does not allow to characterize the polarization noise in the light pathway from the source to the HWP position, and thus if some instrumental polarization comes from the mirror or other sources between the source and

HWP, this technique is unable to characterize precisely this effect; thus systematics errors should be included when estimating the polarized signal from the measured sources. The NIKA2-Pol has a continuously and fast rotating HWP at 3 Hz. The modulation by the HWP can also create a correlated noise in the timelines (detailed analysis of the HWP noise is presented in Ritacco (2016). This technique is the one used in NIKA2-Pol observations, three chapters about NIKA2-Pol are presented in this thesis showing my main contribution to the NIKA2-Pol commissioning and I also present new finding in OMC-1 filament in Orion A molecular cloud (see Chap. 3, Chap. 4 and Chap. 5).

2.2.2.2 Chopping technique

On the ground, the incoming light is always affected by the noise coming from the short timescale fluctuations of the thermal emission from the atmosphere, and one needs to observe an off-source or use a modulation technique (with a frequency >> 1 Hz) to subtract these fluctuations. The "Chopping" technique is based on observing a position free of polarization emission in the sky at high frequency by moving mainly the secondary mirror. Hildebrand et al. (2009) introduced this method for single-dish observations that allows removing the polarization from background of the sky efficiently. This technique uses neighboring reference points in the sky that are assumed to be free of polarized emission and is based on chopping between the source and these reference points. The limitation of this technique is that it requires a significant amount of time. If the reference positions have residual polarized emission, the measured polarization of the sources is biased by systematic errors (Pattle & Fissel, 2019). This technique is also called the Chop-Nod technique, which is used by several polarimeter instruments, such as SOFIA/HAWC+.

2.2.2.3 Scanning technique

The filtering of the sky noise and the measurements of the polarized emission from the source is done by scanning the telescope on faster time scales than the low-frequency (1/f) noise of the detectors and atmospheric fluctuations. For example, the balloon-borne polarimeter BLASTPol has used this technique to measure the Stokes Q and U parameters. It allows scanning the source faster by a detector measuring the orthogonal polarization with a grid in front of the receivers. The typical scan speed of the BLASTPol polarimeter was about $0.2^\circ .\ \mathrm{s}^{-1}$, compared to characteristic 1/f knee frequency of 50 mHz, which allowed to recover the polarized emission from large scales (more detailed information in Pattle & Fissel, 2019; Galitzki et al., 2014).

2.3 Dust polarization observations

Linear polarization observations probe the plane-of-sky (POS) morphology of magnetic fields in star-forming regions. Several instruments have been developed in the last decades to map linear polarization by using different techniques of modulation (e.g., Novak et al., 1989; Platt et al., 1991; Pattle & Fissel, 2019 and references therein). Inferring the B-field geometry using the polarized emission from dust has helped in understanding how the B-field lines change their orientation from Galactic scales to cloud scales and from filamentary structures to core scales. The dust grain alignment efficiency is mainly dependent on the grain size, and the long wavelengths trace the alignment of large grains (Crutcher, 2012). Observations at millimeter and submillimeter wavelengths are important to trace different grain alignments and thus the morphology of the magnetic field in star-forming regions. The filament paradigm based on *Herschel* and *Planck* results suggests the importance of the B-field in regulating star formation in interstellar clouds (André, 2017, see Chap. 1). The unprecedented high angular resolution far-infrared imaging from *Herschel* and pioneering results from its observations raised the need for observations of comparable quality (e.g., angular resolution and dynamic range) in dust polarization toward molecular clouds.

2.3.1 The magnetic field geometry from cloud scales to core scales

In the last century, several linear polarization observations have been carried out in star-forming regions in attempts to understand the role of magnetic fields in the star formation process. For example, one of the widely and well-studied regions is the Orion A molecular cloud (see Chap. 5). Most of the polarization observations have been made using ground-based telescopes (e.g. Ward-Thompson et al., 2000; Siringo et al., 2004a); the big step in the field was after the great result of the *Planck* satellite. *Planck* dust polarization observations of the whole Galactic plane at $10'$ angular resolution and at 353 GHz have revealed unexpected results about the magnetic field morphology in the ISM. According to these observations, the magnetic field lines appear to have a regular, organized morphology on large ($\sim$pc) scales, perpendicular to dense star-forming filaments. On small ($<$0.1 pc) scales, however, there are

hints that the magnetic field may change direction and become more parallel to the long axis of dense star-forming filaments or form an hourglass shape in some cases (Planck Collaboration et al., 2016a,b,c).
Two important reasons to study the magnetic field morphology, (1); Probing the B-field lines from cloud scales to core scales helps to investigate how the field changes with the physical and environmental conditions and allows to build strong observational constraints on its role in regulating the star formation process, (2); The B-field strength varies depending on scales (and environments), this will provide information about whether filaments are magnetically sub-critical, trans-critical or supercritical. (Crutcher, 2012; André, 2017).
The low-resolution of *Planck* polarization observations prevents probing B-fields at filament scales where star formation occurs. Several polarization observations have suggested a significant change in the B-field geometry at filament scales. For example, recent polarization observations with SCUBA2-POL2 at 850 m and 14″ angular resolution have confirmed the observed large-scale hourglass in the OMC-1 region at Orion A cloud (Pattle et al., 2017a). More recent polarization observations from SOFIA/HAWC+ have provided more information about the in change B-field geometry in molecular filaments at different wavelengths (Chuss et al., 2019; Guerra et al., 2021; Lee et al., 2021; Seo et al., 2021).

The B-field lines appear to have a regular morphology at large scales (cloud scale >>10 pc). They tend to be parallel to low-density striations (detected by *Herschel*) and perpendicular to dense filamentary structures in molecular clouds. For example, panel a-) in Fig. 2.1 shows the B-field morphology toward the Orion A cloud inferred from the *Planck* 353 GHz polarization observations and overlaid with the *Herschel* maps at 160 μm (blue), 250 μm (green), and 500 μm (red). The *Planck* beam is shown as a grey disk at the bottom of the map. The grey stream map is the integral line convolution (LIC) map which allows to visualize the B-field geometry nicely from the *Planck* polarization data. The *Planck* results on the geometry of the B-field have pointed out the importance of the B-field at large scales and suggested that it plays a significant role in regulating the evolution of molecular clouds (Planck Collaboration et al., 2016a,b,c). It is clear that at *Herschel* scales (the background image), the *Planck* observations are unable to probe the B-field geometry inside the filamentary structures in the cloud (in Orion A in this case).

In the interior of filaments, the B-field lines either conserve the large-scale behaviors (perpendicular to filament axis) or change their orientation to become more parallel to the filament or a mixture of both. There are hints that the B-field can be distorted in the vicinity of filaments, and the B-field lines tend to form an ordered hourglass pattern. For example, the B-field geometry in OMC-1 filament at Orion A cloud has been shown to form a large-scale hourglass. This hourglass has been confirmed by several instruments such as POLKA, SCUBA, SCUBA2-POL2, and in this thesis with NIKA2 (Siringo et al., 2004a; Johnstone & Bally, 1999; Pattle et al., 2017b). Thanks to the high angular resolution and sensitivity of NIKA2-Pol, I show in Chapter 5 new findings in OMC-1 of a possible local hourglass centered at the Orion-KL (see panel b in Fig. 2.1). For some other filaments, the B-field does not show a clear hourglass morphology. For example, in the case of the B211/B213 filament in the Taurus cloud, which we observed with SOFIA/HAWC+ (Li et al., 2021), and we found that the B-field lines are distorted (see Chap. 6). In NG6334, Arzoumanian et al. (2021) showed that the field lines are distorted in the vicinity and inside the filament. These results show that the B-field geometry depends on the considered spatial scales, the observing wavelength, and the column density of the target filaments.
At core scales ($\sim$ 0.1 pc), the B-field lines are distorted and mostly do not show regular morphology. The recently commissioned polarization mode of ALMA has provided high angular resolution images of polarized dust emission in the vicinity of Orion-KL (Belitsky et al., 2018). Panel c-) in Fig. 2.1 shows the B-field geometry inferred from ALMA polarization observations of the vicinity of Orion-KL in the OMC-1 region. ALMA mosaicing observations suggest the influence of shock waves on the B-field geometry at the position of Orion-KL. These unique polarization observations confirm the importance of the physical environment in shaping the B-field geometry in the star-forming regions.

At core and sub-core scales (<<0.1 pc), the B-field geometry varies from prestellar to protosellar cores. Several polarization observations have reported an hourglass shape of the B-field at cores scales. Therefore, if the B-field is strong enough, the lines tend to form an hourglass shape, indicating that magnetic tension resist the core's gravitational collapse. Panels d-) and e-) in Fig. 2.1 show the well-resolved hourglass pattern seen in a high-mass core and an intermediate-mass Class 0 protostar, respectively. d-) shows the hourglass shape of the B-field imaged in dust polarization at 1.3 mm with ALMA by Beltrán et al. (2019) toward the high-mass core G31.41+0.31 (M_{core} $\sim$ 26 $M_\odot$, and B-field strength of $B_{POS} \sim$ 10 mG). e-) shows the hourglass pattern seen from dust polarization at 0.85 mm with the SMA by Girart et al. (2006) toward the Class 0 object NGC 1333-IRAS4A ($M_{core} \sim$ 8 $M_\odot$, and

B-field strength of $B_{POS} \sim 5$ mG). The hourglass pattern can be used to estimate the B-field strength in the target core and the results can be compared to those obtained with the DCF approach. During this thesis, we submitted an ALMA polarimetry proposal to observe the high mass star-forming NGC6334 filament. The aim was to detect new possible hourglass pattern in intermediate-mass cores previously detected using ALMA observations (in total intensity) by Shimajiri (2019) (PI: Ph. André).

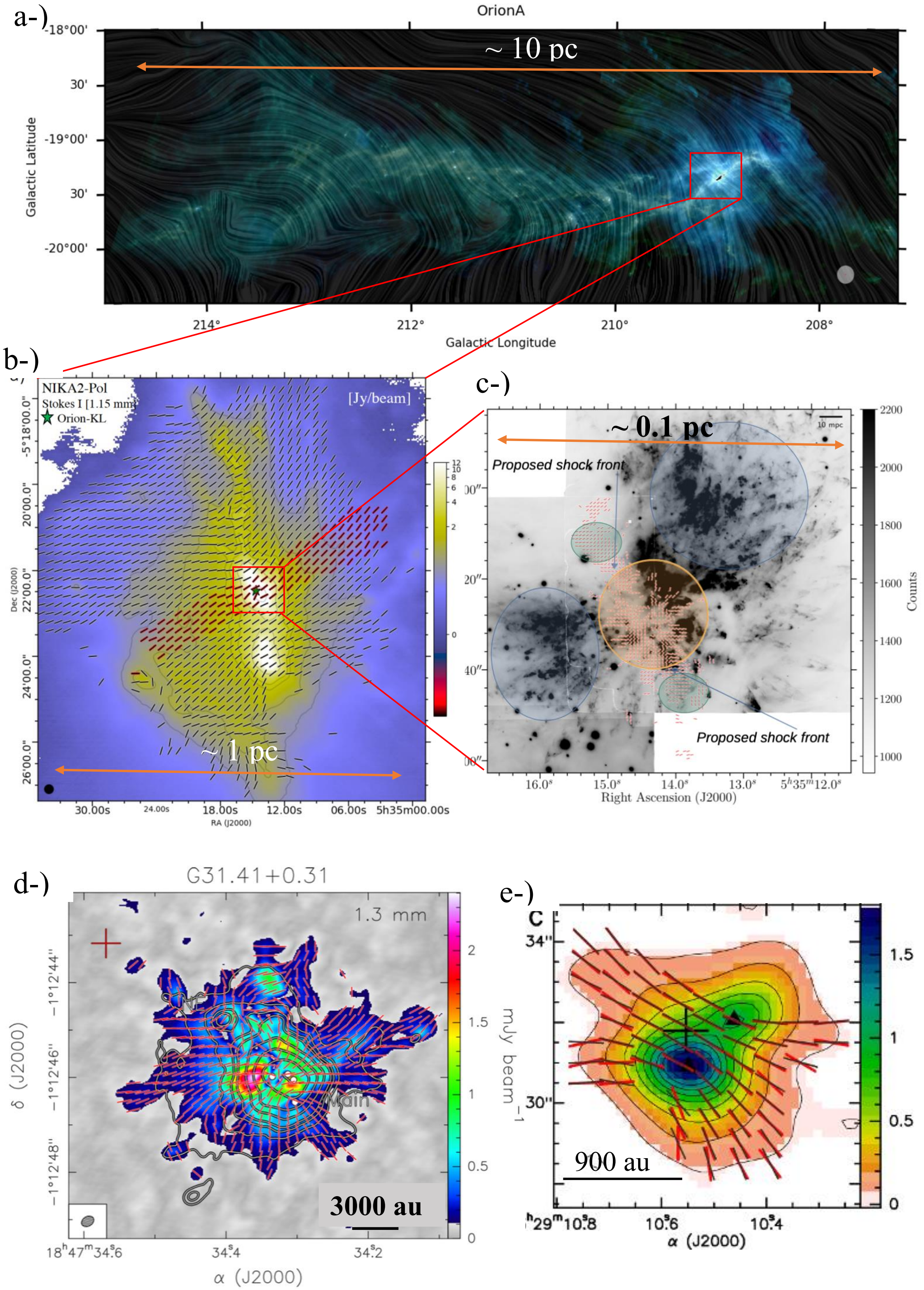

Figure 2.1: B-field geometry from cloud to core scales. a-) B-field in Orion A molecular cloud inferred from *Planck* observations overlaid on *Herschel* image (Soler, 2019). -b) B-field geometry inferred from NIKA2-Pol polarization observations (this thesis, **Ajeddig et al. in prep**). c-) ALMA polarization mosaic observation of Orion-KL vicinity (Cortes, 2019). d-) and e-) hourglass pattern seen in a high-mass core and a Class 0 protostar, respectively (Beltrán et al., 2019; Girart et al., 2006).

Studies of the role of magnetic fields in regulating star formation in the ISM need to be carried out by combining information on the B-field geometry and the B-field strength. Quantifying the change of the B-field angles as a function different parameters (angular resolution, wavelength, and physical conditions) provides additional information about how the B-field morphology changes from low to high column density.
The IRAM 30m large program B-FUN with NIKA2-Pol "Probing the B-Field in star-forming Filaments Using NIKA2-Pol (B-FUN) " 300 hours observations of nearby molecular filaments will help in understanding the role of magnetic fields in filament evolution and fragmentation. It will provide high angular resolution and sensitive polarization data that will investigate the link between large-scale fields and protostellar magnetic fields. B-FUN 30m large program will help to make decisive progress in how magnetic fields regulate star formation, It will provide a 1.2 mm polarimetric imaging survey with NIKA2-POL of ∼8 nearby star-forming filaments spanning a range of line masses from marginally supercritical to highly supercritical (PI: Ph. André).

2.3.2 The magnetic field strength in the ISM

While the magnetic field geometry is essential, as discussed in the previous section, measuring the B-field strength is also important to constrain star formation models. There are two main methods to estimate the B-field strength in the ISM. One way is to use dust polarization observations to infer the strength of the plane of sky B-field based on the observed perturbations of the B-field position angles. The second method is a more direct measurement of the line-of-sight field strength by observing the Zeeman effect. In the present section, I briefly review these two methods of estimating the B-field strength.

2.3.2.1 The Davis-Chandrasekhar-Fermi method

One of the commonly used methods of estimating the field strength from dust polarization observations is the Davis-Chandrasekhar-Fermi (DCF) method, introduced by Davis (1951) and Chandrasekhar & Fermi (1953). This method is based on analyzing the perturbation of the B-field angles inferred from dust polarization observations. It assumes equipartition between the turbulent energy and the magnetic energy in the medium. The perturbations of the mean-field are assumed to be due to the Alfvén waves resulting in distortion of the field lines. Figure 2.2 shows an illustration of how a mean-field perturbed by turbulent motions yields distorted field lines in the medium.

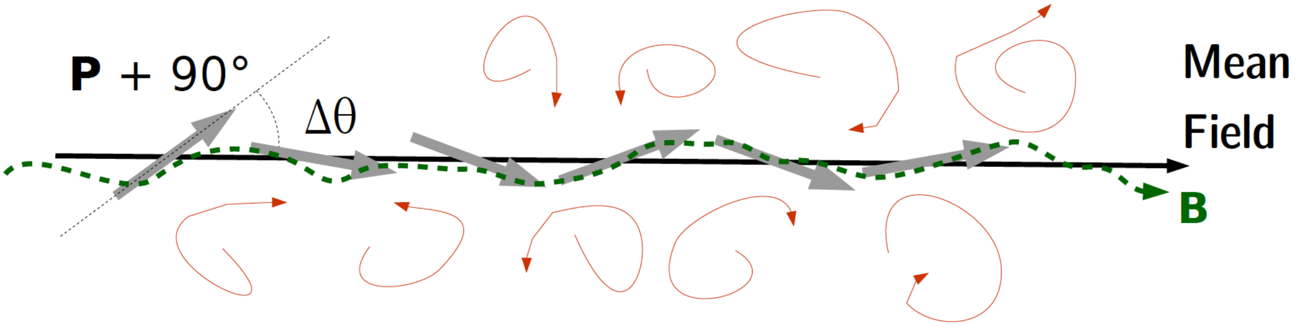

Figure 2.2: Illustration of the main assumption used in Davis-Chandrasekhar-Fermi (DCF) estimates of the magnetic field strength. The field lines are distorted due to the turbulent motions caused by the Alfvén waves. (from Kate Pattle)

The relation between the magnetic field strength in plane-of-sky and turbulent Alfvén waves at large-scale can be expressed as follows :

$$\frac{\delta B}{B_0} \simeq \frac{\sigma_V}{V_A} \tag{2.8}$$

where σ_V is the line-of-sight velocity dispersion and V_A is the Alfvén speed.
The plane-of-sky magnetic field strength from polarization observations and using the DCF method can be estimated as follows :

$$B_{POS} = \xi \sqrt{4\pi\rho} \frac{\sigma_v}{\sigma_\theta} \tag{2.9}$$

where $\rho = mn(H_2)$ is the gas density, σ_v is the velocity dispersion, σ_θ is the dispersion of the polarization angles, and ξ is a correction factor (Ostriker et al., 2001; Crutcher, 2004). A value $\xi = 0.5$ is mostly used to estimate the magnetic field in nearby star-forming regions and it is computed from numerical simulations (Ostriker et al., 2001; Li et al., 2021). The DCF method assumes that the turbulence in the medium is isotropic and the line-of-sight and plane-of-sky velocity dispersions are similar.

Correction factor ξ

The correction factor ξ in the DCF method is between 0 and 1,and was introduced to correct the effect of the finite resolution of the telescope on estimating the magnetic field strength (Myers & Goodman, 1991; Ostriker et al., 2001). The DCF method without this factor typically overestimates the field strength. The ξ factor has been estimated using numerical simulations where the obtained field strength estimates are mostly correct (within a factor of ~2) in the case of a strong field, but the DCF results are typically overestimated in the case of weak field (Heitsch et al., 2001). The correction factor depends on density: For low to intermediate-density regions, ξ is about ~ 0.3 (Padoan et al., 2001), while for high density regions, $\xi \sim 0.5$ (Ostriker et al., 2001). In the case of high density, self-gravitating cores, Crutcher (2004) found that ξ =0.5 is a reasonable value to estimate the field strength in these objects using the DCF method. More detailed discussions about this factor are presented in Pattle & Fissel (2019) and Li et al. (2021) (see the appendix of this thesis).

Regime of applicability of the DCF method (in terms of polarization angle dispersion)

Values of the B-field strength derived using the DCF method are typically overestimated when the magnetic field is highly perturbed Pattle & Fissel (2019). Thus, the standard DCF method is only valid when the polarization angle dispersion is small $\sigma_\theta < 25°$. Outside the validity regime of the standard DCF formula, σ_θ can be replaced by $\tan(\sigma_\theta)$ (e.g, Falceta-Gonçalves et al., 2008; Li et al., 2021). Equation 2.9 becomes :

$$B_{POS} = \xi\sqrt{4\pi\rho}\frac{\sigma_V}{tan(\sigma_\theta)} \tag{2.10}$$

where B_{POS} is the mean B-field in the plane of sky which takes into account only the ordered and structured field. Li et al. (2021) show that the validity regime of this modified DCF formula can be extended to $\sigma_\theta < 45°$ (see demonstration in appendix A1 of this paper).

The structure function version of the DCF method

Hildebrand et al. (2009) introduced the structure-function method that allows to estimate the turbulent field strength using the DCF method. This technique allows to avoid inaccurate estimates of the B-field strength due to large-scale variations of the mean (non-turbulent) field. This method analyzes the difference in polarization angle at different positions in the observed region. The structure function for pairs of positions separated by a displacement l $(x,\, x+l)$ is defined as follows :

$$\left\langle \Delta\Phi^2(l) \right\rangle^{1/2} = \left\{ \frac{1}{N(l)} \sum_{i=1}^{N(l))} \left[\Phi(x) - \Phi(x+l)\right]^2 \right\}^{1/2} \tag{2.11}$$

where $\Phi(x)$ is the polarization angle at a given position x and $\Delta\Phi(x) = \Phi(x) - \Phi(x+l)$ is the difference in polarization angle betwen two points separated by displacement l. The first application of this equation was made by Falceta-Gonçalves et al. (2008), who assumed that the medium is isotropic and that $\Delta\Phi$ depends only on the displacement l. The magnetic field can be decomposed into a large-scale structured B-field $\vec{B}_0(x)$ and a turbulent B-field component $\vec{B}_t(x)$. Thus, the B-field strength at a given position can be expressed as :

$$\vec{B}(x) = \vec{B}_0(x) + \vec{B}_t(x) \tag{2.12}$$

For displacement l with range $\delta < l << d$, where d is the typical length scale for large scale component $B_0(x)$ and δ

is the correlation length of the turbulent component $B_t(x)$. Equation 2.11 can be expanded using Taylor's theorem with $\delta < l << d$ as follows :

$$\left\langle \Delta\Phi^2(l) \right\rangle \simeq b^2 + m^2 l^2 \tag{2.13}$$

For displacement $\delta < l << d$, the polarization angle can be expressed as :

$$\Phi_0(\overrightarrow{x} + \overrightarrow{l}) = \Phi_0(\overrightarrow{x}) + \frac{d\Phi_0(\overrightarrow{x})}{dx}.\overrightarrow{l} + o(\overrightarrow{l}) \tag{2.14}$$

Then, the large scale field contribution $\Delta\Phi_0^2 \propto l^2$.

For very small displacements l, $m^2l^2 << b^2$, the B-field large scale component is negligible compared to the B-field turbulent component. From Eq. 2.11 and Eq. 2.13 we can express the structure function as follows :

$$\begin{aligned} \left\langle \Delta\Phi_t^2(l) \right\rangle &= \left\langle [\Phi_t(x) - \Phi_t(x+l)]^2 \right\rangle \\ &= 2(\left\langle \Phi_t^2 \right\rangle - \left\langle \Phi_t \right\rangle^2) \\ &= 2\sigma_\phi^2 \\ &= b^2 \end{aligned} \tag{2.15}$$

The dispersion in polarization angle is given by $\sigma_\Phi = b/\sqrt{2}$.

Determining $\left\langle \Delta\Phi^2(l) \right\rangle^{1/2}$ allows us to estimate dispersion of the polarization angles at large scales. The relationship between the large-scale mean field and turbulent field can be expressed as :

$$\frac{\left\langle B_t^2 \right\rangle}{B_0} = \frac{b}{\sqrt{2 - b^2}} \tag{2.16}$$

Assuming the correction factor ξ is 0.5, Eq. 2.16 becomes :

$$B_0 = 0.383\sqrt{n(H_2)}\sigma_V \frac{\sqrt{2 - \Delta\Phi_0^2}}{\Delta\Phi_0} \tag{2.17}$$

b can be obtained in the limit of $l = 0$ and $\Delta\Phi_0 = b/\sqrt{2}$ (see Hildebrand et al., 2009; Falceta-Gonçalves et al., 2008 for more detailed about the structure-function analysis). This method is widely used to compute a dispersion of polarization angles that does not include the large-scale mean field. A more detailed derivation of this method is presented in Appendix A2 of the paper Li et al. (2021) (see appendix of this thesis).

2.3.2.2 Magnetic field strength from Zeeman observation

Estimating the B-field strength from dust polarization is challenging, and in most cases, the results are overestimated. The Zeeman splitting technique is the only observational method to measure the line-of-sight (LOS) component of the magnetic field strength directly in molecular clouds by observing paramagnetic molecules (Crutcher et al., 1993). It consists of observing interstellar molecules with unpaired electrons. Most of the molecules in the ISM have their electrons paired (non-paramagnetic) which makes the Zeeman splitting difficult or impossible to observe (Crutcher, 2012). The first detection of the Zeeman effect in the ISM was made for a supernova remnant (Verschuur, 1968), which was detected by observing the absorption line of HI. Following this first detection, several detections of the Zeeman effect were obtained by others in Orion A, Taurus, and other molecular clouds (Crutcher & Kemball, 2019, and references therein).

During the last decades, Zeeman detections using different species have provided B-field strength measurements for a wide range of densities in interstellar clouds. For example, Zeeman observations using HI, OH, and CN lines in extended gas in the ISM allowed measuring the magnetic field strength in different cloud environments. HI observations have allowed the B-field strength to be measured in the cold neutral atomic medium (where the volume density ranges between 1 to 100 cm^{-3}, see Crutcher, 2012). The Zeeman effect in HI absorption and OH emission allows the field strength to be measured in dense molecular regions (with densities $\sim 10^2 - 10^4$cm^{-3}). The Zeeman detection in the CN emission lines probes the B-field strength in high-density regions in the ISM ($10^5 - 10^6$ most detections are in high-mass protostellar objects). See Crutcher & Kemball (2019) for more details.

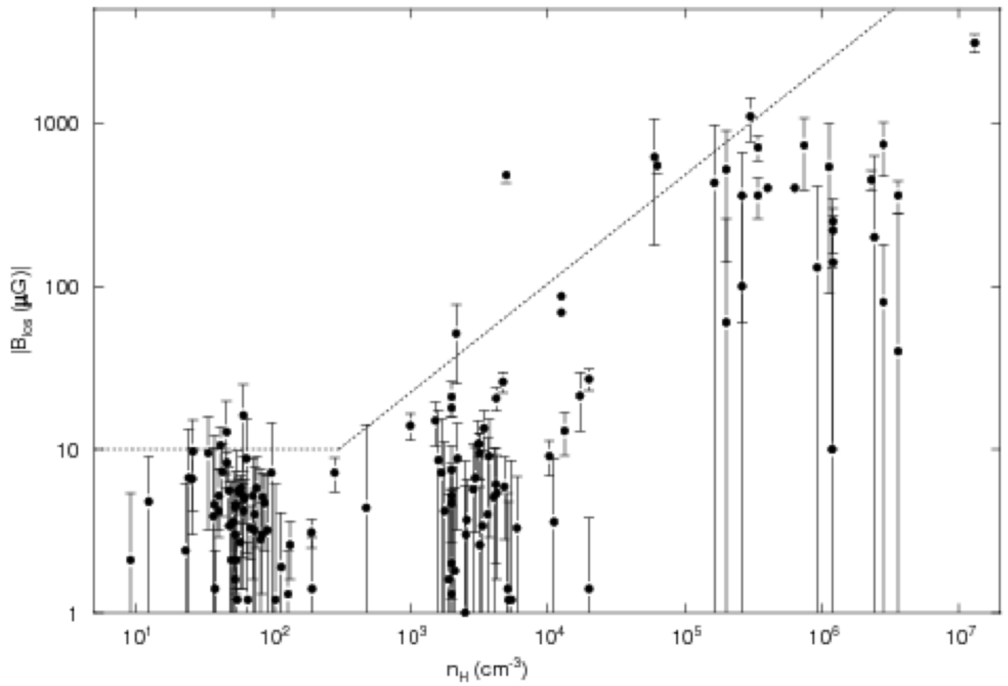

Figure 2.3: Zeeman measurements of the line-of-sight magnetic field in diffuse clouds and molecular clouds are plotted as a function of the volume density n_H. The Zeeman detections give the magnitude and the sign of the line-of-sight component of the B-field. The dotted line is the maximum value for $B_{POS}(n_H)$ determined from a Bayesian analysis (see Crutcher & Kemball, 2019 and references therein)

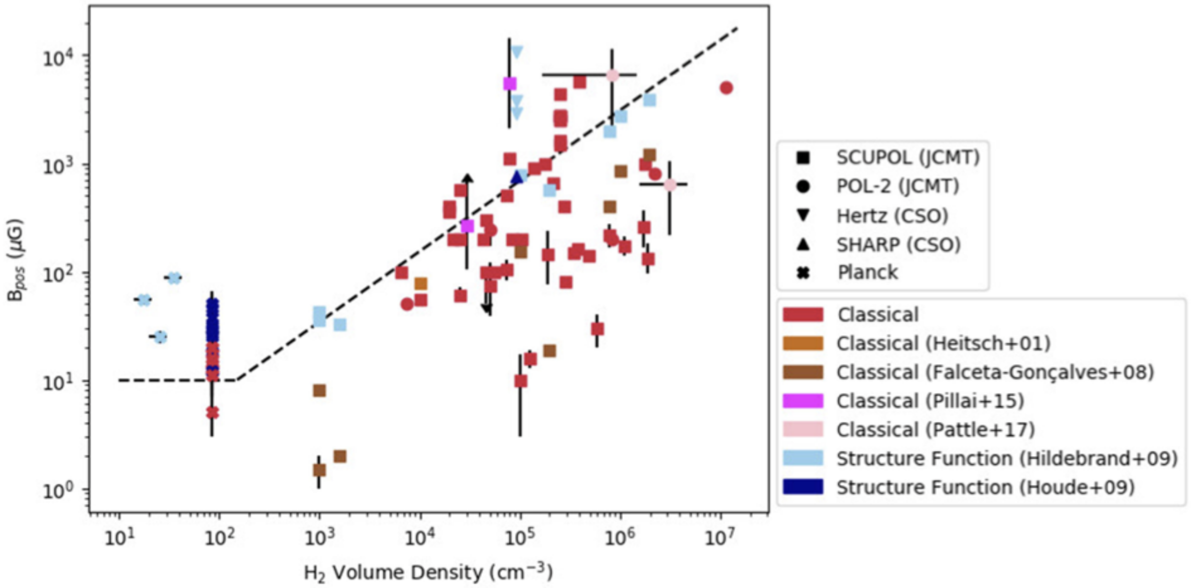

Figure 2.4: Magnetic field strength estimates using the DCF method from single-dish dust polarization observations as a function of measured volume density. The dashed line shows the upper-limit relationship derived by Crutcher et al. (2010). Figure taken from Pattle & Fissel (2019)

Recent Zeeman observations toward several molecular clouds have made it possible to scrutinize the variation of the magnetic field strength with volume density. Figure 2.3 shows the measured line-of-sight magnetic field strength B_{LOS} using the Zeeman effect in diffuse gas and molecular clouds. It shows the variation of B_{LOS} as a function of volume density. The upper-limit relationship between the measured magnetic field strength B_{LOS} and the volume density n_H was introduced by Crutcher et al. (2010) using a Bayesian analysis of available Zeeman measurements. They found that for densities below 300 cm^{-3}, B_{LOS} is approximately constant $\sim 10\ \mu$G, while at higher densities $B_{LOS} \propto n^{0.65}$. It is essential to compare direct measurements of the magnetic field strength with indirect estimates from dust polarization observations using the DCF method. Figure 2.4 shows the magnetic field strength estimated using the DCF method as a function of volume density from dust polarization observations with single-dish telescopes.

Overall DCF estimates are reasonably consistent with the measured magnetic field strength using the Zeeman effect (Pattle & Fissel, 2019; Myers & Basu, 2021). Figure 2.4 suggests that the magnetic field strengths obtained with the DCF method are comparable and constrain the $B-n_H$ relationship of Crutcher et al. (2010). However, some DCF results overestimate the plane-of-sky B_{POS} due to the problem of the line-of-sight/sub-beam variations (cf. Myers & Basu, 2021).

2.4 Summary

Both observations and simulations have shown the vital role played by magnetic fields in regulating star formation from cloud to core scales, but this role is not yet well constrained.

On the one hand, B-field lines at large scales are well ordered and tend to be perpendicular to dense regions and parallel to low-density regions (Planck Collaboration et al., 2016a,b,c). But the change of the B-field geometry from large scales to filament/core scales is not well understood. The detailed analysis of how the B-field geometry changes at different stages of the star formation process (from the parent cloud to embedded protostar) is unclear due to the lack of high angular resolution data. The transition from a well-ordered magnetic field geometry to a distorted morphology or an hourglass shape is also under debate (Soler et al., 2016; Soler & Hennebelle, 2017; André et al., 2019).

On the other hand, magnetic fields strength measurements from Zeeman observations are difficult, and DCF estimates are limited due to beam effects or large-scale perturbations. The transition from a magnetically sub-critical filament to a magnetically super-critical filament is not precisely determined. The filament paradigm for star formation (e.g, André et al., 2014, 2019) suggests that the magnetic field plays an important role in the star formation process, but it does not provide an answer about at which stage exactly the B-field is crucial.

In an attempt to understand the role of B-fields in star formation, as part of this thesis, we have observed prototypical example of an early-stage star-forming filament B211/B213 in Taurus. We used high angular resolution dust polarization observations provided by SOFIA/HAWC+ to infer the magnetic field geometry in this region.In this thesis, I also present new findings of the B-field geometry in the OMC-1 filament in the Orion A cloud using NIKA2-Pol commissioning data (see Chap. 5).

Chapter 3

The NIKA2 instrument and its polarization channel

Contents

3.1 Introduction

The recent and next generations of sub-millimeter/millimeter polarimeter instruments will improve our understanding of the role of magnetic fields in the star formation process in the Universe. The B-field inferred from the polarization observations at sub/millimeter wavelengths and at high spatial resolution will bring out the way on how the magnetic field helps in the formation of prestellar/protostellar cores inside molecular filaments. Observations from the ground with Polka, SCUBA-Pol, SCUBA2-Pol2, and other instruments have opend up a new window on the studies of star-forming regions (Siringo et al., 2004b; Bastien et al., 2011; Pattle et al., 2017a). Polarisation observations from space with Planck revealed the large structures of the magnetic field in the Galactic plane but were unable to probe the B-field properties on small scales (< 0.1 pc) (Planck Collaboration et al., 2016a,b,c). Table 1 in Pattle & Fissel (2019) summarizes the recent and next generations of polarimeters that will observe from space or from the ground the star-forming regions and bring out the key role played by magnetic fields in the process of star formation. The polarization mode of ALMA (Atacama Large Millimeter Array) has been commissioned recently making polarization observations at very small scales possible (< 0.01 pc) (Belitsky et al., 2018; Cortes, 2019; Cortes et al., 2021).

The recent development of new continuum detectors such as Kinetic Inductance Detectors (KIDs), is becoming a great opportunity to increase the sensitivity on which single-dish polarimetric observations at intermediate scales (0.2 pc to 0.01 pc) can be done. The need to map the sky at millimeter wavelengths drove the IRAM 30 telescope community and the NIKA2 international consortium to build a new instrument called NIKA2 (for Néel IRAM Kids

Array 2). The IRAM 30m telescope is located close to Pico Veleta in the Sierra Nevada near Granda, Spain. The telescope is installed at an altitude of 2850 meters which makes it a powerful tool to study the cosmos. The high altitude observations from the ground help reducing the effect of atmospheric fluctuations, especially in the 1.3 mm atmospheric window. With a main dish of 30 meters and the NIKA2 instrument, the IRAM 30m telescope is one of the largest facilities in the world to have such spatial resolution and sensitivity (Adam et al., 2018).
The succeful tests and observations performed with NIKA, the pathfinder of NIKA2, clearly showed that the KIDs detectors technology was very promissing and let to the building of a more ambitious camera with more pixels detector arrays (Ritacco et al., 2017). From NIKA to NIKA2, the new KIDs technology showed its robustness in the quality of observations in total power intensity and polarization observations (this thesis). In the current chapter, I present an overview of the NIKA2 instrument, as well as general information on the IRAM 30m telescope, to allow the reader to understand the basics of the instrument.

3.2 The IRAM 30m telescope

The telescope consists of a parabolic main reflector of 30 meters in diameter mounted in Alt-Azimuth in Cassegrain configuration (Baars et al., 1987). Due to its heavyweight of 800 tons, counterweights are used to balance the telescope. The incident wave-front is received by the main reflector M1 which redirects it to a secondary mirror (M2) and then to the Nasmyth cabin where various instruments are installed. The light enters the Nasmyth cabin with M3 mirror which reflects it to the M4 that can be moved manually to choose between the NIKA2 camera and EMIR heterodyne receiver system. The design of the telescope was established to minimize the deformation of the main dish (M1) by gravitation. Other aspects, such as the thermal deformation and the wind effect on the precision of the pointing have been characterized. A thermal control system (membrane) is installed to keep the telescope operational and to survive extreme weather conditions at this altitude (30 cm of ice and 200 km/hour wind). Generally, the angular resolution of the telescope is given by the Rayleigh diffraction formula as :

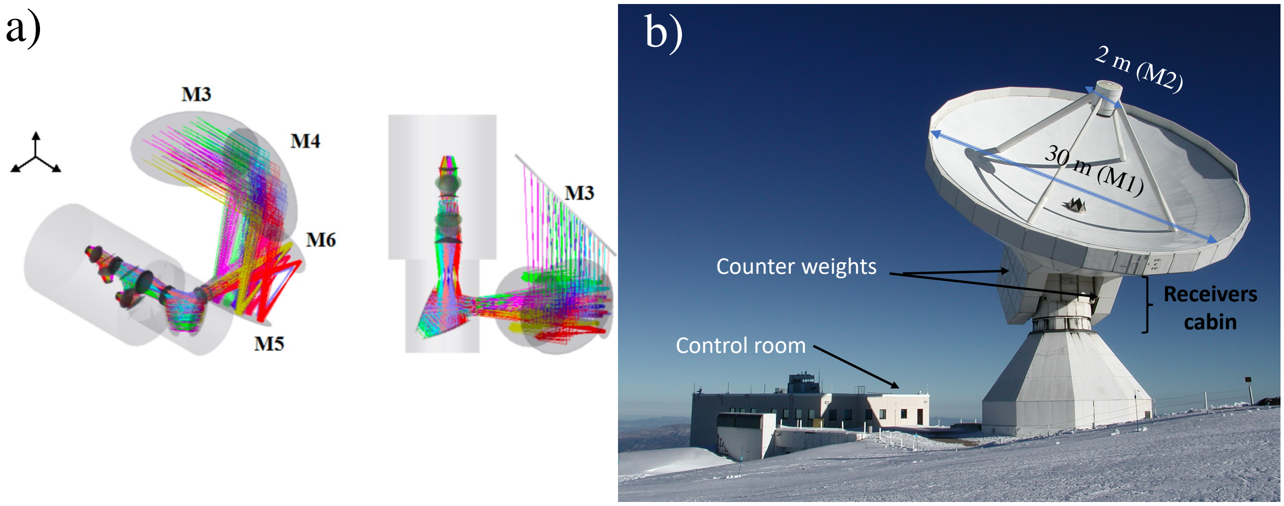

Figure 3.1: (a) shows the pathway of the light in the Nasmyth cabin from M3 to M5. From the M4 mirror, the light is redirected to the EMIR heterodyne or NIKA2 camera. The M5 and M6 are used for NIKA2 to perform the focus (Adam et al., 2018). (b) IRAM 30m at Pico Veleta in Spain, the receiver cabin, M1 and M2, the counterweight, and the control room can be seen in the figure indicated by vectors.

$$\theta = 1.22\frac{\lambda}{D} \tag{3.1}$$

At the 30m telescope, the paractical formula that has been used to compute the angular resolution is as follows :

$$\theta_{HPBW} = 12'' \frac{\lambda}{1.3mm} \tag{3.2}$$

where θ is the spatial angular resolution of the telescope in radians, D is the telescope diameter (30m) and λ is the wavelength of the incident wave. For the NIKA2 camera, the angular resolution is about 11.5 arcsec and 17 arcsec at 1.15 mm and 2 mm wavelengths, respectively (Adam et al., 2018).

3.3 NIKA as a pathfinder for NIKA2

The NIKA prototype camera was designed using the KIDs technology with two 356-pixel arrays, and used as a pathfinder for the NIKA2 instrument. The NIKA camera was composed of: (1) a dilution cryostat regulating the temperature and allow to cool down the detectors to a temperature of 100 mK, (2) The readout electronics allow to read the signal from all KIDs detectors, (3) the warm and cold optics. The two KIDs arrays are cooled down inside the cryostat to a temperature of 4K using a cryocooler and a closed-cycle ^{3}He - ^{4}He dilution (Catalano et al., 2014). The redirected light from the M4 and M5 enters the cryostat by an aluminum mirror optics installed on it (panel (a) in fig. 3.1). This instrument can be characterized by its Full Width at Half Maximum (FWHM), Field of View (FOV), and sensitivity.

The angular resolution for both NIKA and NIKA2 are constrained from the main beam by observing a strong point source. The sensitivity is measured by observing the faint sources. The FoV is the possible circular field that NIKA/NIKA2 can cover in the sky, which is related to the number of pixels in each array. Following the success of NIKA in serving the scientific community from the ISM to cosmology, NIKA2 was designed to have a larger FoV, smaller FWHM, and better sensitivity (Adam et al., 2014; D'Addabbo et al., 2013; Adam et al., 2015). For the polarization mode of NIKA2, the light is modulated by a rotating Half Wave Plate (HWP) installed in front of the cryostat. Only the 1.15 mm arrays are used in polarimetric mode.

3.4 Design of the NIKA2 instrument

The NIKA2 instrument is a dual-band camera designed with new KIDs-technology detectors which need to be characterized. The instrument has 2900 detectors and is able to map a circular Field of View (FoV) of 6.5 arcmin in both the 150 GHz and the 260 GHz window. These detectors are divided into three monolithic arrays A1, A2, and A3. A1 and A3 are used at 260 GHz (1.15 mm) and A2 at 150 GHz (2 mm). The polarimetric mode is available only at 260 GHz with arrays A1 and A3. NIKA2 is currently the most competitive instrument observing a large field of view simultaneously in two bands with KIDs detectors.

3.4.1 The cryostat

The cryogenic system is optimized by the cryostat to ensure optimal operations of all components, such as the focal plane arrays and the optics. The detectors are cooled down to a temperature of 150 mK by a dilution fridge. The weight of the cryostat is about 1.3 tons when assembled and 100 kg in the 150 mK stage including layers of high-density polyethylene. Panels (a) and (b) in figure 3.2 show the cooling layers and the temperature of each part of the cryostat. The A1, A2, and A3 detector arrays are cooled down to 150 mK in the blue dashed part of the illustration. The NIKA2 instrument can observe at 150 GHz (A2) and in both vertical and horizontal linear polarization at 260 GHz (A1, A3) (see fig 3.2)

3.4.2 Optics

The illustration in panel (b) of figure 3.2 shows an overview of the optical system of NIKA2. The mirrors M7 and M8 are placed at the entrance of the cryostat, which allows to redirect the incoming light to the detectors. The angle between M7 and M8 is about 76.2 °, which allows to maximize the number of light rays going to the detectors and to help in focalizing the light. An image stop and a baffle cooled down to a temperature of 4K are installed to reduce stray lights coming from the system. To separate the 150 GHz and 260 GHz channels a dichroic and filters are used to reflect and transmit waves toward their specific detectors. To distinguish between the horizontal and

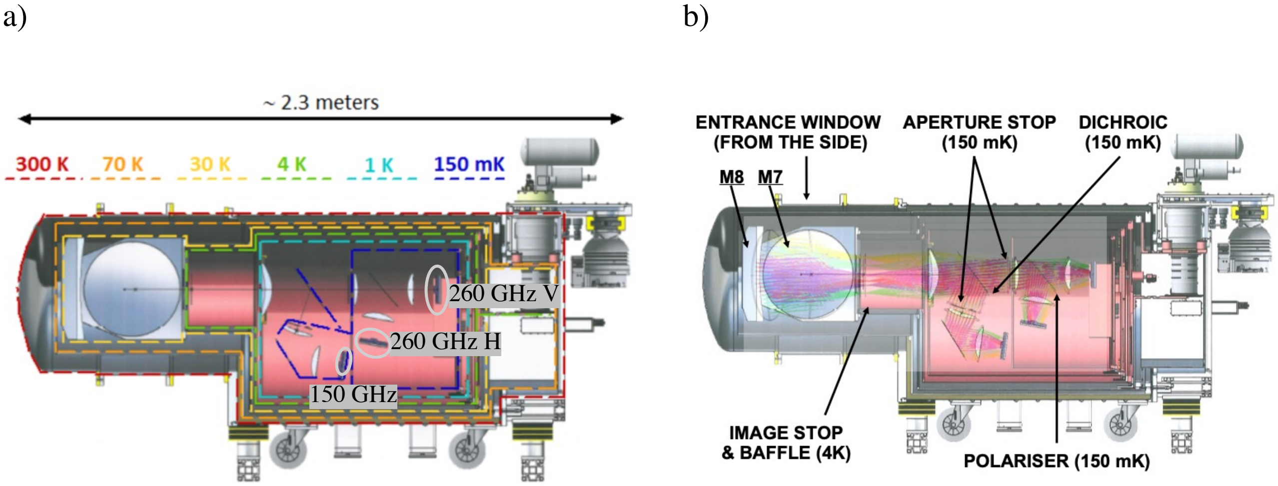

Figure 3.2: (a) Illustration of the NIKA2 instrument showing the different cryogenic stages. The total weight of the cryostat is close to 1300 kg. The 150 mK section includes the arrays, the dichroic, the polariser, and five HDPE lenses(Adam et al., 2014). (b) Illustration of the NIKA2 instrument showing the cold optics and the main elements and surfaces described in the text. The mirror M7, M8, and the pathway of the light from the mirrors to the detector arrays.

vertical polarizations at 1.2 mm, a polarizer cooled to 150 mK is used to split the incoming waves and divide them into the A1 and A3 arrays depending on their polarization.

3.4.3 Bands and detector arrays

The spectral bands of NIKA2 were measured and characterized in different campaigns, which helped to investigate the difference between when a dichroic is present or not (Perotto et al., 2020). Figure 3.3 shows the relative bandpass responses of the three detector arrays (A1, A2, and A3). The effective bandpasses for A1 and A3 at 260 GHz used in polarimetric mode are slightly different, implying a slightly different KIDs response in A1 and A3. The difference is related to the thickness of the aluminum film used in a given detector array (Perotto et al., 2020). The effect of atmospheric transmission affects all three arrays but is especially pronounced at 1.15 mm. To quantify this effect, Uranus and Neptune were observed in different weather conditions to measure the effectiveness of NIKA2. The performance and characterization of the spectral bands made it possible to define a reference frequency for the NIKA2 array (260 GHz for A1 and A3, and 150 GHz for A2).

3.4.4 NIKA2 Half Wave Plate

The method of measuring linear polarization with NIKA2 uses the polarization modulation technique by a birefringent Half-Wave Plate (HWP) which rotates an incident polarized wave by 2θ, where θ is the HWP rotation angle. The HWP allows modulating the incoming polarization so that the three Stokes parameters (I, Q, U) can be measured. The mesh-HWP efficiency established by NIKA allows to consider the same for NIKA2, the transmission and differential phase-shift achieved with this new technology is 90 % compared to the previous ones (Pisano et al., 2020, 2014). The HWP design commonly used at millimeter wavelengths called SAPHIRE which provides a phase-shift of 180° between the ordinary and extraordinary axes (left illustration in panel b of figure 3.4). The mesh-HWP used in NIKA2 combines two anisotropic mesh-filters: the capacitive low-pass and the inductive high-pass (Figure 3.4 right illustration in the panel b). The final design of mesh-HWP consists of series of stack layers of captive

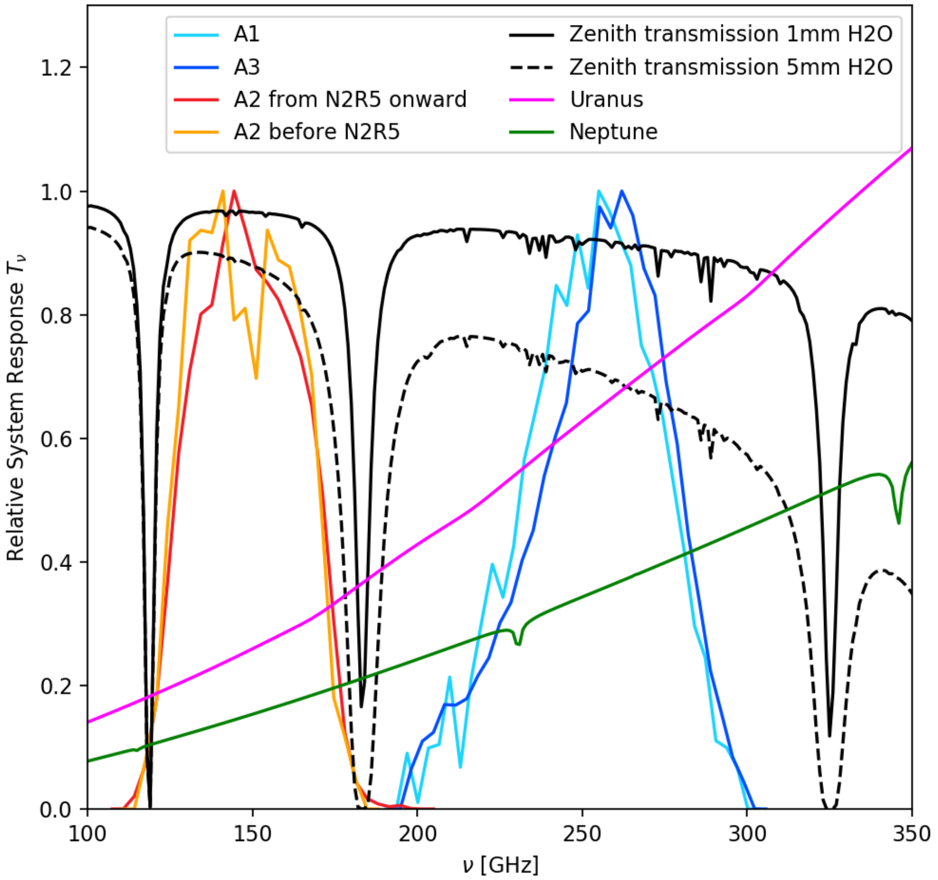

Figure 3.3: Bandpass of filters used in front of the NIKA2 detector arrays A1, A2 and A3 as function of frequency (Perotto et al., 2020). The atmospheric transmission for precipitable water vapor contents of 1 mm and 5 mm are shown in black as predicted by the ATM model from Pardo et al. (2001).

grids and inductive stack layers at orthogonal orientations (see figure 3.4 panel (c)). Panel (a) in figure 3.4 shows a photo of the HWP installed in front of the cryostat. Figure 3.5 shows the pathway optics from the M6 to the inside of the cryostat. The beam size is at the position of the HWP polarization modulator (Adam et al., 2014, 2018).

3.5 Kinetic Inductance Detectors (KIDS)

Kinetic inductance detectors (KIDs) are the new technological superconducting detectors operating at $\sim$ 150 mK. These KIDs detectors are considered powerful tools to study the cosmic microwave background (CMB), as well as star formation in the ISM. NIKA2 is the first instrument based on such technology (Calvo et al., 2016). The KID arrays employed in the NIKA2 instrument were produced to reach the bandwidth of the NIKEL (New Iram Kid electronics) electronics at 150 GHz and 260 GHz wavelengths (Bourrion et al., 2016; Adam et al., 2014). In this section, I describe generally the KIDs design and response.

3.5.1 KIDs array design

NIKA2 uses Lumped Element Kinetic Inductance Detectors (LEKIDs) designed with the Hilbert pattern to absorb both vertical and horizontal polarization. To increase their sensitivity, the LEKIDs detectors were fabricated with thin Aluminum films (18 - 25 nm). The Aluminum film helps to improve the KIDs resistivity and responsitivity to plane radiations. Each array was fabricated using a Silicon wafer with a focal plan diameter of ~80 mm. The focal plane was sampled $\leq 1F\lambda$ to preserve the telescope angular resolution (Calvo et al., 2016). The sampling from 0.7 to $1F\lambda$ corresponds to 2.3–2.8 mm at 150GHz and 1.6–2 mm at 260 GHz, with a total number of detectors of 600–1000 and 1200–2000 respectively. Figure 3.6 shows a real photo of the 260 GHz array installed in NIKA2 after

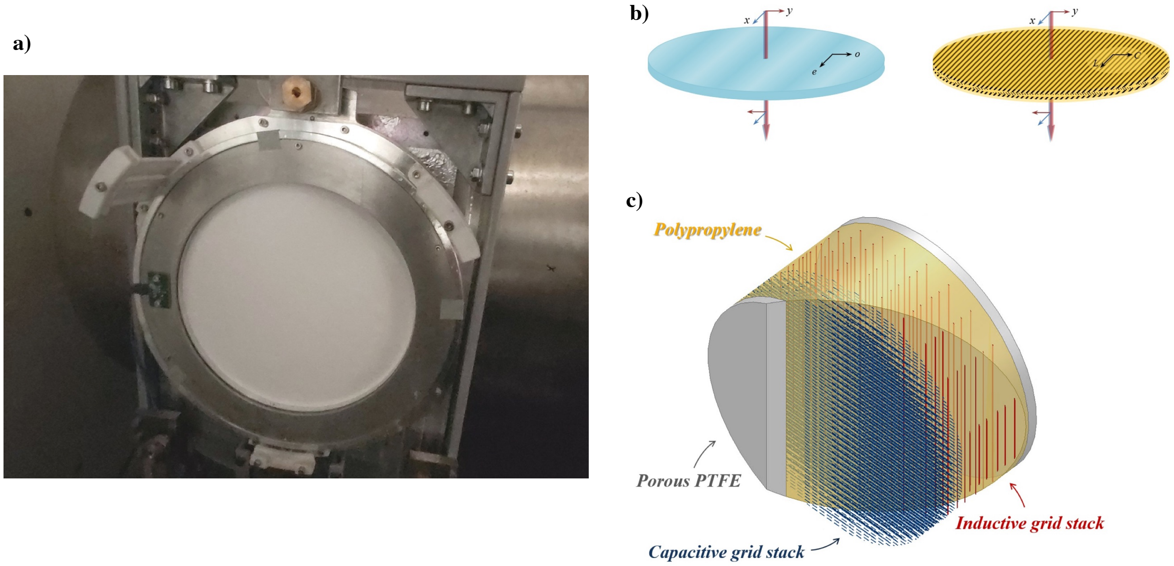

Figure 3.4: NIKA2 instruments and its characteristics. a) photo of NIKA2 mounted in front of the cryostat. b) the mish-HWP SPHIRE used which combine captives and inductive grids used in NIKA2.

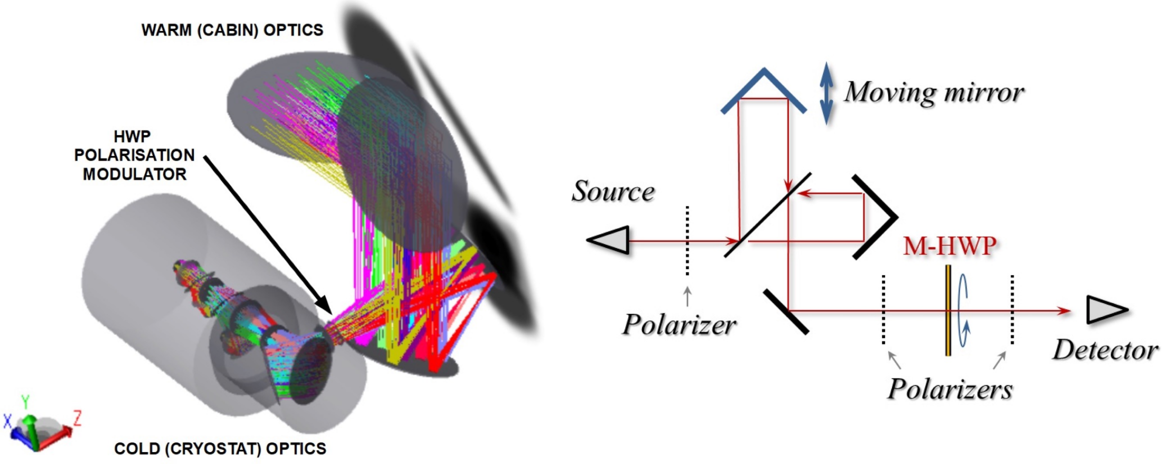

Figure 3.5: Left : The NIKA2 intrement with pathway layers from the M6 to inside of the cryostat. The beam size is showed in the position of HWP polarization modulator. Right : The Martin-Puplett setup used for to characterize the mesh-HWPs used in the NIKA2 instrument.

its packing on the left, and the Hilbert LEKID used in these arrays compared to standard Hilbert detectors on the right.

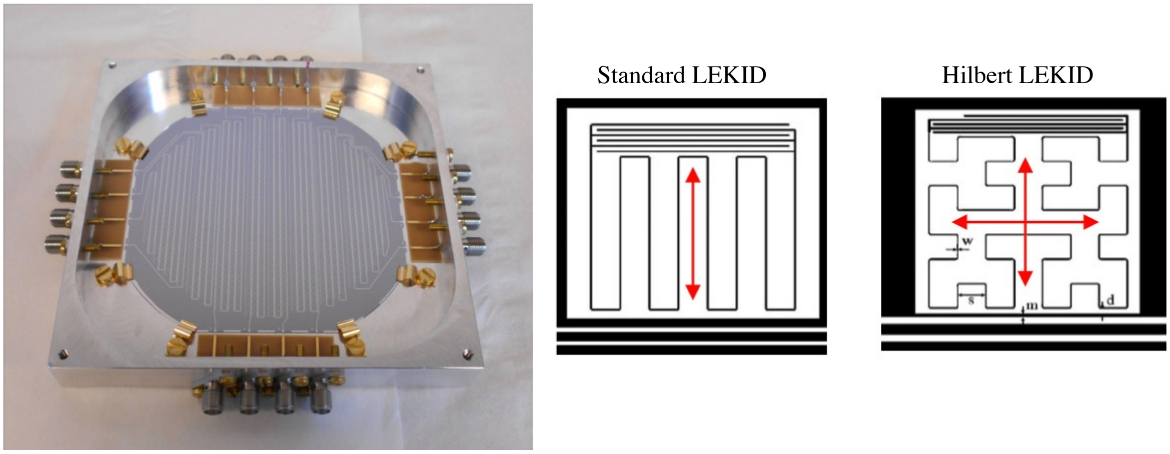

Figure 3.6: Left : The 260 GHz NIKA2 arrays after packaging. 1140 KIDs detectors designed and connected via eight feed-lines and 16 SMA (Sub-Miniature version A) connectors to the external circuit. The front of the wafer can be seen here (Calvo et al., 2016). Middle : standard LEKID design, sensitive to only one polarization. Right, Hilbert LEKID design, sensitive to both horizontal and vertical polarization (D'Addabbo et al., 2013)

3.5.2 KIDS response

To measure the response of the KIDs, the detectors are coupled to transmission feedlines in the circuit. The transmission of a KID circuit can be expressed as the transfer function of the measured circuit which is :

$$S_{21}(f) = C + jB \tag{3.3}$$

Where C and B are the real and imaginary parts of the transfer function, respectively. The transfer function can be characterized by its amplitude $A = \sqrt{C^2 + B^2}$ and its phase as a function of its frequency response ϕ =arctan(B/C). At 150 GHz, the array is connected to four feedlines which measure resonance frequencies between 0.9 and 1.4 GHz (Adam et al., 2018). At 260 GHz, each array is connected to eight different readout lines with frequency resonances between 1.9 and 2.4 GHz.

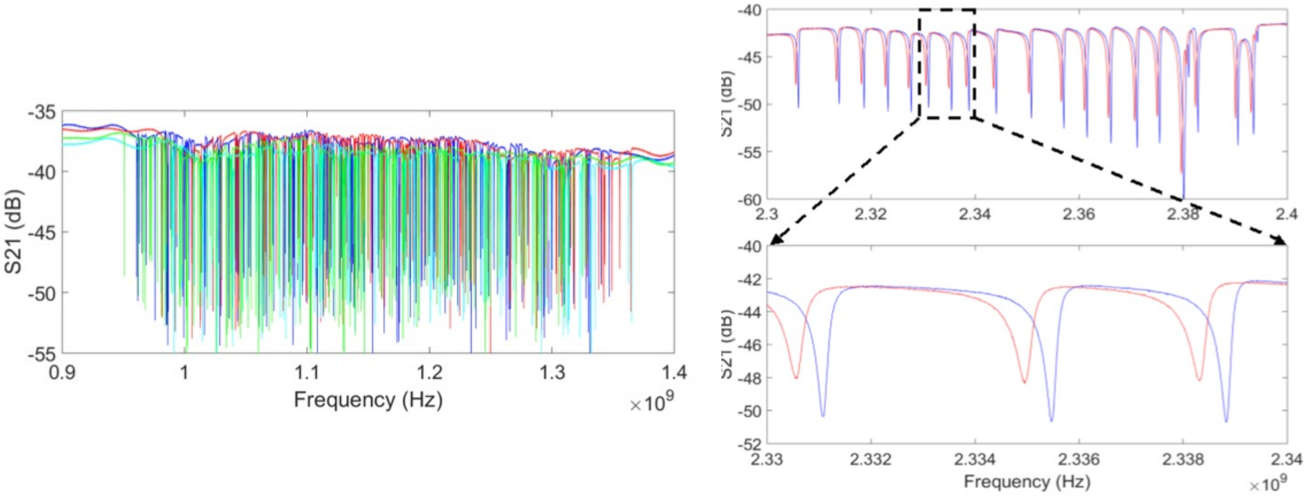

Figure 3.7: Left : Resonance sweep for the four readoutlines of the 150 GHz array. The y-axis represents the transmission of the feedline given by the equation 3.3 (parameter S21) and is expressed in dB. Each dip corresponds to a resonance/pixel. At least 94% of the 616 pixels are identified with a resonance and are thus sensitive to incoming radiation (Adam et al., 2014). Right : Top panel: frequency sweep of a portion of one particular feedline operating at 260 GHz. Bottom panel: zoom on three typical resonances.

Chapter 4

Contribution to the NIKA2-Pol commissioning phase

Contents

4.1 Introduction

The commissioning of NIKA2 in total power performed between October 2015 and October 2017, demonstrated the capability of NIKA2 to deliver high-quality data (Perotto et al., 2020). The first polarization campaign with NIKA2-Pol was carried out in November 2017, where the commissioning team resolved various problems related to acquisition software, Half Wave Plate (HWP) synchronization, and checked the polarization angles of a few quasars (QSOs) for absolute calibration purposes. From 2018 to 2021, we carried out three polarization commissioning runs, in Dec. 2018, Feb. 2020, and Nov. 2020, that allowed us to essentially finalize the NIKA2-Pol commissioning.

In the present chapter, I report the data reduction and analysis for the three campaigns of NIKA2-Pol commissioning in which I participated and contributed in terms of observation, calibration, and data analysis. One major challenge for NIKA2 observations in polarization mode is assessing and correcting for the instrumental polarization. The instrumental polarization leakage (hereafter "leakage" or "IP") can be characterized by observing an unpolarized source (mainly in practice the Planet Uranus e.g, Wiesemeyer et al., 2014).
The instrumental polarization effect is mainly due to the imperfection of the telescope and the instrument. This effect has been investigated with early polarization instruments since the 1970s, and at a wide range of wavelengths, using ground observatories. For example, Spoelstra (1972) investigated the observed IP using the cm range 25-meter radio telescope and found that its origin comes from the asymmetry of antenna pattern and is elevation-dependent. Troland & Heiles (1982) observed a four lobes feature of the IP at 21 cm wavelength using the 26 m radio telescope at Hat Creek Observatory and conducted several tests to characterize and correct for this effect, and found that the IP is mainly generated by the feed legs that induce an angular displacement of the beam. At 1.3 mm wavelength,

the MILIPOL polarimeter installed at NRAO 12-meter telescope had shown the ability to correct for IP <<1% in polarization fraction and estimating the IP leakage level by observing the Moon and other planets (Clemens et al., 1990; Barvainis et al., 1988). The Mimir polarimeter at the 1.8 m Perkins telescope had shown to be affected by the IP leakage, and its intensity varies toward the FoV position where the IP level was estimated to be about 0.2% at the center of the FoV and increase up to ∼4% at the edges (Clemens et al., 2007).

The IP is an intrinsic effect that may come from the instrument, the telescope, or the detectors. The IP effect is one of the common issues as well in all recent polarization experiments, such as PILOT balloon-borne experiment, ALMA in polarization mode, HAWC+ aboard the SOFIA telescope, SCUBA2-POL2 at the JCMT, and many other polarimeters (Engel et al., 2017; Belitsky et al., 2018; Pattle et al., 2017a; Friberg et al., 2018; Cortes, 2019; Michail et al., 2018). To provide reliable polarization data, the IP needs to be characterized and corrected for.

In Section 4.3, I present a detailed analysis of the IP leakage affecting NIKA2-Pol data. My analysis emphasizes the importance of understanding this effect to correct the scientific data. It also helps to investigate the origin of the IP leakage. I show how this leakage depends on different parameters (such as elevation of the telescope, focus position, weather conditions). I present an analytical model that can provide an alternative method to help future observers to correct their scientific data even without using Uranus observations. The leakage analysis is based on data obtained during three commissioning campaigns in which over 500 Uranus scans were observed (taking into account focus series, defocused maps, focused maps, and beam maps).

Our preliminary results on the IP leakage (Ajeddig et al., 2020, 2021) showed the complexity of this effect (sensitive to focus and depending on elevation). However, the current NIKA2 pipeline can correct observed data for this IP leakage down to a residual instrumental polarization of $< 1\%$ (or down to 0.3% in case of a proper estimation of the IP leakage). The leakage correction procedure was developed and successfully tested on Uranus maps, quasars, and two extended sources (OMC-1 and Crab nebula). I also discuss some of the possible origins for the observed leakage. I also show how the leakage correction reduces the scatter of polarization angles in weakly polarized quasars (Sect. 4.4). In Section 4.5, I discuss the absolute calibration of NIKA2-Pol polarization angles using quasars (QSOs). During the NIKA2-Pol commissioning campaigns, we used joint NIKA2-Pol and XPOL observations on quasars to check the polarization angle stability. XPOL is a polarimeter instrument installed at the 30m telescope, and measures the four Stokes parameters (I, Q, U, V) simultaneously using a correlator at 3mm and/or 1mm.

4.2 Observations and calibration checks

The NIKA2 observing modes in both total power and polarization at the IRAM 30m telescope were optimized during the total power and the polarization commissioning. The most commonly used observing mode is "On-The-Fly" (OTF). Each OTF map consists of a series of raster scans at constant azimuth and varying elevation (or at an angle with respect to the Az axis) or constant right ascension (or declination) and varying declination (or right ascension). This mode has been used in all NIKA2 pools for both calibrations and scientific purposes (Perotto et al., 2020). In this section, I will summarize the observing strategy with NIKA2 mainly in polarimetric mode (which does not differ much from that in total power mode).

4.2.1 Focus observations

The typical focus sequence that has been used during NIKA2 observations consists of five consecutive short scans (one minute each) of a bright point-like source (> 1 Jy) at five Z-axis positions of the secondary mirror (M2). Only the central KIDs (located in the central part of the FoV in a region of radius ∼ 100 arcsec) are used to derive an appropriate focus for the telescope. To get the optimal focus setting, the five maps of the focus sequence are fitted by an elliptical Gaussian model that allows us to determine the FWHM intensity and size of the observed source. A parabolic fit to the flux provides the maximum intensity and minimum of the FWHM size, providing a good focus setting along the Z-axis. To ensure well-focused observations, focus scans are repeated several times during daytime/nighttime depending on the stability of the weather conditions. An offset of -0.2 mm is added to the best focus position derived from the fit to account for the effect of the surface curvature of the focal plane that was derived during the NIKA2 total power commissioning (Perotto et al., 2020) and confirmed by ZEMAX simulations. The focus position is checked and optimized every day before and after sunrise and before and after sunset. Besides the standard method of correcting the focus offset, the NIKA2-Pol team carried out series of focus scans using smaller steps than usual as well as defocused maps under different weather conditions. To characterize the instrumental polarization, we took repeated series of Uranus maps at different focus positions. We also used defocused maps to perform a quantitative analysis of the instrumental polarization dependence on the focus Fz.

4.2.2 Pointing

Before any scientific observation, the observer needs to ensure a good pointing of the telescope with respect to the source in the sky. Standard pointing checks at the IRAM 30m telescope consist of a sequence of two cross-type scans, where the telescope scans back and forth in azimuth and back and forth in elevation. The back and forth scans are centered at the expected position of the source. Gaussian fits to the observed source intensity profiles allow one to find appropriate offset corrections to the current pointing position (Perotto et al., 2020). This procedures is repeated every hour or after moving the telescope to a new source in a different part of the sky to ensure a good pointing for the observing target. Either the IDL NIKA2 pipeline (Nicolas Ponthieu, see also Ritacco, 2016; Andrianasolo, 2019) or the PIIC software[1] (Zylka, 2013) can be used to derive appropriate pointing correction offsets. Regular technical pointing observations with NIKA2 in total power were carried out for 30 pointing sources to derive and refine an appropriate pointing model for NIKA2. The typical pointing RMS uncertainty with NIKA2 at the 30m telescope has been found to be less than $3''$ ($2''$ in azimuth, and $1''$ in elevation). Under stable conditions and at sufficiently high elevations where anomalous refraction does not affect the pointing, the RMS pointing error is lower (Greve et al., 2010). Under unstable conditions, one needs to check the telescope pointing more often than usual to ensure satisfactory observing results.

4.2.3 Skydips

Skydips consist of sequences of 11 short scans taken on “blank” sky at a fixed azimuth and at several elevations (from low to high elevations ($19° - 75°$) that allow deriving the atmospheric opacity and calibrating the KIDs responses as a function of the atmospheric emission. The atmospheric emission radiation can be obtained by solving the equation of the radiative transfer as follows :

$$\frac{\mathrm{d}I_\nu}{\mathrm{d}s} = -\kappa I_\nu + j_\nu \tag{4.1}$$

where I_ν is the brightness at a given frequency ν, $\mathrm{d}\tau$ =-$\kappa\mathrm{d}s$ is the opacity of the sky emission. j_ν is the emission coefficient which can be obtained using Kirchhoff's law of equilibrium radiation of the matter and can be expressed as a function of brightness of a black body $\mathrm{B}_\nu(\mathrm{T}_{atm})$ as follows :

$$j_\nu = \kappa B_\nu(T_{atm}) \tag{4.2}$$

where T_{atm} is the temperature of the atmosphere. From Eq. 4.1 and Eq. 4.2, the integration of the radiative equation from opacity τ=0 to a zenith optical opacity $\tau(z)$ yields to atmospheric emission as follows :

$$I_\nu = [1 - e^{-\tau_z \sec(\phi_z)}]B_\nu(T_{atm}) \tag{4.3}$$

where $\mathrm{B}_\nu(\mathrm{T}_{atm})$= $\frac{2kT_{atm}\nu^2}{c^2}$ in he Rayleigh–Jeans approximation, where k is the Boltzman constant, c is light speed, $sec(\phi_z)$ is the air mass for a given elevation and τ_z is the optical depth at zenith. The resonance frequencies of KIDs are shifted by the strong atmospheric emission. For each KID, the frequency resonance taken into account the atmospheric emission effect can be expressed as follows :

$$\nu_{kid} = \nu^d_{kid} + C_k T_{atm}[1 - e^{-\tau_z \sec(\phi_z)}] \tag{4.4}$$

where ν_{kid} is the shifted resonance frequency of the KID, ν^d_{kid} is the frequency resonance of the KID in dark conditions (flat field), C_k is the optical response of each KID. We use the tau-meter to measure the opacity of the atmosphere. The The NIKA2-Pol skydip strategy allow to measure ν^d_{kid} at different elevations. We obtain a common sky opacity at zenith τ by fitting Eq. 4.4 using the three parameters ν^d_{kid}, C_k and τ. Assuming that all KIDs have a common opacity τ, the opacity of each scan at a given elevation can be obtained by applied the ν^d_{kid} and C_k to Eq. 4.4 as follows :

$$\tau_{scan} = -\frac{1}{\sec(\phi_z)}\ln(1 - \frac{\nu_{kid} - \nu^d_{kid}}{C_k T_{atm}}) \tag{4.5}$$

The point-source rms calibration uncertainties using this method are about 3% at 150 GHz and 6% at 260 GHz (Perotto et al., 2020). NIKA2 skydips are repeated at least every day and night (mostly every eight hours) to ensure good calibration of the data. In polarimetric mode, we performed polarized skydips, which are identical to

---

[1] https://publicwiki.iram.es/PIIC

total power skydips, except to a continuously rotating Half Wave Plate (HWP). The presence of the HWP in front of the cryostat creates an additional background noise in the data and one should subtract it from the scientific data. The skydip coefficients are also a way to estimate the variation of the opacity in a wide range of elevations. The atmospheric emission depends on the elevation of the source. The skydip procedure allows to determine the common sky opacity, τ the opacity at zenith, and all the transmission coefficients.

4.2.4 Beam maps

A beam map consists of a series of two scans to fully map a compact source, mostly a planet, with each and every KIDs of the camera. In practice, Uranus is used for NIKA2-Pol. The "Beammap" scans use a step of 4.8″ in elevation to ensure good sampling of the maps (Perotto et al., 2020). This procedure consists of several sub-scans at a fixed elevation/azimuth that allow minimizing air-mass variations along each sub-scan. The beam map is obtained by combining the fixed elevation scanning and the fixed azimuth scanning which helps to cover KIDs in edge of the focal plane and allow to characterize side lobes. Beam maps on Uranus are mainly used to derive KIDs properties (focus, FWHM, frequency resonance, KIDs response) and the focal plane construction. In all NIKA2 campaigns, this method ensures good calibration of the data. In the case of NIKA2-Pol, we also used this procedure to investigate how the leakage varies across the array (see Sect. 4.3.6) and across the field of view of NIKA2. The size of the scan allows to cover the whole array and get the response of each KID even those at the edges. A large map covering the outer parts of the source is essential for proper correlated noise subtraction. Beam maps are important for all observations. Only one is needed under stable weather conditions, but more are required under unstable conditions which provide additional information about the leakage variation.

4.3 Characterizing the instrumental polarization (IP) pattern

The planet Uranus is commonly used to characterize the instrumental polarization because it has a very low polarization fraction (see Wiesemeyer et al., 2014, where a polarization fraction of $0.10 \pm 0.04\%$ is reported for Uranus at 870 μm using LABOCA at APEX). Uranus is also a bright source (47.2 Jy at 1.15 mm) and has a small size (with a typical disc angular diameter $\sim 3''$) compared to the telescope beam and can be considered as a point source for NIKA2-Pol. During the dedicated NIKA2-Pol commissioning runs of Dec. 2018, Feb. 2020, and Nov. 2020, we conducted repeated observations on the planet Uranus, an unpolarized source, to quantify the intensity-to-polarization leakage (instrumental polarization) affecting NIKA2-Pol data.

The first successful commissioning campaign was caried out in **Dec. 2018** which showed how NIKA2-Pol is sensitive to the instrumental polarization (IP) effects (hereafter "the IP leakage"). The need to characterize the leakage is crucial for upcoming scientific observations. The Dec. 2018 campaign allowed us mainly to have an idea about the complexity of the leakage pattern. Qualitatively, the leakage affecting NIKA2-Pol data has the shape of a cloverleaf consisting of a central positive lobe surrounded by a negative quadrupolar pattern (see Fig. 4.1). The four lobes pattern of the IP leakage has been observed at the 26 m radio telescope at Hat Creek Observatory, and interpreted as a displacement of the polarized beam (Troland & Heiles, 1982). Analysis of series of focused/defocused using NIKA2-Pol observations of Uranus showed that the leakage is sensitive to the focus position of the telescope (see Sect. 4.3.1 for more details). Uranus observations at different elevations showed that the leakage pattern remains approximately fixed in Nasmyth coordinates (slightly rotating due to the astigamtism of the telescope, i.g, see Sect. 4.14) but rotates in Az–El or RA–Dec coordinates. Due to the lack of Uranus observations for a wide range of elevations and focus positions, the Dec. 2018 data were however insufficient to characterize precisely and quantitatively the leakage changes.

The second campaign took place in **Feb. 2020**, where we aimed to get more statistics on Uranus observations to quantify the instrumental polarization effects. These observations confirmed the cloverleaf pattern of the leakage as seen in previous data (Dec. 2018). A slight rotation on the leakage pattern was noticed compared to the Dec. 2018 observations. This rotation was likely due to a change in mirror alignment in 2019 (alignment of mirrors 2, 3 and 4 using a laser to get a good match in the optical axis and guarantee a proper alignment of the detectors on the sky).

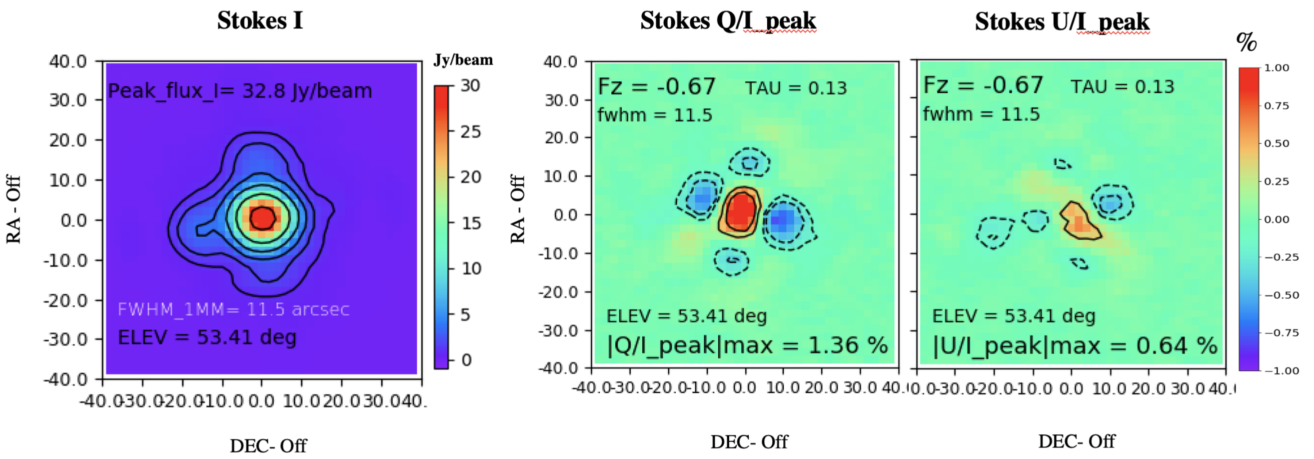

Figure 4.1: Examples of Stokes (I, Q, U) maps obtained for Uranus (in Nasmyth coordinates). Uranus being an unpolarized source, the signals detected in Stokes Q, U correspond to instrumental polarization, which should be corrected for as part of the reduction of NIKA2 polarization data (a.k.a leakage correction). The color bar shows the fraction of U/I_{peak} or Q/I_{peak}. The leakage patterns in both Stokes Q and U vary from high to low elevation with a more deformed pattern in Stokes U. The pattern in Q and U are used to estimate the level of the instrumental polarization in OMC-1 maps and help to correct the scientific data.

The Feb. 2020 run covered Uranus observations from high (65°) to low (20°) elevations, which enabled us to have more statistics to characterize the leakage pattern as function of elevation. Due to the lack of observations of Uranus at small focus offsets (±0.2 mm), the data were insufficient to understand the effect of focus on the leakage. In Feb. 2020, Uranus was mostly visible in the afternoon which added another complication coming from the deformation of the beam pattern during day time. Data analysis of this campaign helped to quantify the leakage under unstable weather conditions. The NIKA2-Pol leakage pattern was characterized using series of short scans on Uranus. Comparing these short scans to beam maps allowed us to decide whether we needed to integrate more to get a suitable leakage map or whether a short scan was sufficient.

The third campaign was carried out in **Nov. 2020** and its observations completed our sample in getting more statistics on Uranus for short scans, long-duration scans, a wide range of elevations under stable weather conditions, and different focus positions. The high-quality observations taken under very stable weather conditions during this third run helped in better characterizing the leakage effect. To investigate the possible source of the instrumental polarization affecting NIKA2-Pol, we observed Uranus on different days and with/without Styrofoam (polystyrene window) installed at the entrance of the receiver cabin to thermally isolate it from the outside. We performed Uranus observations before observations of extended sources to test the leakage correction applied to scientific targets (here for OMC-1, DR21, and the Crab nebula). Correcting the scientific data for the leakage effect was important to test the ability of NIKA2-Pol to provide robust and high-performance polarization data for scientific purposes.

In the present section, I report a detailed analysis of the leakage pattern/intensity during the different commissioning campaigns. I provide a full description of the instrumental polarization depending on the different aspects introduced above. I discuss all issues that have been seen during the commissioning of NIKA2-Pol. I present our results on the leakage correction and address the question of its origin.

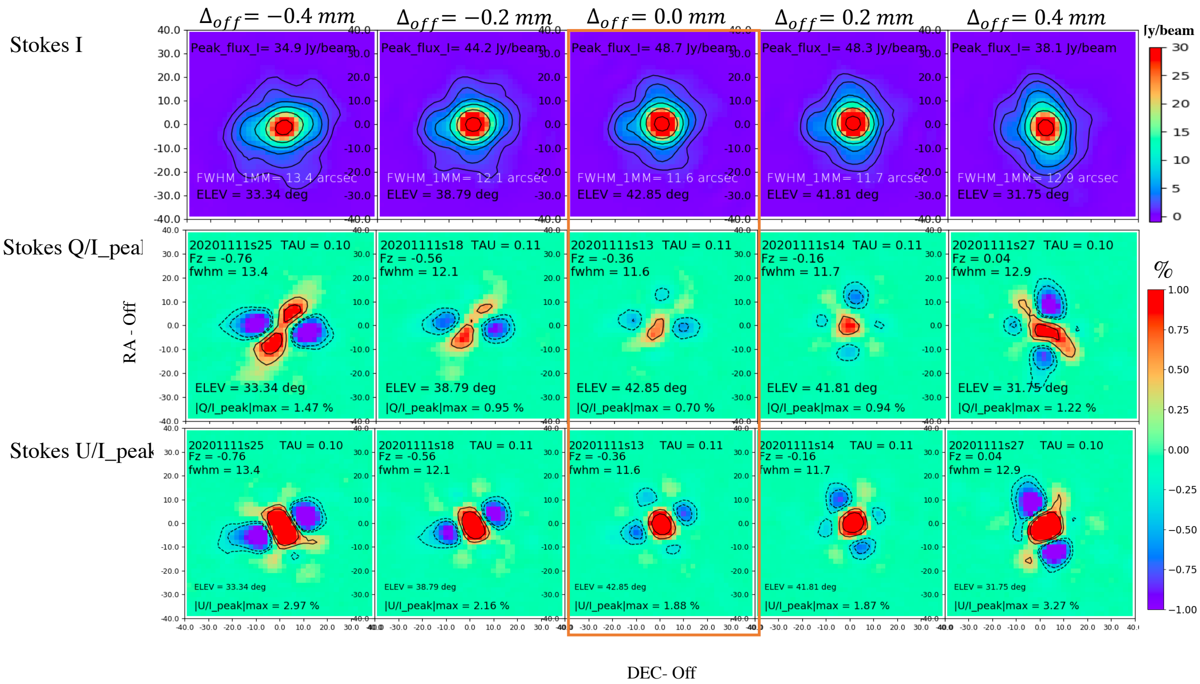

Figure 4.2: Example of a focus sequence on Uranus in Nasmyth coordinates showing how the instrumental polarization pattern (Stokes Q and U emission maps from an unpolarized source) varies as a function of the offset from the optimum focus position (along the Z-axis). The typical cloverleaf pattern seen at the best focus position becomes more severely distorted as the applied focus correction is farther away from its optimum value. The central map here is the one taken at a good focus position and the correction is named by Δ_{off} for positive and negative corrections with respect to the optimum leakage pattern from the left and to the right panel, respectively.

4.3.1 Leakage dependence on focus

During all three NIKA2-Pol commissioning campaigns, we observed focus sequences as well as defocused maps of Uranus to scrutinize the variation of the IP leakage with the focus position of the telescope. Our analysis based on several defocused maps taken under stable weather conditions at different focus offsets shows that the leakage is quite sensitive to the focus (which an out of focus offset of +/- 0.2mm inducing a different IP leakage). The fZ focus position depends on the stability of the weather conditions in a given observing run. Under stable conditions, the focus varies only slightly (±0.3 within 5-6 hours during the night), and the observer must perform a focus check each 2-3 hours. Under unstable conditions, the beam pattern and focus change more rapidly (within an ∼1 hour), and the focus must be done every hour. In daytime, one should generally avoid the afternoon because of the deformation of the 30m main beam pattern. We adopted the same strategy as described in Sect. 4.2.1 to study the variation of the leakage pattern/intensity with the focus position of the telescope. We mainly observed Uranus as a bright unpolarized point source (Wiesemeyer et al., 2014). In order to detect any variation of the leakage pattern, we carried out defocused observations at offsets (between the out of focus position and the optimal focus) of -0.4 mm, -0.3 mm, -0.2 mm, -0.1 mm, +0.1 mm, +0.2 mm, +0.3 mm, +0.4mm. The IP vs focus effect can be seen using a series of focus maps where we changed the focus position to obtain the correction needed for the optimal focus. The standard focus correction (as described in section 4.2.1) is made by observing bright sources at five different focus positions (mostly with 0.4 mm step). The observations made by the NIKA2 team on Uranus as part of the total power commissioning showed how the beam pattern varies at different focus positions. Perotto et al. (2020) noticed features in the diffraction pattern observed in Uranus maps at 1mm and 2mm wavelength caused by the quadrupod secondary support structure (see Fig. 5 in Perotto et al., 2020), which are mainly due to the reflector panels (Greve et al., 2010). Figure 4.2 shows the (I, Q, U) maps observed during a focus sequence where the focus offset varied from -0.4 mm +0.4 mm by step of 0.2 mm. The typical cloverleaf pattern seen at the optimum focus position becomes more distorted as the applied focus correction is farther away from the best focus position. The central map in figure 4.2 is the one taken at a good focus position and the correction is indicated by Δ_{off} for negative and positive corrections with respect to the optimum leakage pattern from the left to the right panel, respectively.

From our analysis of defocused and focused maps, the IP pattern/intensity appears to be sensitive to the focus position of the telescope. We found that the maximum fractional amplitude of the leakage pattern (|Q/Ipeak|max and |U/Ipeak|max) increases by only 0.2 % compared to its optimum value as long as the focus position is off by less than ± 0.2mm from the optimum focus correction (along the Z-axis). However, the shape of the leakage pattern changes quite significantly (and even loses its cloverleaf shape) at even small focus offsets of ± 0.3 mm.

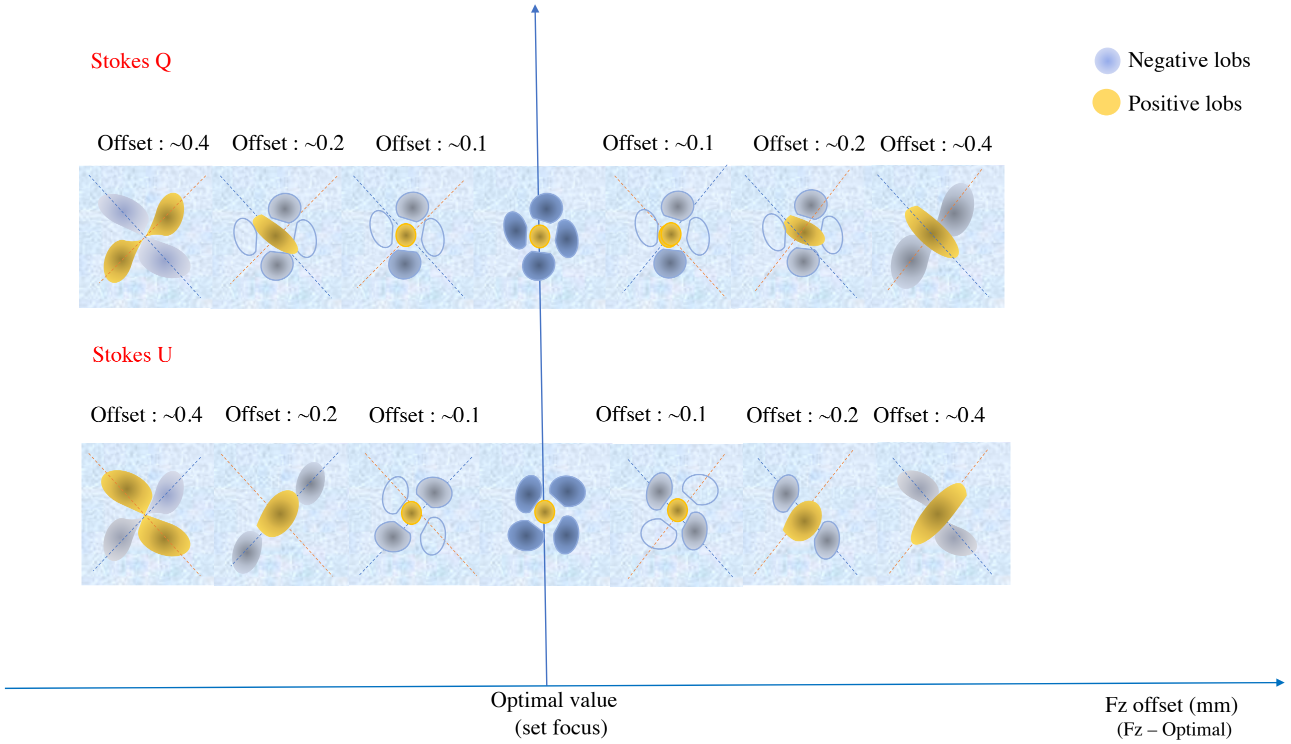

Figure 4.3: Schematic diagram in Nasmyth coordinates summarizing how the instrumental polarization pattern (Stokes Q and U emission maps from an unpolarized source) varies as a function of the offset from the optimum focus position (along the Z-axis). The typical cloverleaf pattern seen at the best focus position becomes more severely distorted as the applied focus correction is farther away from its optimum value. This schematic diagram gives an overview and summary of the leakage versus focus positions analysis using Nov. 2020, Feb. 2020, and Dec. 2018 data.

To further quantify the dependence of the leakage pattern with focus, a larger number of defocused maps of Uranus taken at smaller focus offsets (e.g. ± 0.1 mm, ± 0.15 mm, ± 0.2 mm, ± 0.25 mm) from the optimal focus value were also carried out during these campaigns. Figure 4.3 summarizes the dependence of the leakage with the fZ focus. This schematic diagram presented in Nasmyth coordinates brings out our understanding of how the IP pattern/intensity varies as a function of the offset from the optimum focus position (along the Z-axis). It results from our data analysis of the three campaigns (Nov. 2020, Feb. 2020 and Dec. 2018) which allowed us to characterize the leakage versus focus positions precisely.

4.3.2 Leakage dependence with elevation

Uranus observations from low to high elevations (20° - 65°) helped in analyzing the leakage variation with elevation and its effect (due mainly to the system, e.g. telescope, optical path, or polarimeter) by comparing the IP pattern evolution in Stokes Q and U. Only Uranus observations at the best focus position were used for this purpose to avoid any confusion with the effect of focus. All Uranus scans were taken under stable weather conditions and resulted in FWHM beam sizes of < 13 arcsec. The leakage pattern observed under such conditions is typically quadrupolar in shape in both Stokes Q and Stokes U. The pattern in U is typically rotated with respect of the pattern in Q by 30° to 45°. However, in some cases, the pattern in U has a deformed shape and/or the opposite sign (Fig. 4.4). Based on the Dec. 2018 data, Ajeddig et al. (2020) presented the results of the analysis of this effect and found that the leakage pattern/intensity varies from low to high elevation (20° to 65°). Figure 4.4 shows a series of focused maps taken at different elevations from 43° to 24°. The second row maps shows the variation in the leakage pattern in Q/Ipeak which seems to keep the same shape but with different leakage intensity (2.9% to 2.1%). We also notice a deformed shape of the leakage at low elevation (less than 30 deg). The third row shows Stokes U/Ipeak maps, which show a more complex pattern, different from the Q pattern, and slightly changing at low elevations. This may be due to the deformation of the beam shape at low elevations.

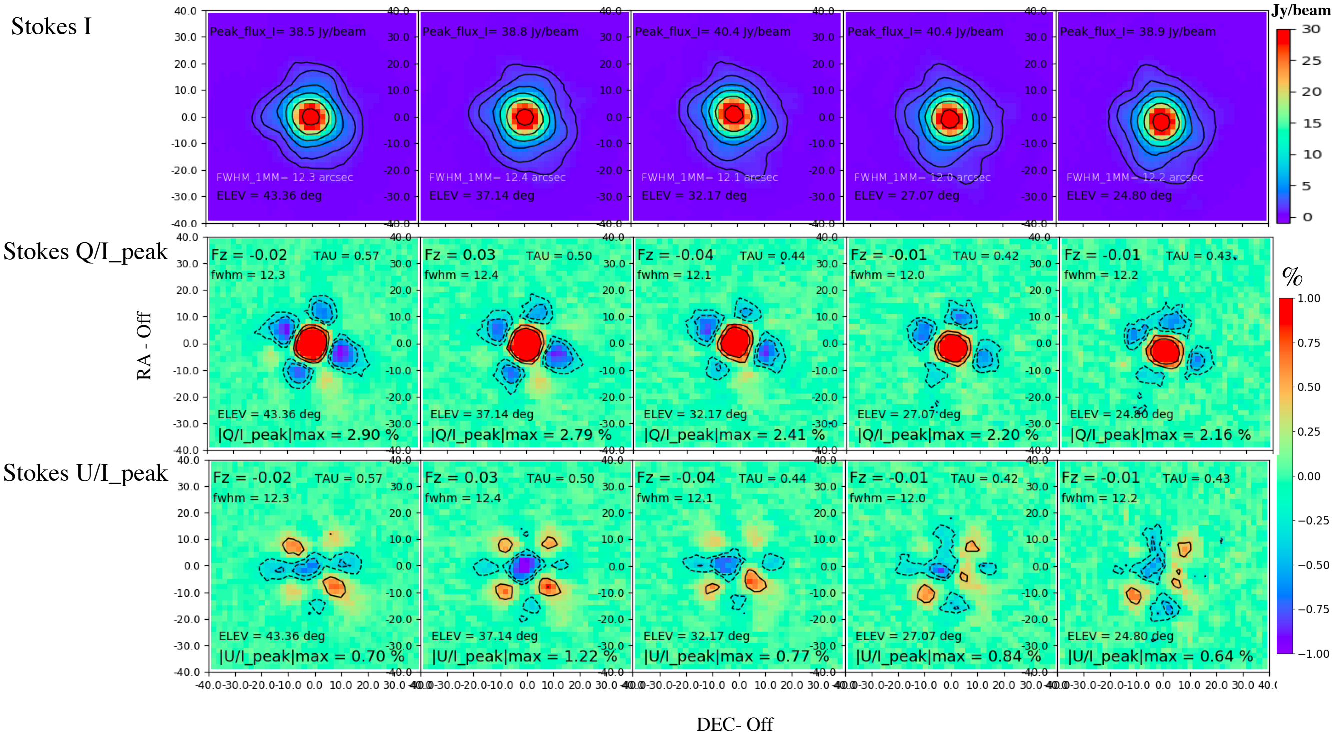

Figure 4.4: Examples of Uranus observations in Nasmyth coordinates showing how the instrumental polarization pattern (Stokes Q and U emission maps from an unpolarized source) varies from high to low elevation using Feb. 2020 data. The same behaviour was noticed in Nov. 2020 data

This variation of the leakage intensity with elevation needs to be considered when correcting the scientific data, thus ideally Uranus maps need to be observed in +/-10 deg of elevation offset from the scientific target. The IP variation with elevation may be due to the deformation of the main beam depending on elevation. Indeed, the beam in Stokes I at low elevation (< 30°) is deformed compared to the beam observed at more typical elevation (40° - 60°). One possible origin of this effect is the astigmatism of the wavefront caused by the deformation of the main beam reflector (Born & Wolf, 1980) (see Sect. 4.3.9).

4.3.3 Day-to-day variations of the leakage pattern

One of the major questions is whether the IP is stable from day to day and whether the observers need to perform observations of a polarization calibrator source (mainly Uranus which is not always in the sky) before mapping a scientific target with NIKA2-Pol. To answer this question, I compared the leakage pattern observed at similar elevations but on different days and observing conditions.

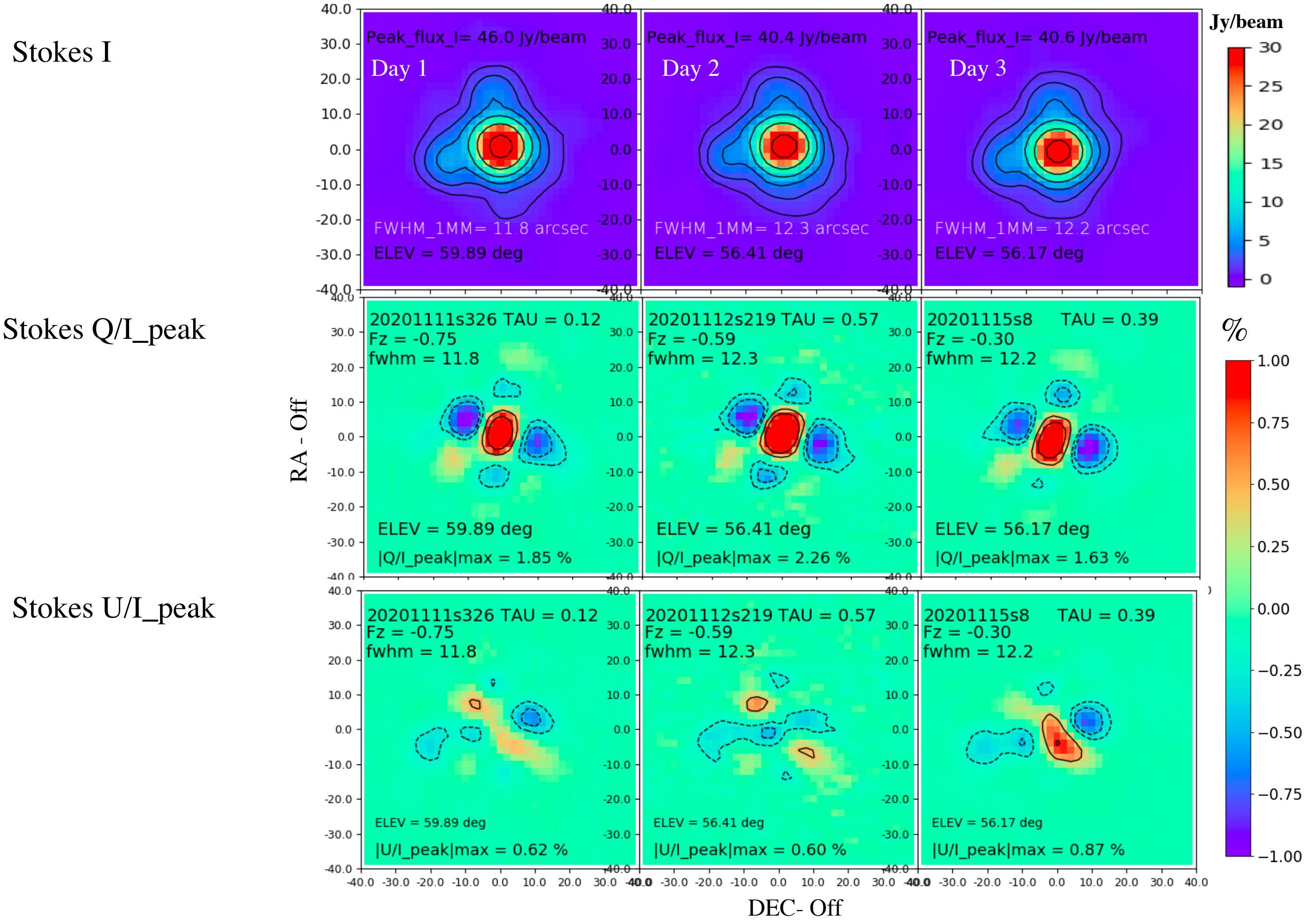

Figure 4.5: Examples of Stokes (I, Q, U) maps obtained for Uranus (in Nasmyth coordinates). The color bar shows the fraction of U/I_{peak} or Q/I_{peak}. The leakage patterns in both Stokes Q and U remain stable from one day to another during the same observing run. The leakage pattern in Stokes U seems to lose its quadripolar shape than the one in Q. The small difference in the leakage comes from the difference in focus position (see section 4.3.1) and different weather conditions. The stability of the leakage pattern from day to day at the same elevation, focus, and weather conditions suggests that observing Uranus every day may not be necessary. The scans shown here were taken on 11, 12, and 15 of November 2020, respectively.

Figure 4.5 shows Uranus observations taken on different days and under different weather conditions. The leakage pattern in Stokes Q remains stable with its cloverleaf shape and negative quadruplar lobes. For Stokes U, the pattern is less clear but has weaker intensity and is slightly different from one day to another. These maps illustrate the stability of the leakage from day to day for a given elevation and a given focus position. The slight observed differences in leakage pattern and intensity may come from slight differences in focus position. **Our analysis shows that the leakage is stable on a day-to-day basis (within 0.2% - 0.3% of difference) when observations are taken at the same focus and elevation, which leads us to conclude that it may not be necessary to observe Uranus every single day, thereby saving a significant amount of time.**

4.3.4 Year-to-year variations of the leakage pattern

From the Uranus observations in Dec. 2018 and Nov. 2020, the leakage pattern seems to be stable with a slight rotation of the quadrupolar pattern, which is probably due to a slight change in mirror alignment done by the IRAM 30m staff in 2019. The IP shape was very stable in 2018 from 5 Dec.2018 and 8 Dec.2018. The Q and U patterns have the same shape (cloverleaf pattern) but rotated by 30° to 45°. Both (Q and U) patterns remained stable during the same observing run in 2020.

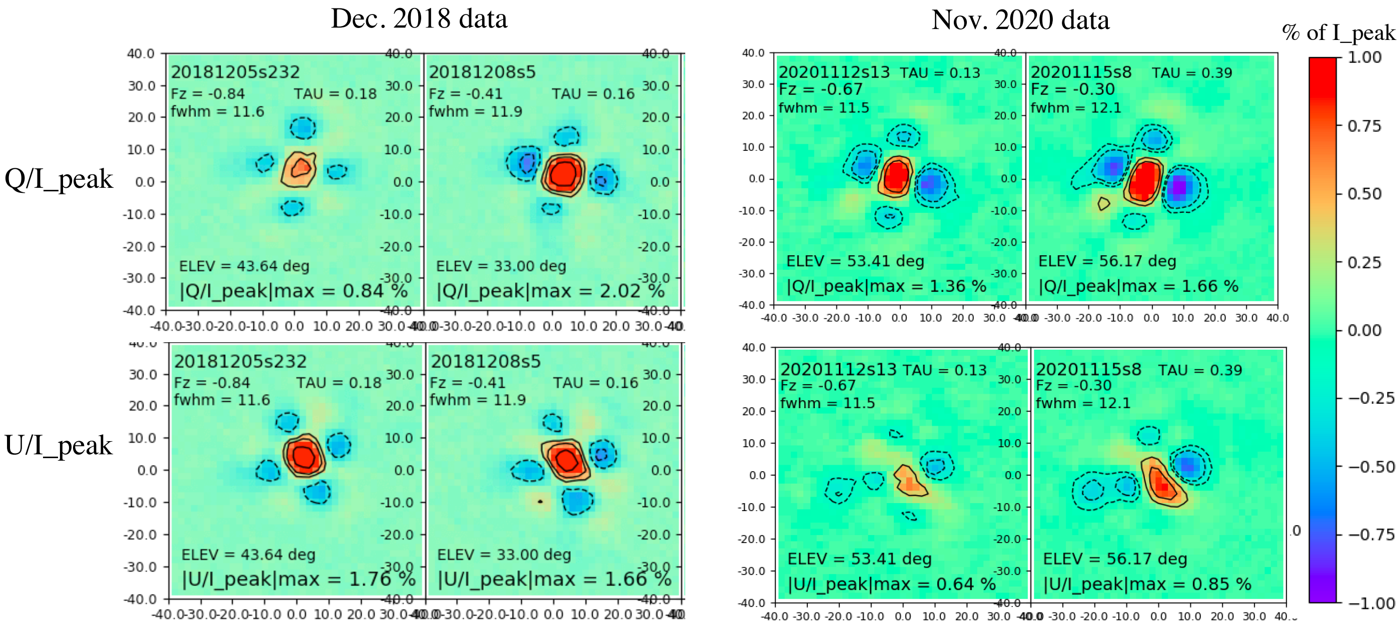

Figure 4.6: Examples of Stokes (Q, U) leakage maps (in Nasmyth coordinates) obtained on Uranus during the Dec. 2018 (left two columns) and Nov. 2020 (right two columns) runs. Uranus being an unpolarized calibrator, these maps provide the pattern of NIKA2-POL instrumental polarization. Note the cloverleaf shape. The leakage pattern in both Stokes Q and Stokes U is stable from day to day under similar observing conditions.

The cloverleaf shape of the leakage pattern can be seen in the data taken in all three commissioning campaigns, but the intensity of the leakage varied depending on observing conditions. **By analyzing the IP using data of the Dec. 2018, Feb. 2020 and Nov. 2020 runs, we found that the leakage appears to be stable over several years from 2018 to 2020. The leakage correction can be done with all three data sets, see section 4.4**

4.3.5 Variation of the leakage pattern in the NIKA2 field of View (FoV)

The focal plane of the NIKA2 instrument is slightly bowl-shaped, thus the focus surface is not perfect, which may add more complications on the characterization of the leakage. The beam pattern changes across the FoV because of the variation of the local focus in different regions of the FoV, thus imply a different leakage pattern. The previous analysis (Sect. 4.2.1 to 4.3.4) was made using short scans of Uranus (∼5 min) which involved only the central KIDs. As the response of the KIDs varies depending on their position in each of the NIKA2 arrays, here, we compare the IP leakage pattern depending on position in the NIKA2 field of view (FoV). The left panel of Figure 4.7 divides the FoV into 9 circular positions (1 to 9). The right panel shows the corresponding leakage observed in Q and U. It can be seen that the central KIDs exhibit the ordinary leakage pattern already observed, while the IP leakage pattern observed in the outer parts of the FoV differ slightly from the standard pattern. Across the FoV, the intensity of the IP leakage varies by about a factor of 2 but the shape of the leakage pattern remains approximately the same.

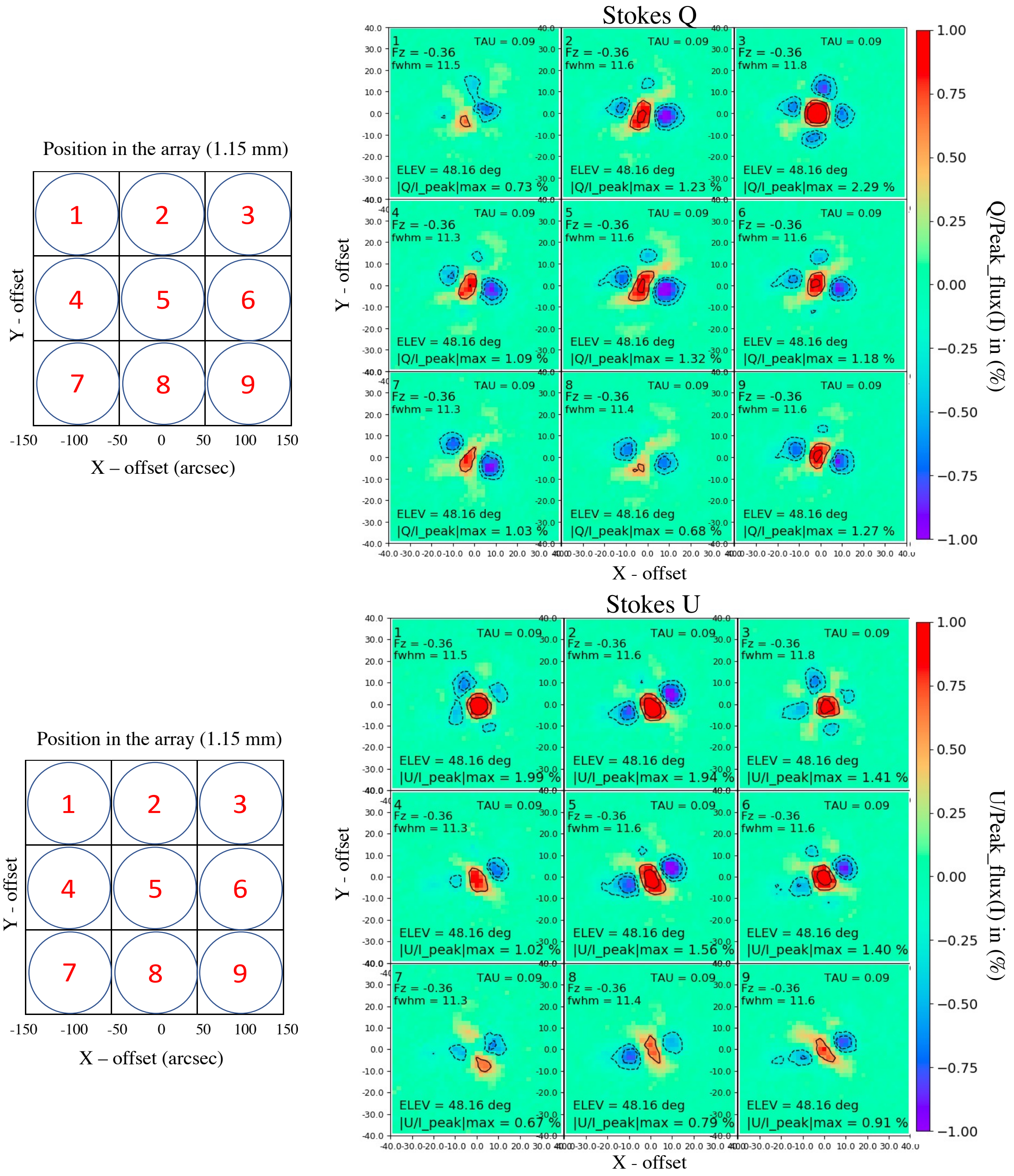

Figure 4.7: Variation of the IP pattern/intensity as function of position in the NIKA2 field of view (FoV). Offsets are in Nasmyth coordinates. **Left** : Location in the FoV marked by numbers from 1 to 9, where for example 5 represents the central area in the FoV. The diameter of each circle is 100 arcsec. **Right** : Leakage pattern in Stokes Q and U for each of the 9 locations in the FoV schematically shown on the left.

4.3.6 Leakage pattern in arrays A1 and A3

At 1.15 mm wavelength, the NIKA2 data obtained with Array 1 (A1) and Array 3 (A3) are usually combined to improve the signal-to-noise ratio of the resulting maps. The effective leakage pattern results from the combination of IP in arrays A1 and A3, which adds another complication to this effect. In our attempt to characterize the IP in detail, we compared the leakage pattern observed separately with arrays A1 and A3 in both Stokes Q and U. Figure 4.8 shows the leakage patterns for A1 and A3, along with the difference between the A1 and A3 patterns. The maximum magnitude of the difference pattern is 0.74% and 0.47% (of the peak of intensity in Stokes I) in Stokes Q and U, respectively.

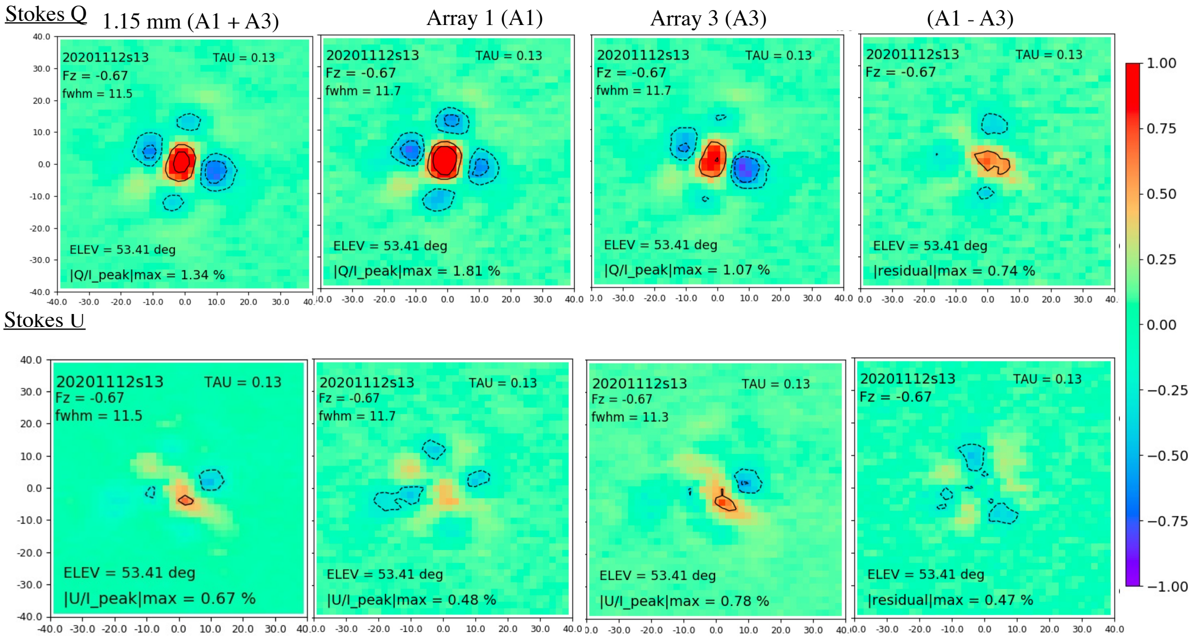

Figure 4.8: The leakage pattern as seen by NIKA2-Pol in arrays 1 and 3. The leakage pattern in Stokes Q is not very different in A1 and A3 but the IP level in A1 seems to be higher than A3 (1.81% and 1.07% in A1 and A3, respectively). However, the IP in Stokes U seems to have a random pattern which is completely different from the IP in Stokes Q. The differences in Stokes Q and U are 0.74% and 0.47% which indicate that the IP differs in A1 and A3. The IP pattern that we usually employ to correct the data is the combination of A1 and A3. The difference maps are in the right panel correspond to $(Q_{A1}/I_{peak,A1} - Q_{A3}/I_{peak,A3})$ and $(U_{A1}/I_{peak,A1} - U_{A3}/I_{peak,A3})$

.

A possible origin of the difference in IP pattern between A1 and A3 can be imperfections of the dichroic or the polariser. The response of the KIDs may not be exactly the same in A1 and A3. **This comparison between arrays 1 and 3 indicates that the leakage intensity varies slightly depending on the array. The leakage patterns in A1 and A3 seem to be more stable in Stokes Q than in Stokes U.**

4.3.7 Leakage behavior according to the reference frame

The IP leakage pattern seen with NIKA2-Pol depends mainly on focus and elevation (as discussed in Sect. 4.2.1 and 4.4). We also investigated the behavior of the leakage in different coordinate systems, especially in Nasmyth and Az-El frames. We analyzed Stokes Q and U of two Uranus scans observed at low and high elevation corresponding to 21° and 60° and under stable weather conditions. This test aimed to investigate the stability of the IP leakage in different coordinate systems. Figure 4.9 shows Stokes Q and U (in the left and right panels, respectively) in Nasmyth and Az-El coordinates in the top and bottom raws, respectively. The IP leakage remains approximately stable in Nasmyth coordinates (apart from a small rotation of the leakage coming from the astigmatism effect, c.f Sect. 4.3.9.1). However, in Az-El coordinates, the IP leakage exhibits much stronger variations between low and high elevations, in both Stokes Q and U (see Fig. 4.9).

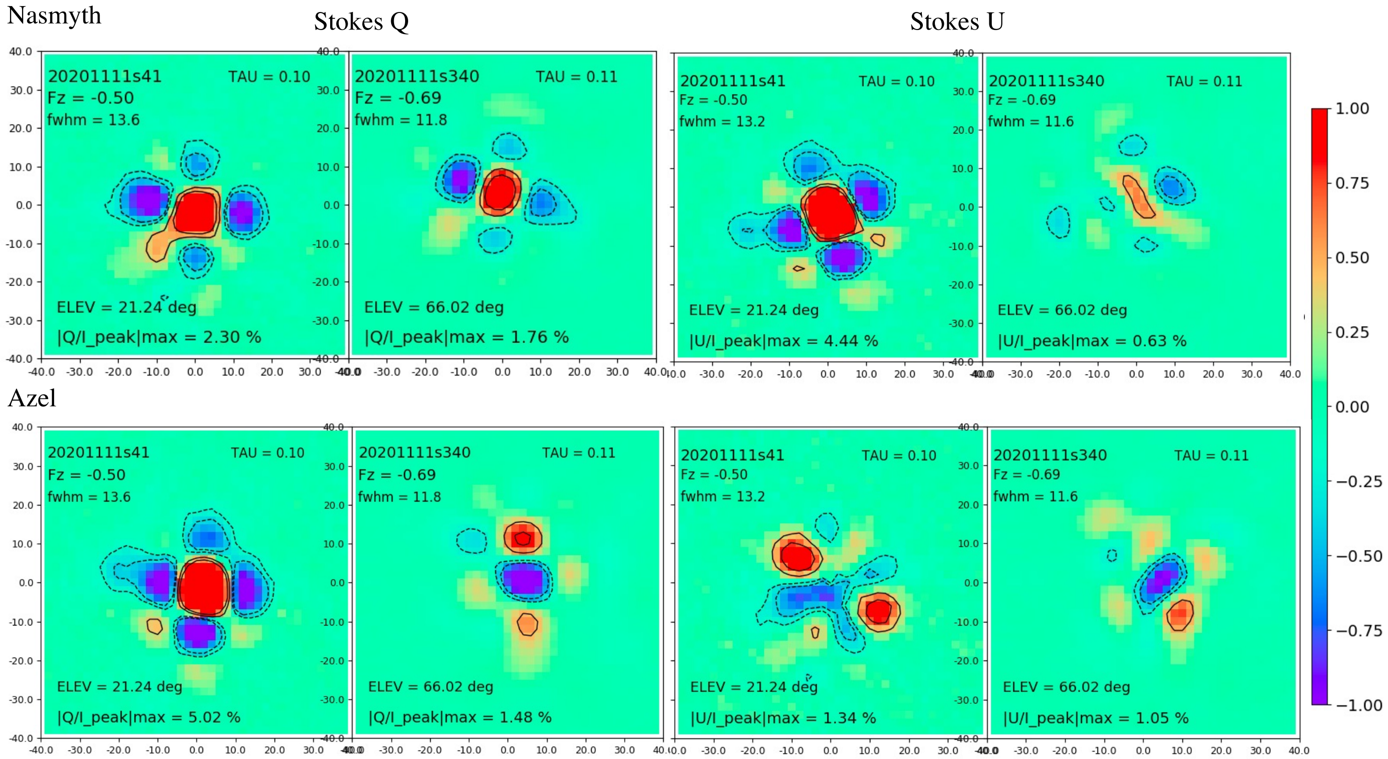

Figure 4.9: The IP leakage in Stokes Q and U in Nasmyth and Az-El coordinates. *Left*: Stokes Q maps of two Uranus scans taken at low and high elevation in Nasmyth and Az-El coordinates, respectively. *Right* : Similar to *left* but for Stokes U.

At low elevation (<30°), the amplitude of the IP leakage intensity appears to be higher than standard measurements (in this case 4 - 5%) which is partly due to the the astigmatism of the telescope at this elevation (see Sect. 4.3.9.1). **We conclude that the IP leakage pattern is stable in Nasmyth coordinates but varies very significantly on short timescales in both RADEC and Az-El Coordinates. This analysis suggests that the leakage is mainly originated by the NIKA2-Pol instrument as opposed to the telescope. Even if the telescope may contribute slightly to the IP leakage through the astigmatism effect.**.

4.3.8 Analytical representation of the leakage

As the Stokes parameters Q, U correspond to differences of intensities measured in two orthogonal linear polarization directions, e.g., $Q = I_{0^\circ} - I_{90^\circ}$ and $U = I_{45^\circ} - I_{-45^\circ}$, and the beam pattern (in both shape and position) is unavoidably slightly dependent on the polarization direction, it is natural to try and express the leakage pattern observed in Q, U as a linear combination of the first terms of a two-dimensional Taylor expansion of the beam in Stokes I. Adopting this approach, we found out that the Q, U leakage patterns observed on Uranus are very well represented by a Taylor expansion of the I-beam B_I up to the fourth order. Thus, the leakage pattern in Q can be expressed as the following linear combination of I-beam derivatives:

$$\begin{aligned}
Q_l = a.B_I &+ c_x \frac{\partial B_I}{\partial x} + c_y \frac{\partial B_I}{\partial y} + c_{xx} \frac{\partial^2 B_I}{\partial x^2} + c_{yy} \frac{\partial^2 B_I}{\partial y^2} + c_{xy} \frac{\partial^2 B_I}{\partial x \partial y} \\
&+ c_{xxx} \frac{\partial^3 B_I}{\partial x^3} + c_{yyy} \frac{\partial^3 B_I}{\partial y^3} + c_{xxy} \frac{\partial^3 B_I}{\partial x^2 \partial y} + c_{xyy} \frac{\partial^3 B_I}{\partial x \partial y^2} \\
&+ c_{xxxx} \frac{\partial^4 B_I}{\partial x^4} + c_{yyyy} \frac{\partial^4 B_I}{\partial y^4} + c_{xxxy} \frac{\partial^4 B_I}{\partial x^3 \partial y} + c_{xyyy} \frac{\partial^4 B_I}{\partial x \partial y^3} \\
&+ c_{xxyy} \frac{\partial^4 B_I}{\partial x^2 \partial y^2}
\end{aligned} \tag{4.6}$$

Where a and $c_{[x,y,xx,yy,xy,...]}$ are the coefficients of the model. An equation similar to Eq. 4.6 holds also for the leakage pattern in Stokes U.

$$\begin{aligned}
U_l = a.B_I &+ c_x \frac{\partial B_I}{\partial x} + c_y \frac{\partial B_I}{\partial y} + c_{xx} \frac{\partial^2 B_I}{\partial x^2} + c_{yy} \frac{\partial^2 B_I}{\partial y^2} + c_{xy} \frac{\partial^2 B_I}{\partial x \partial y} \\
&+ c_{xxx} \frac{\partial^3 B_I}{\partial x^3} + c_{yyy} \frac{\partial^3 B_I}{\partial y^3} + c_{xxy} \frac{\partial^3 B_I}{\partial x^2 \partial y} + c_{xyy} \frac{\partial^3 B_I}{\partial x \partial y^2} \\
&+ c_{xxxx} \frac{\partial^4 B_I}{\partial x^4} + c_{yyyy} \frac{\partial^4 B_I}{\partial y^4} + c_{xxxy} \frac{\partial^4 B_I}{\partial x^3 \partial y} + c_{xyyy} \frac{\partial^4 B_I}{\partial x \partial y^3} \\
&+ c_{xxyy} \frac{\partial^4 B_I}{\partial x^2 \partial y^2}
\end{aligned} \tag{4.7}$$

The NIKA2-Pol team has devised a way to exploit Eqs. 4.6 and 4.7 without computing the direct derivatives of the observed intensity maps to avoid adding too much noise to the data. In practice, we introduce a convolution with a Gaussian approximation of the main beam in I and express the leakage pattern as follows:

$$\begin{aligned}
Q_l = a_q.B_I * B_{IG} &+ cq_x \frac{\partial B_{IG}}{\partial x} * B_I + cq_y \frac{\partial B_{IG}}{\partial y} * B_I + cq_{xx} \frac{\partial^2 B_{IG}}{\partial x^2} * B_I + cq_{yy} \frac{\partial^2 B_{IG}}{\partial y^2} * B_I + cq_{xy} \frac{\partial^2 B_{IG}}{\partial x \partial y} * B_I \\
&+ cq_{xxx} \frac{\partial^3 B_{IG}}{\partial x^3} * B_I + cq_{yyy} \frac{\partial^3 B_{IG}}{\partial y^3} * B_I + cq_{xxy} \frac{\partial^3 B_{IG}}{\partial x^2 \partial y} * B_I + cq_{xyy} \frac{\partial^3 B_{IG}}{\partial x \partial y^2} * B_I \\
&+ cq_{xxxx} \frac{\partial^4 B_{IG}}{\partial x^4} * B_I + cq_{yyyy} \frac{\partial^4 B_{IG}}{\partial y^4} * B_I + cq_{xxxy} \frac{\partial^4 B_{IG}}{\partial x^3 \partial y} * B_I + cq_{xyyy} \frac{\partial^4 B_{IG}}{\partial x \partial y^3} * B_I \\
&+ cq_{xxyy} \frac{\partial^4 B_{IG}}{\partial x^2 \partial y^2} * B_I
\end{aligned} \tag{4.8}$$

where B_{IG} denotes a 2D Gaussian beam with the same FWHM as the actual NIKA2 main beam (11.7″). And a similar representation for the leakage pattern in U :

$$\begin{aligned}
U_l = a_u.B_{IG} * B_{IG} &+ cu_x \frac{\partial B_{IG}}{\partial x} * B_{IG} + cu_y \frac{\partial B_{IG}}{\partial y} * B_{IG} + cu_{xx} \frac{\partial^2 B_{IG}}{\partial x^2} * B_{IG} + cu_{xx} \frac{\partial^2 B_{IG}}{\partial x \partial y} * B_{IG} + cu_{yy} \frac{\partial^2 B_{IG}}{\partial y^2} * B_{IG} \\
&+ cu_{xxx} \frac{\partial^3 B_{IG}}{\partial x^3} * B_{IG} + cu_{yyy} \frac{\partial^3 B_{IG}}{\partial y^3} * B_{IG} + cu_{xxy} \frac{\partial^3 B_{IG}}{\partial x^2 \partial y} * B_{IG} + cu_{xyy} \frac{\partial^3 B_{IG}}{\partial x \partial y^2} * B_{IG} \\
&+ cu_{xxxx} \frac{\partial^4 B_{IG}}{\partial x^4} * B_{IG} + cu_{yyyy} \frac{\partial^4 B_{IG}}{\partial y^4} * B_{IG} + cu_{xxxy} \frac{\partial^4 B_{IG}}{\partial x^3 \partial y} * B_{IG} + cu_{xyyy} \frac{\partial^4 B_{IG}}{\partial x \partial y^3} * B_{IG} \\
&+ cu_{xxyy} \frac{\partial^4 B_{IG}}{\partial x^2 \partial y^2} * B_{IG}
\end{aligned} \tag{4.9}$$

Equations 4.8 and 4.9 provide an analytical representation of the leakage pattern for Stokes Q and Stokes U, respectively. Taken at face value, equations have 15 terms and coefficients (cq_x, cq_y, cu_x ...). However, a detailed analysis of the broad set of Uranus data from Nov. 2020 and Feb 2020 shows that the fourth derivatives of the beam (5 coefficients) dominate. The reason why this is the case is that one of the fourth derivatives of the beam ($\frac{\partial^4 B_I}{\partial x^2 \partial y^2}$) exhibits a symmetric cloverleaf pattern very similar to the observed leakage pattern, apart from a different orientation (see Fig. 4.11).

Figure 4.10 shows one example of the observed leakage in Q, U (left column of the figure), the corresponding best-fit model following Eqs. 4.8 and 4.9 (middle column), and the residuals (right column).

It can be seen that the model represents the observed leakage very well. **It is important to stress that this analytical representation provides a good representation of all leakage patterns observed on Uranus with NIKA2-Pol during the commissioning campaigns of Dec. 2018, Feb. 2020 and Nov. 2020 ($>$ 500 scans).**

This model is currently being employed extensively on the commissioning data to try and describe the dependence of the coefficients in Eq. 4.8 and Eq. 4.9 with, e.g., elevation and focus in terms of simple analytical functions. In the future, we hope to be able to correct real data for IP using such an analytical model, without the need to monitor the leakage pattern on Uranus at frequent intervals.

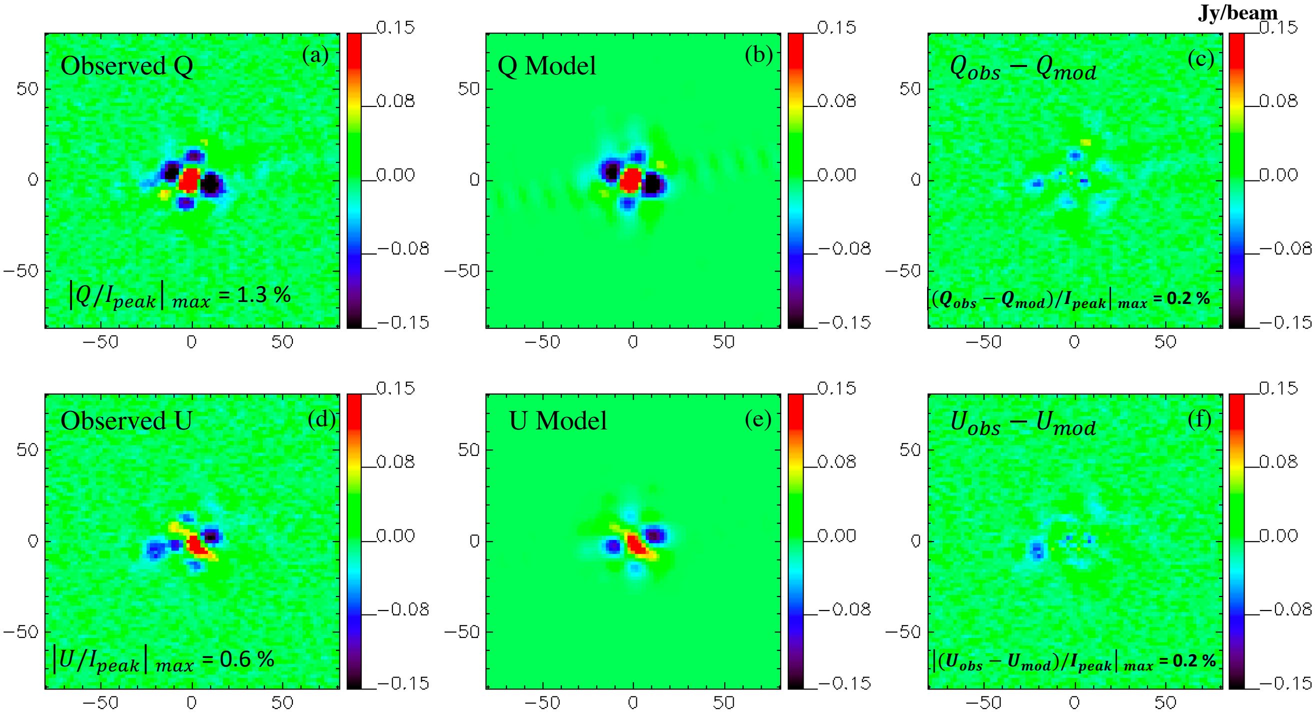

Figure 4.10: Example of a leakage pattern observed in Q, U on Uranus (letft column), corresponding model leakage using Eq. 4.8 and Eq. 4.9 (middle column), and residuals (right column). All maps are in Nasmyth coordinates and the offsets given in arcsec.

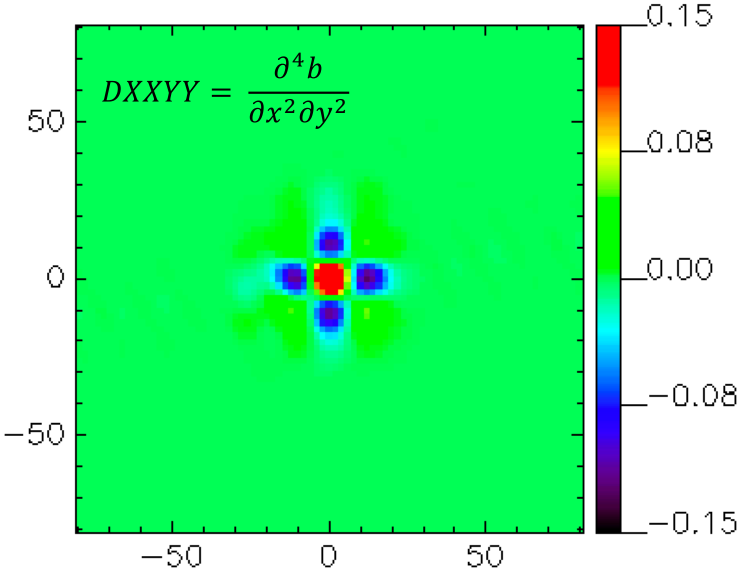

Figure 4.11: Fourth derivative of a (nearly Gaussian) beam, $\frac{\partial^4 B_I}{\partial x^2 \partial y^2}$, in Nasmyth coordinates (offsets given in arcsec). Note the cloverleaf pattern very similar to the leakage pattern observed in Q, U on Uranus (cf. left column of Fig. 4.10).

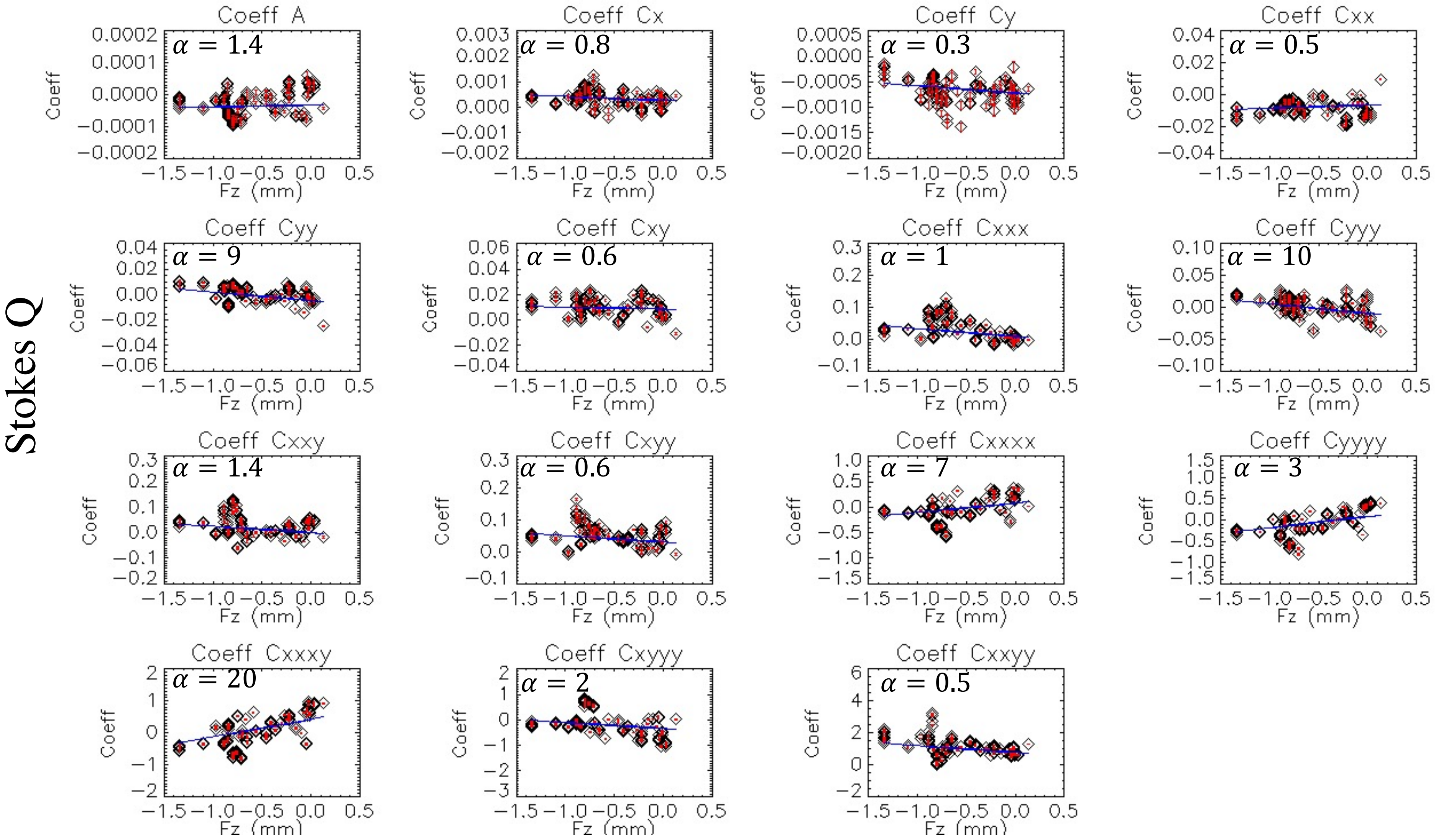

Figure 4.12: Variation of the 15 coefficients of the leakage model in Stokes Q as a function of focus position Fz (mm). The ratio α = std/mean where std is the standard deviation is given for each coefficient. α quantifies the variation of each coefficient with the absolute focus position (all scans were observed at the best focus position). The third and fourth-order coefficients appear to be variable from day to day and under different weather conditions. The blue line in each plot is the result of a linear regression of the coefficient with the focus position.

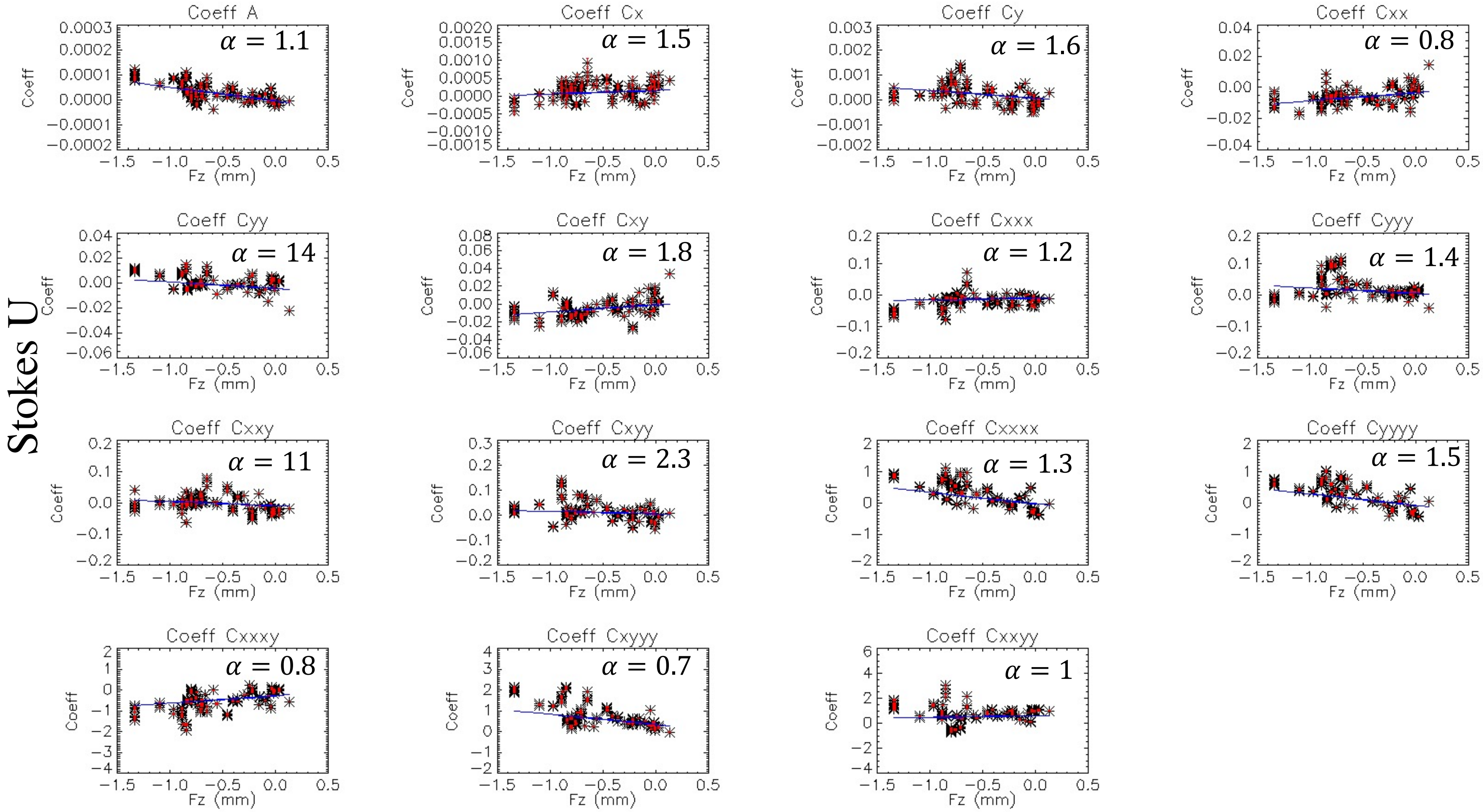

Figure 4.13: Variation of the 15 coefficients of the leakage model in Stokes U as a function of focus position Fz (mm). The ratio α = std/mean where std is the standard deviation is given for each coefficient. α quantifies the variation of each coefficient with the absolute focus position (all scans were observed at the best focus position). The third and fourth-order coefficients appear to be variable from day to day and under different weather conditions. The blue line in each plot is the result of a linear regression of the coefficient with the focus position.

Stability of the model coefficients

The analytical model may help to correct the scientific data when no Uranus maps are available especially when the planet cannot be observed. The coefficients of the model can be derived using Uranus maps observed at different elevations and weather conditions. Figures 4.12 and 4.13 show the evolution of these coefficients depending on the absolute focus position (Fz), where only maps taken at the best focus and under stable weather conditions were used. The coefficients of the first and second derivatives are very small compared to the third and fourth-order coefficients. The leakage model is dominated by the third and fourth derivative components of the model, which simplifies it to 9 coefficients instead of 15 for each of the Stokes parameters (Q, U). Using this model to improve the correction procedure on polarization data will help to get reliable scientific data with NIKA2-Pol. Devising a proper correction strategy with this model is still on going work.

4.3.9 Possible origin of the leakage

Observations of Uranus made in all three campaigns allowed us to precisely characterize the leakage pattern/intensity in different conditions. But, one of the remaining challenging questions, is to understand where the leakage seen by NIKA2-Pol comes from, e.g, whether it is coming from the telescope reflectors, the NIKA2-Pol instrument itself, the detectors or another source. Although this a complex problem, we were able to test some of the possible sources, such as the astigmatism of the telescope and the effect of the Styrofoam window. A possible origin of the observed cloverleaf pattern of the IP leakage may be the telescope secondary reflector feed legs (cF. Troland & Heiles (1982)). In this section, I present a preliminary analysis toward finding the origin of the observed IP leakage.

4.3.9.1 Effect of the telescope astigmatism

The astigmatism is the diffraction of the wave-front due to imperfections of the main beam which come from the deformation of the reflector surface of the telescope. This effect is common in Cassegrain reflector telescopes and mainly due to their design. Greve et al. (2010) investigated the effect of astigmatism in changing the main beam at the IRAM 30m telescope. Their analysis was based on in-and-out-of-focus diffraction images from point sources. This effect can be seen using our Uranus observations during the polarization campaigns, where we performed several focus sequences every day. **We found that the main beam in Stokes I, is elongated in the orthogonal directions when the focus setting offset is about +0.4 mm and -0.4 mm from the optimal focus position, respectively**. On one hand, our IP leakage model attributes the leakage to small difference in the beam in two orthogonal polarizations, and can explain all the patterns seen in Stokes Q and U. Thus a small deformation of the I beam can lead to different leakage patterns. On the other hand, the astigmatism of the main beam changes with elevation and leads to different leakage patterns depending on observing conditions. We believe that the direction of the astigmatism axis can help to find the precise orientation of the cloverleaf pattern seen in the IP leakage.

When the telescope is out of focus (e.g. $\Delta_{off} = \pm 0.4$ mm in Fig. 4.14), the Uranus beam in Stokes I is elongated in two orthogonal directions which give the orientation of the telescope astigmatism. The data indicate that the astigmatism orientation is not fixed in either Nasmyth or Az-El coordinates. It appears to vary with observing conditions and may be strongly sensitive to the thermal state of the 30m antenna. This orientation can be determined reasonably accurately by fitting an elliptical Gaussian to the defocused intensity images obtained on a strong point source at extreme focus offset positions (see bottom left and right panels of Fig. 4.14). The correction of the leakage using the model described earlier in this chapter (Sect. 4.4.5) could be potentially improved by taking into account this astigmatism effect but this would require more statistics on Uranus polarization data.
By comparing images taken in- and out-of-focus, our analysis suggests that the IP leakage follows the astigmatism axis which depends on the observing conditions. Figure 4.14 illustrates the dependence of the orientation of the leakage pattern with the astigmatism imperfections of the telescope. It shows an example of a focus sequence and a scan at the best focus ($\Delta_{off} = 0$ mm) at low elevation presenting the leakage in Q and U with the orientation of astigmatism estimated from Stokes I maps (in orange lines). **The leakage pattern in Q and U appears to slightly rotate (by $\sim \pm 10^\circ$) in Nasmyth coordinates from low to high elevation which we believe may come from the astigmatism effect.** In the example shown in Fig. 4.14, the leakage conserves its quadrupolar cloverleaf shape, and the Stokes Q and U patterns follow the orientation of the astigmatism axis.

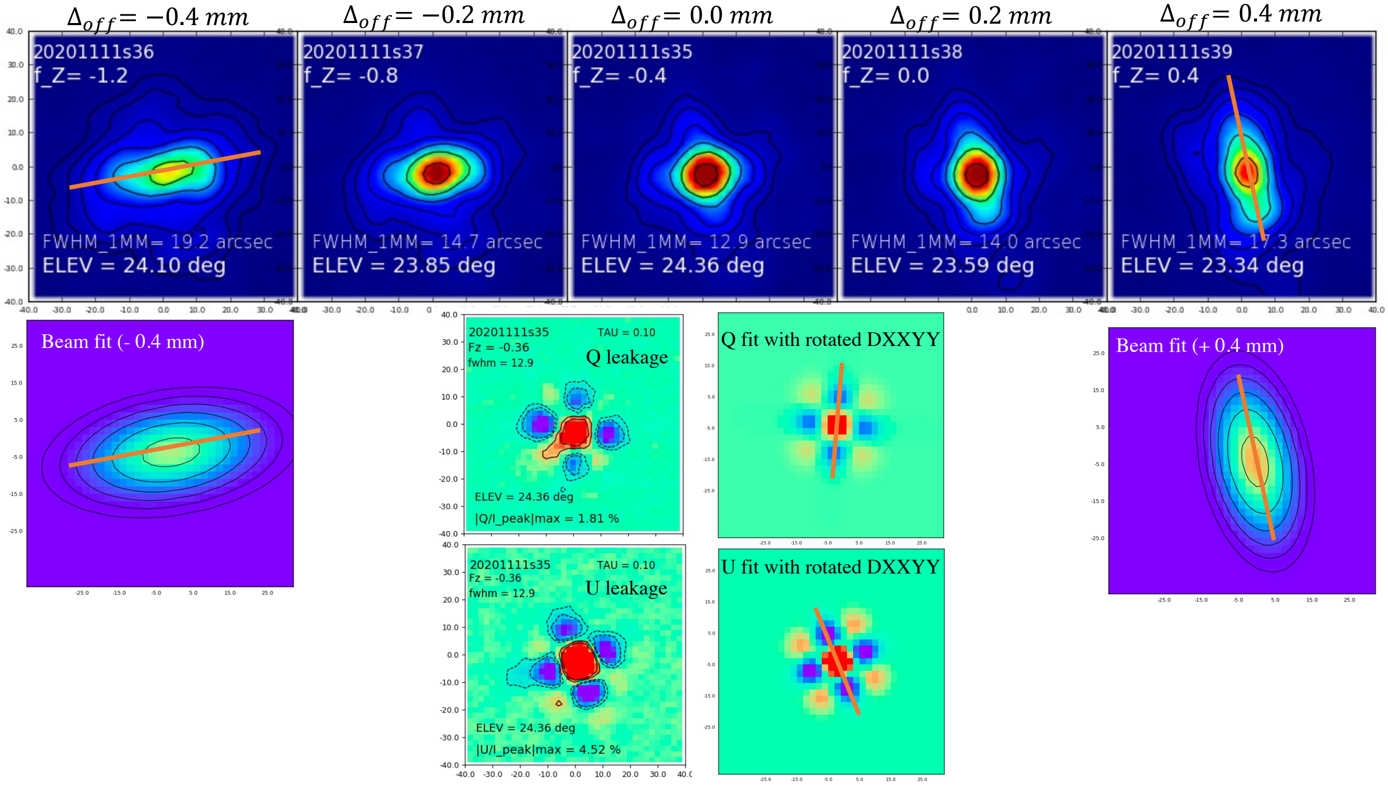

Figure 4.14: *Top row:* Examples of Stokes I images (in Nasmyth coordinates) obtained during a focus sequence on Uranus. The central image shows the beam observed at the best focus position ($\Delta_{off} = 0.0$). Note how the beam (in I) becomes elongated along two orthogonal directions at the two extreme focus offset positions ($\Delta_{off} = \pm 0.4$ mm). *Bottom left and right panels:* Elliptical Gaussian fits to the elongated beam shapes observed $\Delta_{off} = \pm 0.4$ mm, defining the orientation of the astigmatism effect. *Central panels at the bottom:* Cloverleaf leakage patterns observed in Q and U at the best focus position $\Delta_{off} = 0.0$ on the left, and simple fits to these cloverleaf patterns using a rotated version of the fourth-order derivative of a Gaussian beam $\frac{\partial^4 B_I}{\partial x^2 \partial y^2}$ (cf. Fig. 4.11) on the right.

When a clear overleaf shape is visible, the orientation of the leakage pattern can easily be quantified by fitting a rotated version of the fourth derivative of a Gaussian beam to the Q, U data (cf. four central panels at the bottom of Fig. 4.14).

We could perform a joint analysis of the astigmatism and leakage orientations for a total of 25 focus sequences in Q and 23 focus sequences in U. The results are shown in Fig. 4.15 and suggest a strong correlation between the position angle of the leakage pattern (in both Q and U) and the orientation of the telescope astigmatism, with a correlation coefficient of 80–90%.

This correlation with astigmatism, together with the above-mentioned dependence on focus and elevation, may largely account for the observed day-to-day variations in the leakage pattern. The simple model of the leakage pattern introduced in Sect. 4.3.8 can be employed more extensively on the existing commissioning data to try and describe the dependence of the coefficients in Eq. 4.8 and Eq. 4.9 with, e.g., focus, elevation, and astigmatism in terms of simple analytical functions.

The precision on leakage correction could also be improved in the future by deriving and applying a dedicated leakage model representing better the leakage pattern in different areas of the focal plane. As for the precise derivation of the analytical model coefficients, such a detailed correction will require a large dataset to be tested against, that only regular polarization observations will provide.

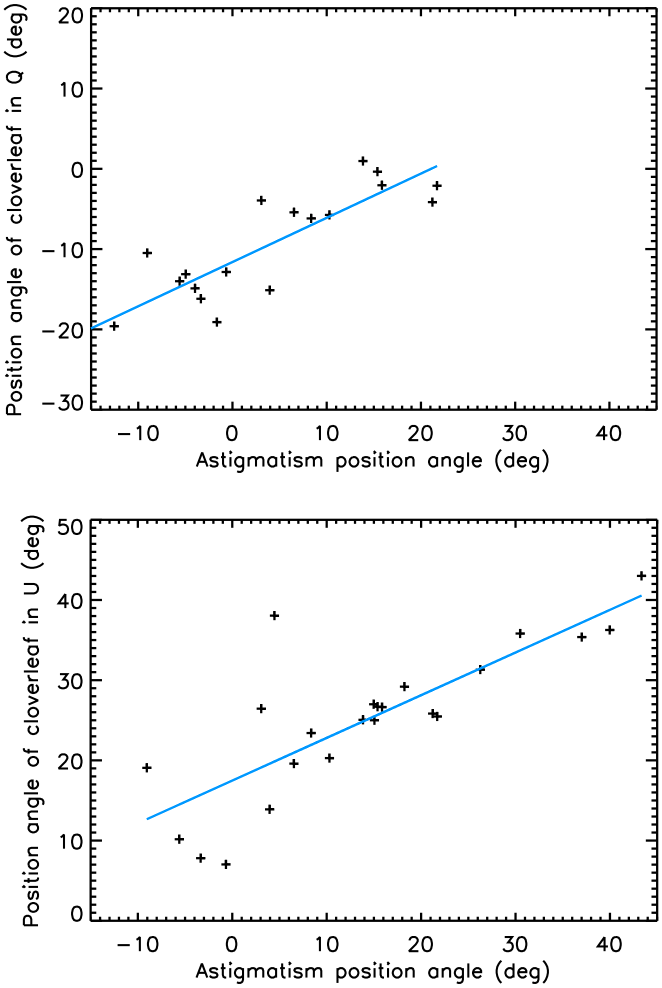

Figure 4.15: Position angle of the cloverleaf leakage pattern observed in Q (top panel) and U (bottom panel) as a function of the position angle of the astigmatism effect, for 23–25 focus sequences observed on Uranus in 2018–2020 for which the leakage pattern exhibits a clear cloverleaf shape. The position angles were derived using Gaussian fits to the I data and "cloverleaf" fits to the Q, U data as illustrated in Fig. 4.14. The blue solid lines show linear fits to the data points, which have a slope of ∼0.5 for both Q and U.

4.3.9.2 Effect of the Styrofoam window

The Styrofoam vertex window is made in polystyrene material which is placed at the entrance of the receiver cabin used as a thermal isolation material of the outside of the receiver cabin. For SCUBA2-POL2, Friberg et al. (2018) found that the IP leakage mainly comes from the Gore-Tex wind blind that is used to protect the JCMT telescope. We wanted to know if the Styrofoam window that is used in the 30m cabin contributes to the leakage observed with NIKA2-Pol and can be one of its possible origins. We thus carried out Uranus observations at different elevations with and without the Styrofoam. Figure 4.16 shows the differences between observations with and without the Styrofoam. The leakage pattern in Stokes Q and U seems to be stable with its ordinary shape while the intensity increases slightly when the Styrofoam is present. These two examples show that the presence of the Styrofoam does not contribute significantly to the IP leakage effect. The difference in the IP leakage intensity may come from a slight difference in focus Fz rather than from the Styrofoam. **Based on this, the Styrofoam window is not the origin of the IP leakage seen by NIKA2-Pol, but it may contribute slightly to its intensity.**

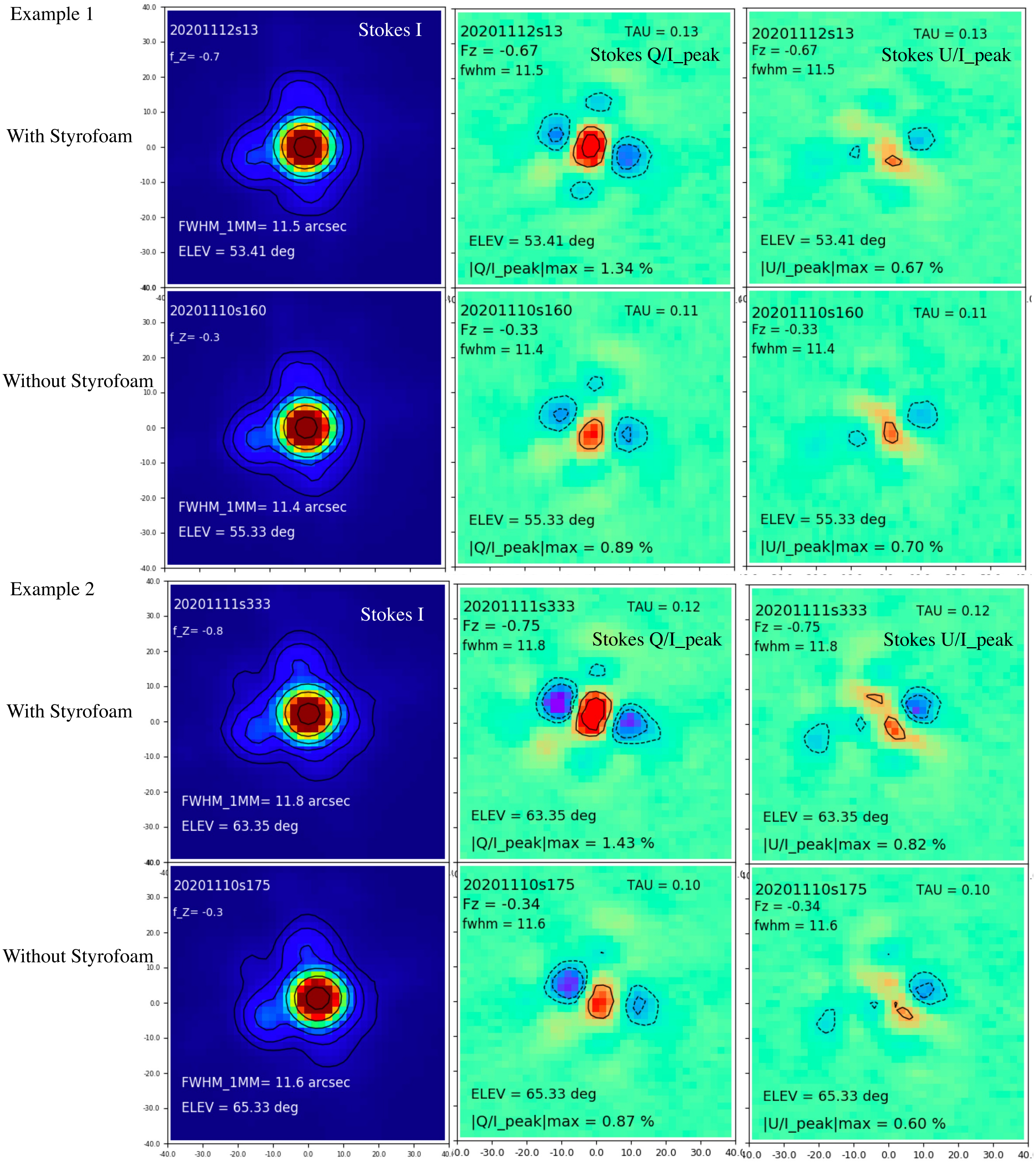

Figure 4.16: Two different examples showing the differences between NIKA2-Pol observations with and without the presence of the Styrofoam window (examples 1 and 2, respectively). The leakage pattern in Stokes Q and U seems to be stable regardless of the presence or absence of the Styrofoam while the leakage intensity increases slightly when the Styrofoam is present.

4.4 Correcting NIKA2-Pol data for the IP effect

While NIKA2-Pol data are significantly affected by the IP leakage effect, they can be corrected for this effect down to less than 1 % in instrumental polarization fraction when appropriate Uranus maps are available or using the newly developed model. If Uranus maps are available, the IP correction works robustly. If not, the model with coefficients derived from existing Uranus maps can be used. The dependence of the IP leakage on numerous parameters makes the correction limited. In the next subsections, I describe in detail the correction procedure that is already implemented in the NIKA2 IDL pipeline and its application to Uranus, quasars, and OMC-1 data.

4.4.1 Method of correcting data for instrumental polarization with Uranus

The IP leakage is defined as the leak of incident (unpolarized) total intensity to polarized signal in Stokes Q and U. As a consequence of this effect, the Stokes parameters Q and U observed toward a polarized source include a contribution from the instrument itself and the source intensity. Although NIKA, the pathfinder of NIKA2, had a different IP pattern, the IP correction method is inspired from the work of Ritacco et al. (2017). A similar method was also used to correct the IP leakage for POLKA polarization data (Wiesemeyer et al., 2014). The method that is used in the NIKA2 pipeline was mainly developed during Aina Andrianasolo's Ph.D. (Andrianasolo, 2019), which employs the final maps in contrast of the Ritacco et al. (2017) method that worked on the Time Ordered Information (TOI) data. The observed Stokes parameters toward a real source can be expressed as :

$$\begin{aligned} \mathcal{I}_N &= \mathcal{B}_I * \mathcal{I}_N^R + \mathcal{N}_I \\ \mathcal{Q}_N &= \mathcal{B}_I * \mathcal{Q}_N^R + \mathcal{L}_N^{IQ} * \mathcal{I}_N^R + \mathcal{N}_Q \\ \mathcal{U}_N &= \mathcal{B}_I * \mathcal{U}_N^R + \mathcal{L}_N^{IU} * \mathcal{I}_N^R + \mathcal{N}_U \end{aligned} \tag{4.10}$$

In the above equation, $\mathcal{I}_N$, $\mathcal{Q}_N$ and $\mathcal{U}_N$ are the observed Stokes parameters, $\mathcal{B}_I$ is the main beam, $\mathcal{L}_N^{IQ}$ and $\mathcal{L}_N^{IU}$ are the IP leakage in Stokes Q and U, respectively. $\mathcal{N}_I$, $\mathcal{N}_Q$ and $\mathcal{N}_U$ represent noise terms. We define $Q_{real} = \mathcal{B}_I * \mathcal{Q}_N^R$ and $U_{real} = \mathcal{B}_I * \mathcal{U}_N^R$ as the real Stokes Q and U of the source, respectively. Equation 4.10 expresses the fact that the observed in Stokes Q and U parameters are the combination of the convolution of the real Stokes $\mathcal{I}_R^N$ of the source with the main beam $\mathcal{B}_I$ and the IP leakage $\mathcal{L}_N^{IQ}$ and $\mathcal{L}_N^{IU}$. We define $Q_{leak} = \mathcal{L}_N^{IQ} * \mathcal{I}_N^R$ and $U_{leak} = \mathcal{L}_N^{IU} * \mathcal{I}_N^R$ as the effective leakage affecting the observed Stokes Q and U maps, respectively. The leakage correction procedure when using a map of Uranus can be summarized in four steps as follows :

1. Finding a suitable map of Uranus taken at a similar focus and elevation as the observed data to give a reliable estimation of the leakage intensity and pattern. If no observation of Uranus has been made, the observer needs to find the Uranus observation taken another day but under similar conditions (Fz focus, elevation, FWHM ...). If no Uranus observation is available, an alternative method is to use the analytical model described in section 4.4.2. The (I, Q, U) maps of the selected scan of Uranus gives an estimation of $\mathcal{B}_I$, $\mathcal{L}_N^{IQ}$ and $\mathcal{L}_N^{IU}$ as:

$$\begin{pmatrix} I_{uranus} \\ \\ Q_{uranus} \\ \\ U_{uranus} \end{pmatrix} \propto \begin{pmatrix} \mathcal{B}_I \\ \\ \mathcal{L}_N^{IQ} \\ \\ \mathcal{L}_N^{IU} \end{pmatrix} \tag{4.11}$$

   This first step is important for the leakage correction due to the need to select appropriate Uranus maps which can be used to correct the scientific data.

2. Rotating the IP leakage from Nasmyth to RA-DEC coordinates. As the leakage maps on Uranus are reduced in Nasmyth coordinates, the second step consists of rotating the IP leakage from Nasmyth to RA-DEC coordinates. This rotation consists of two steps, (1); rotation of the (Q_{Uranus}, U_{Uranus}) images from the Nasmyth to RA-DEC reference frame (rotation by an angle $\eta - el$, where η is the parallactic angle and el is the elevation); (2) rotation of the Stokes parameters themselves by an angle ψ which is the combination of

elevation and parallactic angle. The rotation of the Stokes parameters can be described as :

$$\begin{pmatrix} Q \\ \\ U \end{pmatrix}_{RADEC} = \begin{pmatrix} \cos 2\psi & -\sin 2\psi \\ \\ \sin 2\psi & \cos 2\psi \end{pmatrix} \begin{pmatrix} Q_{Uranus} \\ \\ U_{Uranus} \end{pmatrix}_{Nasmyth} \tag{4.12}$$

Where $\psi(°) = \eta - el - 76.2° + 90°$, el is the elevation of the source, η is the parallactic angle and the term "$-76.2° + 90°$" was introduced to account for the offset coming from the M4 and M5 mirror designs.

3. Computing the leakage term in equation 4.10 is done in Fourier space. To get the effective leakage, we convolve the Stokes Q and U maps of Uranus by the Stokes I images of the source I$_N$ as follows :

$$\begin{aligned} \mathcal{L}_N^{IQ} * \mathcal{I}_N &= \mathcal{L}_N^{IQ} * (\mathcal{B}_I * \mathcal{I}_N^R) \\ &= \mathcal{B}_I * Q_{leak} \\ \mathcal{L}_N^{IU} * \mathcal{I}_N &= \mathcal{L}_N^{IU} * (\mathcal{B}_I * \mathcal{I}_N^R) \\ &= \mathcal{B}_I * U_{leak} \end{aligned} \tag{4.13}$$

The Q_{leak} and U_{leak} maps can then be obtained by simple deconvolution in Fourier space of equation 4.13. Thus, the final leakage maps are given by :

$$\begin{aligned} Q_{leak} &= FFT^{-1}\left[\frac{FFT(\mathcal{I}_N)}{FFT(\mathcal{B}_I)} \times FFT(\mathcal{L}_N^{IQ})\right] \\ U_{leak} &= FFT^{-1}\left[\frac{FFT(\mathcal{I}_N)}{FFT(\mathcal{B}_I)} \times FFT(\mathcal{L}_N^{IU})\right] \end{aligned} \tag{4.14}$$

Q_{leak} and U_{leak} are the IP leakage estimated from Uranus data which need to be subtracted from the data to give the "real" Q and U maps of the source.

4. Subtracting the leakage from the observed Stokes images. The intrinsic polarization $\mathcal{Q}_{Real}$ and $\mathcal{U}_{Real}$ of the source can be corrected for the IP leakage by subtracting the leakage terms Q_{leak} and U_{leak} from the observed maps. The final result can be expressed as :

$$\begin{aligned} Q_{Real} &= Q_N - Q_{leak} \\ U_{Real} &= U_N - U_{leak} \end{aligned} \tag{4.15}$$

This method was initially introduced in the NIKA2 pipeline by Andrianasolo (2019). To avoid any artifact when deconvolving maps, I adjusted the apodization parameters to only use the high signal-to-noise region to reduce the noise when dividing by the beam of the leakage. The rotation of the maps are done by rotation the map axes and then the Stokes Q and Stokes U as given by Eq. 4.12. The previous version of the pipeline did not take into account the offset introduced in the rotation angle ψ (-76.2°+90°). I corrected this offset introduced in the rotation angle from Nasmyth to RA-DEC coordinates in order to generate correct leakage maps in RA-DEC coordinates. Note that this method includes a deconvolution step of the leakage maps convolved with the observed I map (cf. Eq. 4.14).

4.4.2 IP correction using the analytical model

The analytical model of the leakage as described in section 4.3.8 provides an almost perfect representation of the observed leakage. The Stokes Q and U of the IP leakage can be obtained by equations 4.8 and 4.9, respectively. The observed Stokes are expressed in Eq. 4.10, where the $\mathcal{L}_N^{IQ} * \mathcal{I}_N^R$ and $\mathcal{L}_N^{IU} * \mathcal{I}_N^R$ are the observed leakage in Q and U, respectively. The IP correction using a leakage map as described in Section 4.4 involves a deconvolution to obtain the final IP leakage maps which makes this method a bit tricky. An alternative method to correct the data for the leakage is to use the analytical model of Sect. 4.3.8. Assuming the I-beam is approximately Gaussian. For

Uranus, the observed leakage following the model given by Eq. 4.8 and Eq. 4.9 can be expressed as:

$$\begin{aligned}
Q_l \equiv \mathcal{L}_N^{IQ} = a_q.\mathcal{B}_I * \mathcal{B}_{IG} &+ cq_x \frac{\partial \mathcal{B}_{IG}}{\partial x} * \mathcal{B}_I + cq_y \frac{\partial B_{IG}}{\partial y} * \mathcal{B}_I + cq_{xx} \frac{\partial^2 \mathcal{B}_{IG}}{\partial x^2} * \mathcal{B}_I + cq_{xy} \frac{\partial^2 \mathcal{B}_{IG}}{\partial x \partial y} * \mathcal{B}_I + cq_{yy} \frac{\partial^2 \mathcal{B}_{IG}}{\partial y^2} * \mathcal{B}_I \\
&+ cq_{xxx} \frac{\partial^3 \mathcal{B}_{IG}}{\partial x^3} * \mathcal{B}_I + cq_{yyy} \frac{\partial^3 \mathcal{B}_{IG}}{\partial y^3} * \mathcal{B}_I + cq_{xxy} \frac{\partial^3 \mathcal{B}_{IG}}{\partial x^2 \partial y} * \mathcal{B}_I + cq_{xyy} \frac{\partial^3 \mathcal{B}_{IG}}{\partial x \partial y^2} * \mathcal{B}_I \\
&+ cq_{xxxx} \frac{\partial^4 \mathcal{B}_{IG}}{\partial x^4} * \mathcal{B}_I + cq_{yyyy} \frac{\partial^4 \mathcal{B}_{IG}}{\partial y^4} * \mathcal{B}_I + cq_{xxxy} \frac{\partial^4 \mathcal{B}_{IG}}{\partial x^3 \partial y} * \mathcal{B}_I + cq_{xyyy} \frac{\partial^4 \mathcal{B}_{IG}}{\partial x \partial y^3} * \mathcal{B}_I \\
&+ cq_{xxyy} \frac{\partial^4 \mathcal{B}_{IG}}{\partial x^2 \partial y^2} * \mathcal{B}_I
\end{aligned} \tag{4.16}$$

A similar expression holds for the leakage in Stokes U, $U_l \equiv \mathcal{L}_N^{IU}$.
Convolving Eq. 4.16 with the real Stokes $\mathcal{I}_N^R$ of the source, one may obtain the effective leakage affecting the source images as follows :

$$\begin{aligned}
Q_{leak} \equiv \mathcal{L}_N^{IQ} * \mathcal{I}_N^R = a_q.\mathcal{I}_N * \mathcal{B}_{IG} + cq_x \frac{\partial \mathcal{B}_{IG}}{\partial x} * \mathcal{I}_N + cq_y \frac{\partial B_{IG}}{\partial y} * \mathcal{I}_N + cq_{xx} \frac{\partial^2 \mathcal{B}_{IG}}{\partial x^2} * \mathcal{I}_N + cq_{xy} \frac{\partial^2 \mathcal{B}_{IG}}{\partial x \partial y} * \mathcal{I}_N& \\
+ cq_{yy} \frac{\partial^2 \mathcal{B}_{IG}}{\partial y^2} * \mathcal{I}_N + cq_{xxx} \frac{\partial^3 \mathcal{B}_{IG}}{\partial x^3} * \mathcal{I}_N + cq_{yyy} \frac{\partial^3 \mathcal{B}_{IG}}{\partial y^3} * \mathcal{I}_N + cq_{xxy} \frac{\partial^3 \mathcal{B}_{IG}}{\partial x^2 \partial y} * \mathcal{I}_N& \\
+ cq_{xyy} \frac{\partial^3 \mathcal{B}_{IG}}{\partial x \partial y^2} * \mathcal{I}_N + cq_{xxxx} \frac{\partial^4 \mathcal{B}_{IG}}{\partial x^4} * \mathcal{I}_N + cq_{yyyy} \frac{\partial^4 \mathcal{B}_{IG}}{\partial y^4} * \mathcal{I}_N + cq_{xxxy} \frac{\partial^4 \mathcal{B}_{IG}}{\partial x^3 \partial y} * \mathcal{I}_N& \\
+ cq_{xyyy} \frac{\partial^4 \mathcal{B}_{IG}}{\partial x \partial y^3} * \mathcal{I}_N + cq_{xxyy} \frac{\partial^4 \mathcal{B}_{IG}}{\partial x^2 \partial y^2} * \mathcal{I}_N + noise&
\end{aligned} \tag{4.17}$$

where cq_i are model coefficients of the leakage model. These coefficients can be derived by fitting the model to series of Uranus maps (see section 4.4.5 below). The real Stokes Q and U maps of the source can then be expressed as :

$$\begin{aligned}
Q_{Real} &= Q_N - \mathcal{L}_N^{IQ} * \mathcal{I}_N^R \\
U_{Real} &= U_N - \mathcal{L}_N^{IU} * \mathcal{I}_N^R
\end{aligned} \tag{4.18}$$

Not that this correction using the analytical model does not involve any deconvolution, therefore avoiding any artifact associated with map deconvolution.

4.4.3 Tests of the IP correction method on Uranus maps

Employing our current method of IP correction using Uranus leakage maps, we performed a series of tests on Uranus data. The main goal of these tests is to quantify the limitations of this method (Ajeddig et al., 2020). We used the best Stokes Q, U maps of Uranus taken during the Dec. 2018 commissioning week to verify that a leakage correction procedure similar to that derived by Ritacco et al. (2017) for NIKA1 and improved during Aina Andrianasolo's PhD and with our implementation, was properly implemented in the NIKA2 IDL pipeline. First, we applied the leakage correction directly to the Uranus map used to estimate the leakage pattern (i.e., observed at 52° elevation). The residual Stokes $\mathrm{Q/I_{peak}}$ and $\mathrm{U/I_{peak}}$ maps obtained after correcting the data for the leakage pattern are displayed in Fig. 4.17f and Fig. 4.17l, respectively. These residual $|Q/I_{\mathrm{peak}}|$ and $|U/I_{\mathrm{peak}}|$ maps are less than 0.1% in amplitude, suggesting that the leakage-correction procedure has been properly implemented in the NIKA2 pipeline. Figure 4.17 also shows the residual Stokes $\mathrm{Q/I_{peak}}$, $\mathrm{U/I_{peak}}$ maps obtained when applying the leakage-correction procedure to Uranus maps taken at other elevations than the map used to estimate the leakage pattern. We found that for maps taken at elevations $> 45°$, the magnitude of the residuals is lower than $\sim 0.3\%$ (in $|\mathrm{Q/I_{peak}}|$) and 0.5% (in $|\mathrm{U/I_{peak}}|$) after leakage correction, but for maps at low elevations (∼20°–30°) the residuals become significantly higher, up to 0.8% in $|\mathrm{Q/I_{peak}}|$ and 2% in $|\mathrm{U/I_{peak}}|$ (Fig. 3) (Ajeddig et al., 2020).

The procedure of the IP correction was tested for Feb. 2020 and Nov. 2020 data on Uranus maps taken at the best focus position to establish its limitation. **Under stable conditions (mainly focus and FWHM)**

the leakage is unchanged and the NIKA2-Pol pipeline can correct the IP to less than 1%, e.g, the leakage estimated from Uranus map at 30° elevation can correct a scan taken at 50° of elevation to less than 1% of the residual polarization. This analysis also shows that the IP correction can be performed to less than 0.3 % when a leakage map is taken at similar elevation within 10° as the target. However, for instance, using a leakage map at elevation 50° cannot correct data taken at low elevation (30° in this case, see panel (g) and (a)). An additional difficulty at low elevation arises from the astigmatism of the telescope which is more pronounced at low elevation (see Sect. 4.3.9.1). In case of unstable conditions, observers need to perform the Uranus observations before going to their source and perform series of focus and focused Uranus maps to make sure that the data can be corrected for the IP leakage. This method is based on the availability of Uranus in the sky at a focus and elevation similar to the target, which makes it quite limited. The alternative method to correct the data for IP is to use the model as described in section 4.4.2.

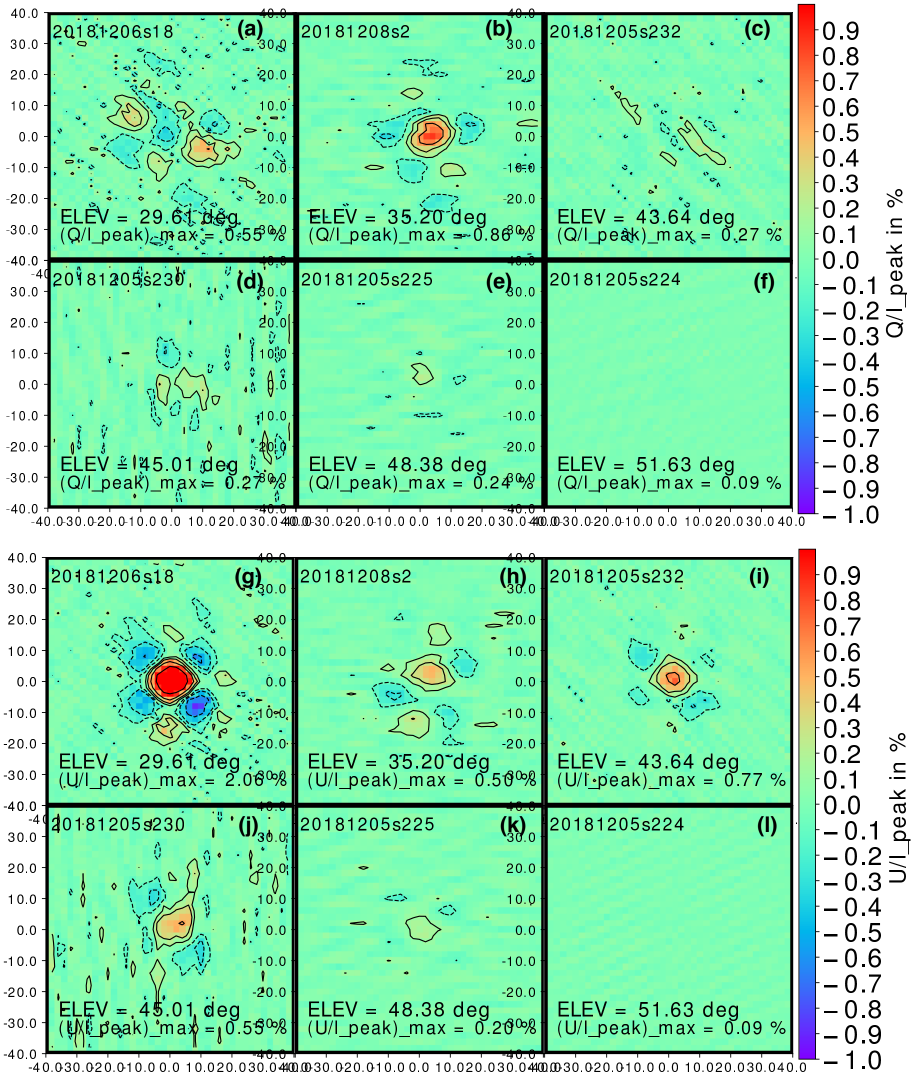

Figure 4.17: Residual Stokes Q/I$_{peak}$ and U/I$_{peak}$ maps (expressed in %) obtained after correcting each of the individual Uranus maps, taken at different elevations, by a single leakage pattern (from Uranus map taken at 52 deg elevation, (f) and (l) panels). The contours show levels of −2%, −1%, −0.5%, −0.2%, +0.2%, +0.5%, +1.0%, +2.0%. Note how the maps taken at elevations different from the one used to correct for the leakage show non-negligible residuals (up to ∼ 2%) (Ajeddig et al., 2020).

4.4.4 Test of IP corrections in arrays A1 and A3

In Section 4.3.6 above, we showed how the leakage pattern/intensity differs slightly in arrays A1 and A3. To improve the leakage correction strategy for NIKA2-Pol data, we tested correcting Uranus maps in A1 and A3 separately by a combined map at 1.15 mm. We used the same leakage correction procedure as described above. Figure 4.18 shows the leakage map used in this test (in left) and the residual Stokes Q and U maps at 1.15 mm, A1, and A3 after leakage correction. In this case, the leakage correction applied to the combined 1.15 mm map is better than correcting A1 and A3 individually. The residuals in Stokes Q/I$_{peak}$ for A1 and A3 are 0.41 % and 0.30 % and in Stokes U/I$_{peak}$ are 0.41% and 0.33 %, respectively. Thus the leakage correction in A3 is better than in A1 when using the combined 1.15 mm map as the estimated leakage map from Uranus.

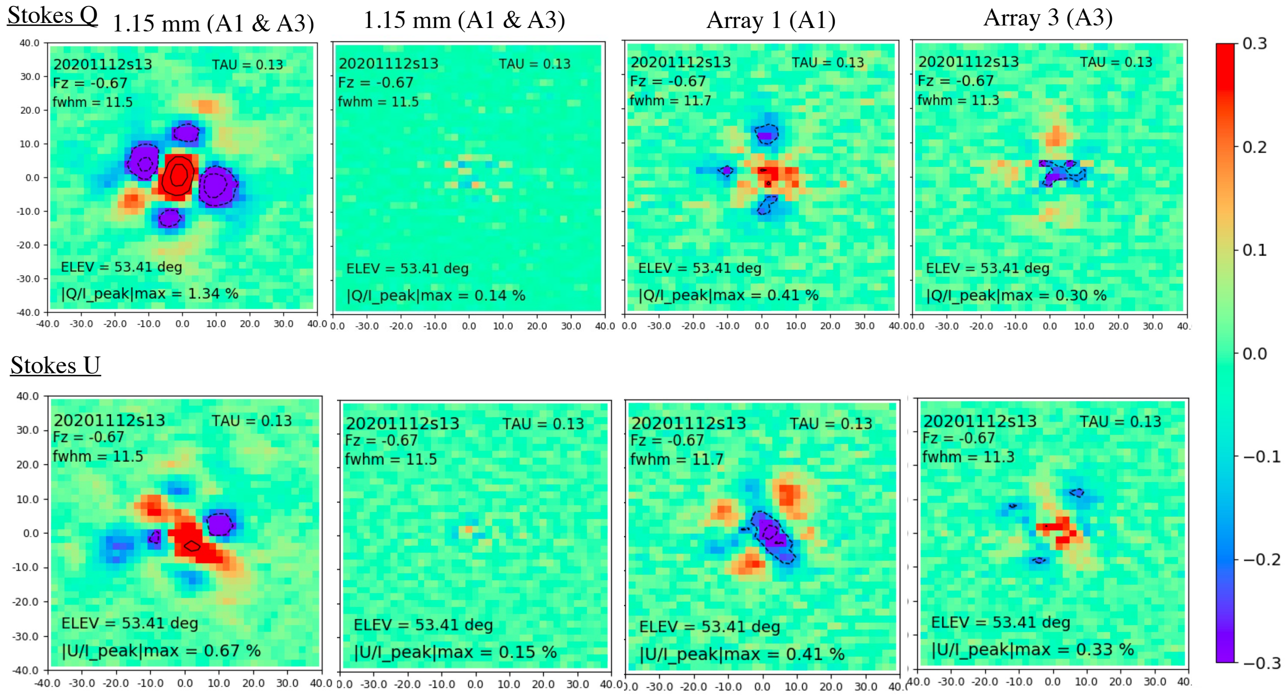

Figure 4.18: The IP correction of arrays A1 and A3 using combined 1.15 mm Uranus map. *Left* : Stokes Q and U maps were obtained at 1.15 mm by combining A1 and A3. From the second panel on left, residual Stokes Q/I$_{peak}$ and U/I$_{peak}$ maps (expressed in %) obtained after IP correction using the combined map at 1.15 mm applied to itself, and separately to A1 and to A3. The leakage correction by correcting each of the arrays A1 and A3 by the combined maps does not improve the IP correction, this test suggests that correcting the data of each array by its corresponding leakage would improve the overall correction slightly.

4.4.5 Test of the IP correction using the analytical model

The alternative method of the IP leakage correction is to use the analytical model given by equations 4.8 and 4.9 which depends on 15 parameters in Stokes Q and 15 parameters in Stokes U. In section 4.3.8, we showed that these parameters vary as a function of elevation (see Fig. 4.12 and Fig. 4.13). The Stokes I images in Figs. 4.2 and 4.4 show side lobes in the beam pattern which change as a function of observing conditions. The beam size (FWHM) may influence the leakage pattern. Thus fitting the model coefficients we need to consider the variation of the beam size when fitting the model coefficients. Figure 4.20 and 4.21 show the variation of one of the third and fourth derivative coefficients (c_{xyy} and c_{xxyy}) as a function of the focus position of the telescope, elevation, and size of the beam (FWHM). Using hundreds of Uranus scans taken at different elevations, focus and weather conditions, each coefficient can be written as a function of these three parameters as follow :

$$C_i^k = A_i^k * ELEV + B_i^k * FZ + D_i^k * FWHM + E_i^k \tag{4.19}$$

where C_i^k represents the various coefficients for each of the Stokes parameters, indexed by k → (Q or U), and i (i=1 to 15) is the coefficient index (15 coefficients for Q and 15 for U), while A_i^k, B_i^k, D_i^k, and E_i^k are the regression parameters obtained by fitting each coefficient with its variation as a function of elevation (ELEV), focus position (FZ) and FWHM. I used Uranus data taken in all campaigns to derive a reliable regression for the various coefficients in equation 4.19. Only Uranus observations taken at a good focus position and under stable weather conditions were used in this analysis. 122 Uranus scans were used with an elevation varying between 20° and 65°. Due to the complexity of the leakage and the variation of its pattern/intensity, we used all coefficients to fit even small deformations of the leakage pattern. While using 15 parameters in each of Stokes Q and U, only a few of them are dominant (see table 4.1). The dominated coefficients in both Stokes Q and Stokes U are highlighted in red color in Table 4.1.

Figure 4.19 gives an example of using the analytical model to correct Uranus maps at 1.15 mm. Each row corresponds to a Uranus map before and after leakage correction for each of the campaigns. The observed leakage in these examples can be perfectly reconstructed using our model, leading to very satisfactory results. For example, when applying the IP correction to the Uranus observation taken in Dec. 2018, the observed polarized intensity is 1.9 % before IP correction, and is reduced to 0.3 % after leakage correction. The model coefficients as described in equations 4.8 and 4.9 were determined using equation 4.19. Note that the fitted parameters do not allow us to correct all data. We lack more Uranus data for a proper fitting of these coefficients, which would lead to perfectly corrected data in all cases.

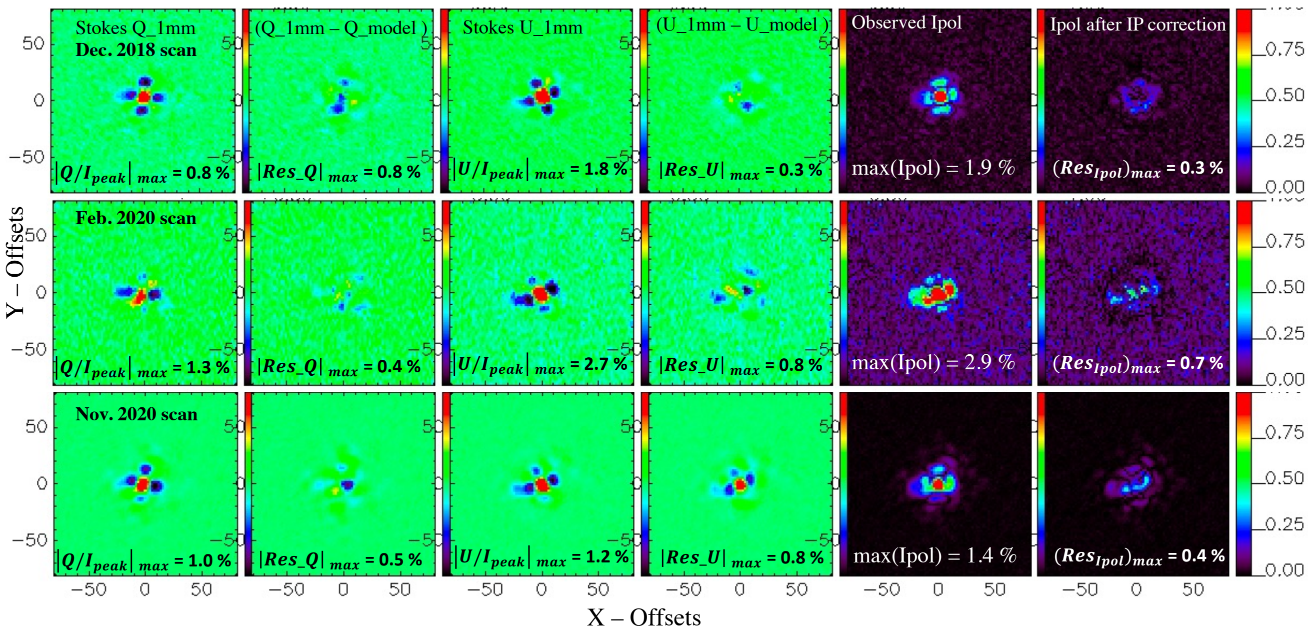

Figure 4.19: Leakage correction results using the analytical model as described in equations 4.8 and 4.9. Each row gives an example of a Uranus observation taken in a given campaign. The three leakage patterns shown here are similar in both Stokes Q and U. The residuals of the leakage in Stokes Q and U are given in columns 2 and 4, respectively. The observed polarized intensity is shown in column 5 and the same after leakage correction in column 6.

Leakage correction using the analytical model is a powerful alternative method to correct for the IP. **The analytical model shows that NIKA2-Pol data can be corrected for the IP leakage without observing Uranus, which can save a significant amount of observing time.** The model is under development and needs more statistics and tests on both quasars and extended sources to prove its robustness.

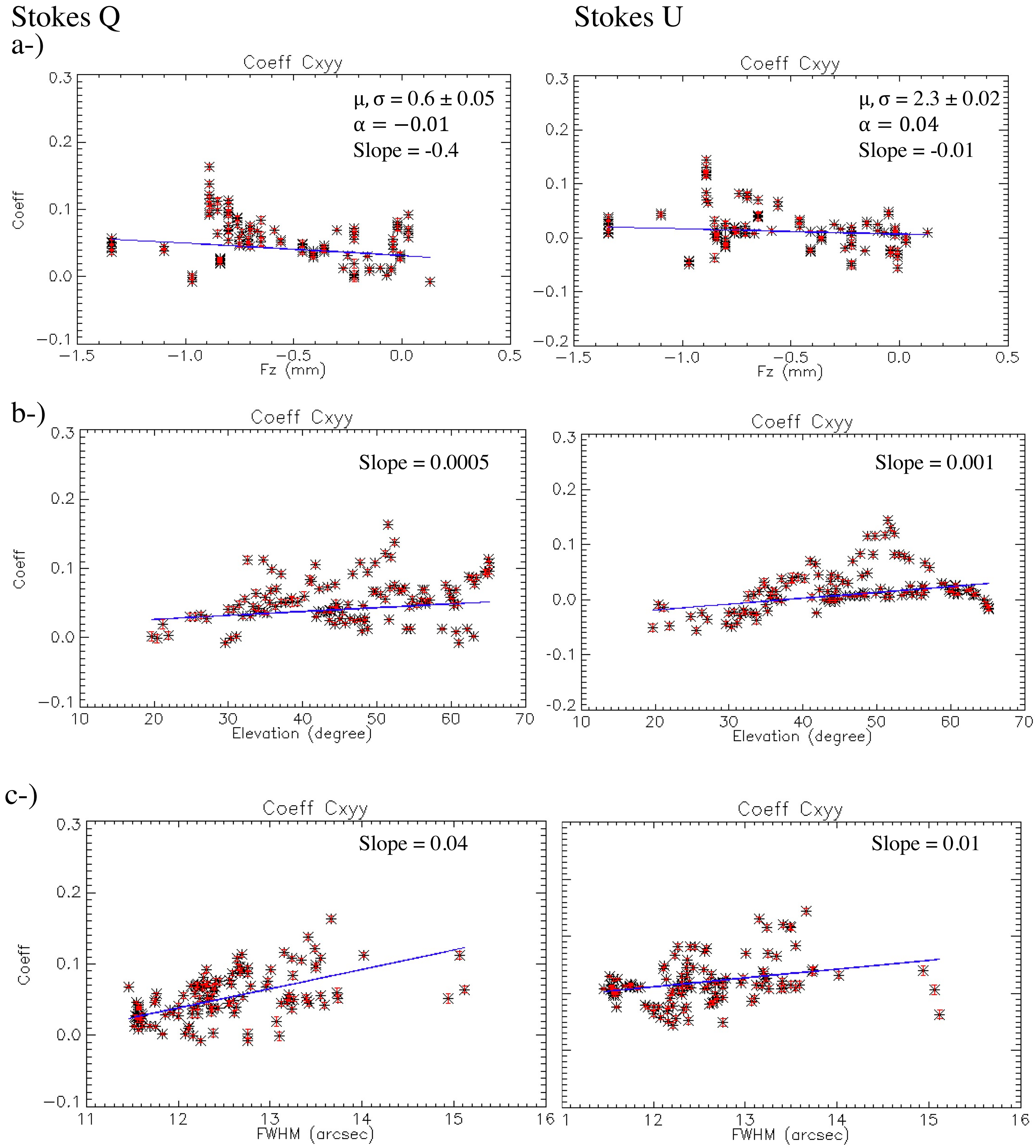

Figure 4.20: Variation of the coefficient c_{xyy} involving the third-order derivatives of the I-beam. *a)* : Variation of c_{xyy} as a function of focus position Fz (mm) in Stokes Q and U on the left and right, respectively. *b)* and *c)* Same plot but as a function of elevation and I-beam FWHM.

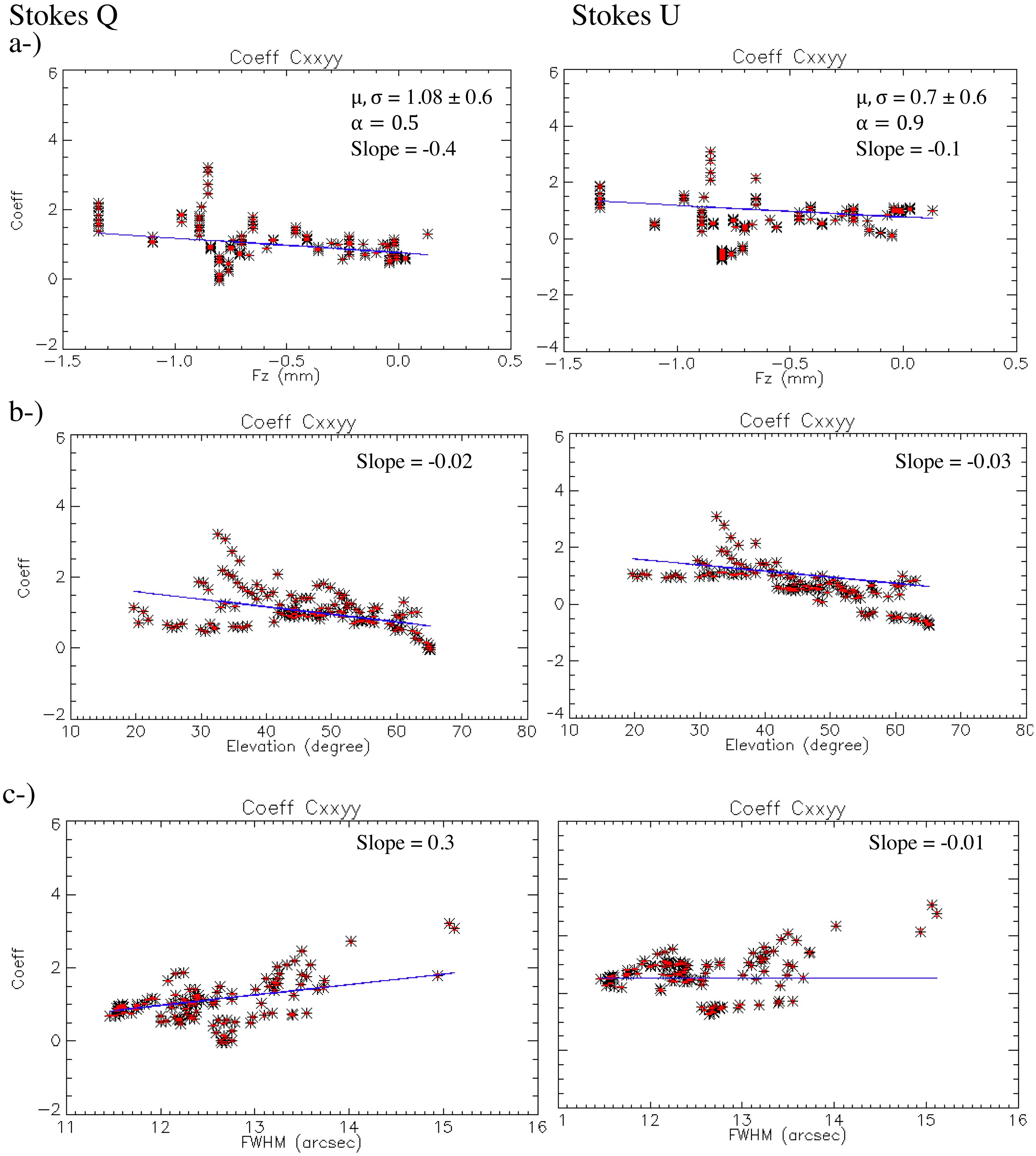

Figure 4.21: Variation of the coefficient c_{xxyy} involving the fourth-order derivatives of the I-beam. *a* : Variation of c_{xxyy} as a function of focus position Fz (mm) in Stokes Q and U on the left and right, respectively. *b)* and *c)* Same plot but as a function of elevation and I-beam FWHM.

Table 4.1 shows the results obtained from fitting 122 scans of Uranus with the analytical model of 4.3.8 as a function of elevation, focus, and FWHM according to Eq. 4.19. The fit parameters for the fourth and third derivatives in the analytical model have higher values than the other parameters as can been seen in the table. To examine quality of the fit, I evaluated both the reduced chi-square and F-test statistic. The reduced χ^2 values are significantly larger than one suggesting than another parameter besides El, Fz, FWHM is needed to account for the observed variations of the leakage.

Regression parameters						
Model coefficient	A_k^i	B_k^i	D_k^i	E_k^i	Reduced χ^2	F-test
Stokes Q coefficients of the model						
A_q	-2.21e-06	3.40e-05	1.92e-05	-1.48e-04	1.43e+01	8.76e+01
cq_x	6.61e-06	-1.16e-04	7.18e-05	-8.99e-04	1.83e+01	6.45e+00
cq_y	-4.49e-06	-1.65e-04	-5.10e-05	1.07e-04	1.19e+01	6.42e+00
cq_{xx}	2.01e-04	5.70e-04	-6.21e-04	-9.22e-03	5.95e+01	1.30e+01
cq_{yy}	5.68e-05	-2.61e-03	5.12e-03	-6.76e-02	9.53e+01	2.66e+01
cq_{xy}	3.48e-04	-1.61e-03	1.90e-03	-3.09e-02	7.29e+01	1.44e+01
cq_{xxx}	1.32e-03	-1.68e-02	2.38e-02	-3.38e-01	1.82e+02	4.71e+01
cq_{yyy}	-3.21e-04	-9.85e-03	5.10e-03	-5.33e-02	3.69e+01	2.84e+01
cq_{xxy}	3.14e-04	-5.49e-03	3.08e-02	-3.76e-01	1.31e+02	1.72e+01
cq_{xyy}	8.15e-04	-2.53e-03	2.82e-02	-3.40e-01	7.08e+01	2.85e+01
cq_{xxxx}	-5.55e-03	1.65e-01	-6.31e-02	1.10e+00	4.39e+02	1.53e+01
cq_{yyyy}	-9.50e-03	2.51e-01	-1.09e-01	1.85e+00	5.72e+02	3.11e+01
cq_{xxxy}	-1.11e-02	4.54e-01	-2.52e-01	3.93e+00	3.75e+02	3.28e+01
cq_{xyyy}	1.85e-02	-2.36e-01	1.22e-01	-2.70e+00	3.40e+02	2.26e+01
cq_{xxyy}	-1.90e-02	-2.26e-01	2.01e-01	-6.41e-01	2.71e+02	2.97e+01
Stokes U coefficients of the model						
A_u	-1.21e-06	-4.51e-05	1.16e-05	-8.07e-05	1.23e+01	6.78e+01
cu_x	-8.60e-07	1.55e-04	1.21e-04	-1.23e-03	1.08e+01	7.45e+00
cu_y	1.28e-05	-2.65e-04	1.16e-04	-1.94e-03	2.77e+01	1.35e+01
cu_{xx}	8.80e-05	5.19e-03	7.43e-04	-1.67e-02	7.58e+01	7.42e+00
cu_{yy}	-1.39e-04	-2.32e-03	4.73e-03	-5.35e-02	5.98e+01	3.11e+01
cu_{xy}	-3.22e-04	6.63e-03	-3.24e-03	5.34e-02	1.49e+02	9.97e+00
cu_{xxx}	7.35e-04	1.98e-03	-9.55e-03	6.75e-02	5.98e+01	2.61e+01
cu_{yyy}	1.20e-03	-1.03e-02	2.23e-02	-3.17e-01	2.42e+02	2.31e+01
cu_{xxy}	4.23e-04	-1.38e-02	-1.70e-03	-9.20e-03	3.87e+01	4.89e+00
cu_{xyy}	1.10e-03	-4.55e-03	1.55e-02	-2.31e-01	7.24e+01	1.34e+01
cu_{xxxx}	4.63e-03	-3.14e-01	2.25e-01	-2.93e+00	5.98e+02	4.21e+01
cu_{yyyy}	1.54e-03	-3.08e-01	1.98e-01	-2.49e+00	7.24e+02	3.07e+01
cu_{xxxy}	9.37e-03	3.15e-01	-1.01e-01	4.46e-01	2.89e+02	1.47e+01
cu_{xyyy}	-1.52e-02	-3.65e-01	2.90e-01	-2.31e+00	2.61e+02	4.59e+01
cu_{xxyy}	-3.28e-02	1.52e-01	6.33e-03	2.16e+00	3.11e+02	3.28e+01

Table 4.1: Table of fitted parameters according to Eq. 4.19 that allows to estimate all of the model coefficients used in Eq. 4.8 and Eq. 4.9. The coefficients were determined for Stokes Q and U using the 122 scans of Uranus and fitted with their elevation, focus position and beam size (FWHM). Highlighted values shown in red are the most significant parameters of the analytical representation of the leakage. The chi-square used in this analysis is the reduced chi-square and the F-test is the Fisher-test applied to all the presented parameters A_k^i, B_k^i, D_k^i and E_k^i.

Moreover, the Fisher F-tests, I performed (with F-test statistic $\gtrsim$7 in all cases) confirm that the three parameters already identified (El, Fz, FWHM) play a statistically significant role in the variation of the leakage (e.g, in case of defocused maps, low elevations, and large FWHMs). In table 4.1, I only showed results of a global Fisher test including all three four parameters. I also performed the same analysis on a parameter by parameter basis for elevation, focus, and FWHM, and the results show a significant dependence of the model on all three parameters.

4.4.6 Smoothing effect on the leakage pattern

The leakage seen with NIKA2-Pol as described above has a cloverleaf pattern with positive and negative lobes. Thus, when smoothing the leakage map with a kernel of size comparable to the cloverleaf pattern, the combined negative and positive lobes tend to cancel out in the final map of the smoothed leakage. In our attempt to characterize the leakage effect on NIKA2-Pol, we smoothed the leakage map by a 2D Gaussian kernel. We aim in this test to check whether the leakage remains significant or not after degrading the resolution. We tried to smooth the data to different resolutions from 12″ to more than 17″ to investigate the variation of the leakage with different angular resolutions. Figure 4.22 shows our results obtained on Uranus maps before and after smoothing to 17″ resolution. The leakage intensity decreases significantly after smoothing to less than 1% polarization fraction in both Stokes Q and U.

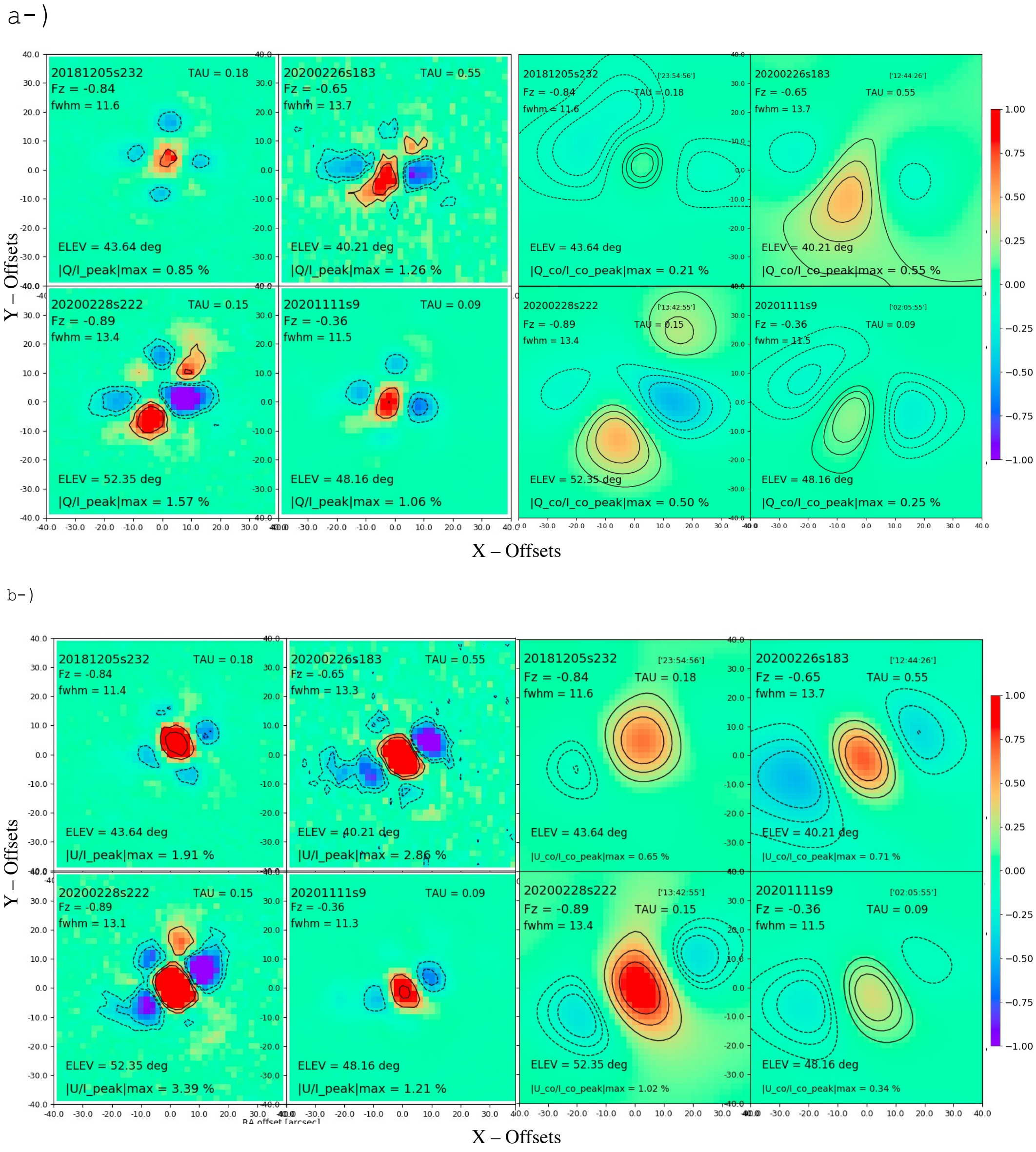

Figure 4.22: *a-)*: the Observed and smoothed Stokes Q/I$_{peak}$ maps in right and left (expressed in %) of Uranus obtained in different observing campaigns Dec. 2018, Feb. 2020, and Nov. 2020, respectively. Most of them have a cloverleaf pattern with positive and negative lobes. *b-)*: Similar to a-) but for the observed and smoothed Stokes U, respectively.

To quantify the effect of smoothing the leakage by a 2D Gaussian kernel, I smoothed the leakage observed on Uranus using a range of kernel FWHM sizes. Figure 4.23 shows two examples of the variation of the instrumental polarization fraction as a function of the size of the Gaussian smoothing kernel for two distinct maps of Uranus. The maximum instrumental polarization fraction was derived after smoothing all Stokes parameters (I, Q, U) depending on the kernel size. Under stable weather conditions (nighttime), small FWHM (11.5 arcsec) and well-focused Uranus maps, the instrumental polarization fraction drops to less than 0.3% when smoothing the data with a 15″ Gaussian kernel (left panel). The initial IP fraction, in this case, is small (1.4 %) and at an elevation of ∼50°. But, in the case of the Uranus map taken in daytime (afternoon), where FWHM is about 12.7 arcsec, the IP leakage fraction is strong (2.9%). Thus, smoothing can only bring down the IP leakage to less than 0.7% (right panel). Figure 4.23 allows us to assess the effect of the resolution on the IP leakage effect, and indicates that the performance of NIKA2-Pol is ultimately limited by the observing conditions.

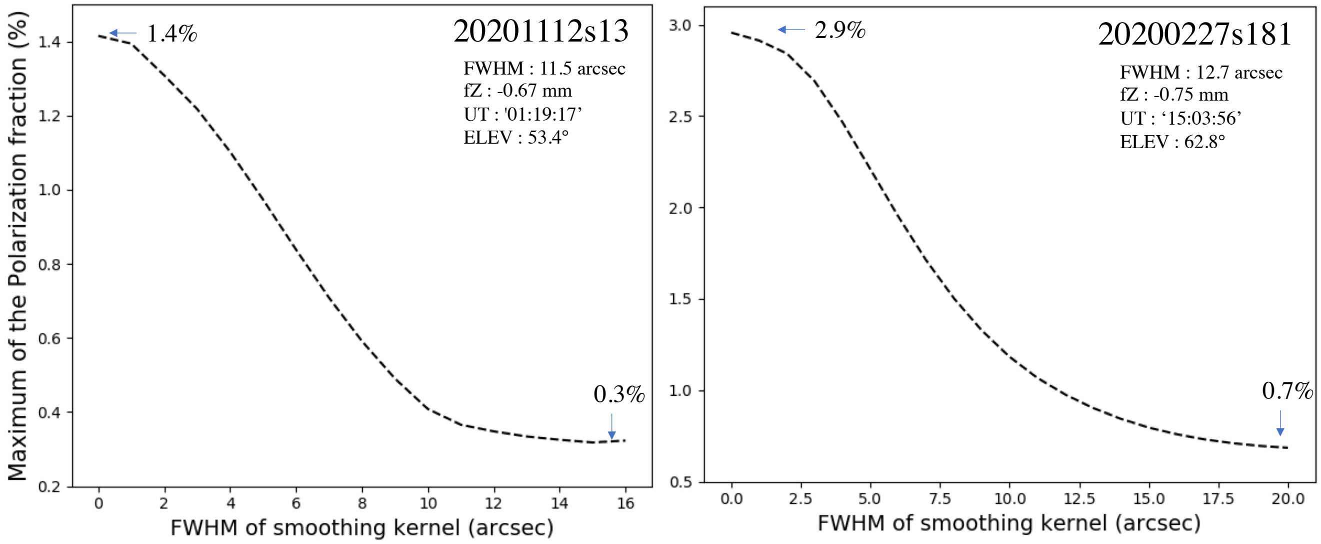

Figure 4.23: Maximum IP fraction as a function of the FWHM size of the smoothing kernel. Left: Test of the IP fraction as function of the FWHM kernel size for a Uranus scan taken under stable conditions during nighttime. Right: Similar to left plot but for a Uranus scan taken during daytime in the afternoon.

4.4.7 IP correction of quasars using Uranus maps

Our IP leakage analysis showed a marked dependence of the leakage on elevation. Thus to successfully correct data one needs to have leakage maps at different elevations. To test the leakage correction applied to quasars, I used two sources, 3C286 which is compact and highly polarized, and 0923+392 which is compact and weakly polarized. (Only Dec. 2018 data were used in this analysis).

Applying a“simple leakage correction” (using only one leakage map to correct all the data) to the maps of weakly polarized quasars allowed me to reduce the dispersion in polarization angles observed with time and elevation. For example the dispersion shrinks from ∼ 7.1° to ∼ 3.8° for 0923+392 (weakly polarized quasar with $p \sim 2.5\%$, see right panel of Fig. 4.24). The leakage correction does not improve the dispersion in polarization angles for maps of strongly polarized sources which are not significantly affected by instrumental polarization, such as 3C286 ($p \sim 12\%$ – see left panel of Fig. 4.24). A fairly large scatter in measured polarization angle as a function of elevation nevertheless remains after "simple leakage correction", presumably due to the dependence of the leakage pattern with elevation, identified earlier. As a first attempt at establishing an elevation-dependent leakage correction, we produced two independent leakage maps obtained at different elevations. We applied them to the quasars data in two bins of elevation (above and below 46°). The leakage correction efficiency decreases when using a scan at different elevations, confirming the significant dependence of the leakage pattern with elevation. This suggests that the NIKA2 intensity-to-polarization leakage can only be satisfactorily calibrated out by deconvolving the data from a leakage pattern obtained at an elevation close to that of the data to be corrected.

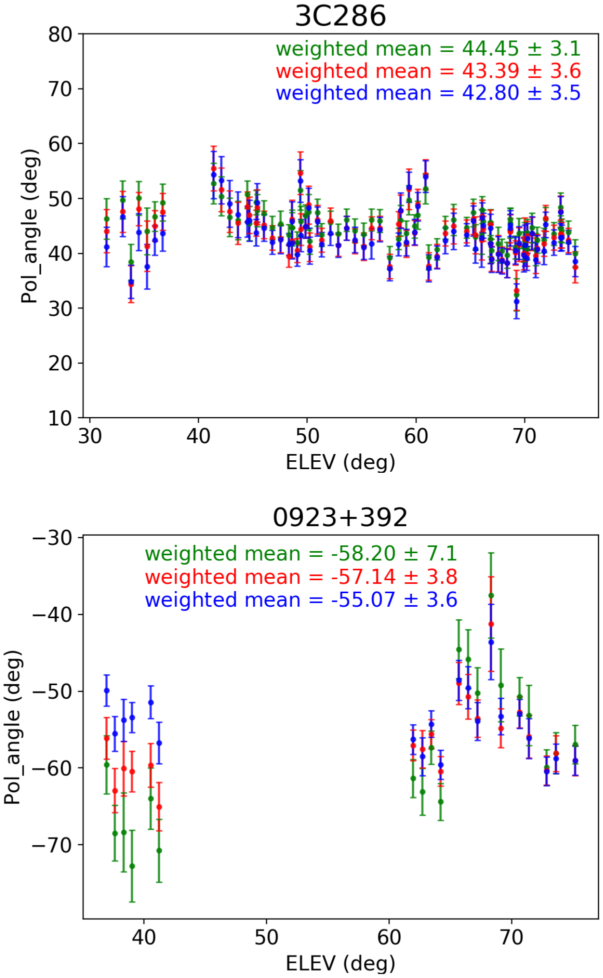

Figure 4.24: Polarization angles obtained for individual scans towards two quasars of our sample (left: 3C286 with $p \sim 12\%$ and right: 0923+392 with $p \sim 2.5\%$), as a function of elevation. The green points are the polarization angles (electric vector position angles, EVPAs) obtained without leakage correction, the red points the ones after a simple leakage correction and the blue points are the EVPAs obtained after applying the dual elevation-dependent leakage correction described in the text.

This method of using two different leakage patterns obtained at two different elevations again slightly reduces the dispersion of observed polarization angles with time and elevation for some quasars such as 0923+392 or 3C273 (see right panel of Fig. 4.24). The reduced dispersion in polarization angles obtained in some cases when a finer elevation-dependent leakage correction is applied (right panel of Fig. 4.24) suggests that **a better sampling of the leakage pattern as observed on an unpolarized source(s) at different elevations would allow us to successfully correct NIKA2-POL data of weakly polarized emission taken over a wide range of elevations.**

4.4.8 Smoothing effect on quasars

During the commissioning campaigns, we performed several observations of the quasars to test the polarization angle stability with the NIKA2-Pol instrument. As discussed in 4.4.7, weakly polarized quasars are more affected by the leakage. Thus the polarization angle variation is mainly affected by the IP leakage. The leakage smoothing expirement described in Sect. 4.4.6 shows that at low resolution (17 arcsec or less), the leakage is much less significant. In our attempt to correct for the leakage and to investigate the influence of the leakage on the polarisation angle stability, we smoothed the polarization data of 3C279, which is a weakly polarized quasar (3%). The joint NIKA2-Pol and XPOL observations in the same campaigns allowed us to characterize the polarization angle stability with NIKA2-Pol. Figure 4.25 shows a plot of the polarization angle as a function of the elevation of the telescope before and after smoothing the data. Each blue or orange point in the left panel is the obtained polarization angle in each scan before and after smoothing, respectively. The right panel is similar but for the polarization fraction variation as function of elevation. The polarization data of 3C279 were smoothed to 17 arcsec to reduce or even eliminate the leakage affecting the data of this quasar. At low elevation, the leakage intensity becomes strong, or likely due to the astigmatism of the telescope (see section 4.3.9.1). For example, in figure 4.25 all the points inside the ellipse (with an angle of about -75°) do not agree with the other data points of the polarization angle of 3C279. But, after smoothing, all these points jump to the same level as others, thus at this elevation, the polarization data are sensitive to the leakage. The polarization angle of 3C279 is stable on a daily basis and does not show a significant variation with elevation after smoothing.

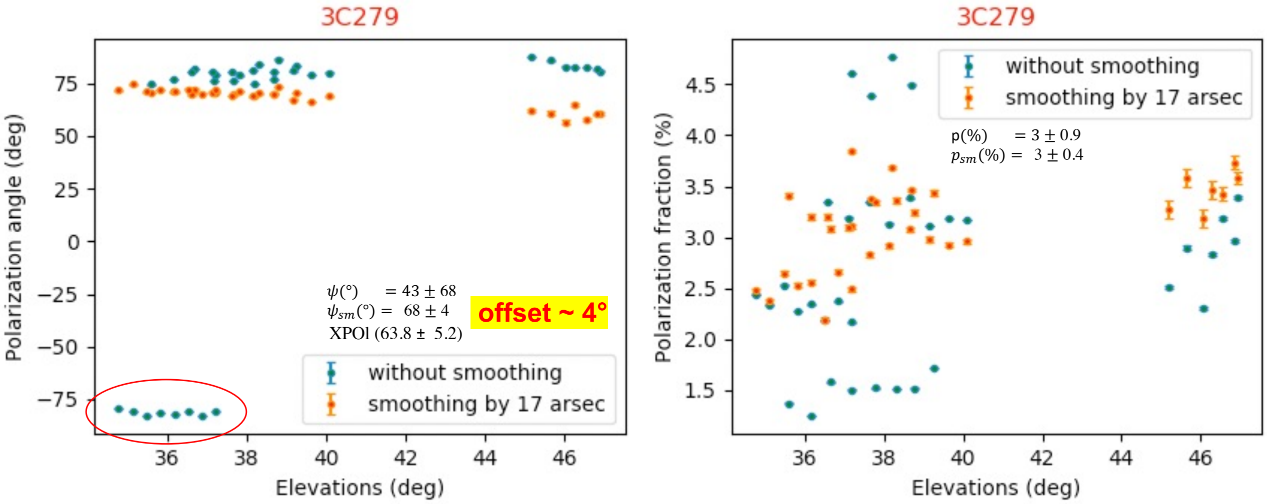

Figure 4.25: The effect smoothing the quasars data. *Left* : Polarization angle stability of 3C279 quasar as a function of elevation, where blue and orange are the polarization angle obtained in each scan before and after smoothing to 17 arcsec resolution by a 2D Gaussian kernel. The red ellipse shows the points affected significantly by the IP leakage. *Right*: Similar to the left panel but for the polarization fraction for 3C279 before and after smoothing.

Before smoothing the data, the difference in polarization angle between NIKA2-Pol and XPOL is quite large (about ∼25°), while after the smoothing, the difference decreases to ∼4°. Similar results were obtained for the polarization fraction stability. The smoothing (to 17 arcsec resolution) by a 2D kernel allows to significantly reduce the leakage affecting this quasar. **This analysis emphasizes that the polarization angles obtained on point-like sources with NIKA2-Pol are stable but need a proper leakage correction**. The smoothing method is another way to eliminate the leakage effect, but one loses the high angular resolution provided by NIKA2-Pol. A similar test has been performed for other quasars, such as 3C273 which is weakly polarized (with a polarization fraction ∼4%), and showed results similar to those presented in this section.

4.4.9 New method of IP correction: Correcting for the Leakage Using the Data (CLUD) and the analytical model

The IP correction described in Sect. 4.4.3 relies on the availability of Uranus in the sky just before and/or after the scientific observations. In Sect. 4.4.5, I described an alternative method using the IP leakage model which is also based on deriving the fit parameters of the model in Eq. 4.16 using Uranus data. Both methods need Uranus data, which makes them limited due to the unavailability of Uranus at all times close to the scientific target. In the present section, I introduce a new method for IP correction which is based on estimating the parameters of the analytical model using the data themselves instead of Uranus maps. In the following, I call this method

CLUD (for "Correction for the Leakage Using Data"). This CLUD method only assumes that the IP leakage is stable within groups of consecutive scans for which the difference in elevation is $|\Delta_{el}| <10°$ and the focus is stable $|\Delta_{fz}| <0.2$mm (where $|\Delta_{el}| = |el_N - el_0|$, $|\Delta_{fz}| = |fz_N - fz_0|$ and N,0 indicate the last and first scans in a given group, respectively). CLUD method uses the IP leakage model introduced in Eq. 4.8 in which the IP leakage in both Stokes Q and Stokes U can be represented by the convolution of 2D Gaussian beam with its derivatives up to the fourth order. The aim of this method is to determine the 30 coefficients of the IP leakage model in each group of scans providing a good estimate of the leakage. Thus, the leakage correction using the CLUD method is done group by group.
The IP leakage correction steps using CLUD can be summarized as follows :

1. We divide observations of a given source in groups of consecutive scans which were observed during the same run and satisfying the conditions of $|\Delta_{el}| <10°$ and $|\Delta_{fz}| <0.2$mm.

2. We build the IP leakage in Nasmyth coordinates using a 2D kernel Gaussian as expressed in Eq. 4.9. We associate each scan with a leakage map in RA-DEC coordinates by rotating the leakage model from Nasmyth to RA-DEC coordinates. This rotation depends on the elevation and parallactic angle of the source in a given scan (this rotation is described in Sect. 4.4.1).

3. We find all pairs within a group of consecutive scans for a given source.

4. We compute for each pair in the group the differences between the observed Stokes Q and Stokes U maps and the associated leakage maps in RA-DEC coordinates as follows :

$$\begin{bmatrix} Q_{o,i}^{radec} - Q_{o,j}^{radec} \\ U_{o,i}^{radec} - U_{o,j}^{radec} \end{bmatrix} = \begin{bmatrix} \sum_{l=0}^{l=14} C_{q,l}(Q_{leak,i}^{radec} - Q_{leak,j}^{radec}) \\ \sum_{l=0}^{l=14} C_{u,l}(U_{leak,i}^{radec} - U_{leak,j}^{radec}) \end{bmatrix} \tag{4.20}$$

   where $Q_{o,i}$ and $U_{o,i}$ are the observed Stokes Q and Stokes U for a given scan in the group (indicated by the i index), respectively. The terms $Q_{leak,i}^{radec}$ and $U_{leak,i}^{radec}$ represent the IP leakage obtained with the model in RA-DEC coordinates, respectively. $C_{q,l}$ and $C_{u,l}$ for $l = 0$ to $l = N$ are the coefficients of the analytical model in Stokes Q and Stokes U, respectively.

5. We assume that the 30 coefficients of the IP model are stable from one scan to another within each group, and we perform a multi-dimensional regression fit to obtain the 30 coefficients of the model for each group.

6. We use the coefficients obtained in this way to estimate the IP leakage in each group and apply the leakage correction for each scan of that group.

I applied the CLUD method to a few quasars to check its ability to correct the NIKA2-Pol data observed on point sources for IP. The intrinsic polarization angle of the observed quasars is assumed to be stable during the same run. These quasars were observed by both NIKA2-Pol and XPOL instruments during the same run. I then compared the polarization angles obtained 1) without any IP correction, 2) with smoothing the data, and 3) by applying the CLUD method.

Figure 4.26 shows the results of this analysis and demonstrate the possibility to correct the data for IP without the need to observe Uranus. For a weakly polarized quasar 3C279 (4%), this method allowed me to decrease the drastic variation of polarization angles from one scan to another (see panel a Fig. 4.26). Two different groups of consecutive scans were used in the case of 3C279 as indicated by the dashed-line in Fig. 4.26 and correspond to two different days. I showed the polarization angle result obtained by XPOL at 1.3mm during the same run in cyan bar of each case of quasars. For 3C273 (6% of polarization fraction), I used two different groups of data taken in 25 Feb. 2020 and 27 Feb. 2020. In the case of this quasar, the CLUD method seems to work and allowed me to obtain a good agreement in the measured polarization angles in different days (seen panel b-) in F. 4.26). I also used the quasar OJ287 for which the polarization fraction is about ∼3%, and applied the CLUD method to three groups of scans (taken on three different days). The IP correction of OJ287 data using CLUD reduced the dispersion of polarization angles in the OJ287 data from 5° to 2° and allowed me to have a good agreement with the XPOL polarization measurements of this quasar.

The CLUD method is thus very promissing and will help to save a significant amount of observing time. The goal of this analysis was to test and validate this method on weakly polarized point sources. This work is still under development, and the application of the CLUD method to extended sources such as OMC-1 will further quantify the ability of this method to correct scientific data for IP.

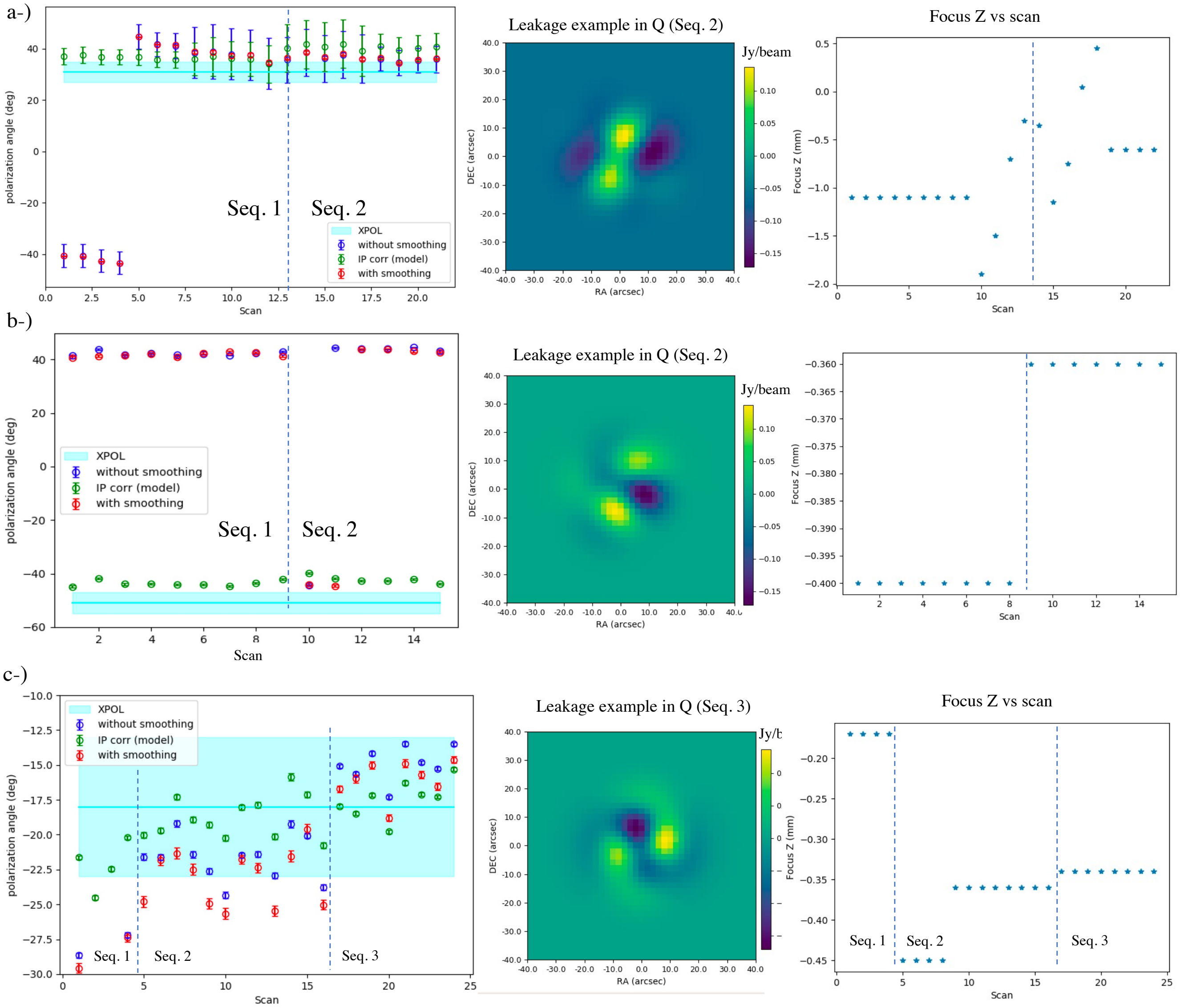

Figure 4.26: IP leakage correction using the CLUD method applied to weakly polarized quasars observed during parallel NIKA2-Pol and XPOL observations. *a-)*: Example of applying the CLUD method to data taken on the quasar 3C279. Left : Variation of the measured polarization angle as a function of scan for two different groups of scans (Seq. 1 and Seq. 2) observed on different days. The blue symbols are the observed polarization angles, while the red and green symbols are polarization angles obtained after smoothing and applying the CLUD method, respectively. The polarization angle measured by XPOL is shown by the cyan bar. The dashed line separates the two groups used in this analysis. (Middle) Estimated leakage map for the second group using the CLUD method. Right : Variation of the focus Fz value as a function of scan. *b-)* and *c-)* are similar to *a-)* but for quasars 3C273, 0J287, respectively.

4.4.10 Correcting OMC-1 data for IP leakage using Uranus maps

One commonly used calibrator for polarization observations is the OMC-1 region located in the Orion A giant molecular cloud (see Chap. 5). This section shows how the leakage correction improves the consistency between independent data sets, especially toward the strong, weakly polarized point source Orion-KL.

I only used only the commissioning data from Nov. 2020 data because of their excellent quality/calibration and I only considered significantly polarized data (with signal-to-noise SNR >3 in polarized intensity). Figure 4.27 presents the Stokes Q and U maps obtained at high angular resolution ($11.7''$) with NIKA2-Pol toward OMC-1.

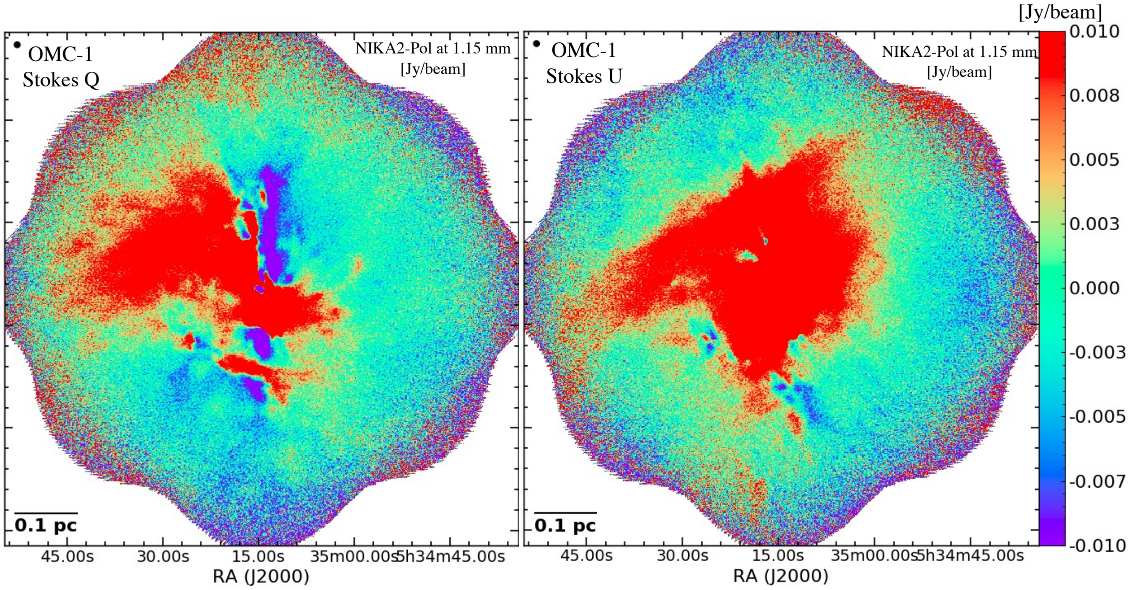

Figure 4.27: Stokes Q and U maps of OMC-1 with NIKA2-Pol at 1.15mm wavelength. *Left*: Stokes Q map of OMC-1 in Jy/beam. *Right*: Stokes U obtained with NIKA2-Pol toward OMC-1. Both Stokes Q and U maps have a positive and negative polarization emission (as seen by other polarimetric instruments, e.g., Pattle et al., 2017a).

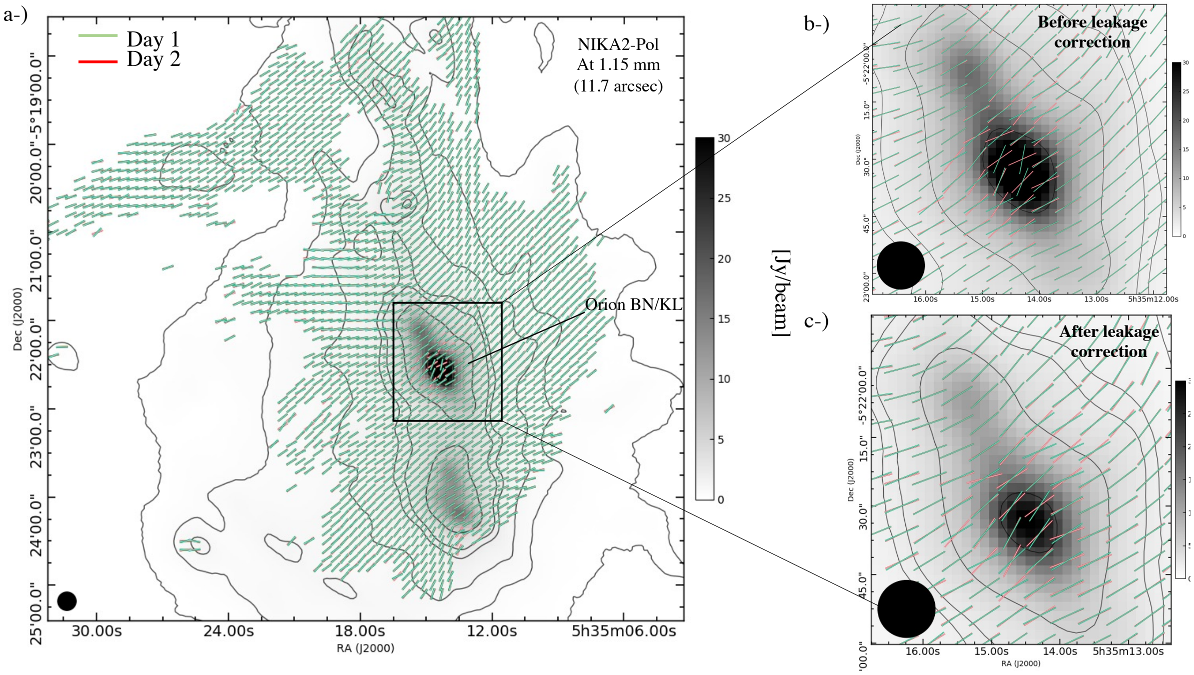

Figure 4.28: Test of the leakage correction procedure described in Sect. 4.4.1 on OMC-1, especially at the Orion-KL position. (*a*): B-field vectors from NIKA2-Pol polarization data at positions of significant detections in polarized intensity (i.e., $\mathrm{I}_{pol}/\sigma_{I_{pol}} > 3$) on two different days, day 1 and day 2, corresponding to the green and red colors, respectively. (*b*): Closeup view of the vicinity of the Orion-KL position overlaid with B-field vectors obtained before leakage correction. (*c*) similar to panel *b* but after correcting for instrumental polarization.

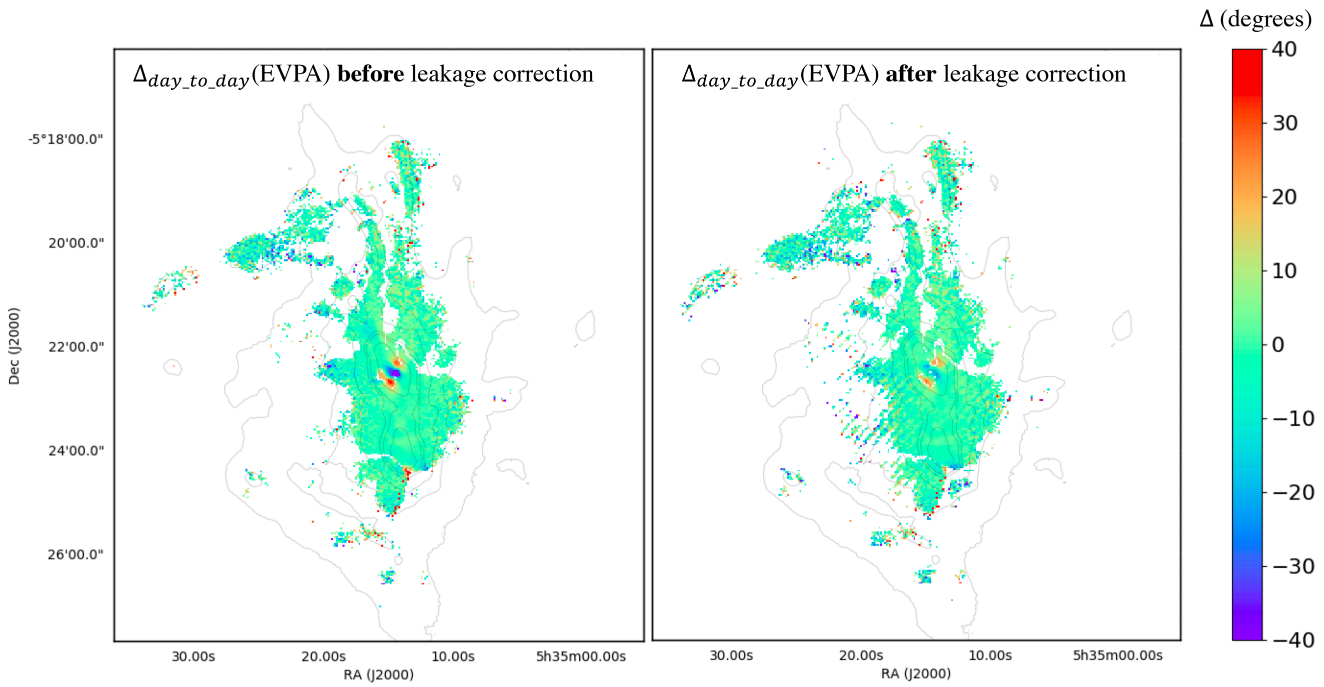

Figure 4.29: The left map shows the difference in polarization angles before applying the leakage correction. The weakly polarized Orion-KL is affected by the leakage and makes $\Delta_{day-to-day}$ significantly different from one day to another (these data were taken four days apart). The data used here were taken under different weather conditions, elevation, and focus positions. Uranus observations were carried out before each OMC-1 observation. The right panel shows $\Delta_{day-to-day}$ after leakage correction. Here we corrected each data set by a suitable leakage.

To test the repeatability of NIKA2-Pol results, OMC-1 was observed on several nights and under good weather conditions in Nov. 2020. Figure 4.28 shows the difference between data taken on Nov. 12 and 15, 2020 before and after leakage correction, in panels a) and b), respectively. On the same night, the leakage pattern was observed on Uranus under similar conditions of focus and elevation, which guarantee an optimal correction of instrumental polarization (IP). Without IP correction, the OMC-1 polarization data taken on different days are in good agreement (e.g., with a root mean square difference in polarization angles of $< 3°$), except at the location of the compact source Orion-KL, which is strong in Stokes I but weakly polarized ($P \sim 1\%$ or less), and thus more strongly affected by IP. Prior to IP correction, a very significant difference in polarization angles ($\sim 50°$) is observed near Orion-KL between data sets taken on two different nights (see Fig. 4.28b).
Indeed, the impact of IP is more pronounced in areas of the sky where the signal in Stokes I is strong and structured on small angular scales rather than extended and slowly varying. After subtracting the IP estimated using Uranus data observed before OMC-1, however, the polarization data from different nights agree well with each other, with a maximum difference in polarization angles reduced to $< 20°$ near Orion-KL (see Fig. 4.28c) and $\leq 2°$ outside of Orion-KL. This analysis illustrates the ability of NIKA2-Pol to provide robust (repeatable), high-quality polarization maps for scientific purposes (cF. Fig. 4.30 and Chap. 5).

4.5 Absolute calibration of the polarization angles measured by NIKA2-Pol

One of the challenges on the NIKA2-Pol commissioning is the absolute calibration of the observed polarization angles on the sky. To perform this calibration, we carried out joint XPOL observations of a few quasars (QSOs), such as 3C286, 3C279, 3C273, and others. Due to the effect of the leakage and the slight variability of the polarization angle of 3C279 and 3C273, we only used the quasar 3C286 which is a highly polarized for the absolute calibration. The stability of this quasar is commonly used to characterizing the absolute orientation of polarimeter instruments.

We also used OMC-1 and the Crab nebula as secondary calibrators for this issue. In this section, I present the absolute calibration of NIKA2-Pol polarization angles on the sky obtained by comparison with other instruments such as SCUBA2-POL2, XPOL, and ALMA.

4.5.1 Absolute angle calibration using quasars : NIKA2-Pol vs XPOL

To calibrate the NIKA2-Pol polarization data on the sky, we observed quasars which are polarized point sources whose polarization is stable on short ($\leq$ 1 day) timescales at mm wavelengths. Coordinated polarization observations of 3C286 between NIKA2-Pol and XPOL at the 30m telescope were carried out in Dec. 2018, Feb. 2020, and Nov. 2020. We used 3C286 as a calibrator of the angle (together with OMC-1 and the Crab nebula) which is not affected by the IP leakage due to its high polarization fraction. Other quasars were observed but they are more strongly affected by the IP leakage (3C279, 3C273, 3C84, etc). The mean polarization angle of 3C286 (without leakage correction) over the three campaigns is 43.8° with 5° uncertainty from the three data sets. XPOL observation of 3C286 found a mean polarization angle about $37.5° \pm 1.5°$ at 1.3mm, with a polarization fraction of about $\sim 18.5\% \pm 0.9\%$. ALMA observed 3C286 at 233GHz on 20200224: the observed polariazation angle is $38° \pm 3°$ (mean polarization fraction $\sim 16\% \pm 2\%$). Our NIKA2-Pol measurement of polarization angle on 3C286 suggests the presence of $5° - 6°$ offset compared to XPOL and ALMA observations ,which may come from a systematic offset in the zero point angle of the HWP..

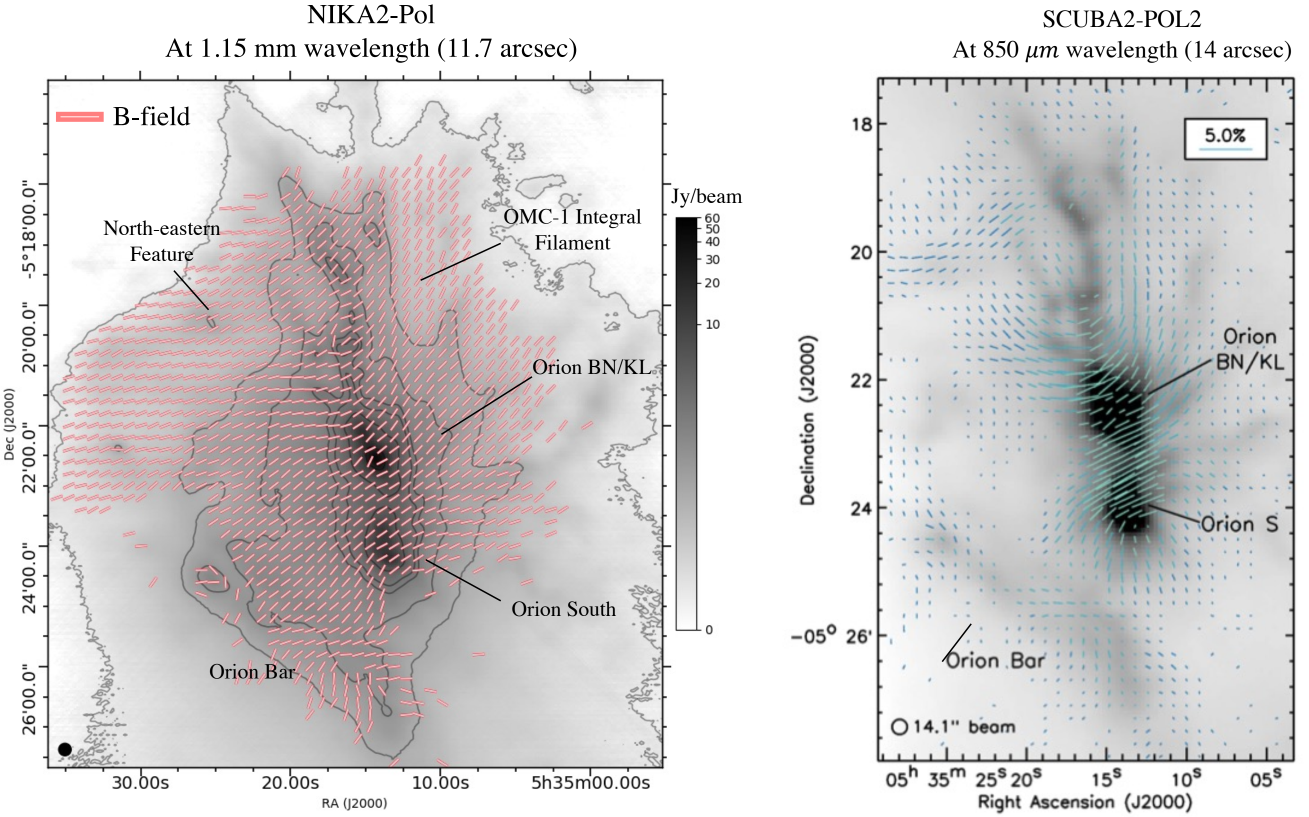

Figure 4.30: Comparison of the NIKA2-POL maps (left panel) and SCUBA2-Pol2 maps (right panel, (Pattle et al., 2017a)) on OMC-1. The grayscale background image in the left panel represents the total intensity observed with NIKA2 at 1.15 mm; the over-plotted segments correspond to the B-field vectors inferred from the NIKA2-Pol results, **combining all of the data from campaign # 3, after IP correction (5 hours on-source)**, with one vector plotted every beam (i.e, every 11.7 arcsec). All vectors are shown with equal lengths for better clarity. The right panel is taken from the SCUBA2-Pol2 850 μm paper by Pattle et al. (2017a). **The NIKA2-POL polarization angles compare very well with the SCUBA2-Pol2 ones where both are detected (see Figure 4.31 for a quantitative analysis), and reveal both higher-resolution details near Orion KL and more polarization information in the outskirts of the field.**

4.5.2 Absolute angle calibration using OMC-1

The observation of the extended source Orion OMC-1 allowed us to use this source as another calibrator of the polarization orientation of NIKA2-Pol on the sky. To calibrate this angle, we compared the NIKA2-Pol data with SCUBA-POL2 data (14 arcsec resolution), after smoothing the NIKA2-Pol data to the same resolution as SCUBA2-POL2 data (Pattle et al., 2017a). In this analysis, I used only high signal-to-noise data $I_{pol}\sigma \geqslant 3$, where I_{pol} is the polarized intensity and took into account data from all campaigns. We found a stable offset of $-5.5^\circ \pm 1^\circ$ between SCUBA2-Pol2 and NIKA2-Pol over the years. Figure 4.31 shows a quantitative comparison between NIKA2-Pol and SCUBA2-Pol2 over the years. The plots show the histogram of the distribution of the B-field angle of NIKA2-Pol after subtracting the offset of 5.5 deg against a similar histogram for POL2. From right to left, the offset between the two data sets at the same resolution is about -6.1, -5.2, and -5.6 for the Dec. 2018, Feb. 2020, and Nov. 2020 data, respectively. **The offset between NIKA2-Pol and SCUBA2-Pol2 is stable over the years and is about** $-5.5^\circ \pm 1^\circ$. This analysis was performed on a pixel-by-pixel basis at positions with $I_{pol} \geqslant 3\sigma_{I_{pol}}$ in all data sets. The origin of this offset between NIKA2-Pol polarization data and POL2 is still under investigation. This $-5.5^\circ \pm 1^\circ$ offset must be subtracted from the NIKA2-Pol data to get properly calibrated polarization angles on the sky.

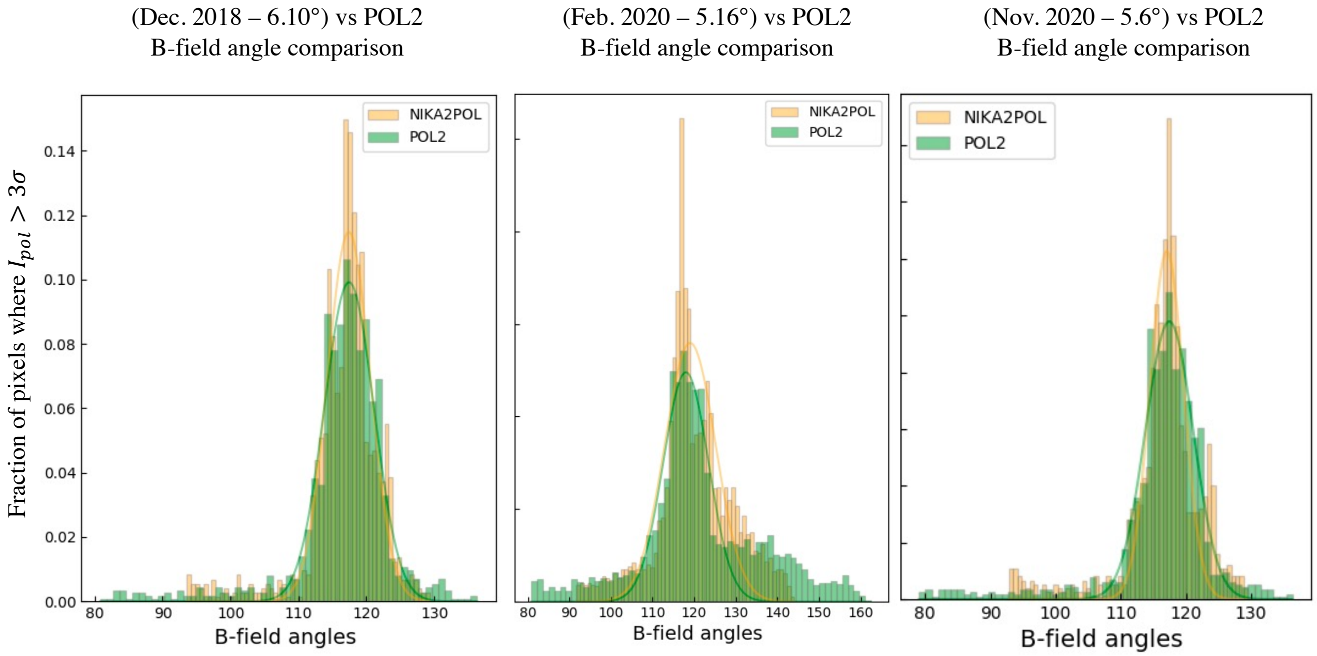
(Dec. 2018 – 6.10°) vs POL2
B-field angle comparison

(Feb. 2020 – 5.16°) vs POL2
B-field angle comparison

(Nov. 2020 – 5.6°) vs POL2
B-field angle comparison

Figure 4.31: Histograms of polarization angles measured with NIKA2-POL in the OMC-1 filament for the three campaigns Dec. 2018, Feb. 2020, and Nov. 2020 from left to right in yellow color and compared to the POL2 distribution over the same area (green histogram). The best overlap angle distributions is found by subtracting an offset of $6.1^\circ \pm 1^\circ$ from the Dec. 2018 data, $5.16^\circ \pm 1^\circ$ from Feb. 2020, and $5.6^\circ \pm 1^\circ$ from Nov. 2020.

Figure 4.30 also shows how the NIKA2-Pol observations detect polarized emission beyond the SCUBA2-POL2 observations. Figure 4.32 shows the map and the histogram (in panel a and b, respectively) of the difference between NIKA2-Pol data and POL2 data at the same angular resolution and high signal-to-noise ratio of the polarized intensity ($I_{pol} > 5\sigma_{I_{pol}}$). The high resolution and sensitivity of NIKA2-Pol provide a unique opportunity to resolve complex structures in the dense ISM. More analysis and discussion about the OMC-1 region are presented in the next chapter (Chap. 5).

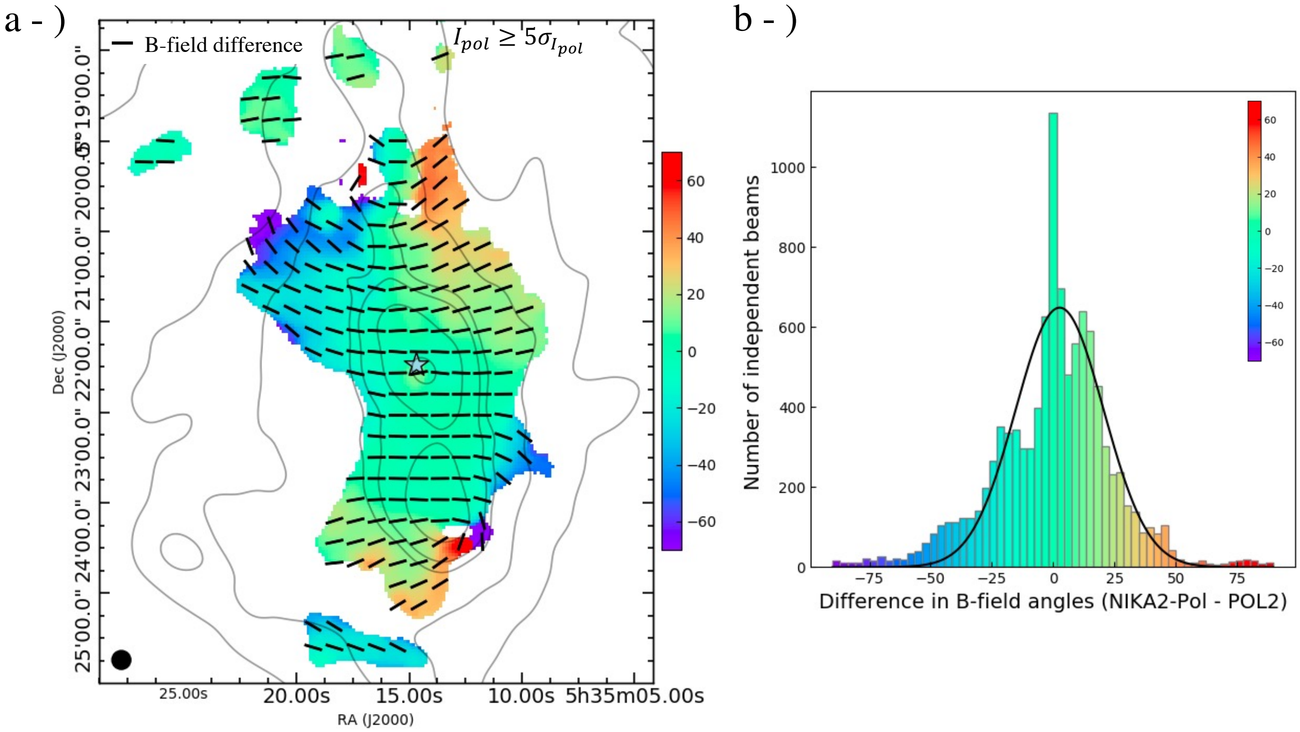

Figure 4.32: Differences in B-field angle between NIKA2-Pol and POL2 data in OMC-1 at the same angular resolution (14″) and for positions with high signal-to-noise ratio in polarized intensity ($I_{pol} > 5\sigma_{I_{pol}}$ for both NIKA2-Pol and POL2). *a-)*: Map of the differences in B-field angle (NIKA2-Pol − POL2). The overlaid black segments display difference vectors plotted every 14″ beam. *b-)*: Histogram of the differences in B-field angle (NIKA2-Pol − POL2). **The amplitude of the difference in B-field angle between NIKA2-Pol and POL2 is less than 10° for 67% of the positions.**

4.5.3 Polarization angle stability based on observations of the Crab nebula

The Crab nebula is one of the commonly used calibrators for polarization experiments. The synchrotron radiation generated by the pulsar at the center of the Crab nebula induces high polarized intensity, and the resulting distributions of polarization angles and polarization fractions are expected to be constant over time at millimeter wavelengths. The Crab has been observed in all three NIKA2-Pol commissioning campaigns to check the stability of polarization angles and provides an absolute calibration of these angles in the sky. Our NIKA2-Pol observations covered a $> 7'$ diameter area in the region. The Stokes parameters are similar to the ones obtained previously with NIKA1 and other instruments. Our analysis shows that the angles in the Crab Nebula must be corrected by an offset of -5.6 deg for absolute angle calibration on the sky as measured in OMC1 and 3C286. The median using aperture photometry over a diameter of $7'$ and at $SNR > 3$ is about -87.2 ± 0.8 deg and very stable over two years (with a standard deviation 0.3 deg). The polarization intensity was estimated to be about $P = 13.2 \pm 0.2$ %. The polarization data of the Crab nebula show high superior quality data with very stable polarization angles and polarization fractions. ~~We found that an offset −5.6 deg is also required to correct the Crab polarization data, which is stable as seen in OMC-1 and 3C286.~~

4.6 Conclusions

Summary of my contribution to the NIKA2-Pol commissioning
In this chapter, I presented a detailed analysis of the most challenging issues of the NIKA2-Pol commissioning, namely the characterization of the instrumental polarization (IP), correction, and the absolute calibration of NIKA2-Pol polarization angles on the sky. The three successful campaigns of the polarization commissioning allowed us to characterize the NIKA2-Pol performance and to prove its ability to deliver reliable polarization data even for compact and weakly polarized sources. The observation of Uranus under different weather conditions helped in scrutinizing the IP leakage pattern (Ajeddig et al., 2020, 2021) and its correction. We used OMC-1, 3C286, and Crab allowed to calibrate NIKA2-Pol on the sky. We provided a detailed analysis report on the commissioning of NIKA2 in the polarization mode as a support for the coming scientific observations. Some important conclusions on this part are :

1. Under stable weather conditions and for well-focused polarization data, the IP or leakage pattern takes the form of a characteristic "cloverleaf" structure, with a central positive spot surrounded by a negative quadruple, in both Stokes Q and (a lesser extent) Stokes U (see, e.g., Fig. 4.6).
2. The IP level and pattern are quite sensitive to the focus position of the telescope, with a focus offset of ± 0.2 mm leading to a significantly different IP.
3. The level of IP varies with elevation and shows a different pattern at elevations $< 30\,\mathrm{deg}$, which is mainly due to the astigmatism of the telescope.
4. Under similar observing conditions (in terms of elevation, focus, atmospheric opacity), the IP leakage presents both a similar pattern and a similar level.
5. There are no significant changes to the IP pattern/intensity with or without Styrofoam.
6. The astigmatism of the telescope is affecting the leakage and maybe one of its origins. Comparing the leakage at low and high elevation, our analysis leads to the conclusion the the IP pattern seems to rotate with astigmatism axis of the telescope. We also showed how this astigmatism effect can help on determining the orientation of the leakage.
7. **We proposed an analytical model, which can be an alternative method to correct NIKA2-Pol polarization data for the IP effect. To use the model one needs to quantify the variation of the model coefficients as a function of elevation, focus position and FWHM. Our fitting results of these coefficients are promising and allow to correct most of Uranus data taken from the three campaigns. To strengthen this model, this analysis needs more Uranus data to cover all possible leakage patterns/intensities.**
8. Based on extensive tests performed on Uranus maps taken under similar conditions, **scientific data can be corrected for the leakage effect down to a residual IP of $< 1\%$, provided that leakage data observed under similar (e.g., elevation, focus) conditions on, e.g., Uranus are available (down to 0.3% in case of a leakage map is estimated within $|\Delta_{el}| < 10$ and $|Fz| <$0.2 mm offset between the scientific target and Uranus)**. Another alternative method is to use the analytical model which does not need any deconvolution steps and can correct the NIKA2-Pol polarization data when no suitable map of Uranus is available.
9. I developed a new method for IP correction called CLUD ("Correction for the Leakage Using Data"). This method will save a significant amount of observing time as it does not require observations of Uranus and relies on the data taken on the science target itself. The CLUD method uses the analytical model to estimate the leakage map in a group of consecutive scans assuming that the IP leakage is stable in Nasmyth coordinates and varies in RADEC coordinates in that group. The multi-dimensional regression between the analytical model and the data allows us to determine the 30 coefficients of the analytical model.
10. **Our analysis of the NIKA2-Pol data towards the 3C286 and OMC-1 independently points towards the same value of the angle offset of NIKA2-POL polarization angles to recover the source polarization angles obtained with other astronomical facilities. It probably represents the calibration for absolute angles of the NIKA2-Pol camera on the sky. We also checked that**

this offset allows to recover the expected angles towards the Crab nebula. Observations of primary and secondary calibrators allowed us to determine the orientation of the NIKA2-Pol polarization data on the sky.

Overall conclusion

The NIKA2-Pol commissioning has been finalized using three campaigns in Dec. 2018, Feb. 2020 and Dec. 2020, which showed the ability of this polarimeter to deliver a high quality of polarization data. The sensitivity of the instrument is shown to be better than specifications, especially in Stokes Q and U, and they have been stable over the three commissioning campaigns (20 mJy. $s^{1/2}$ in Q and U, 30 mJy. $s^{1/2}$ in I). The polarization maps obtained with NIKA2-Pol on the OMC-1 extended source, go beyond what has already been published. The high angular resolution provided by NIKA2-Pol revealed new findings in OMC-1 region and allowed us to start using these data for scientific purposes (see next chapter).

4.7 Proceeding paper I (refereed) : Preliminary results on the instrumental polarization of NIKA2-Pol at the IRAM 30m telescope

EPJ Web of Conferences **228**, 00002 (2020) https://doi.org/10.1051/epjconf/202022800002
mm Universe @ NIKA2

Preliminary results on the instrumental polarization of NIKA2-Pol at the IRAM 30m telescope

H. Ajeddig[1,*], *R.* Adam[3,4], *P.* Ade[5], *Ph.* André[1], *A.* Andrianasolo[6], *H.* Aussel[1], *A.* Beelen[7], *A.* Benoît[8], *A.* Bideaud[8], *O.* Bourrion[2], *M.* Calvo[8], *A.* Catalano[2], *B.* Comis[2], *M.* De Petris[9], *F.-X.* Désert[6], *S.* Doyle[5], *E. F. C.* Driessen[10], *A.* Gomez[11], *J.* Goupy[8], *F.* Kéruzoré[2], *C.* Kramer[12], *B.* Ladjelate[12], *G.* Lagache[13], *S.* Leclercq[10], *J.-F.* Lestrade[14], *J.F.* Macías-Pérez[2], *A.* Maury[1], *P.* Mauskopf[5,15], *F.* Mayet[2], *A.* Monfardini[8], *L.* Perotto[2], *G.* Pisano[5], *N.* Ponthieu[6], *V.* Revéret[1], *A.* Ritacco[12], *C.* Romero[10], *H.* Roussel[16], *F.* Ruppin[17], *K.* Schuster[10], *Y.* Shimajiri[1,18,19], *S.* Shu[10], *A.* Sievers[12], *C.* Tucker[5], and *R.* Zylka[10]

[1] Laboratoire d'Astrophysique (AIM), CEA, CNRS, Université Paris-Saclay, Université Paris Diderot, Sorbonne Paris Cité, 91191 Gif-sur-Yvette, France
[2] Univ. Grenoble Alpes, CNRS, Grenoble INP, LPSC-IN2P3, 53, avenue des Martyrs, 38000 Grenoble, France
[3] LLR (Laboratoire Leprince-Ringuet), CNRS, École Polytechnique, Institut Polytechnique de Paris, Palaiseau, France
[4] Centro de Estudios de Física del Cosmos de Aragón (CEFCA), Plaza San Juan, 1, planta 2, E-44001, Teruel, Spain
[5] Astronomy Instrumentation Group, University of Cardiff, UK
[6] Univ. Grenoble Alpes, CNRS, IPAG, 38000 Grenoble, France
[7] Institut d'Astrophysique Spatiale (IAS), CNRS and Université Paris Sud, Orsay, France
[8] Institut Néel, CNRS and Université Grenoble Alpes, France
[9] Dipartimento di Fisica, Sapienza Università di Roma, Piazzale Aldo Moro 5, I-00185 Roma, Italy
[10] Institut de RadioAstronomie Millimétrique (IRAM), Grenoble, France
[11] Centro de Astrobiología (CSIC-INTA), Torrejón de Ardoz, 28850 Madrid, Spain
[12] Instituto de Radioastronomía Milimétrica (IRAM), Granada, Spain
[13] Aix Marseille Univ, CNRS, CNES, LAM (Laboratoire d'Astrophysique de Marseille), Marseille, France
[14] LERMA, Observatoire de Paris, PSL Research University, CNRS, Sorbonne Universités, UPMC Univ. Paris 06, 75014 Paris, France
[15] School of Earth and Space Exploration and Department of Physics, Arizona State University, Tempe, AZ 85287
[16] Institut d'Astrophysique de Paris, CNRS (UMR7095), 98 bis boulevard Arago, 75014 Paris, France
[17] Kavli Institute for Astrophysics and Space Research, Massachusetts Institute of Technology, Cambridge, MA 02139, USA
[18] National Astronomical Observatory of Japan, Osawa 2-21-1, Mitaka, Tokyo 181-8588, Japan
[19] Department of Physics and Astronomy, Graduate School of Science and Engineering, Kagoshima University, 1-21-35 Korimoto, Kagoshima, Kagoshima 890-0065, Japan

Abstract. Clarifying the role of magnetic fields in the star formation process is crucial. Observations have already shown that magnetic fields play an important role in the early stages of star formation. The high spatial resolution (~0.01 to 0.05 pc) provided by NIKA2-Pol 1.2 mm imaging polarimetry of nearby clouds will help us clarify the geometry of the B-field within dense cores and molecular

---

[*] e-mail: hamza.ajeddig@cea.fr

filaments as part of the IRAM 30m large program B-FUN. There are numerous challenging issues in the validation of NIKA2-Pol such as the calibration of instrumental polarization. The commissioning phase of NIKA2-Pol is underway and is helping us characterize the intensity-to-polarization "leakage" pattern of the instrument. We present a preliminary analysis of the leakage pattern and its dependence with elevation. We also present the current leakage correction made possible by the NIKA2 pipeline in polarization mode based on the NIKA2-Pol commissioning data taken in December 2018. Based on reduced Stokes I, Q, U data we find that the leakage pattern of NIKA2-Pol depends on elevation and is sensitive to the focus of the telescope.

1 Introduction

Herschel observations of nearby molecular clouds support a filament paradigm for star formation in which molecular filaments represent a key evolutionary step [2, 3, 8, 9]. The *Herschel* data indicate that filaments have a common inner width of $\sim$ 0.1 pc [5, 6]. In parallel, dust polarization observations of the whole sky with the *Planck* satellite have revealed a regular morphology for magnetic field lines on large scales in interstellar clouds; the orientation of the field tends to be parallel to low-density structures and perpendicular to high-density filaments [11]. This suggests that the magnetic field plays a crucial role in the growth of ISM structure leading to star formation. The transition between the two regimes (with a B-field mostly parallel and mostly perpendicular to the orientation of structures, respectively) is still poorly understood. Clarifying the nature of this transition requires higher spatial resolution than *Planck* and a detailed statistical analysis. The angular resolution of *Planck* polarization data [1] is also insufficient to investigate the link between the large-scale (>>0.1 pc) magnetic field in molecular clouds and the small-scale (<<0.1 pc) magnetic field relevant to the formation of individual protostars in dense cores.

NIKA2-Pol is the polarization channel of NIKA2, the new millimeter continuum camera on the IRAM 30m telescope [1]. NIKA2-Pol will soon provide 1.2 mm polarimetric imaging of a selected sample of star-forming molecular filaments at 12 arcsec resolution (or $\approx$ 8 mpc in the nearest clouds at $d \sim 140\,$pc), as part of the large program B-FUN[2](see also [4] for the scientific motivation). When observing in polarization mode, numerous effects coming from the polarimeter itself or the telescope influence the polarization measurements, which need to be characterized before starting science observations. In particular, instrumental polarization, i.e., the conversion of a fraction of unpolarized incident signal into polarized emission, here expressed in the form of an intensity-to-polarization leakage pattern (cf. Fig. 1), needs to be carefully calibrated as part of the polarimeter's commissioning. The NIKA2-Pol polarimeter, currently in the commissioning stage[3], benefits from previous experience of polarization measurements with the NIKA1 pathfinder, which tested and demonstrated the feasibility of millimeter continumm polarimetry with KIDs and a fast (3Hz) and continuously rotating half-wave plate [12]. The NIKA2 instrument was itself tested in polarization mode during the week of December 5–11, 2018 at Pico Veleta. As part of current efforts to characterize the performance of NIKA2-Pol and its ability to deliver reliable polarization maps, the present paper gives an overview of the instrumental polarization affecting the data.

---

[1] ~10 arcmin or ~0.4 pc in the nearest star-forming clouds at $d \sim 140\,$pc

[2] http://www.iram.es/IRAMES/mainWiki/Continuum/NIKA2/Main

[3] https://lpsc-indico.in2p3.fr/Indico/event/1765/speakers

2 Instrumental polarization: "leakage" pattern

During the Dec. 2018 commissioning week, we repeatedly observed the planet Uranus, an unpolarized source (see [14], where a polarization fraction of 0.10 ± 0.04% is reported for Uranus), in order to quantify the instrumental polarization affecting NIKA2-Pol data. We analyzed the resulting data in Stokes I, Q, U obtained at different elevations and focus positions. Qualitatively, the leakage pattern observed with NIKA2-Pol has the shape of a cloverleaf consisting of a central positive lobe surrounded by a negative quadrupolar pattern (see Fig. 1). The reason for this pattern is still under investigation. To first order at least, the leakage pattern in Stokes U can be obtained by rotating the leakage pattern in Stokes Q by $\sim 45°$. As part of the NIKA2-Pol commissioning run, we performed several observations of Uranus to determine if/how the leakage pattern changes with elevation (due to the system, e.g. telescope, optical path, or polarimeter) and/or whether it changes with the focus position. Instrumental polarization affecting other millimeter and submillimeter polarimeters, such as POL-2/SCUBA-2 on the James Clerk Maxwell Telescope (JCMT) [7], POLKA/LABOCA at the APEX telescope [14], or XPOL at the IRAM 30m telescope [13], has been characterized following a similar approach (observing an unpolarized source such as Uranus).

2.1 Dependence of the leakage pattern on elevation

The Uranus maps taken at low and high elevations show that the leakage pattern varies with elevation, and suggest that the level of instrumental polarization is higher at low elevation. As an illustration, Fig. 1 shows Stokes I, Q and U maps obtained for Uranus at two elevations, $\sim 52°$ (top panel) and 31° (bottom panel). As can be seen in Fig. 1, the maximum fractional instrumental polarization varies from 0.45 % to 1.84 % in $|U/I_{\rm peak}|$ and from 1.27 % to 2.16 % in $|Q/I_{\rm peak}|$ when source elevation changes from 52° to 31°, while the leakage pattern conserves the same cloverleaf shape. Due to the lack of good Uranus data at closely spaced elevations, the detailed manner in which the instrumental polarization level varies with elevation remains very uncertain, especially in the critical elevation range between $\sim 20°$ and $\sim 45°$ at which many potential scientific targets would be observed.

2.2 Dependence of the leakage pattern on focus

We found that the leakage pattern changed significantly even for small (±0.3 mm) differences in the focus position of the telescope (see Fig. 2). We tried to assess how much the leakage pattern would depart from the nominal pattern (for well-focused observations) in the case of observations taken while the telescope is (slightly) out of focus. Figure 2 shows a schematic diagram summarizing the typical evolution of the leakage pattern as a function of offset from the good focus position. This was estimated from a series of Uranus defocused maps. We found that the maximum fractional amplitude of the leakage or instrumental polarization pattern ($|{\rm Q/I_{peak}}|_{\rm max}$ and $|{\rm U/I_{peak}}|_{\rm max}$) increases by only $\sim 0.2\%$ as long as the focus position is off by less than ±0.3 mm from the optimum focus correction (along Z). However, the *shape* of the leakage pattern changes quite significantly (and even loses its cloverleaf shape) at even small focus offsets of ±0.3 mm. To further quantify the dependence of the leakage pattern with focus, a larger number of defocused maps of Uranus taken at smaller focus offsets (e.g. ± 0.1 mm, ± 0.15 mm, ± 0.2 mm, ± 0.25 mm) from the optimal focus value will have to be observed. This will be one of the main purposes of the next NIKA2-Pol commissioning run.

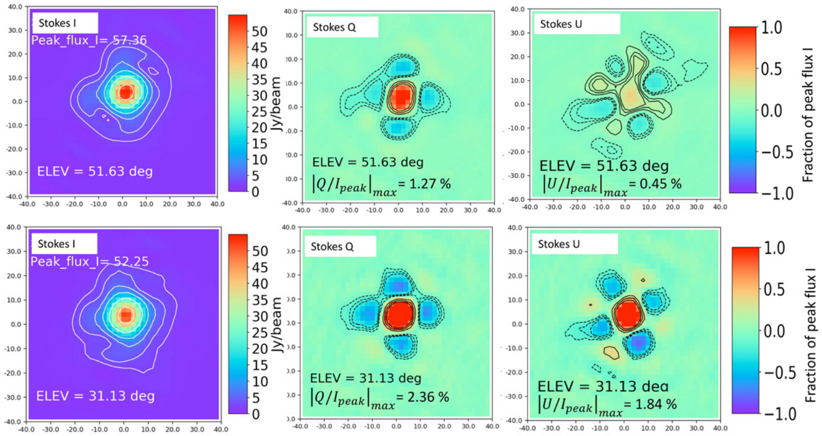

Figure 1. Examples of Stokes (I, Q, U) maps obtained for Uranus (in Nasmyth coordinates). Uranus being an unpolarized source, the signals detected in Stokes Q, U correspond to instrumental polarization, which should be corrected for as part of the reduction of NIKA2 polarization data (a.k.a leakage correction). The color bar shows the fraction of U/I_{peak} or Q/I_{peak}. The leakage patterns in both Stokes Q and U vary from high to low elevation with a more deformed pattern in Stokes U. The level of instrumental polarization (expressed as a fraction U/I_{peak} or Q/I_{peak}) increases from 0.45 % to 1.84 % in Stokes U (right column) and from 1.27 % to 2.36 % in Stokes Q (middle column) when source elevation decreases from 52° to 31°.

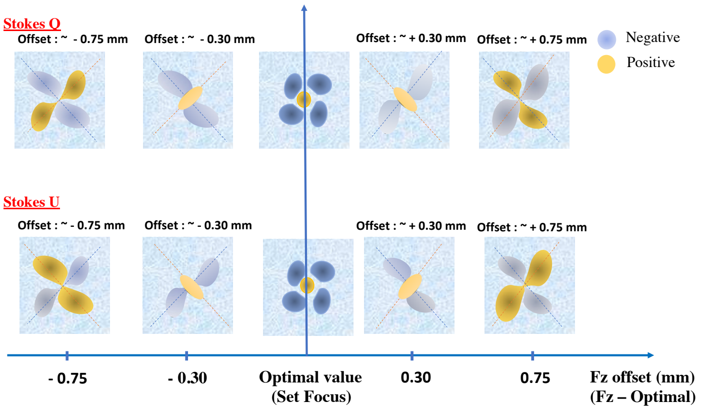

Figure 2. Schematic diagram in Nasmyth coordinates summarizing how the instrumental polarization pattern (Stokes Q and U emission maps from an unpolarized source) varies as a function of the offset from the optimum focus position (along the Z axis). The typical cloverleaf pattern seen at the best focus position becomes more severely distorted as the applied focus correction is farther away from its optimum value.

3 Correcting for the leakage pattern

We used the best Stokes Q, U maps of Uranus taken during the Dec. 2018 commissioning week to verify that a leakage correction procedure similar to that devised by Ritacco et al. [12]

for NIKA1 was properly implemented in the NIKA2 IDL pipeline (still under development). First, we applied the leakage correction directly to the Uranus map used to estimate the leakage pattern (i.e., observed at 52° elevation, shown in the top row of Fig. 1). The residual Stokes Q/I_{peak} and U/I_{peak} maps obtained after correcting the data for the leakage pattern are displayed in Fig. 3f and Fig. 3l, respectively. These residual $|Q/I_{\text{peak}}|$ and $|U/I_{\text{peak}}|$ maps are less than 0.1% in amplitude, suggesting that the leakage-correction procedure has been properly implemented in the NIKA2 pipeline. Figure 3 also shows the residual Stokes Q/I_{peak}, U/I_{peak} maps obtained when applying the leakage-correction procedure to Uranus maps taken at other elevations than the map used to estimate the leakage pattern. We found that for maps taken at elevations > 45° the magnitude of the residuals is lower than 0.3% (in |Q/I_{peak}|) and 0.5% (in |U/I_{peak}|) after leakage correction, but for maps at low elevations (~20°–30°) the residuals become significantly higher, up to 0.8% in |Q/I_{peak}| and 2% in |U/I_{peak}| (Fig. 3). Similar correction tests will be investigated with polarization residuals obtained at other elevations (e.g ~ 31°) to test this hypothesis. According to these preliminary results, it seems

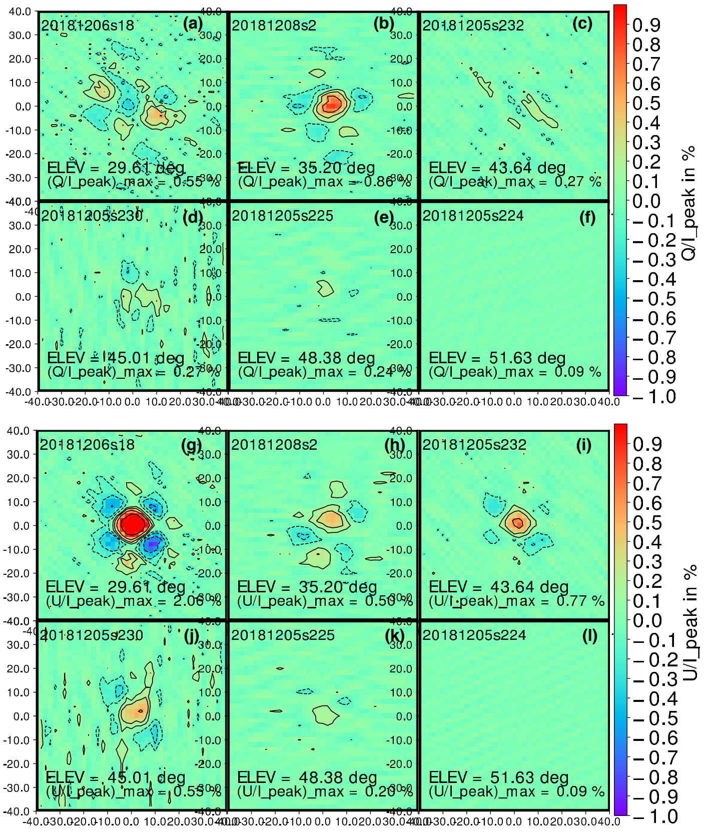

Figure 3. Residual Stokes Q/I_{peak} and U/I_{peak} maps (expressed in % of I_{peak}) obtained after correcting each of the individual Uranus maps, taken at different elevations, by a single leakage pattern (from Uranus map taken at 52 deg elevation, (f) and (l) panels). The contours show levels of −2%, −1%, −0.5%, −0.2%, +0.2%, +0.5%, +1.0%, +2.0%. Note how the maps taken at elevations different from the one used to correct for the leakage show non-negligible residuals (up to ~ 2%).

that a proper correction of NIKA2-Pol observations for instrumental polarization effects will require a good characterization of the leakage pattern at an elevation close to that of the observed data (~ ±5°).

4 Conclusions

NIKA2-Pol will peer into the magnetic field of star-forming filaments as part of the IRAM 30m large program B-FUN. The instrumental polarization of NIKA2-Pol will be better characterized in forthcoming commissioning runs. The current NIKA2-Pol pipeline includes a method to correct for instrumental polarization which was already validated as shown in this paper. One of the next commissioning steps will be to obtain good maps of Uranus in polarization mode at closely-spaced elevations and for a fine grid of focus settings. Determining how the intensity-to-polarization leakage pattern varies with elevation and focus in more detail will allow us to use our correction method on NIKA2-Pol scientific data.

Acknowledgements

We would like to thank the IRAM staff for their support during the campaigns. The NIKA dilution cryostat has been designed and built at the Institut Néel. In particular, we acknowledge the crucial contribution of the Cryogenics Group, and in particular Gregory Garde, Henri Rodenas, Jean Paul Leggeri, Philippe Camus. This work has been partially funded by the Foundation Nanoscience Grenoble and the LabEx FOCUS ANR-11-LABX-0013. This work is supported by the French National Research Agency under the contracts "MKIDS", "NIKA" and ANR-15-CE31-0017 and in the framework of the "Investissements d'avenir" program (ANR-15-IDEX-02). This work has benefited from the support of the European Research Council Advanced Grant ORISTARS under the European Union's Seventh Framework Programme (Grant Agreement no. 291294). We acknowledge fundings from the ENIGMASS French LabEx (R. A. and F. R.), the CNES post-doctoral fellowship program (R. A.), the CNES doctoral fellowship program (A. R.) and the FOCUS French LabEx doctoral fellowship program (A. R.). R.A. acknowledges support from Spanish Ministerio de Economía and Competitividad (MINECO) through grant number AYA2015-66211-C2-2.

References

[1] R. Adam *et al.*, Astron. Astrophys. **609**, A115 (2018)
[2] Ph. André *et al.*, Astron. Astrophys. **518**, L102 (2010)
[3] Ph. André *et al.*, in *Protostars and Planets VI*, 27–51 (2014)
[4] Ph. André *et al.*, PASA. **36**, e029 (2019)
[5] D. Arzoumanian *et al.*, Astron. Astrophys. **529**, L6 (2011)
[6] D. Arzoumanian *et al.*, Astron. Astrophys. **621**, A42 (2019)
[7] P. Friberg *et al.*, Millimeter, Submillimeter, and Far-Infrared Detectors and Instrumentation for Astronomy IX **10708** 3M (2018)
[8] V. Könyves *et al.*, Astron. Astrophys. **584**, A91 (2015)
[9] P. Palmeirim *et al.*, Astron. Astrophys. **550**, A38 (2013)
[10] L. Perotto *et al.*, submitted to Astron. Astrophys.
[11] Planck collaboration *et al.*, Astron. Astrophys. **594**, A1 (2016)
[12] A. Ritacco *et al.*, Astron. Astrophys. **599**, A34 (2017)
[13] C. Thum *et al.*, PASP. **120**, 777–790 (2008)
[14] H. Wiesemeyer *et al.*, PASP. **126**, 1027 (2014)

Chapter 5

NIKA2-Pol reveals new finding toward the OMC-1 filament

Contents

5.1 The OMC-1 filamentary clump in the Orion A molecular cloud

One of the most active star-forming regions among nearby interstellar clouds is the Orion cloud complex which forms both low and high-mass stars and provides an excellent target to study star formation at various evolutionary steps, e.g, from the parent cloud to dense cores and young stars (Bally, 2008). Using observations at 22 μm wavelength with a beam of 30″, Kleinmann & Low (1967) discovered an extended infrared source located in the Orion Nebula (NGC 1976) which has been referred to as the Orion-KL nebula since-then. The Orion A cloud exhibits three main of filamentary clumps named OMC-1, OMC-2, and OMC-3. Following these results, using observations of the Orion nebula at 69 μm wavelength, Fazio et al. (1974) detected the existence of two different components in the OMC-1 region and other nearby extended sources like OMC-2. The observation of OMC-1 at different wavelengths and at different angular resolutions allowed to detect several molecular lines such as : CO, Ammonia, Methanol, CH3CN, NH2, HC1, HCN, C2H2, H2S, H3O+ (Erickson et al., 1981; Loren et al., 1981; Ziurys et al., 1981; Blake et al., 1985; Lacy et al., 1989; Minh et al., 1990; Wootten et al., 1991). These observations have made OMC-1 one of the main scientific targets to study the chemistry and evolution of molecular clouds. The Orion A cloud exhibits a large-scale filament called the Integral Shaped Filament (ISF) (e.g, Bally et al., 1987; Johnstone & Bally, 1999) and including the OMC-1, OMC-2 and OMC-3 clumps.

The origin of the bright sources (spots) in the OMC-1 filament has been studied for decades. Mundy et al. (1986) suggested that these sources are the result of shock compression driven by the H II region. In addition, Murata et al. (1990) found the existence of filamentary structures around Orion KL using the Nobyama telescope from observations of NH3 molecular lines at 23.7 GH. Recent observations from Herschel Gould Belt Survey (HGBS) revealed a high filamentary structure in the Orion A cloud (André et al., 2010, 2014). More recent observations of Orion A using the ArTéMiS bolometer camera at APEX covering the OMC-1, OMC-2, and OMC-3 regions at 350 μm and 450 μm indicated the importance of this region for the study of core fragmentation in filaments (Schuller et al., 2021). In this section, I present an overview of the OMC-1 region in the Orion A cloud.

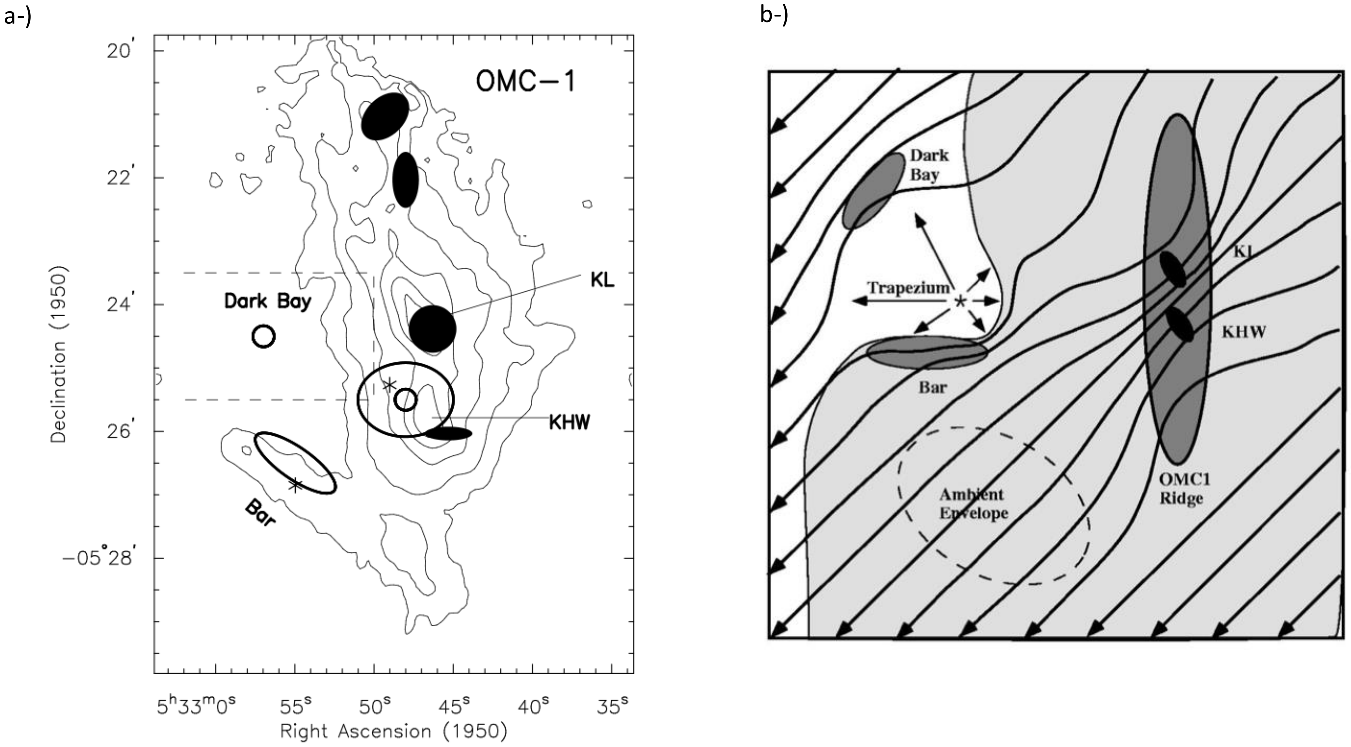

Figure 5.1: *a)* : Different clumps in OMC-1 using large-scale map of the gas and dust . *b)* : schematic representation of the OMC-1 envirement and different parts of the filament. Figure taken from Schleuning (1998).

5.1.1 A prominent molecular outflow in OMC-1

The study of Bally et al. (1987) highlighted the filamentary structure of OMC-1 based on a large-scale ^{13}CO survey map with an angular resolution of 30″. Observations of high-velocities SiO and CO emission towards Orion-KL led Ziurys & Friberg (1987) to suggest for the first time the existence of an outflow source in the vicinity of Orion-KL. High angular resolution observations at 6″ and 9″ of ^{13}CO molecular lines confirmed the existence of the outflow (Masson et al., 1987). Observations using the IRAM 30m telescope toward the outflow source 1.5 arcmin south from Orion-KL showed that the Orion-S flow may be driven by a young, highly obscured star (Ziurys et al., 1990). The detection of line polarization using v=1-0 S(1) observations with 12 km/s resolution toward OMC-1 revealed the presence of isolated bow shocks in the outflow region (Burton et al., 1991).

5.1.2 Presence of C-shock waves

Sub-millimeter observations are important to trace the material making up the molecular clouds since many molecular lines are detected at sub-millimeter wavelengths (Loren & Wootten, 1986). Emission from shock-excited molecular hydrogen H_2 has has been observed in OMC-1 such as S(13) and O(7), indicating the presence of the shock waves responsible for the excitation of these lines at 2.10-3.85 μm (Burton et al., 1989). The authors suggested that these molecular structures are formed by C-shock surfaces caused by the strong stellar wind originally from the Orion-KL region. Smith & Brand (1990) interpreted the molecular hydrogen lines in the molecular cloud as a signature of a C-shock in this region, assumed the shock plane is seen face-on. CN, ^{13}CO, and ^{13}CS molecular line observations of the molecular gas containing the high mass embedded source in OMC-1 show variations in centroid velocity and line width indicating three distinct sub-regions. At least one of them is rotating, and shocks compressed the material to collapse which may explain the presence of high-mass stars in this region (Greaves & White, 1991). Smith (1991) analysed the presence of shocks in the OMC-1 region by interpreting the H_2 emission line spectrum and concluded that the bow shocks may lead to an unusually high magnetic field strength in this region. The first near-infrared observations with the Hubble Space Telescope revealed the properties of the H_2 region in the OMC-1 molecular cloud, and these observations showed several H2-emitting clumps surrounding the

Orion-BN/KL indicating the form of bow-shocks with V-shaped tips (Stolovy et al., 1998).

The [CN:HCN] abundance ratio helps to trace the intensity of the UV radiation field in molecular clouds. In the OMC-1 Northeastern bright bar), Greaves & Church (1996) found that this bar is evidence of shocks UV due to the Trapezium stars (see Fig. 5.1) in the middle of the Orion main bright bar, South-Eastern and northeastern bars. Observations of CII and OI lines by Herrmann et al. (1997) in OMC-1 region showed a consistent temperature and density between the main bar and the northeastern part. Rodriguez-Franco et al. (1998) published a large-scale mapping of CN(1-0) observations of the OMC-1 region which revealed filamentary structures toward the north and south of the Trapezium cluster and surrounding M43. The observed CN(1-0) lines indicates a filament-like structure which supports the idea that the CN filaments are the interfaces between the molecular cloud and the ionization front (in this case, M42 and M43).

5.1.3 Presence of rotating clumps in OMC-1 (?)

A large number of high-resolution observations have been carried out toward the OMC-1 region, investigating whether there is a rotating cloud or two merged clouds near the Orion-KL source. IRAM 30m observations of J =5-4 (K=0 to 3) lines of CH3C2H showed a number of clumps in the OMC-1 region which does not support the model of rotating clouds near to Orion-KL (Wang et al., 1993). But, it has been proposed that the bars around the Orion-KL region are rotating and showing a velocity gradient from the southwest to the north-eastern part of OMC-1. Others claim that these features are different clouds and are not related to any Keplerian motion as discussed in Wiseman & Ho (1998). Several studies relate this bar to a photo-dissociation region (PDR) between the molecular cloud and the HII region (Tielens & Hollenbach, 1985). The dark bay in the north-eastern of the OMC-1 (see Fig. 5.1) is seen in the optical and indicating the front of the M43 and HII region. Their results at high resolution showed a distribution of clumpy filaments radiating away from the Orion-KL nebula. The north-eastern part of the OMC-1 filament has a different velocity and may be due to heating radiations from IRc1.

5.2 Magnetic field in the OMC-1 region

Dust polarization observations in both extinction and emission have been a powerful tool to infer the magnetic field morphology in the ISM. The B-field geometry varies with the wavelength and the angular resolution of the instrument (Crutcher, 2012). Polarization observations toward the OMC-1 filament have been used to study the star formation process in filaments. From the optical/infrared to sub-millimeter/millimeter wavelengths, OMC-1 has been used as a good target to study the role of magnetic fields in a high-mass star-forming filament (Siringo et al., 2004a; Pattle et al., 2017a; Dowell et al., 2010). In this section, I present a summary of previous results on the B-field geometry and strength toward the OMC-1 region.

5.2.1 Morphology of the large-scale B-field in OMC-1 : Evidence of a large-scale hourglass

The magnetic field line geometry in OMC-1 has been under investigation for more than two decades. Early far-infrared polarimetric observations revealed the magnetic field structure in the molecular cloud and highlighted the importance of B-field in regulating star formation in this region (Hildebrand et al., 1995). Schleuning (1998) reported the presence of an hourglass shape in the B-field geometry based on an $8' \times 8'$ mapping of OMC-1 at 100 μm with $35''$ angular resolution. Gravitational collapse pinches the B-field lines to form an hourglass structure around Orion-KL. **?** suggested that the OMC-1 ridge (see Fig. 5.1) was the result of the gravitational collapse of a cloud that was initially supported by the magnetic field. More recent submillimeter polarization observations with the SOFIA/HAWC+ (214 μm), SCUBA2-POL2 (850 μm) and POLKA (870 μm) polarimeters (Guerra et al., 2021; Pattle et al., 2017a; Siringo et al., 2004a) have confirmed the large-scale hourglass B-field geometry in OMC-1 and the weak polarization fraction near Orion-KL ($\sim$1%–2%).
The B-field lines in the south-bar (also called KHW, see Fig. 5.1), detected at sub-millimeter wavelengths by Keene et al. (1982) from the ridge are different from the large-scale structure, which may suggest that the bar is not connected to the Orion A ridge. This region has a low temperature compared to that of KL, which may be due to the external heating by the Trapezium stars. The B-field lines tend to be uniform in the north-eastern bar of the filaments with high numbers of dust clumps (Coppin et al., 2000). The B-field lines morphology in the OMC-1 South region seems to be presumably due to the detected optical outflow in this region (Smith et al., 2004; Pattle

et al., 2017a). The B-fields lines tend to be perpendicular to the outflow in Orion-KL, which triggers the question of interpreting the polarization data (Vaillancourt et al., 2007; Vallée & Fiege, 2007; Pattle et al., 2017a).

5.2.2 Magnetic field strength and polarization fraction in OMC-1

Different methods have been used to estimate the magnetic field strength ; (1) Direct measurement using Zeeman observations of molecular lines such as CN, OH, SiO or others (Crutcher, 2012), (2) Indirect estimation using the Davis-Chandrasekhar-Fermi (DCF) method based on the assumption that the observed dispersion in polarization angles is mainly due to the Alfvén-wave perturbations of the B-field (Chandrasekhar & Fermi, 1953), (3) Indirect estimate using the force equilibrium method which assumes approximate balance between gravitational and magnetic field forces (Girart et al., 2006; Koch et al., 2012; Ewertowski & Basu, 2013; Bino & Basu, 2021; Bino et al., 2022). Zeeman observations of CN, HI, or OH lines toward OMC-1 provide B-field strength ranging from -49 ± 4 μG to -125 ± 20 μG (Troland et al., 1986). Using observation of CN lines at 3 mm with the IRAM 30m telescope, Crutcher et al. (1996) observed two molecular cores located at 3 arcmin north of Orion-KL (OMC-N4) and found B-field strength of $B(OMC-N4) = +79 \pm 99$ μG The attempts to understand the SO observations in the Orion nebula by analysing the Zeeman effect lead Clark et al. (1978) to estimate an upper limit of the B-field strength of < 40 μG.
Based on SCUBA-POL2 observations, Pattle et al. (2017a) estimated a plane-of-sky (POS) magnetic field strength in OMC 1 about 6.6 mG. From recent polarization observations with SOFIA/HAWC+, Guerra et al. (2021) estimated the magnetic field strength about 2 mG at the BN/KL position, and up to a few hundreds μG in the OMC-1 bar .

5.3 NIKA2-Pol observations toward OMC-1

We used high angular resolution ($11.7''$) polarization data obtained during the NIKA2-Pol commissioning campaigns to investigate the geometry and strength of the magnetic field in the OMC-1 region. In the present analysis, I only focus on the high-quality data taken during the November 2020 campaign. I present possible new findings based on the high-quality of the NIKA2 data in the vicinity of Orion-KL. I estimated the B-field strength using the DCF method. I used CO molecular line data obtained by the Nobeyama 45m telescope to estimate the 1D velocity dispersion that we used in the DCF estimate (Tanabe et al., 2019). The B-field geometry and strength derived from NIKA2-Pol data help to understand the role of magnetic fields in the evolution and fragmentation of the OMC-1 filament.

5.3.1 A possible new hourglass centered at the Orion-KL position

Based on their SCUBA-POL2 polarization observations, Pattle et al. (2017a) proposed a scenario in which the magnetic field dynamically regulates the evolution of the OMC-1 region. In this scenario, the large-scale gravitational collapse of the OMC-1 region and/or a central explosive outflow is responsible for the large-scale hourglass (see section 5.2.1). At the Orion-KL position, however, the B-field geometry was unclear. For instance, Vaillancourt et al. (2008) pointed out that the B-field angles inferred at 350 μm and 450 μm differ by 25° and reported a drop-in 450/350 μm polarization ratio by a factor of 2 toward Orion-KL. In addition, in their SHARP data, the B-field lines seemed to be distorted at the Orion-KL position (see Fig. 1 of Vaillancourt et al., 2008).

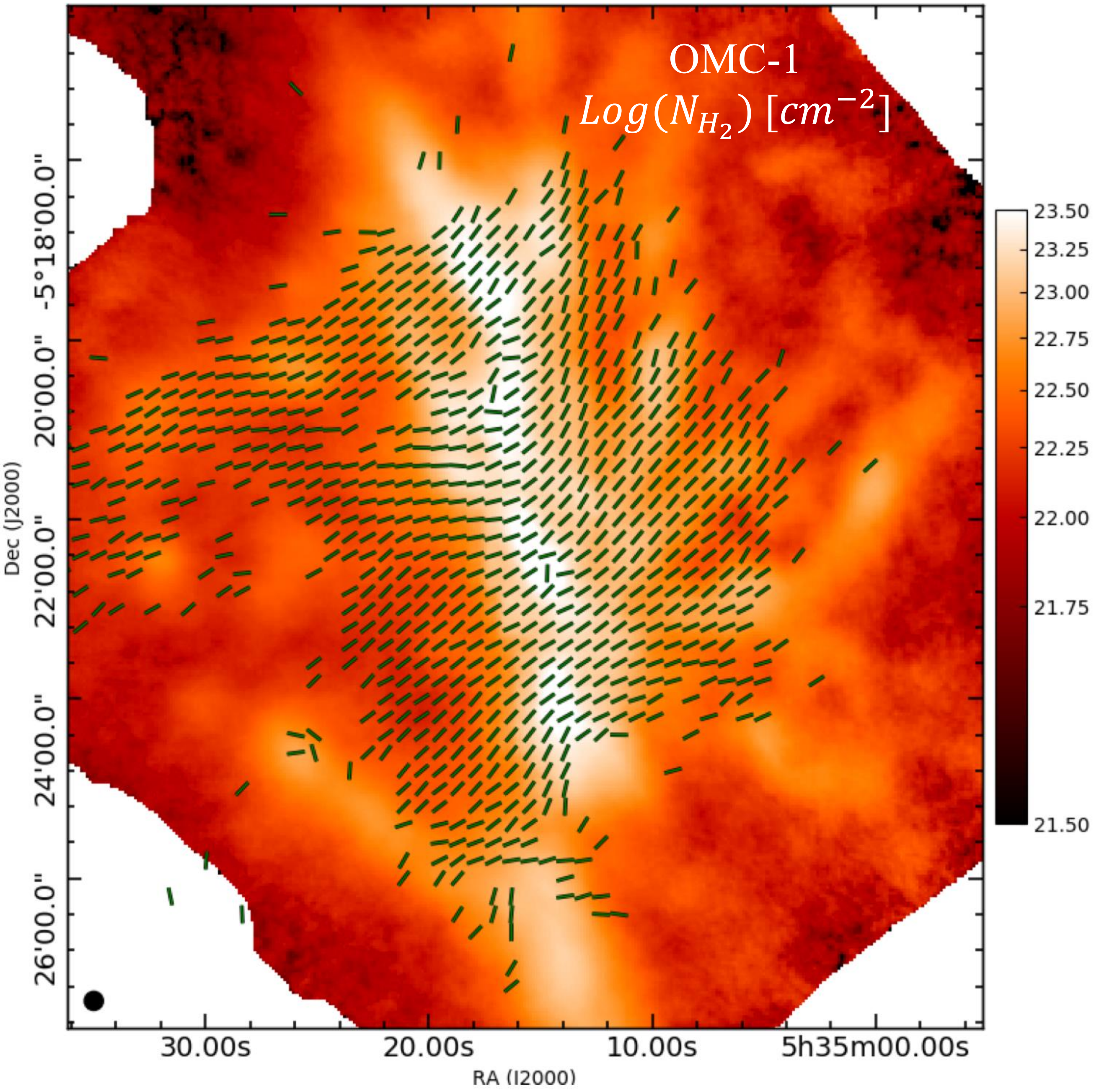

Figure 5.2: Magnetic field vectors inferred from less than three hours of NIKA2-Pol commissioning observations. Overlaid on a column density map of the OMC-1 region derived from consined ArTeMiS and Herschel data (Schuller et al., 2021). Vectors are shown at positions where $I_{pol}/\sigma_{I_{pol}}$ >3 from NIKA2-Pol data.

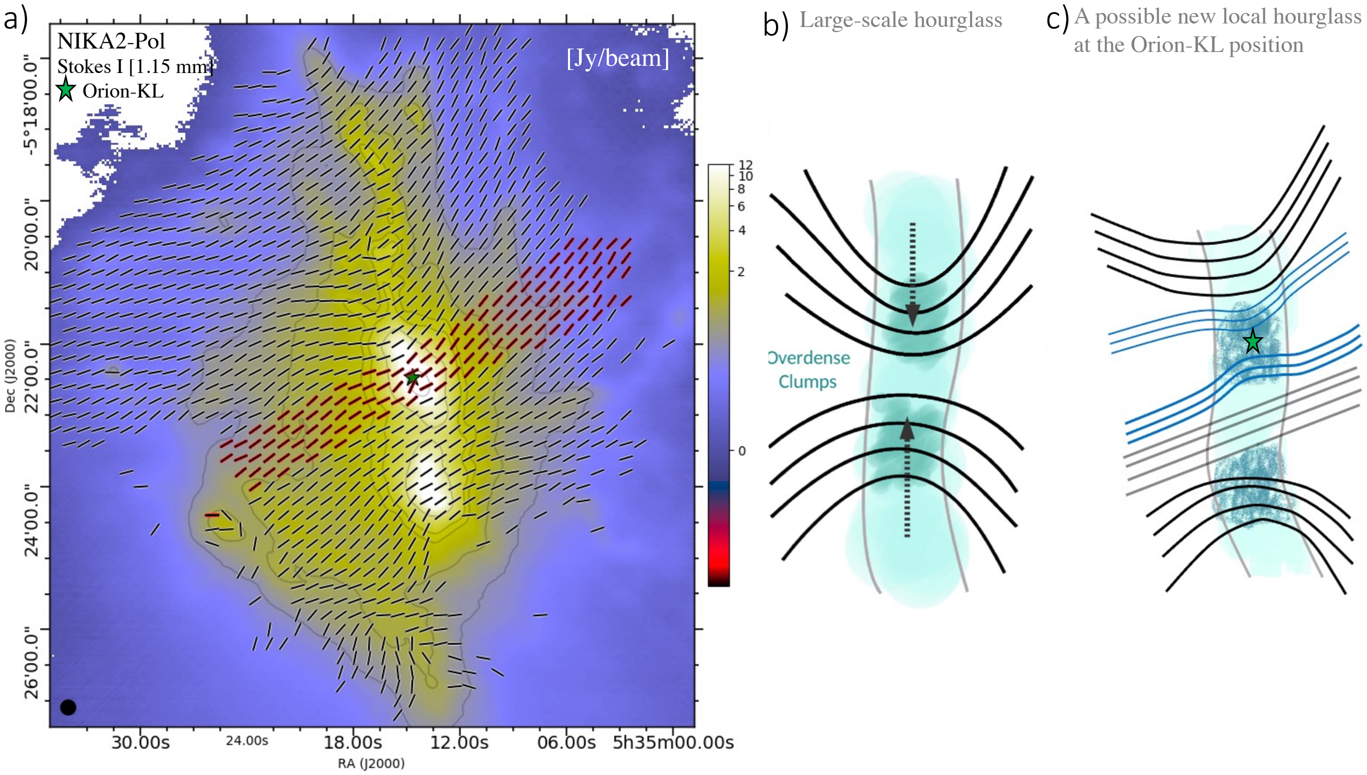

Figure 5.3: *a-)* Stokes I 1.15 mm map of OMC-1 region obtained from NIKA2-Pol commissioning data, with magnetic field vectors overlaid at positions where $I_{pol}/\sigma_{I_{pol}}$ >3. The red vectors emphasize the possible new local hourglass revealed by NIKA2-Pol. *b)*: Illustration of the large-scale magnetic field as seen by POL2 from Pattle et al. (2019). *c)* Schematic illustration of the large-scale hourglass geometry as seen with NIKA2-Pol (in black lines) and the new possible local hourglass at the position of Orion-KL revealed by the high sensitivity and resolution of NIKA2-Pol (in blue bars).

Thanks to the high angular resolution and sensitivity provided by the NIKA2-Pol instrument at 1.15 mm, a possible new hourglass centered at the Orion-KL position has been revealed (see Fig. 5.3a). The large-scale hourglass observed earlier is sketched in Fig. 5.3b from Pattle et al. (2017a), while the possible new local hourglass revealed by the NIKA2-Pol polarization data is shown and contrasted with the large-scale hourglass in Fig. 5.3c.

5.3.2 B-field strength in the OMC-1 region using the Davis-Chandrasekhar-Fermi (DCF) method

A common method of estimating the B-field strength from dust polarization data is the DCF method (Davis, 1951; Chandrasekhar & Fermi, 1953). This method is based on the assumption that the observed dispersion in B-field position angles is mainly due to the perturbation caused by Alfvén-waves propagating in the medium. Under this assumption , the B-field strength in plane-of-sky B_{POS} can be expressed as function of the polarization angle dispersion σ_θ and the velocity dispersion $\sigma_V = \mathrm{FWHM}/(8\ln 2)^{1/2}$, and can be written as $B_{POS} = \xi\,\frac{(4\pi\rho)^{1/2}\sigma_V}{\sigma_\theta}$, where ξ is a correction factor that comes from simulation results, and ρ is the gas volume density.
Adopting a correction factor $\xi = 0.5$ from the simulation results of Ostriker et al. (2001) and the Falceta-Gonçalves et al. (2008) approximation ($\sigma_\theta \sim \tan\sigma_\theta$), the B-field strength can be expressed in the following practical form, $B_{POS} = 0.383\sqrt{n(H_2)}\,\frac{\sigma_V}{\tan\sigma_\theta}\quad \mu\mathrm{G}$, where $n(H_2)$ is the number density of H_2 molecules in cm^{-3}, σ_V is measured in km s, and σ_θ is the dispersion in the orientation of the magnetic field orientations. A more detailed analysis is given in Section 6.3.1 (see also chapter 2) and in the paper in the appendix of this thesis.
In the present analysis, we derived σ_θ from NIKA2-Pol polarization data, and σ_V was estimated using the ^{13}CO from Nobeyama + CARMA observations (Tanabe et al., 2019). Figure 5.4 presents the data used in the DCF estimate of B_{POS}: the NIKA2-Pol high-quality data (left panel), the column density map used to calculate the volume density in each part of the OMC-1 filament (middle panel from schuller2021), the 1D velocity dispersion from Nobeyama + CARMA at 8″ resolution (right panel).

Nbr of ind. measurements (each half-beam)	Polarization angle dispersion (σ_θ)	1D velocity dispersion (σ_V)	Column density N$_{H_2}$ (10^{22}cm^{-2})	Volume density n$_{H_2}$ (10^4cm^{-3})	B-field strength B$_{POS}$(mG)	μ_ϕ
1319	19	1.4	2.8	9.5	0.4	0.5
1051	20	1.2	5.2	17.6	0.5	0.8
1006	24	1.2	12.9	43.2	0.7	1.4
213	13	1.2	31.3	104.3	2.0	1.2

Table 5.1: Table of the parameters used in the DCF estimate, the B_{POS} strength results and the mass to flux ratio associated to each sub-region of the OMC-1 filament. Values in colors are indicating parameters and results for a given region in same color in Fig. 5.5.

In order to have a reliable estimation of the B_{POS} strength, I divided the OMC-1 region into several column density regions. The polarization angle dispersion in OMC-1 varies depending on the location where it is computed. The B-field in the central part of the OMC-1 ridge (red vectors in figure 5.3) tends to be perpendicular to the filament, and the angle dispersion σ_θ is 13°. The B-field lines in the envelope of the central ridge in OMC-1 are more perturbed than in the other parts (orange vectors in Fig. 5.3), where σ_θ is about 24°. The polarization angle dispersion in all of the sub-regions is less than 25° (within the validity regime of the DCF method).
Using these values, I found that the B-field strength in OMC-1 filament varies from 0.4 mG to 2 mG from the low-density to the high-density region (see Table 5.1 and Fig. 5.5). These results are in good agreement with previously published estimates of the B-field strength in this region, which indicated a field strength ranging from a few hundred μG to a few mG (6.6 mG with SCUBA-POL2 (Pattle et al., 2017a), $\sim$ 2 mG at the Orion-KL position to a few hundred μG in the vicinity of Orion-Kl obtained with SOFIA/HAWC+ (Guerra et al., 2021)). See section 5.2.2 for more information about previous B-field strength estimates in the OMC-1 region.

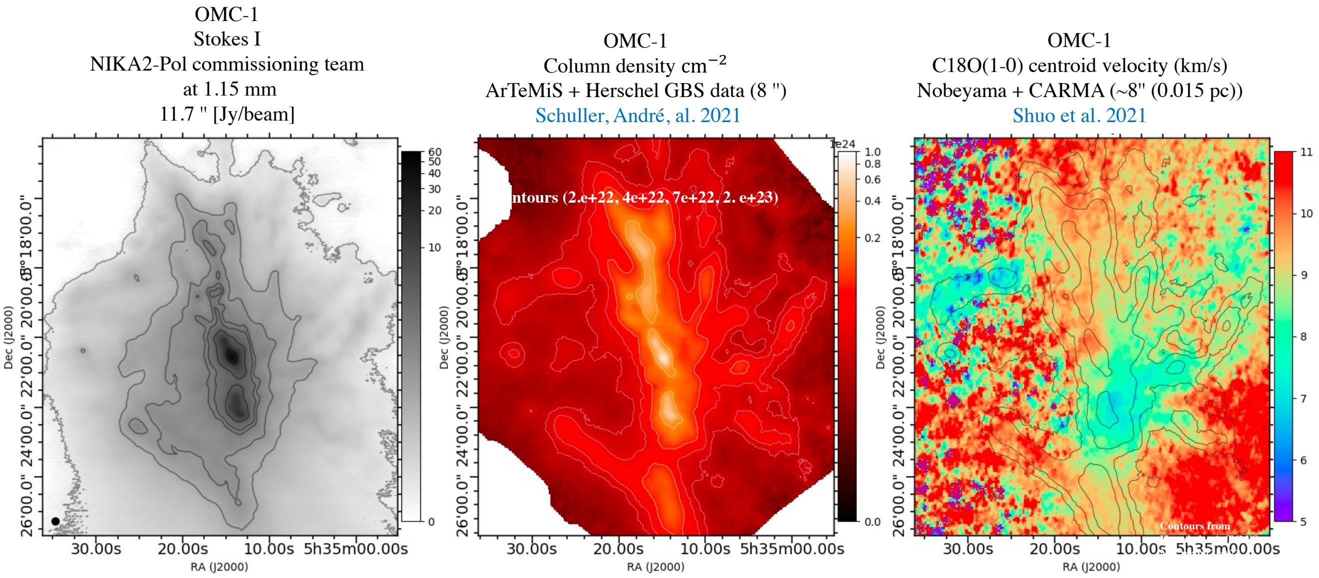
OMC-1
Stokes I
NIKA2-Pol commissioning team
at 1.15 mm
11.7 " [Jy/beam]

OMC-1
Column density cm^{-2}
ArTeMiS + Herschel GBS data (8 ")
Schuller, André, al. 2021

OMC-1
C18O(1-0) centroid velocity (km/s)
Nobeyama + CARMA (~8" (0.015 pc))
Shuo et al. 2021

Figure 5.4: Different data were used for the DCF estimate in the OMC-1 region. Left: High angular resolution polarization (11.7″) data from NIKA2-Pol commissioning (from November campaign). Middle panel : Column density map from combined ArTeMiS and Herschel GBS data at 8″ angular resolution (Schuller et al., 2021). Right: 1D velocity dispersion obtained from C^{18}O molecular data from the combined Nobeyama and CARMA data at 8″ angular resolution (Tanabe et al., 2019).

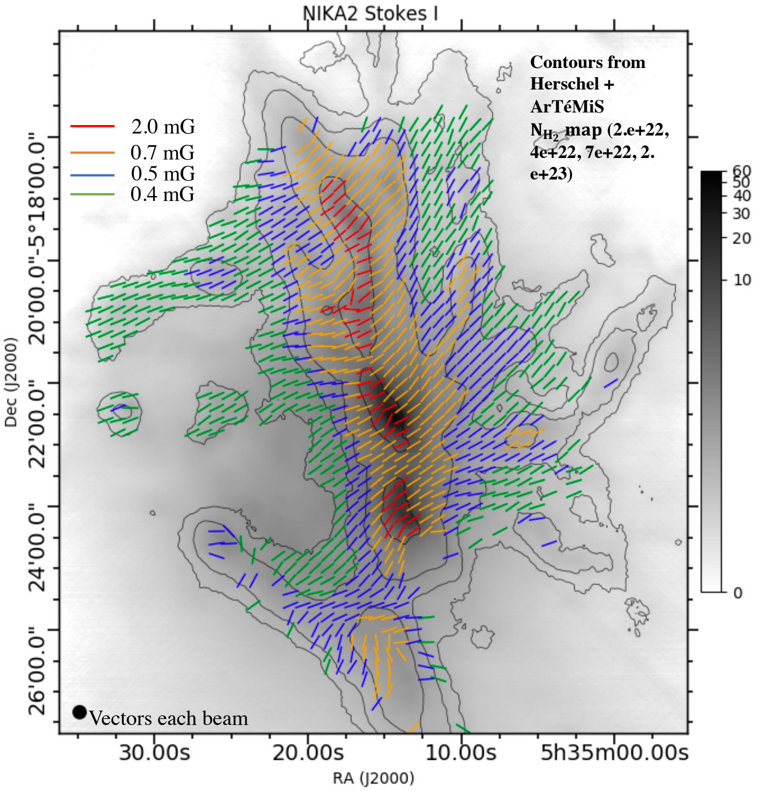

Figure 5.5: Stokes I map overlaid with B-field vectors from NIKA2-Pol commissioning data. Different colors indicate the vectors used in the DCF estimate of the B_{POS} strength.

5.4 Summary

Dust polarization observations using high angular resolution (11.7 arcsec) provided by NIKA2-Pol at 1.15 mm wavelength have revealed new finding toward the OMC-1 filament. The NIKA2-Pol data showed the evidence of local pinching of the B-field lines in the form of hourglass pattern centered at the position Orion-KL in the OMC-1 filament. In addition to the larger-scale hourglass already seen by other instruments such as Pol2.

These data probe the ability of NIKA2-Pol to provide high quality polarization data for scientific purpose. Using the NIKA2-Pol commissioning data toward the OMC-1 led to new possible finding and also confirmed the previous results in this region. These geometry of B-fields in the vicinity of Orion-KL suggest a new local hourglass which can be interpreted as a multi-collapse process in this filament.

I present the first attempts to estimate magnetic fields strength using the DCF method and I found similar value to what is previously published with POL2 and SOFIA/HAWC+. Although, the DCF estimates are limited and especially in high-mass star-forming region. In the case of OMC-1 filament, the magnetic fields distribution have an hourglass pattern that can be used to estimate the field strength. To compare these results of B-field strengths in the OMC-1 filament with other methods, my up coming work will concentrate on estimating the B-field strength using the force equilibrium method (Girart et al., 2006; Koch et al., 2012; Ewertowski & Basu, 2013; Bino & Basu, 2021; Bino et al., 2022). NIKA2-Pol commissioning makes possible to advance our understanding of the B-field morphology in star-forming filaments and dense cores and will give an impulse to start soon IRAM 30m large program B-FUN.

5.5 Proceeding paper II (refereed) : Probing the role of magnetic fields in star-forming filamtents: NIKA2-Pol commissioning results toward OMC-1

Probing the role of magnetic fields in star-forming filaments: NIKA2-Pol commissioning results toward OMC-1

H. Ajeddig[1,*], *R.* Adam[2], *P.* Ade[3], *P.* André[1], *E.* Artis[4], *H.* Aussel[1], *A.* Beelen[5], *A.* Benoît[6], *S.* Berta[7], *L.* Bing[8], *O.* Bourrion[4], *M.* Calvo[6], *A.* Catalano[4], *M.* De Petris[9], *F.-X.* Désert[10], *S.* Doyle[3], *E. F. C.* Driessen[7], *A.* Gomez[11], *J.* Goupy[6], *F.* Kéruzoré[4], *C.* Kramer[12], *B.* Ladjelate[12], *G.* Lagache[8], *S.* Leclercq[7], *J.-F.* Lestrade[13], *J.-F.* Macías-Pérez[4], *A.* Maury[1], *P.* Mauskopf[3,14], *F.* Mayet[4], *A.* Monfardini[6], *M.* Muñoz-Echeverría[4], *L.* Perotto[4], *G.* Pisano[3], *N.* Ponthieu[10], *V.* Revéret[1], *A. J.* Rigby[3], *A.* Ritacco[5,15], *C.* Romero[16], *H.* Roussel[17], *F.* Ruppin[18], *K.* Schuster[7], *S.* Shu[19], *A.* Sievers[12], *C.* Tucker[3], and *R.* Zylka[7]

[1] AIM, CEA, CNRS, Université Paris-Saclay, Université Paris Diderot, Sorbonne Paris Cité, 91191 Gif-sur-Yvette, France
[2] LLR (Laboratoire Leprince-Ringuet), CNRS, École Polytechnique, Institut Polytechnique de Paris, Palaiseau, France
[3] School of Physics and Astronomy, Cardiff University, Queen's Buildings, The Parade, Cardiff, CF24 3AA, UK
[4] Univ. Grenoble Alpes, CNRS, Grenoble INP, LPSC-IN2P3, 53, avenue des Martyrs, 38000 Grenoble, France
[5] Institut d'Astrophysique Spatiale (IAS), CNRS, Université Paris Sud, Orsay, France
[6] Institut Néel, CNRS, Université Grenoble Alpes, France
[7] Institut de RadioAstronomie Millimétrique (IRAM), Grenoble, France
[8] Aix Marseille Univ, CNRS, CNES, LAM (Laboratoire d'Astrophysique de Marseille), Marseille, France
[9] Dipartimento di Fisica, Sapienza Università di Roma, Piazzale Aldo Moro 5, I-00185 Roma, Italy
[10] Univ. Grenoble Alpes, CNRS, IPAG, 38000 Grenoble, France
[11] Centro de Astrobiología (CSIC-INTA), Torrejón de Ardoz, 28850 Madrid, Spain
[12] Instituto de Radioastronomía Milimétrica (IRAM), Granada, Spain
[13] LERMA, Observatoire de Paris, PSL Research University, CNRS, Sorbonne Université, UPMC, 75014 Paris, France
[14] School of Earth and Space Exploration and Department of Physics, Arizona State University, Tempe, AZ 85287, USA
[15] Laboratoire de Physique de l'École Normale Supérieure, ENS, PSL Research University, CNRS, Sorbonne Université, Université de Paris, 75005 Paris, France
[16] Department of Physics and Astronomy, University of Pennsylvania, 209 South 33rd Street, Philadelphia, PA, 19104, USA
[17] Institut d'Astrophysique de Paris, CNRS (UMR7095), 98 bis boulevard Arago, 75014 Paris, France
[18] Kavli Institute for Astrophysics and Space Research, Massachusetts Institute of Technology, Cambridge, MA 02139, USA
[19] Caltech, Pasadena, CA 91125, USA

Abstract. Dust polarization observations are a powerful, practical tool to probe the geometry (and to some extent, the strength) of magnetic fields in star-forming regions. In particular, Planck polarization data have revealed the importance of magnetic fields on large scales in molecular clouds. However, due to in-

---

[*] e-mail: hamza.ajeddig@cea.fr

sufficient resolution, Planck observations are unable to constrain the B-field geometry on prestellar and protostellar scales. The high angular resolution of 11.7 arcsec provided by NIKA2-Pol 1.15 mm polarimetric imaging, corresponding to 0.02 pc at the distance of the Orion molecular cloud (OMC), makes it possible to advance our understanding of the B-field morphology in star-forming filaments and dense cores (IRAM 30m large program B-FUN). The commissioning of the NIKA2-Pol instrument has led to several challenging issues, in particular, the instrumental polarization or intensity-to-polarization "leakage" effect. In the present paper, we illustrate how this effect can be corrected for, leading to reliable exploitable data in a structured, extended source such as OMC-1. We present a statistical comparison between NIKA2-Pol and SCUBA2-Pol2 results in the OMC-1 region. We also present tentative evidence of local pinching of the B-field lines near Orion-KL, in the form of a new small-scale hourglass pattern, in addition to the larger-scale hourglass already seen by other instruments such as Pol2.

1 Introduction

Observations of nearby molecular clouds by the *Herschel Gould Belt Survey* have shown the crucial role of filaments in the star formation process [3, 4], but the detailed fragmentation manner of star-forming filaments remains under debate. In parallel to *Herschel*, dust polarization observations from the *Planck satellite* have highlighted the role of magnetic fields in interstellar clouds [14, 15]. The magnetic field inferred from *Planck* polarization observations appears to have a regular, structured geometry on large scales (>> 0.1 pc), suggesting it is dynamically important. Stars form inside molecular filaments characterized by a common inner width of ~0.1 pc [7] and the angular resolution of *Planck* is insufficient to probe the geometry of the B-field in the <0.1 pc interior of such filaments. The IRAM 30m large program B-FUN will perform high-resolution polarization observations of a broad sample of nearby star-forming filaments imaged by *Herschel* [3], in an effort to improve our understanding of the role of magnetic fields in core/star formation along filaments. It is important to characterize the B-field at different wavelengths and high angular resolution to understand how it is involved in the star formation process [5, 8, 13].

NIKA2-Pol, the polarization channel of the NIKA2 camera [1] on the IRAM 30m telescope (Pico Veleta, Spain), is under commissioning and will provide 1.15 mm continuum polarization observations with high angular resolution (11.7 arcsec). Polarimetric imaging observations are challenging due, in particular, to the intensity-to-polarization leakage (hereafter "leakage"), which needs to be characterized and corrected for before proper scientific observations can be made. Qualitatively, the leakage affecting NIKA2-Pol data has the shape of a cloverleaf with a central positive lobe surrounded by a negative quadrupolar pattern [2]. The leakage effect can be characterized by observing a strong unpolarized point-like source such as the planet Uranus, and then subtracted from the Stokes Q, U data using a “deconvolution” technique described in detail in [6, 18, 24]. A similar instrumental polarization effect is also present in the case of other polarimeters such as XPOL, SCUBA2-POL2, and NIKA1 [10, 17, 24].

Here, we report on the results of NIKA2-Pol commissioning observations of Orion OMC-1 that were used to characterize the leakage effect in an extended source. OMC-1 is a well documented source that has been observed by all polarimetric instruments (see, e.g., Sect. 4 below). As part of our attempts to finalize the NIKA2-Pol commissioning, we discuss the leakage effect in OMC-1 and compare our polarization findings with recently published data (here from SCUBA2-POL2 [23]). As OMC-1 is one of the targets of the B-FUN large program, we also present a preliminary scientific analysis of the results (see Sect. 4), illustrating the great potential of NIKA2-Pol.

2 Correcting NIKA2-Pol data for instrumental polarization

To test the repeatability of NIKA2-Pol results, OMC-1 was observed on several nights and under good weather conditions in Nov. 2020. Figure 1 shows the difference between data taken on Nov. 12 and 15, 2020 before and after leakage correction, in panels a) and b), respectively. On the same night, the leakage pattern was observed on Uranus under similar conditions of focus and elevation, which guarantee an optimal correction of instrumental polarization (IP). Without IP correction, the OMC-1 polarization data taken on different days are in good agreement (e.g., with a root mean square difference in polarization angles of < 3°), except at the location of the compact source Orion-KL, which is strong in Stokes I but weakly polarized ($P \sim 1\%$), and thus more strongly affected by IP. Prior to IP correction, a very significant difference in polarization angles (~ 50°) is observed near Orion-KL between data sets taken on two different nights (see Fig. 1b). Indeed, the impact of IP is more pronounced in areas of the sky where the signal in Stokes I is strong and structured on small angular scales rather than extended and slowly varying. After subtracting the IP estimated using Uranus data observed before OMC-1, however, the polarization data from different nights agree well with each other, with a maximum difference in polarization angles reduced to < 20° near Orion-KL (see Fig. 1c) and ≤ 2° outside of Orion-KL. This analysis illustrates the ability of NIKA2-Pol to provide robust (repeatable), high-quality polarization maps for scientific purposes (see Fig. 3a below).

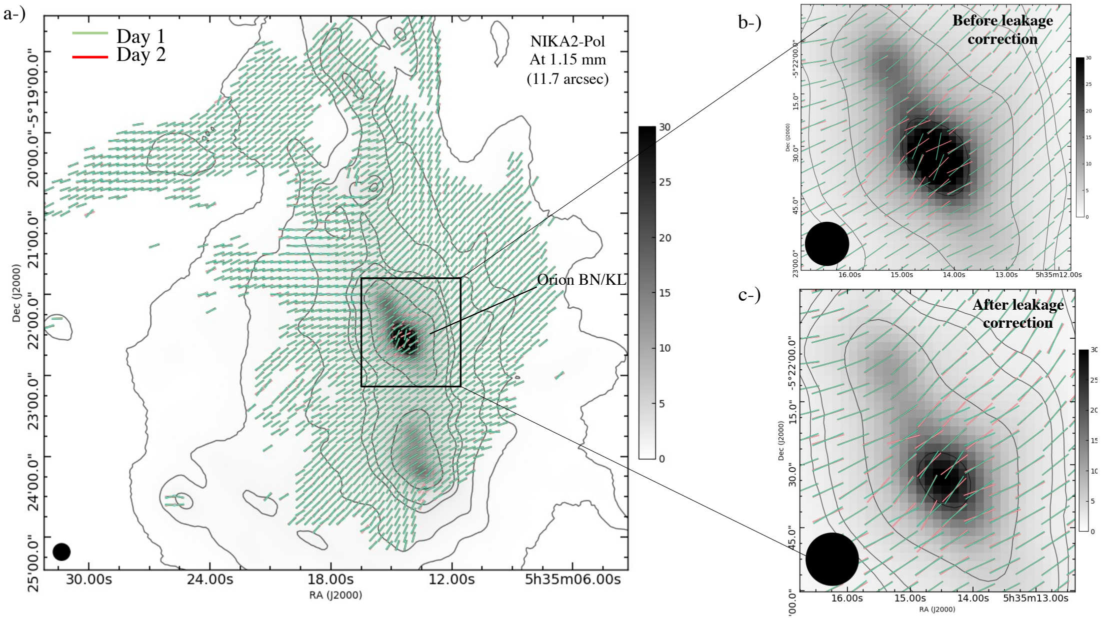

Figure 1. (*a*): B-field vectors from NIKA2-Pol polarization data at positions of significant detections in polarized intensity (i.e., $I_{pol}/\sigma_{I_{pol}}$ >3) on two different days, day 1 and day 2, corresponding to the green and red colors, respectively. (*b*): Closeup view of the vicinity of Orion-KL position overlaid with B-field vectors before correcting for instrumental polarization. (*c*) similar to panel *b* but after correcting for instrumental polarization.

3 Comparison of NIKA2-POL vs SCUBA2-POL2 results

In order to compare NIKA2-Pol polarization observations at 1.15 mm with published SCUBA2-POL2 data at 850 μm [23], we re-projected the POL2 and NIKA2-Pol data to the same grid, and smoothed the NIKA2-Pol data to the POL2 angular resolution (14 arcsec). Figure 2a shows B-field angle vectors from POL2 (in blue) and NIKA2-Pol (in gray) data, which trace a large-scale hourglass in both cases. Where the signal-to-noise ratio in polarized intensity is high ($I_{pol}/\sigma_{I_{pol}}$ >14) for both instruments, the NIKA2-Pol and POL2 data are in excellent agreement, within a typical 1° uncertainty (standard deviation of the mean difference in polarization angles – see Fig. 2*b*). This result has been confirmed using three independent data sets from the NIKA2-Pol commissioning campaigns of December 2018, February 2020, and November 2020.

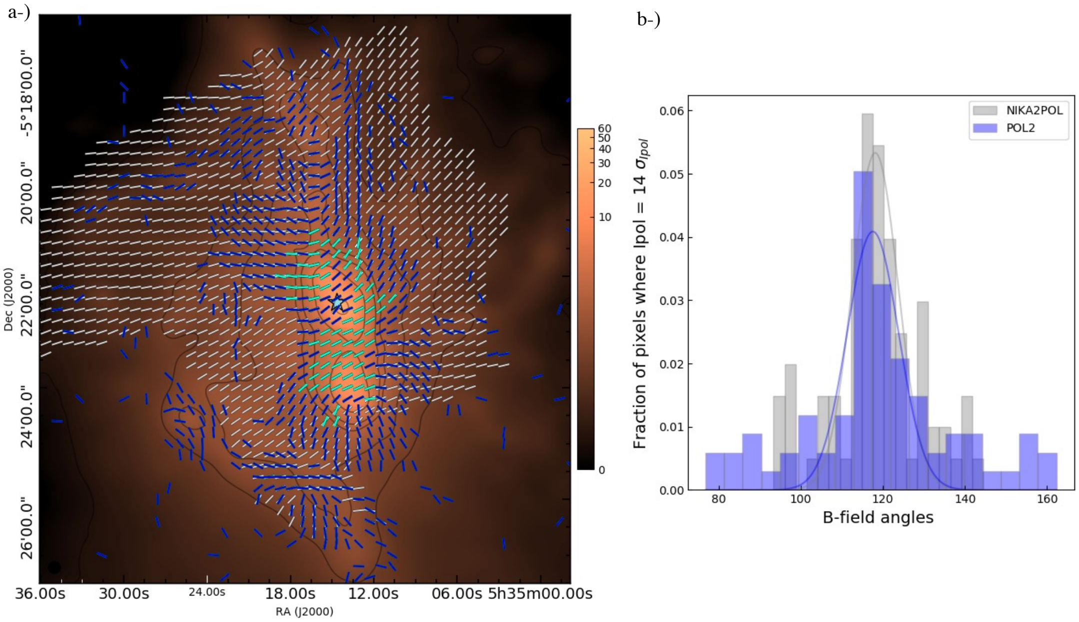

Figure 2. Comparison between NIKA2-Pol and POL2 polarization data in the OMC-1 region. *a-)*: NIKA2-Pol Stokes I image at 1.15 mm, with overlaid magnetic field vectors inferred from polarization data from both NIKA2-Pol (gray segments) and POL2 instruments (blue), respectively. The green star is the Orion-KL position. Panel *b-)*: Histogram distribution of B-field position angles for high signal-to-noise ratio in polarized intensity ($I_{pol}/\sigma_{I_{pol}}$ >14 corresponding to cyan B-field vectors in panel a) for both NIKA2-Pol and POL2 data.

4 A possible new local hourglass at the Orion-KL position

The magnetic field line geometry in OMC-1 has been under investigation for more than two decades. Schleuning (1998) [19] reported an hourglass shape of the B-field geometry based on a $8' \times 8'$ mapping of OMC-1 at 100 μm and 35 arcsec resolution. More recent submillimeter polarization observations with the SOFIA/HAWC+ (214 μm), SCUBA2-POL2 (850 μm) and POLKA (870 μm) polarimeters [9, 10, 20] have confirmed this large-scale hourglass B-field geometry in OMC-1 and the weak polarization fraction around Orion-KL (~1–2%). In particular, based on their SCUBA-POL2 study, Pattle et al. (2019) [13] proposed a scenario in which the evolution of the OMC-1 region is dynamically regulated by the magnetic field. In this scenario, the large-scale gravitational collapse of the OMC-1 region and/or a central

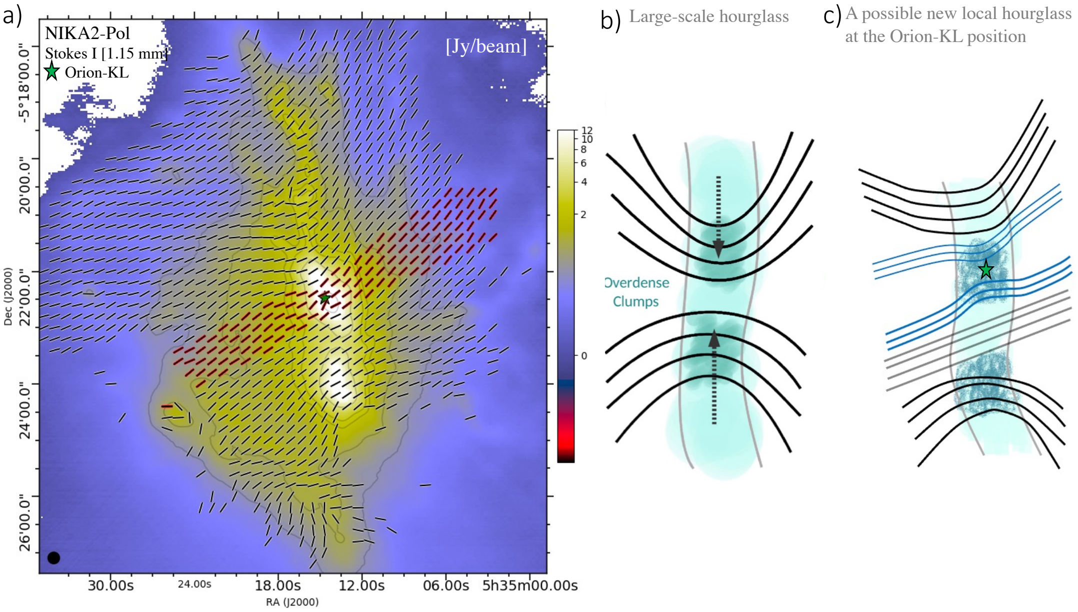

Figure 3. *a-)* Stokes I 1.15 mm map of OMC-1 region obtained from NIKA2-Pol polarization commissioning data, with magnetic field vectors at positions where $I_{pol}/\sigma_{I_{pol}} > 3$. The red vectors emphasize the possible new local hourglass revealed by NIKA2-Pol. *b)*: Illustration of the large-scale magnetic field as seen by POL2 from Pattle et al. (2019). *c)* Schematic illustration of the large-scale hourglass geometry as seen with NIKA2-Pol (in black lines) and the new possible local hourglass at the position of Orion-KL revealed by the high sensitivity and resolution of NIKA2-Pol (in blue lines).

explosive outflow are responsible for the large-scale hourglass.

At the Orion-KL position, however, the B-field geometry was unclear. For instance, Vaillancourt et al. (2008) [22] pointed out that B-field angles inferred at 350 μm and 450 μm differ by 25° and reported a drop in 450/350 μm polarization ratio by a factor of 2 toward Orion-KL. In addition, in their SHARP data, the B-field lines seemed to be distorted at the Orion-KL position (see Fig. 1 of [22]). Thanks to the high angular resolution and sensitivity provided by NIKA2-Pol at 1.15 mm, this distortion seems to be confirmed and even looks like another hourglass, on smaller scales, centered on Orion KL, which is suggestive of local gravitational collapse at this location (see Fig. 3a). The large-scale hourglass observed earlier is sketched in Fig. 3b from [13], while the possible new local hourglass revealed by the NIKA2-Pol polarization data is shown and contrasted with the other hourglass in Fig. 3c.

5 Concluding remarks

The NIKA2-Pol commissioning data have led to a better characterization of the reliability of the NIKA2 instrument in polarization mode. In this paper, we showed how NIKA2-Pol observations taken toward a region with extended and structured emission such as Orion OMC-1 can be corrected for instrumental polarization in practice. We achieved consistency between NIKA2-Pol data taken two years apart and also with independent observations from POL2. The NIKA2-Pol observations confirm the presence of a large-scale hourglass pattern seen by previous polarimeters in OMC-1. In addition, the NIKA2-Pol data reveal a possible new local hourglass centered at the Orion-KL position. The NIKA2-Pol commissioning results obtained on OMC-1 are very promising and suggest that high-quality scientific data will be obtained as part of the IRAM 30m large program B-FUN.

Acknowledgements

We would like to thank the IRAM staff for their support during the campaigns. The NIKA2 dilution cryostat has been designed and built at the Institut Néel. In particular, we acknowledge the crucial contribution of the Cryogenics Group, and in particular Gregory Garde, Henri Rodenas, Jean Paul Leggeri, Philippe Camus. This work has been partially funded by the Foundation Nanoscience Grenoble and the LabEx FOCUS ANR-11-LABX-0013. This work is supported by the French National Research Agency under the contracts "MKIDS", "NIKA" and ANR-15-CE31-0017 and in the framework of the "Investissements d'avenir" program (ANR-15-IDEX-02). This work has benefited from the support of the European Research Council Advanced Grant ORISTARS under the European Union's Seventh Framework Programme (Grant Agreement no. 291294). F.R. acknowledges financial supports provided by NASA through SAO Award Number SV2-82023 issued by the Chandra X-Ray Observatory Center, which is operated by the Smithsonian Astrophysical Observatory for and on behalf of NASA under contract NAS8-03060.

References

[1] Adam, R *et al.*, Astron. Astrophys. **609**, A115 (2018)

[2] Ajeddig, H *et al.*, EPJWC. **228**, 00002 (2020)

[3] André, Ph *et al.*, Astron. Astrophys. **518**, L102 (2010)

[4] André, Ph *et al.*, in *Protostars and Planets VI*, 27–51 (2014)

[5] André, Ph *et al.*, PASA. **36**, e029 (2019)

[6] Andrianasolo, Aina, http://www.theses.fr/2019GREAY077, (2019)

[7] Arzoumanian, D *et al.*, Astron. Astrophys. **529**, L6 (2011)

[8] Crutcher, R. M. 2012, , 50, 29. doi:10.1146/annurev-astro-081811-125514

[9] Dowell, C. D., HAWC+ Instrument Team, & HAWC+ Science Team 2018,

[10] Friberg, P *et al.*, Millimeter, Submillimeter, and Far-Infrared Detectors and Instrumentation for Astronomy IX **10708** 3M (2018)

[11] Houde, M., Dowell, C. D., Hildebrand, R. H., et al. 2004, , 604, 717. doi:10.1086/382067

[12] Gonatas, D. P., Engargiola, G. A., Hildebrand, R. H., et al. 1990, , 357, 132. doi:10.1086/168898

[13] Pattle, K. & Fissel, L. 2019, Frontiers in Astronomy and Space Sciences, 6, 15. doi:10.3389/fspas.2019.00015

[14] Planck Collaboration, Ade, P. A. R., Aghanim, N., et al. 2013, , 557, A53.

[15] Planck collaboration *et al.*, Astron. Astrophys. **594**, A1 (2016)

[16] Rao, R., Crutcher, R. M., Plambeck, R. L., et al. 1998, , 502, L75. doi:10.1086/311485

[17] Ritacco, A *et al.*, Astron. Astrophys. **599**, A34 (2017)

[18] Ritacco, A , http://www.theses.fr/2016GREAY018, (2016)

[19] Schleuning, D. A. 1998, , 493, 811. doi:10.1086/305139

[20] Siringo, G., Kreysa, E., Reichertz, L. A., et al. 2004, The Magnetized Interstellar Medium, 215

[21] Thum, C *et al.*, PASP. **120**, 777–790 (2008)

[22] Vaillancourt, J. E., Dowell, C. D., Hildebrand, R. H., et al. 2008, , 679, L25. doi:10.1086/589152

[23] Ward-Thompson, D., Pattle, K., Bastien, P., et al. 2017, , 842, 66. doi:10.3847/1538-4357/aa70a0

[24] Wiesemeyer, H *et al.*, PASP. **126**, 1027 (2014)

Chapter 6

Revealing the magnetic field properties of star-forming filament in Taurus with SOFIA/HAWC+ polarization observations at 214 um

Li, P.; Enrique Lopez-Rodriguez; **Hamza Ajeddig**; Philippe André et al. 2021, MNRAS.tmp.
doi:10.1093/mnras/stab3448 **Accepted**

Contents

Molecular filaments are known to present highly complex structures over different scales. A clue to understanding the star formation process in the ISM comes from connecting small scale (less than 0.01 pc) to large scale-structure in filaments (1 - 2 pc). Filamentary structures have been studied with the *Herschel* Space Observatory and these studies emphasized the crucial role of filaments in the star formation process (André et al., 2010, 2014). Dust emission and molecular line observations show that only self-gravitating trans-critical or supercritical filaments with $M_{line} \geq M^{the}_{line,crit}/2$ (where $M_{line,crit} \sim 16\ M_{\odot}\ \ pc^{-1}$ for an isothermal cylindrical filament) can form stars (Hacar et al., 2013; Könyves et al., 2015). Moreover, the core mass function (CMF) over a sample of filaments observed in Herschel Gould Belt Survey (HGBS) appears to have a similar shape as the observed initial mass function (IMF) (André et al., 2010; Könyves et al., 2015; Marsh et al., 2016). A attractive scenario of star formation is the "filament paradigm" in which the large scale compressions of magnetohydrodynamic turbulence (MHD) forms a quasi-universal web of ∼0.1 pc broad filamentary structures which fragment to cores under gravitational instability (André et al., 2014; Arzoumanian et al., 2019). Observations of the cold ISM suggest that the fragmentation of self-gravitating molecular filaments may explain the formation process of solar-type stars. However, this process is still not straightforward and cannot explain in details the core mass function/initial mass function (CMF/IMF), the angular momentum of cores, and core properties. Nevertheless, the detailed role of magnetic fields in star formation remains unclear. Dust polarization observations revealed emphasized the role of the B-field in molecular clouds (Heiles et al., 1993; Crutcher, 2012).

Recent dust polarization observations from the Planck telescope revealed the large structure of B-fields in the Galactic ISM. These observations showed a regular morphology of the B-field at a large scale, which tends to be parallel to low-density filamentary structures and perpendicular to high-density filaments (Planck Collaboration et al., 2016a,b,c). The angular resolution and sensitivity of Planck polarization data were unable to provide information of the B-field geometry in the $\sim$ 0.1 pc interior of filaments (less than 0.1 pc) where prestellar cores and protostars form. Thus, from Planck data, the B-field appears to regulate the formation of large-scale filamentary structures, but the manner in which the B-field is organized at core scales and the detailed role of B-fields in filament fragmentation are still unclear. Inferring the B-field geometry from dust polarization at different wavelengths and various scales can help in understanding its role in star formation (Crutcher, 2012; Pattle & Fissel, 2019; Siringo et al., 2004b).

This chapter presents our main results from SOFIA/HAWC+ and IRAM 30m observations of the B211 filament located in the Taurus molecular cloud. Section 6.1 presents the B211 filament in Taurus and why it is a good target for this project. The following sections present the dust polarization observations and analysis toward B211 filament using SOFIA/HAWC+ and the IRAM 30m telescope. We also present our estimation of the B-field strength in this region using the Davis-Chandrasekhar-Fermi method (DCF).

6.1 The B211 filament in the Taurus molecular cloud

The L1495 dark cloud also known as "Barnard's Cloud" was discovered in 1907 (Barnard, 1907). It presents a complex velocity structure in the Taurus molecular cloud at d$\approx$ 140 pc (Duvert et al., 1986). The B211 filament corresponds to a dense portion within L1495 dark cloud and hosts starless dense cores, which makes it an excellent target to study the early stages of star formation (Tafalla et al., 2002). Dust emission observations at near-infrared wavelengths show highly fragmented sub-structures inside L1495/B211. Young stellar objects were detected in this filament with a total mass of about (84 ± 5) $M_\odot$ (Schmalzl et al., 2010). The critical factor in the star formation process has been under debate for decades: Whether ISM turbulence, magnetic fields or a combination of both (Myers et al., 1986; Mouschovias, 1976; Crutcher, 2012). Dust polarization observations showed the importance of the B-field in regulating the mass growth and star formation in the Taurus L1495 region. The B-field lines infered from the polarization observations at near-infrared wavelengths tend to be parallel to the striations detected by Goldsmith et al. (2008), showing the importance of the magnetic field in the evolution of this filament and star formation (Moneti et al., 1984; Goodman et al., 1992; Chapman et al., 2011; Planck Collaboration et al., 2016a,b,c). Herschel Gould Belt observations revealed the detailed structure of the B211 filament and its environment with the presence of low-density striations perpendicular to the main the filament of Taurus and aligned along the field lines (Palmeirim et al., 2013; Marsh et al., 2016). The B211 filament also represents an excellent target to study the nature of multiple velocity components present in early stage star-forming filaments. Hacar et al. (2013) found evidence of fiber-like velocity components in B211, which shows the complex velocity structure of this filament.

6.2 Polarization observations with the SOFIA/HAWC+ polarimeter

Dust polarization observations were caried out using the HAWC+ polarimeter (Dowell et al., 2010) at 214 μm wavelength aboard SOFIA 2.7 m telescope (ID: 07 0017, PI: Li, P.S.) . The field of view (FoV) of HAWC+ covers 4.2×6.2 arcmin^2 and scans simultaneously two orthogonal components of linear polarization with a 32 x 40 array of detectors. The HAWC+ beam size (FWHM) is 18.2 arcsec at 214 μm (Harper et al., 2018). Observations were made using the On-The-Fly (OTF) mode, which consists of four Lissajous scans with different Half-Wave-Plate (HWP) positions in each scan. This observation technique is still being tested for polarimetry, although it was already successfully employed in the case of galaxy Centaurus A (Lopez-Rodriguez et al., 2018; Lopez-Rodriguez, 2021).

6.2.1 Observations and data reduction

To reduce overheads in HAWC+ observations, the OTFMAP mode was adopted instead of the chop-node mode. Using this observing mode, the overheads were reduced from 2.2 in the chop-node technique to 1.1 in the OTFMAP mode. Polarimetric observations with HAWC+ using the OTFMAP mode allow reasonable estimation of the background and reduce observing overheads by integrating the source and the off-source in the FoV. The CRUSH software was used to reduce all scans to estimate the correlated atmospheric effect and instrumental signals, determining the detector gains and the noise weighting of the time streams in an iterated pipeline scheme. Each reduced scan produces two images associated with each array.

At a given HWP position angle, CRUSH produces two images for each scan associated with orthogonal components of linear polarization in each array. Stokes parameters (I, Q, and U) are measured by a double-difference method similar to that used in standard chop-nod HAWC+ observations (Harper et al., 2018). To estimate the instrumental polarization (IP) at 214 um with HAWC+, OTFMAP polarization observations of planets were used. The IP level in Stokes Q and U are estimated to be about $Q/I = -1.0\%$ and $U/I = -1.4\%$ at 214 μm, respectively, with an estimated uncertainty of 0.8%. The IP level using the OTFMAP mode is similar to what was estimated using chop-nod observations. To ensure the correction of the position angle of the instrumental polarization depending on the sky, we took each set with a fixed line-of-sight (LOS) of the telescope. For each set, the Stokes Q and U were rotated from instrument to sky coordinates. The polarization fraction (P) was debiased (Wardle & Kronberg, 1974) and corrected by a polarization efficiency of 97.8% at 214 μm. The final Stokes I and its associated errors were calculated and down sampled to the beam size (18.2″). The final Stokes (Q; U) parameters, polarization fraction (P), polarization angle (PA), polarized intensity (PI), and their associated errors were calculated and re-sampled to a super-pixel corresponding to 3×3 detector pixels, equivalent to a re-sampled pixel size of 28″ (or 0.019 pc at the distance of the Taurus cloud). See the paper in the Appendix of this thesis for further debates.

6.2.2 Magnetic field line morphology

The morphology of the magnetic field in the plane of sky was inferred from the dust polarization data, considering only polarization measurements with $P/\sigma_P \geq 2$ (cf. Appendix of Wardle & Kronberg, 1974). Figure 6.1 shows the B-field vectors inferred from the HAWC+ polarization measurements after rotating the observed polarization vectors by 90° at 214 μm for the 1200″ × 1200 ″ region of L1495/B211 observed with SOFIA/HAWC+.

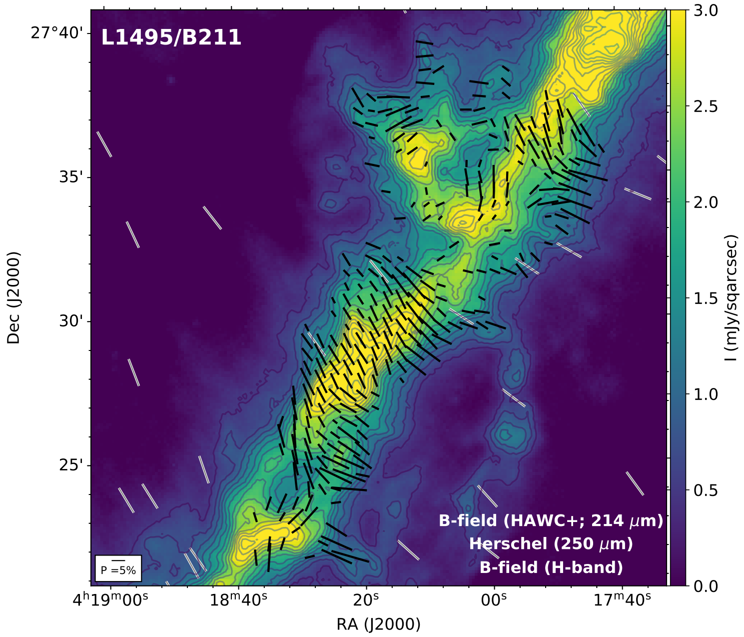

Figure 6.1: The magnetic field morphology as inferred from the 214 μm HAWC+ (black lines) and H-band (Chapman et al., 2011) observations (grey vectors) are overlaid on the Herschel 250 μm image (color-scale) of the Taurus/B211 studied with SOFIA/HAWC+ (figure from Li et al., 2021).

All polarization angles (PAs) used in this chapter have been rotated in this manner. The length of the vectors in the map is proportional to the polarization fraction, where a 5% polarization measurement is shown as a reference. The final 214 μm HAWC+ polarization measurements contain pixels with the following quality cuts: 1) pixels with a scan coverage $\geq$ 30% of all observations, 2) pixels which Stokes I measurements have an uncertainty $\geq 2.5\sigma_I$, where σ_I is the minimum uncertainty in Stokes I, 3) pixels with a surface brightness of $\geq$ 1 mJy/sqarcsec, 4) pixels with $P \leq 30\%$ given by the maximum polarized emission found by *Planck* observations (Planck Collaboration et al., 2016a,b,c), and 5) polarization measurements with $P/\sigma_P \geq 2$. We find that 14% (40 out of 282) of the measurements are within $2 \leq P/\sigma_P \leq 3$. The magnetic field orientations derived from the near-infrared H-band observations of Chapman et al. (2011) have been overlaid in Fig. 6.1.
Note that the inferred magnetic field from the H-band arises from dichroic absorption, while the SOFIA/HAWC+ 214 μm measurements arise from dichroic emission. The mapping of the 0.82 pc region allowed the detection of multiple structures of the magnetic field inside the 2 pc long B211 filament from the HAWC+ polarization observations at smaller scales 56″ compared to the lower-resolution (10′) of Planck observations (see Fig. 6.2). We note that the magnetic field in the lower half of the observed area is more uniform and close to being perpendicular to the B211 filament axis. Based on the *Herschel* intensity map of the region (Palmeirim et al., 2013), this part of B211 appears to have two filamentary substructures crossing each other in an X-shaped appearance near RA of $4^{\mathrm{h}}18^{\mathrm{m}}20^{\mathrm{s}}$ and DEC of 27°29′. The two structures may be spatially nearby and appeared to be overlapped along the line-of-sight (LOS). The magnetic field could be a combined result of the overlapping projection. In the upper half, the magnetic field structure appears to be in a highly non-uniform chaotic state. It is consistent with the turbulent appearance of the underlying intensity map. The B-field inferred from SOFIA/HAWC+ data deviate very significantly from the uniform large-scale field direction indicated by Planck observations.

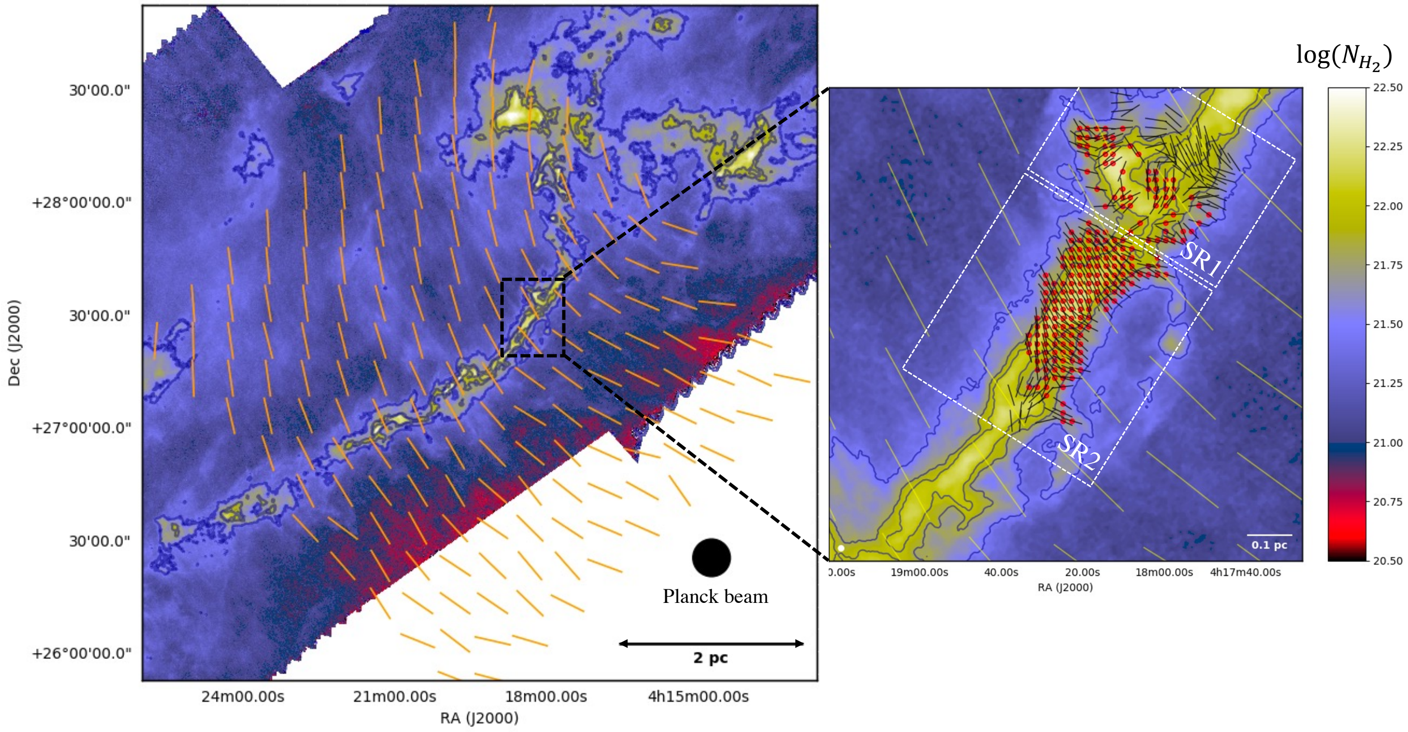

Figure 6.2: *Left: Herschel* column density map 18.2″ (from Herschel Gould Belt Survey (HGBS) data) with the magnetic field vectors derived from *Planck* polarization data at 10 resolution displayed in orange/yellow (and spaced every 10). Contours are 3×10^{21}, 6.7×10^{21}, and 10^{22} cm^{-2}. *Right:* Blow-up of the left image in the area mapped with SOFIA/HAWC+. Yellow vectors are from *Planck* and are here spaced by half a beam (5). Smaller black segments show the magnetic field vectors derived from HAWC+ at 28 resolution. The solid red circles mark positions where both significant HAWC+ polarization measurements and C^{18}O line data from the IRAM 30m telescope are available. The white dashed rectangles display the two sub-regions (SR1 and SR2) for which a DCF analysis has been carried out.

The *left* panel of Fig. 6.2 shows the column density map (from HGBS data) with magnetic field vectors derived from *Planck* polarization data at 10 resolution displayed in orange (and spaced every 10). Contours are 3×10^{21}, 6.7×10^{21}, and 10^{22} cm^{-2}. The black square shows the B211 filament region observed in IRAM 30m and SOFIA/HAWC+ telescopes. The *Right:* panel of Fig. 6.2 shows the B211 portion with separated sub-regions 1 and 2 (SR1 & SR2). Smaller black segments show the magnetic field vectors derived from HAWC+ at 56 resolution. The solid red circles mark positions where both significant HAWC+ polarization measurements and C^{18}O line data from the IRAM 30m telescope are available. The white dashed rectangles display the two sub-regions (SR1 & SR2) for which I carried out a DCF analysis.

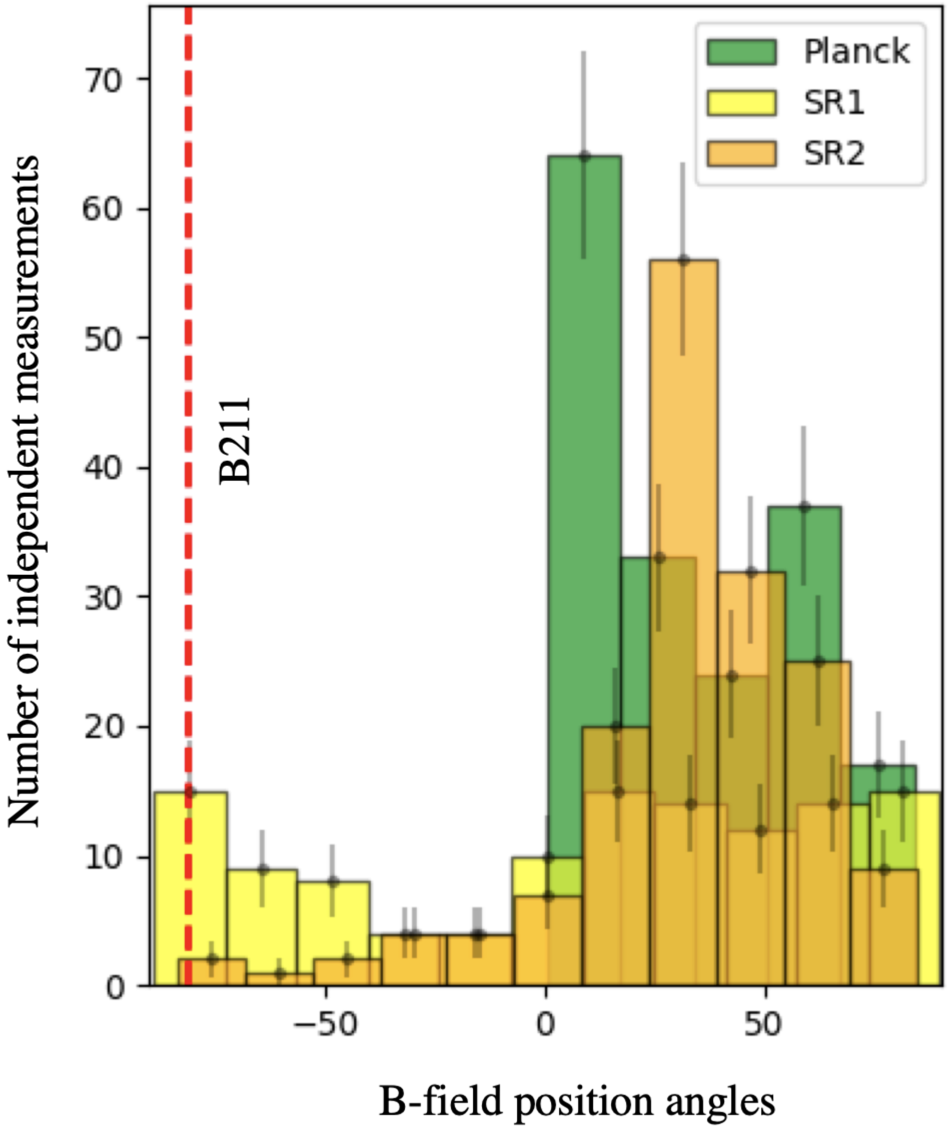

Figure 6.3: Histogram of all inferred magnetic field orientations from HAWC+ polarization observations of the B211 filament at resolution of ~ 56 arcsec shown in Fig. 6.2 for SR1 and SR2 (right panel) in yellow and orange colors, respectively. The green histogram shows the B-field angles inferred from Planck polarization observations of the entire Taurus/B211 region at resolution of 10 arcmin shown in Fig. 6.2 (left panel). The bin width of 16.4° is chosen to be larger than the measurement uncertainty of the PAs. The vertical dashed line indicates the orientation of the B211 filament at PA = −62° equivalent to +118° (Palmeirim et al., 2013).

Figure 6.3 shows the distribution of B-field angles in the sub-regions SR1 and SR2 observed by HAWC+ using only data with $P/\sigma_P > 2$, compared with the distribution of the large scale B-field from Planck polarization data (Planck Collaboration et al., 2016a,b,c). The peak of the B-field distribution in SR2 is near 30°, which is very close to the mean large-scale magnetic field orientation of $26° \pm 18°$ and perpendicular to $118° \pm 20°$ the B211 filament axis (Palmeirim et al., 2013). The B-field distribution in SR1, presented in yellow, changes from parallel to perpendicular to the filament axis. Our observations show that the B-field lines become more distorted and chaotic at small scales, especially in SR1. The histogram distributions in Fig 6.3 show the strong perturbation of the field lines at small scales compared to large scales. The dispersion of polarization angles (PA) from Planck data is about 37° taking into account all vectors shown in Fig 6.2 in orange. The resolution of the large-scale field map from Planck is ~ 0.4 pc, which is about 11 times the size of the super-pixel that was adopted for the HAWC+ results. A numerical simulation was used to discuss how the resolution of a polarization map can affect the interpretation of magnetic field structures. See the paper in the appendix.

6.3 Estimation of the magnetic field strength

In this project, I estimated the B-field strength in Taurus/B211 by applying the Davis-Chandrasakher-Fermi method to HAWC+ (Davis, 1951; Chandrasekhar & Fermi, 1953), IRAM 30m, and Herschel data. The IRAM 30m $C^{18}O$ data allowed to estimate the velocity dispersion in the same area as the HAWC+ observations. The dust polarization observations from HAWC+ were used to derive the dispersion of polarization angles. All the parameters and results used in this method are presented in Table 6.1. Due to the high polarization dispersion in the B211 map from HAWC+ data, I estimated the B-field strength in two different sub-regions, SR1, and SR2 (see Fig. 6.4).

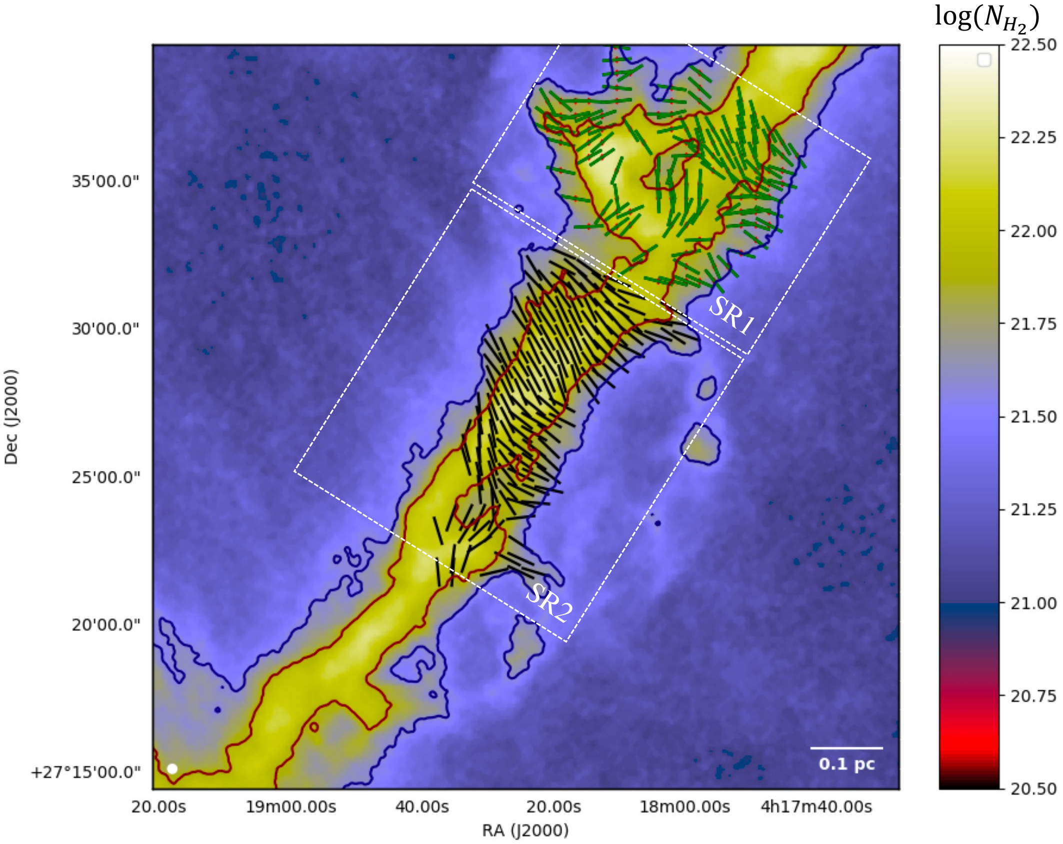

Figure 6.4: *Herschel* column density map (from HGBS data) with magnetic field vectors derived from HAWC+ measurements. SR1 and SR2 are marked by white boxes with their corresponding B-field angles, respectively. The length of the B-field vectors here is constant and were displayed only to show the data points used in the analysis of each sub-region.

6.3.1 The Davis-Chandrasekhar-Fermi (DCF) method

The Davis-Chandrasekhar-Fermi (DCF) method assumes that the observed dispersion in polarisation angles comes from perturbations of the B-field lines due to turbulent Alfvén waves in the medium. A second assumption is that the measured velocity dispersion along the line-of-sight (LOS) is similar to 1D velocity dispersion in the plane-of-sky (POS). Under these assumptions, the B-field strength in the plane-of-sky $B_{\rm POS}$ can be expressed as a function of the 1D velocity dispersion of the gas, $\sigma_V = {\rm FWHM}/(8\ln 2)^{1/2}$, the dispersion of observed polarization angles and the volume density. In this work, we used two different methods to infer the dispersion of polarization angles σ_θ. The first one followed the standard DCF approach, which assumes a constant direction for the mean magnetic field in the region of interest, and is valid only when σ_θ is small (less than 25 degrees). The standard DCF method can be expressed as follows :

$$B_{POS} = \xi\,\frac{(4\pi\rho)^{1/2}\sigma_V}{\sigma_\theta}, \tag{6.1}$$

where ξ is a correction factor coming from numerical simulation results and ρ is the gas mass density. Falceta-Gonçalves et al. (2008) extended the regime of DCF validity by approximating σ_θ to $\tan\sigma_\theta$ and Eq. 6.1 becomes :

$$B_{POS} = \xi\frac{(4\pi\rho)^{1/2}\sigma_V}{\tan\sigma_\theta} \tag{6.2}$$

Adopting a correction factor $\xi = 0.5$ from simulation results of Ostriker et al. (2001), and the Vaillancourt et al. (2008) approximation, the DCF expression for the mean POS field can be expressed in the following practical form :

$$B_{POS} = 0.383\sqrt{n(H_2)}\,\frac{\sigma_V}{\tan\sigma_\theta} \quad \mu{\rm G}, \tag{6.3}$$

where $n(H_2)$ is the number density of H_2 molecules in cm^{-3}, σ_V is measured in km s^{-1}, and σ_θ is the dispersion of the magnetic field orientations. Li et al. (2021) extended the validity regime of the DCF method to dispersion of polarization angles $\sigma_\theta < 45°$.

A second method of inferring the turbulent field strength from the spatial variation in polarization angles is the structure function method introduced by Hildebrand et al. (2009) and extended by Houde et al. (2009) and Houde et al. (2016). This method is more general since it allows for a smooth variation in the orientation of the mean magnetic field. The structure function is defined as

$$\langle\Delta\Phi(\ell)^2\rangle \equiv \frac{1}{N(\ell)}\sum_{i=1}^{N(\ell)}[\Phi(\mathbf{x}) - \Phi(\mathbf{x}+\boldsymbol{\ell})]^2, \tag{6.4}$$

where $\Phi(\mathbf{x})$ is the polarization angle at position $\mathbf{x}$, $\boldsymbol{\ell}$ is a displacement, and $N(\ell)$ is the number of polarization angle pairs with separation ℓ. As shown in Appendix A of the paper in the Appendix of the present thesis and in Chap. 2, on scales larger than the turbulent correlation length, δ, this is approximately

$$\langle\Delta\Phi(\ell)^2\rangle \simeq \frac{2\sigma_{\delta B}^2}{B_{\rm rms}^2} + m^2\ell^2, \tag{6.5}$$

where $m\ell$ measures the effect of large-scale variations in the mean field and we have made the small angle approximation ($< 25°$). (The more general result without this approximation is given in the paper) In order to infer the field dispersion, $\Delta\Phi(\ell)$ is extrapolated to $\ell = 0$, which gives $\Delta\Phi_0 = \sqrt{2}\sigma_{\delta B}/B_{\rm rms}$. Noting that $B_{\rm rms}^2 = B_{\rm POS}^2 + \sigma_{\delta B}^2$ and including the factor $\xi = 0.5$, equations (6.1) and (6.5) give

$$B_{\rm POS} = 0.383\,n(H_2)^{1/2}\sigma_V\,\frac{(2-\Delta\Phi_0^2)^{1/2}}{\Delta\Phi_0}. \tag{6.6}$$

More discussion on determination σ_θ and $\Delta\Phi_0$ is discussed in the paper. More explanations of this method are given in Chap. 2.

6.3.2 IRAM 30m $C^{18}O$ data and Velocity Dispersion

$C^{18}O$(1–0) mapping observations of a portion of the B211 field imaged with HAWC+ were carried out with the Eight MIxer Receiver (EMIR) receiver on the IRAM-30m telescope at Pico Veleta (Spain) in April 2016, as part of another project (Palmeirim et al. in preparation). At 109.8 GHz, the 30 m telescope has a beam size of ∼23 (HPBW), a forward efficiency of 94%, and a main beam efficiency of 78% [1]. As a backend, we used the VESPA autocorrelator, providing a frequency resolution of 20 kHz, which corresponds to a velocity resolution of ∼0.05 km s^{-1} at 110 GHz. The standard chopper wheel method[2] was used to convert the observed signal to the antenna temperature T_A^* in units of K, corrected for atmospheric attenuation. During the observations, the system noise temperatures ranged from ∼85 K to ∼670 K. The telescope pointing was checked every hour and found to be better than ∼3 throughout the run. Thanks to their high sensitivity, the IRAM 30m molecular line data highlight the kinematic complexity of the region mapped by HAWC+, and the presence of multiple velocity components. These multiple velocity components are consistent with the presence of filamentary substructures in this region, as discussed by Hacar et al. (2013). The variety of observed $C^{18}O(1–0)$ spectra is illustrated in Fig. 6.5, which shows clear changes in the number of velocity components and overall centroid velocity as a function of position within and around the B211 filament.

$C^{18}O(1–0)$ molecular line data trace the kinematics of the gas and can be used to estimate the level of non-thermal motions due to turbulence in the region. As the $C^{18}O(1–0)$ transition is usually optically thin, multiple peaks in the spectra, when present, likely trace the presence of independent velocity components as opposed to self-absorption effects. For better characterization of the different velocity peaks, I performed multiple Gaussian fits, which allowed me to identify the centroid position of each velocity component where multiple components are observed. Comparing all of the $C^{18}O(1–0)$ spectra observed in a given sub-region, I was able to identify a dominant velocity component[3] in each case.

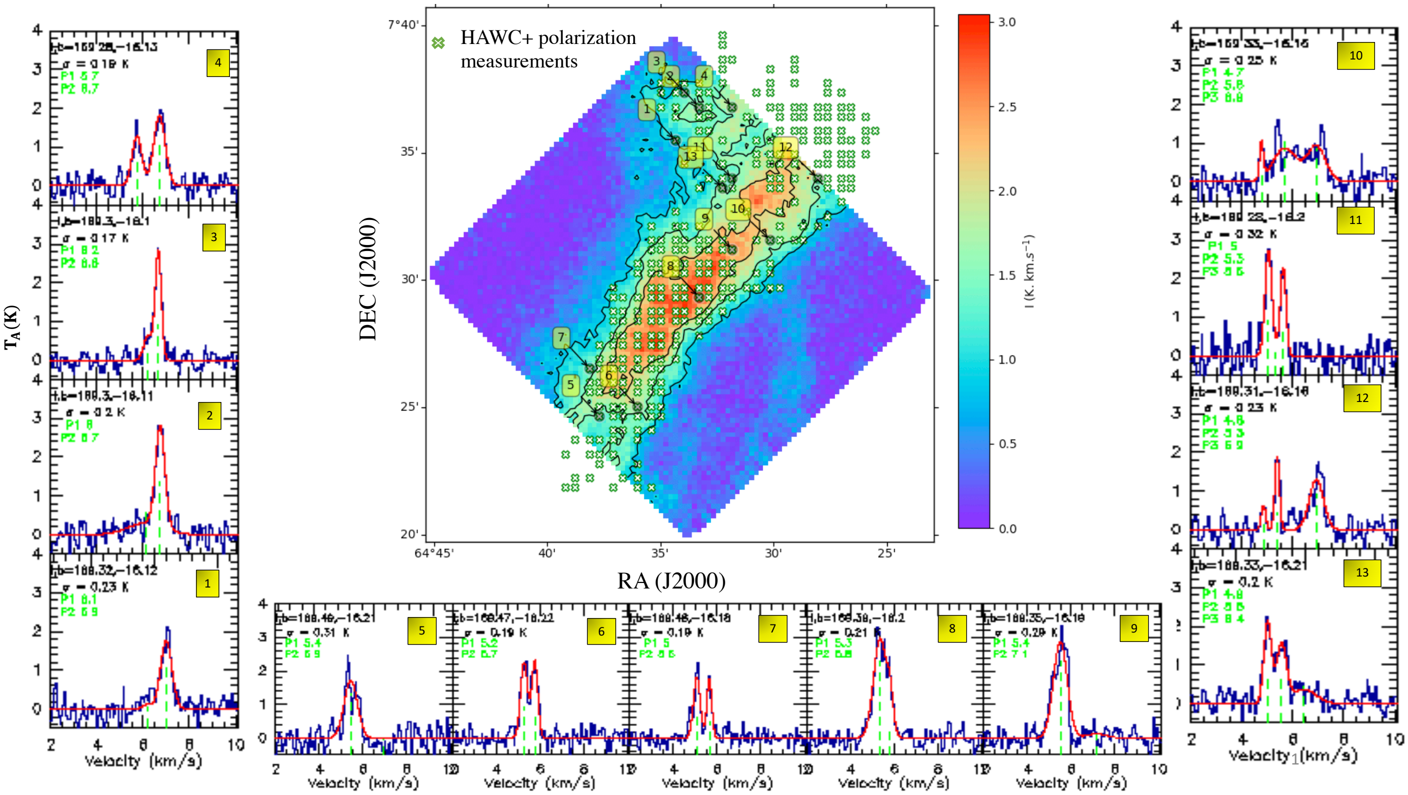

Figure 6.5: $C^{18}O(1–0)$ intensity map integrated over all channel velocities from 4.5 to 7 km.s^{-1}. The contours correspond to 30%, 50 %, and 70% of the maximum integrated intensity (3 K km s^{-1}). Markers (×) in green indicate positions where statistically significant polarization measurements were obtained with HAWC+. Representative $C^{18}O(1–0)$ spectra observed with the IRAM 30m telescope at selected positions in the field are shown to the left, bottom, and right of the map.

---

[1] http://www.iram.es/IRAMES/mainWiki/Iram30mEfficiencies

[2] Chopper wheel method used in IRAM-30m can be found at https://safe.nrao.edu/wiki/pub/KPAF/KfpaPipelineReview/kramer_1997_cali_rep.pdf

[3] Centroid velocity detected in all positions.

Table 6.1 provides the centroid velocity and the velocity dispersion considering either only the dominant velocity component or all velocity components in each sub-region. I only used the significant HAWC+ detection where $P/\sigma_P \geq 2$, where P represents the polarization degree (first row for each sub-region in Table 6.1). The centroid velocities of the relevant velocity components range from V_{LSR} =5.4 km.s^{-1} to V_{LSR} =5.9 km.s^{-1}, and the associated line-of-sight velocity dispersion range from σ_V ∼0.2 to ∼0.3 km.s^{-1} for the dominant components and from ∼0.4 to ∼0.5 km.s^{-1} if all velocity components are considered.

6.3.3 Polarization angle dispersion

The SOFIA HAWC+ polarization data reveal a strongly perturbed structure of the magnetic field in the B211 region. In this work, I estimated the dispersion in polarization angles using independent polarization measurements in two sub-regions of B211. Taking into account measurement errors in our polarization data, I estimated σ_θ as the weighted standard deviation σ_θ of polarization angles in each sub-region:

$$\sigma_\theta^2 = \frac{N}{N-1}\,\frac{1}{w}\sum_{i=1}^{N} w_i\,(\theta_i - \bar{\theta}_w)^2, \tag{6.7}$$

where N is number of independent measurements in each sub-region, $w_i = 1/\sigma_i^2$ the weight of measurement i given the measurement error in PA σ_i, $w = \sum\limits_{i=1}^{N} w_i$, and $\bar{\theta}_w = (1/w)\sum\limits_{i=1}^{N} w_i\,\theta_i$ is the weighted mean polarization angle in the sub-region. In sub-region 1 (SR1 from Fig. 6.2), where there are 56 independent HAWC+ measurements, the dispersion in polarization angles is 53° ± 7°, which is a rather large value considering that the main regime of applicability of the DCF method ($\sigma_\theta \leq 25°$ – see Ostriker et al., 2001). The error in the dispersion of polarization angles was estimated as $\sigma_\theta/\sqrt{N}$. In sub-region 2 (SR2), there are 162 independent HAWC+ measurements, and the dispersion in polarization angles is 20° ± 2° (see Table 6.1).

W also analyzed the data using the structure function (SF) variant of the DCF method (Hildebrand et al., 2009). In Figure 6.6, we fit $\langle \Delta\Phi(\ell)^2\rangle^{1/2}$ for the two sub-regions using the SF method after correcting for measurement error by computing the error-weighted $\Delta\Phi^2(\ell)$ as in equation (6.7).

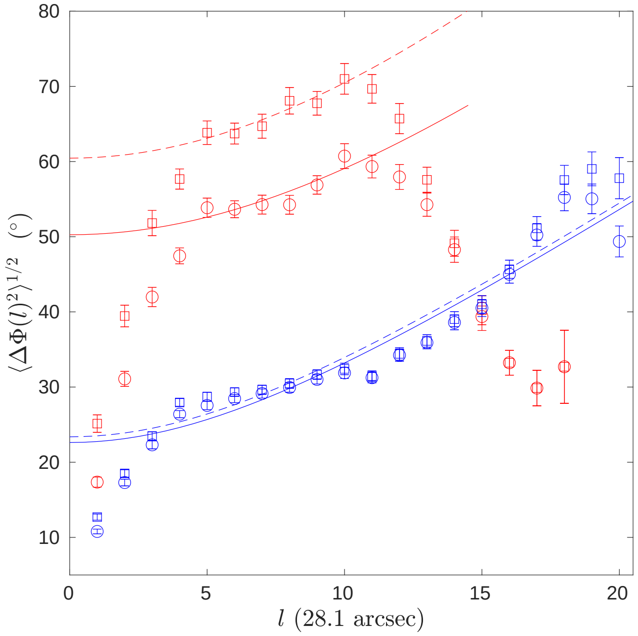

Figure 6.6: Structure functions and fits for sub-regions SR1 (red) and SR2 (blue) using with $\Delta\Phi$ restricted to less than 90° (circles and solid curve) and with no restriction on $\Delta\Phi$ (squares and dash curve) as functions of scale in units of HAWC+ superpixels. For SR1, the fitting is from $\ell = 5$ to 10. The fitted intercepts with restriction and no restriction are $50.9 \pm 4.3°$ and $60.9 \pm 3.0°$, respectively. Error bars are the standard deviations of angle differences at a given distance. For SR2, the fitting is from $\ell = 4$ to 18. The fitted intercepts with restriction and no restriction are $23.2 \pm 3.5°$ and $24.0 \pm 3.6°$, respectively.

It is common practice to restrict $|\Delta\Phi|$ to be less than 90°; that is, whenever $|\Delta\Phi|$ is larger than 90°, it is replaced by $|180^\circ - \Delta\Phi|$. As discussed in the Appendix, this often results in an underestimate of the dispersion in field angles and a corresponding overestimates of the field; in some cases, however, it can improve the accuracy of the field determination. We, therefore, provide both values. The intercepts of the fits at $\ell = 0$ in Fig. 6.6 are $\Delta\Phi_0 = 50.3 \pm 4.4^\circ$ and $\Delta\Phi_0 = 60.5 \pm 3.0^\circ$ for the restricted and unrestricted approaches, respectively. The difference is only 10°. The corresponding angular dispersions contributed from the turbulence ($\sigma_\theta \sim \Delta\Phi_0/\sqrt{2}$) are about 36° and 43°, respectively. From the fitting, the turbulent correlation length scale of SR1 and SR2 is about 4 to 5 super-pixels, corresponding to 0.075 to 0.095 pc, about the size scale of the filamentary substructures. We divide the SR1 into four smaller regions, each with 30 polarization measurements. The root-mean-square of the angular dispersion of these four smaller regions is 30.3°, close to the angular dispersion of the turbulence from the SF analysis. The intercepts of fitting at $\ell = 0$ in Fig. 6.6 are $23.2 \pm 3.5^\circ$ and $24.0 \pm 3.6^\circ$ from the restricted and un-restricted approaches, almost the same. The summary of all the measured parameters and the results of the DCF and SF analysis are listed in Table 6.1. The estimation for the ambient cloud around the entire L1495 is also provided in the table for comparison.

6.3.4 Volume density

The average volume density in each of the two portions of the B211 filament marked in Fig. 6.2 was estimated using the surface density map at 18.2 resolution published by Palmeirim et al. (2013) and Marsh et al. (2016) from *Herschel* Gould Belt survey (HGBS) data[4]. To do so, we assumed that the depth of each sub-region along the LOS is the same as the mean projected outer width. This is a very reasonable assumption, especially for SR2 which corresponds to a segment of the filament, since there is good observational evidence that B211 is a true cylinder-like filament as opposed to a sheet seen edge-on (Li & Goldsmith, 2012). The mean outer width was obtained using the projected area of pixels above the minimum surface density with a detected polarization signal [$\log N(\mathrm{H_2}) = 21.59$], divided by the length of each sub-region. The average surface density $< N(\mathrm{H_2}) >$ above $\log N(\mathrm{H_2}) = 21.59$ in each sub-region was derived from the *Herschel* column density map, and the resulting value was divided by the mean outer width, namely $L \sim 0.15$ pc for SR2 and $L \sim 0.3$ pc for SR1. This provided the average density, $<n(\mathrm{H_2})> = <N(\mathrm{H_2})>/L$, given in Table 6.1.

6.3.5 Magnetic field strength

Using Equation (6.3) with the volume densities, velocity dispersions, and dispersions in polarization angles estimated in previous sections, we can determine the field strengths for the two sub-regions marked by white dashed rectangles in Fig. 6.2. The results are summarized in Table 6.1. In SR2, the field has a small dispersion, $\sigma_\theta = 20^\circ$. The field strength ranges between 43 μG and 66 μG from the standard DCF method and 79 μG to 82 μG with the structure function (SF) variant. Knowing the magnetic field, it is possible to determine the POS mass-to-flux ratio relative to the critical value, $\mu_{\Phi,\mathrm{POS}}$, and the alfvén Mach number (see Appendix of the paper). SR2 is trans-Alfvénic, with $\mathcal{M}_\mathrm{A} \simeq 1.0 - 1.3$ and magnetically critical to mildly supercritical, $\mu_{\Phi,\mathrm{POS}} \simeq 0.9 - 1.7$, depending on the method of analysis that is adopted. The critical mass per unit length, $M_{\mathrm{crit},\ell}$, is that value of M_ℓ such that the pressure and magnetic forces are in balance with gravity. The SR2 filament segment is slightly sub-critical, with $M_\ell \simeq 0.7 M_{\mathrm{crit},\ell}$–i.e., it is gravitationally stable against radial collapse. In the absence of perpendicular magnetic fields, filaments that are moderately subcritical ($0.9 \geq M_\ell/M_{\mathrm{crit},\ell} \geq 0.2$, with an optimum value of $M_\ell/M_{\mathrm{crit},\ell} \sim 0.5$) are subject to fragmentation into prestellar cores (i.e., starless cores with $M \geq M_\mathrm{BE}$) since gas can flow along the filament. Perpendicular fields suppress fragmentation for $\mu_\Phi < 1$. SR2 contains at least 5 candidate prestellar cores (Marsh et al., 2016), which suggests that the lower estimates of the field in Table 6.1 are more accurate. By contrast, SR1 has a chaotic field with a large dispersion in polarization angles, $\sigma_\theta = 54^\circ \pm 5^\circ$. This dispersion substantially exceeds the upper limit of applicability of the DCF method recommended by Ostriker et al. (2001), as well as the less stringent criterion in Appendix of the paper. The standard method yields $B_0 \sim 7 - 13$ μG, depending on whether the velocity dispersion is estimated from the dominant velocity component (B_0^d) or the total line width (B_0^m). For the two sub-components of SR1, the DCF method gives $B_0 \sim 10 - 11$ μG for SR1a and $B_0 \sim 22 - 28$ μG for SR1b. The large dispersion in angles is due in part to large scale variations in the field structure that are allowed for in the DCF/SF analysis. Using that method with the total line width, the estimated magnetic field strength B_0^m is 23 or 16 μG, depending on whether $|\Delta\Phi|$ is restricted to be less than 90° or not. The turbulent magnetic field strength $\delta B_0^m = 18$ μG, comparable to B_0^m. We note that Marsh et al. (2016) found only

---

[4] cf. http://gouldbelt-herschel.cea.fr/archives

one candidate prestellar core in the sub-region SR1 (see the paper in the Appendix of this thesis for more discussion).

6.4 Results and conclusions

Our aim in this project was to observe a pristine portion of the well-documented B211 filament in Taurus with HAWC+ on board SOFIA to investigate the magnetic field morphology in thin filamentary clouds. This observation was challenging because of the low surface brightness of the filamentary cloud. We needed to re-sample 3×3 detector pixel data to a super-pixel of $28''$ to optimize the SNR. We detected at level of $P/\sigma_P \geq 2$ for 282 independent measurement in this region. Due to high polarization angle dispersion, the observations revealed two different sub-regions, designated SR1 and SR2, in the observed B211 filament. We used IRAM IRAM 30m $C^{18}O$ (1-0) molecular line data to estimate the magnetic field strengths using the standard DCF method and the alternative DCF structure-function variant of the DCF method.

1. *B-field lines morphology of the two sub-regions in B211.* The B-field line in SR1 appear to be chaotic indicating a strong pertubations of the field, while SR2 has a regularly organized magnetic field structure, which tend to be perpendicular to the filamentary cloud axis. The organized field in SR2 matches the large-scale field from Planck observation very well. The dispersion of the PAs in SR1 is 54 deg, almost three times that in SR2.

2. *Filamentary substructures in B211.* The IRAM 30m $C^{18}O$ (1-0) data revealed multiple velocity components in the observed B211 region, similar to what has been reported in a previous study of L1495 (e.g. Hacar et al., 2013). There are at least three velocity components in SR1 and two velocity components in SR2. Multiple filamentary substructures are seen in the high-resolution Herschel map. The chaotic appearance of substructures, polarization vectors, and the multiple-component line profiles in SR1 may indicate strong interaction among substructures.

3. *Magnetic fields strength of the two sub-regions* Using the DCF and DCF/SF methods, the estimated field strength based on the total LOS velocity dispersion in SR1 is in the range 13 to 23 μG. Because of the very large dispersion of the polarization angles ($\sigma_\theta = 54^\circ$), the field estimate in this region is very uncertain, but the field is small. By contrast, the estimated field strength of SR2 is from 66 to 82 μG, significantly larger than that in SR1. These estimates are based on the assumption that the numerical coefficient introduced to correct for the approximations in the DCF method, ξ, is 0.5 (Ostriker et al., 2001).

In table 4 of the paper (in the Appendix of this thesis), we showed the physical properties of the observed sub-regions in the B211 filament. From the mass-to-flux ratios and alfvén Mach numbers, SR1 is magnetically supercritical and slightly super-Alfvénic. The magnetic field in SR2 is significantly greater than that in SR1. Both the standard DCF analysis and the DCF/SF method suggest that SR2 is approximately magnetically critical and that it is trans-Alfvénic. The ratio of the line mass to the critical line mass is slightly less than unity for SR1, SR2. We found that this filament has approximately $M_\ell/M_{\mathrm{crit},\ell} \sim 0.5$, which suggests that the B211 filament is fragmenting into cores. Only by taking into account magnetic fields that the B211 filament seems to be fragmenting into cores. These results highlight the role of magnetic fields in regulating the star-forming regions, such as the B211 filament. In this chapter, I only discussed the observation aspects of our result on the B211 filament; other results and conclusions are given in the paper (see Appendix of this thesis).

Table 6.1: Summary of parameters and results of the DCF and SF analysis.

Region[5]	SR1	SR2	Taurus/B211[6]
N_i[7]	120	162	175
V^d_{LSR}[8]- V^m_{LSR}[9](km s^{-1})	5.4–5.9	5.5–5.5	6.6
σ^d_V[10]- σ^m_V[11](km s^{-1})	0.26–0.48	0.27–0.41	0.85 ± 0.01
σ_θ[12](°)	54 ± 5	20 ± 2	24 ± 2
$N(\mathrm{H_2})$[13](10^{21}cm^{-2})	8 ± 3	11 ± 4	1.5 ± 0.2
Depth[14](pc)	0.3	0.15	$0.5\,^{+0.5}_{-0.25}$
$n(\mathrm{H_2})$[15](10^4cm^{-3})	1.0 ± 0.4	2.3 ± 1.0	$0.1^{+0.1}_{-0.05}$
DCF analysis			
B^d_0[16]- B^m_0[17](μG)	7–13	43–65	23^{+12}_{-6}
δB^d - δB^m[18](μG)	10–18	16–24	10^{+7}_{-5}
μ_Φ [19]	5.0–2.7	1.8–1.2	$0.5\,^{+0.1}_{-0.1}$
$\mathcal{M}_\mathrm{A}/\cos\gamma$[20]	4.8	1.3	1.6
DCF/SF analysis			
$\Delta\Phi_{0,\mathrm{res}}$[21]$/\sqrt{2}$ (°)	35 ± 3	16 ± 3	14 ± 2
$\Delta\Phi_{0,\mathrm{nores}}$[22]$/\sqrt{2}$ (°)	42 ± 2	17 ± 3	14 ± 2
B^m_0[23](μG)	17–23	79–82	41^{+21}_{-11}
δB^m[24](μG)	18	24	10
μ_Φ	2.5–2.1	1.0	0.3
$\mathcal{M}_\mathrm{A}/\cos\gamma$ [25]	2.6-3.5	1.0	0.9

---

[1] Sub-region of B211 in which the analysis was conducted.

[2] Estimation on a large scale covering the Taurus/B211 region using *Planck* polarization data (Palmeirim et al., 2013) and molecular line observations (Chapman et al., 2011).

[3] Number of independent SOFIA/HAWC+ polarization measurements for which $P/\sigma_P \geq 2$, where P is the polarized intensity.

[4] Average centroid velocity of the dominant velocity component in each sub-region.

[5] Average centroid velocity in each sub-region, including all velocity components.

[6] Average non-thermal velocity dispersion of the dominant component over each sub-region.

[7] Average value of the total non-thermal velocity dispersion over each sub-region.

[8] Dispersion of polarization angles with individual measurements weighted by $1/\sigma^2_{\theta_i}$). The uncertainty in this dispersion was was estimated as $\sigma_\theta/\sqrt{N}$, where N is the number of independent polarization measurements in each sub-region. (cf. Pattle et al., 2021)

[9] Weighted mean surface density derived from Herschel GBS data at the HAWC+ positions.

[10] Adopted depth of each subregion estimated from the width measured in the plane of sky.

[11] Average volume density estimated from $N(\mathrm{H_2})$ and Depth.

[12] Plane-of-sky mean field strength from the standard DCF method (eq. 6.3) using the dispersion of the dominant velocity component.

[13] Plane-of-sky mean field strength from the standard DCF method (eq. 6.3) using the total non-thermal velocity dispersion.

[14] The turbulent component of plane-of-sky B-field strength ($\delta B = B_0 \tan\sigma_\theta$, see Appendix of the paper eq. A11).

[15] Estimated mass to flux ratio relative to the critical value based on the rms POS field, $B_{\mathrm{tot}} = (B_0^2 + \delta B^2)^{1/2}$ (eq. B5).

[16] $\mathcal{M}_\mathrm{A}$ is the 3D alfvén Mach number ($\propto \sqrt{3}\sigma_V/B_{0,\mathrm{3D}} = \sqrt{3}\sigma_V \cos\gamma/B_0$) with respect to the mean 3D field (eq. A13).

[17] Intercept of the fitted structure function at $\ell = 0$ with large-angle restriction.

[18] Intercept of the fitted structure function at $\ell = 0$ without large-angle restriction.

[19] The range of B_0 estimated from $\Delta\Phi_{0,\mathrm{nores}}$ and $\Delta\Phi_{0,\mathrm{res}}$, respectively, using the total non-thermal velocity dispersion (eq. 6.6).

[20] The turbulent component of plane-of-sky B-field strength $\delta B^m = \sigma_{\delta B} = (4\pi\rho)^{1/2}\sigma^m_V$ (eqs. A27 and A28).

[21] $\mathcal{M}_\mathrm{A}$ is the 3D AlfvénMach number ($\propto \sqrt{3}\sigma_V/B_{0,\mathrm{3D}} = \sqrt{3}\sigma_V \cos\gamma/B_0$) with respect to the mean 3D field for the DCF/SF method (eq. A26).

Chapter 7

Velocity power spectrum of star-forming filaments in the Aquila region using IRAM 30m molecular line observations

Hamza Ajeddig; Philippe André et al. in prep.

Contents

7.1 Introduction

The Herschel results support a “filament paradigm” in which large-scale MHD turbulence compress the interstellar material and lead to the formation of a cobweb of filamentary structures with common inner width of $\sim$ 0.1 pc. Some of these filaments will then collapse under the gravitational instability to form stars (André et al., 2014). The detailed formation process of dense cores in filaments has been under debate for decades. The density/velocity fluctuation can provide an insight into the formation and evolution of interstellar filaments. The analysis of the density/velocity power spectrum can explain the observed angular momentum in the fragmented filaments. Misugi et al. (2019) found that the 1D Kolmogorov spectrum is a more favorable scenario than the 3D Kolmogorov spectrum in explaining the observed angular momentum of cores in filaments (cf. Fig. 3 in their paper). These results are consistent with Roy et al. (2015) where they found that the column density power spectrum is consistent with the 1D Kolmogorov spectrum, but this did not provide direct measurements of the velocity fluctuations. In this chapter, I present observations and analysis of the IRAM 30m molecular lines toward the Aquila molecular cloud complex. We used 27 filaments detected with Herschel in this region (Könyves et al., 2015) to analyze the velocity fluctuations and the velocity power spectrum in sub-, trans-, and super-critical filaments.

7.2 Filament sample in the Aquila region

In the context of the velocity power spectrum analysis that we aim to provide in this project, we identified all possible filaments in the Aquila region that can be used for this purpose. We used the filament crests extracted with the DisPerSE algorithm applied to 250 μm images from HGBS in the Aquila region (Arzoumanian et al., 2019; Könyves et al., 2015).

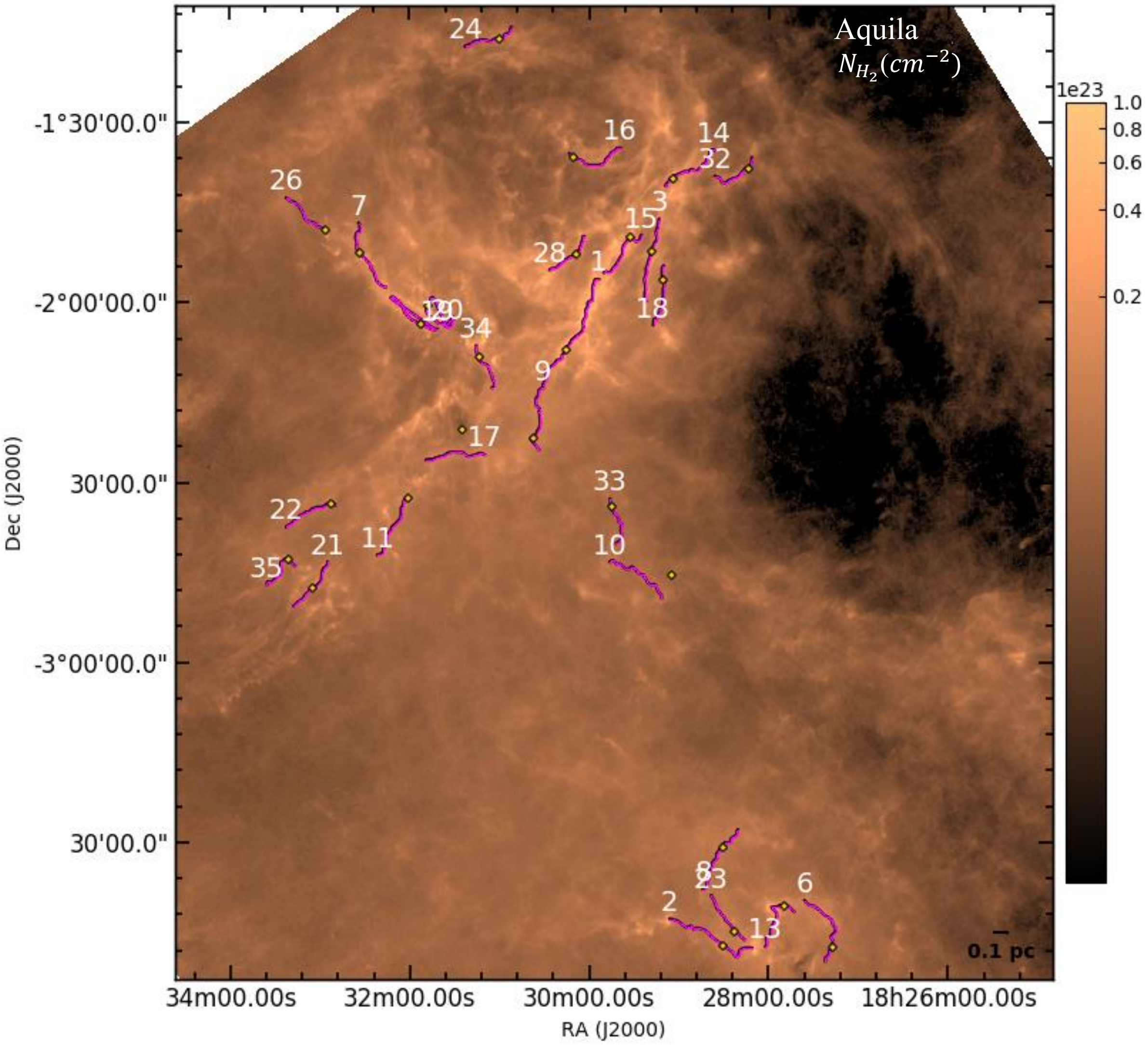

Figure 7.1: High-resolution (18″) column density map of the Aquila region from the Herschel Gould Belt Survey (HGBS) (André et al., 2010). The overlaid skeletons are the observed filaments in this region which were observed to derive their velocity power spectrum. 13 sub-critical filaments, 12 trans-critical filaments and two super-critical filaments were observed during four observing campaigns using the EMIR receiver at the IRAM 30m telescope (see Table 7.1). The yellow circles are the positions of the spectra for each individual filament shown in Fig. 7.5, 7.6, 7.7

To identify possible variations of the velocity power spectrum depending on filament line-mass, we observed 13 sub-critical, 12 trans-critical, and two super-critical filaments. The whole sample consists of 27 filaments, which provide enough statistics to analyze the velocity power spectrum in the Aquila region. Figure 7.1 shows the column density map $N_{H_2}(\mathrm{cm}^{-2})$ of the Aquila region from the HGBS (André et al., 2010) with the crests of the filaments from Könyves et al. (2015) used in this project overlaid as purple curves. The number of each filament is indicated and the yellow rectangles mark the position of the 30m spectra shown in Fig. 7.5, 7.6 and 7.7. The observed filaments and number of pointings toward each are given in table 7.1. Starless and protostellar cores were identified

Table 7.1: The observed filament and their characteristics.

Filament	nbr. of points	Along the filament $\parallel$	perpendicular to the filament $\perp$	$V_{LSR}(km/s)$ comp
Sub-critical filaments				
21	53	(✓)	(✓)	2
14	63	(✓)	(✓)	2
9	67	(✓)	(✓)	2
17	60	(✓)		1
2	94	(✓)		2
11	65	(✓)		2
10	67	(✓)		1
22	53	(✓)		1
6	73	(✓)		2
24	51	(✓)		2
32	49	(✓)		2
35	45	(✓)		1
34	45	(✓)		1
Trans-critical filaments				
3	77	(✓)	(✓)	2
7	71	(✓)	(✓)	1
20	87	(✓)		2
15	59	(✓)	(✓)	1
16	58	(✓)		1
8	71	(✓)		1
18	57	(✓)		2
23	51	(✓)		2
13	63	(✓)		1
26	49	(✓)		1
33	47	(✓)		2
28	49	(✓)		1
Super-critical filaments				
1	119	(✓)	(✓)	1
19	101	(✓)	(✓)	1

Table 7.2: Summary of the observed filament along the Aquila region showed in Fig. 7.1. The filaments in Aquila are different by their line mass, such as the sub-critical, trans-critical, and super-critical filaments according to Arzoumanian et al. (2013). The number of data points in each filament is given in column 2, ($\parallel$) and ($\perp$) corresponding to the observing mode along the filament and On-The-Fly (OTF) map across the filament. V_{LSR} comp. is the number of the detected 1D centroid velocity components in each filament in the sample (see Fig. 7.1)

by Könyves et al. (2015) in some of these filaments using *getsources* (Men'shchikov et al., 2012). The sample contains filaments in different locations of the Aquila region, also located close to W40 and MWC297 HII region shown in Fig. 2 of Könyves et al. (2015). Only filaments with a length $> 8'$ were considered to ensure sufficient data points for the power spectrum analysis. A total of 1744 positions towards 27 filaments in the Aquila region were observed with the IRAM 30m telescope to provide sufficient statistics for a velocity power spectrum analysis. The target sampled filaments were classified as sub-critical, trans-critical, or super-critical based on their line mass or mass per unit length, being less than 8 $M_\odot$ /pc, between 8 $M_\odot$ /pc and 32 $M_\odot$ /pc, and exceeding the 32 $\mathrm{M}_\odot$ /pc, respectively.

7.3 Setup and observation strategy

Molecular line observations of the filament sample described above were carried out with the Eight MIxer Receiver (EMIR) receiver (Carter et al., 2012) on the IRAM-30m telescope at Pico Veleta (Spain) during four campaigns in Aug. 2020, Nov. 2020, Jan. 2021, and April 2021 under the 30m projects ID 010-20 and 113-20 (PI: Ph. André). We used the EMIR instrument to observe simultaneously the C^{18}O(1–0) and ^{13}CO(1–0) molecular line along the crests of 27 filaments in the Aquila region detected in the Herschel column density map. the ^{13}CO(1–0) molecular line data constrain the velocity components of the lowest-density filaments in the sample. The observed positions toward each filament were half-beam spaced with an average of 53 positions per filament (filaments 1 and 19 are the longest in the sample, see Table 7.5). We used the frequency-switching observing mode for these CO observations that allowed us to save significant telescope time. In addition, the high spectral resolution provided by VESPA allowed us to resolve the narrow lines and measure the line widths and the velocity gradients in the filament sample. We observed C^{18}O(1–0) and ^{13}CO(1–0) lines for all 27 filaments in the Aquila region, while N_2H^+ observations were carried out for densest (thermally supercritical) filaments. We used only C^{18}O(1–0) observations for the velocity power spectrum analysis.

Two different observing modes were employed in this project; using the same spectral setup, we first observed a series of independent positions along the crest of each filament (hereafter (||) mode). Second, we used the OTF mapping mode acros or perpendicular to a subset of the filament (hereafter (⊥) OTF mode).

7.4 IRAM 30m C^{18}O(1–0) along the filaments

The 1D centroid velocity observed with the IRAM 30m telescope traced by the C^{18}O(1–0) line varies from filament to filament. Arzoumanian et al. (2013) detected multiple velocity components in some filaments in the Aquila region, especially for sub-critical and trans-critical filaments. The presence of multiple velocity components indicates a possible fiber-like structure in the Aquila region, which provides additional information on the turbulence motion in the medium (Hacar et al., 2013). We detected in some cases more than two velocity components which are located between 3 km/s and 12 km/s. We used Gaussian fits to identify different velocity components detected with the VESPA and FTS backends around the C^{18}O(1–0) line frequency (109.782 GHz). Figures 7.5 7.6, 7.7 show the C^{18}O(1–0) molecular line spectra of all *sub-critical, trans-critical and super-critical* filaments observed in the Aquila region. The blue curve presents the spectrum while the solid red line shows the applied Gaussian fit, which allowed a precise determination of the 1D centroid velocity and the line-of-sight (LOS) velocity dispersion. The upper numbers shown at the top of each spectrum correspond to the positions of the yellow circles in Fig. 7.1.

We observed a subset of the filaments in our sample both along and across the filaments crests as indicated in table 7.1. In the current analysis of the velocity power spectrum, we used the first moment from 5 km/s to 10 km/s where the detection is present. The 1D velocity component considered in our analysis was computed from the first moment of the spectra observed at half-beam-spaced positions along each crest. VESPA (20 KHz) and FTS (50 KHz spectral resolution) data were used to check if there was any effect of the spectral resolution on the resulting velocity power spectrum of each filament.

7.4.1 Centroid velocity fluctuations along each filament

To first order, filament structures have a cylindrical geometry, and they characterized by their mass per unit length (line-mass) (e.g, Inutsuka, 2001). C^{18}O(1–0) line observations along a filament in the Aquila region provide a piece of information about the fluctuations of the centroid velocity toward each filament. Figure 7.2 shows an example of centroid velocity fluctuations along transcritical filament 7 in the Aquila region. Figure 7.2a presents closer look of filament 7 and its observed positions along the identified crest overlaid with the Herchel column density. While Fig. 7.2b shows an example of C^{18}O(1–0) spectra of one position in filament 7 (offset RA-DEC; 50.4", 51.1"), the blue curve shows the spectrum while the solid red line shows a Gaussian fit to the spectrum at this position. The C^{18}O(1–0) line was detected at all positions along filament 7, allowing us to perform a proper velocity fluctuation and velocity power spectrum analysis in this case. Only a single velocity component was identified at all positions. In addition to the observations along filament (||), we also observed an OTF cut perpendicular to this filament. Figure 7.2c shows in black color the centroid velocity fluctuations vs. the position along the crest of filament 7 in arcsec, where the 0″ offset indicates one end of the filament and 840″ the other end. In this case, the cyan line shows the linear regression fit of the velocity fluctuation with a slope of 0.55 (km/s).pc^{-1} and intercept of 6.96 km/s. The centroid velocity increased from 7.03 km/s to 8.52 km/s at its end (840″), indicating a shift in the centroid velocity in filament 7.

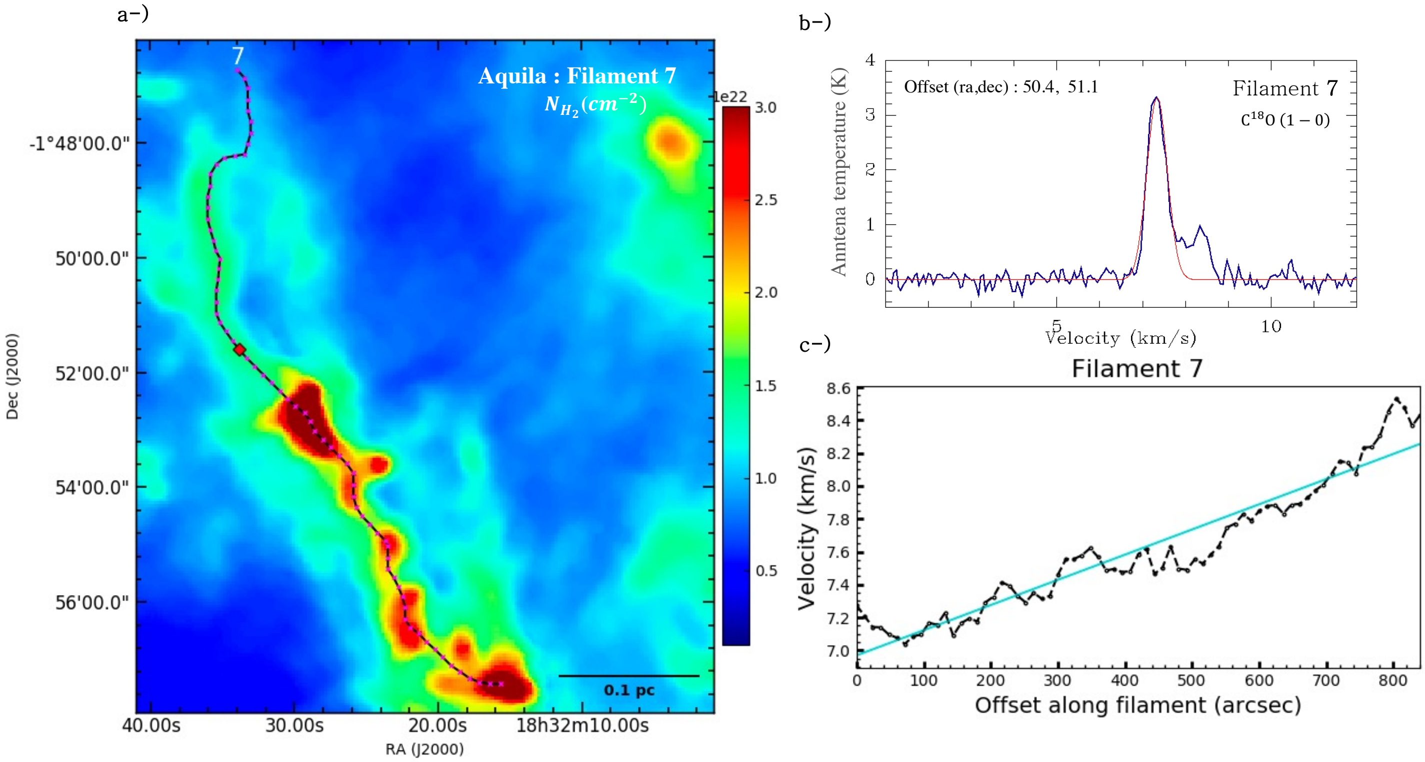

Figure 7.2: a-) Closeup view of the crest of filament 7 marked as a black line, with observed positions shown as pink dots, the background image is the column density N_{H_2} map from the HGB survey (Könyves et al., 2015) in cm^{-2}. b-) Detected C^{18}O(1–0) spectrum for filament 7 at the position marked by a red square in panel (a). The spectrum and the Gaussian fit are shown by the blue and red curves, respectively. c-) Line-of-sight velocity fluctuations along this filament (in black color), with a linear regression line in cyan (with a slope of 0.55 (km/s).pc^{-1} and intercept of 7.03 km/s)

7.4.2 Line-of-sight velocity dispersion along each filament

In order to obtain the line-of-sight velocity dispersion within each filament identified in the Aquila region, we computed the total velocity dispersion at each position. We estimated the non-thermal velocity dispersion by subtracting the thermal velocity dispersion from the observed line-width (Myers, 1983). For C^{18}O molecule, the thermal velocity dispersion may be expressed as :

$$\sigma_{T_{C^{18}O}} = \sqrt{\frac{k_B T}{\mu_{C^{18}O} m_H}} \tag{7.1}$$

where k_B is the Boltzman constant, μ is the atomic weight of $C^{18}O$, in this case, $\mu_{C^{18}O} = 30$, we used $T = 10K$ as the kinetic temperature of the gas, which is consistent with the dust temperature measured by Herschel in the case of Aquila filaments. The non-thermal velocity dispersion thus is given by :

$$\sigma_{NT} = \sqrt{\sigma_{obs}^2 - \sigma_T^2} \tag{7.2}$$

Where $\sigma_{obs} = \Delta V/(8\ln 2)$ is the line-width of the observed spectra at each position. For a typical molecular gas of mean molecular weigth $\mu = 2.33$, the total velocity dispersion can be written as :

$$\sigma_{tot} = \sqrt{\sigma_{NT}^2 + \sigma_T^2(\mu)} \tag{7.3}$$

where $\sigma_T(\mu) \sim 0.2$ km/s for gas at T $\sim$ 10K. Figure 7.3 shows the variations of the total velocity dispersion along filament 7 based our $C^{18}O(1–0)$ line observations. The dispersion was derived using the first moment measurement of the observed spectra. No significant variations in the total velocity dispersion are seen along filament 7 (similar results were obtained by Arzoumanian2013 for another Aquila filament in ^{13}CO and $C^{18}O$).

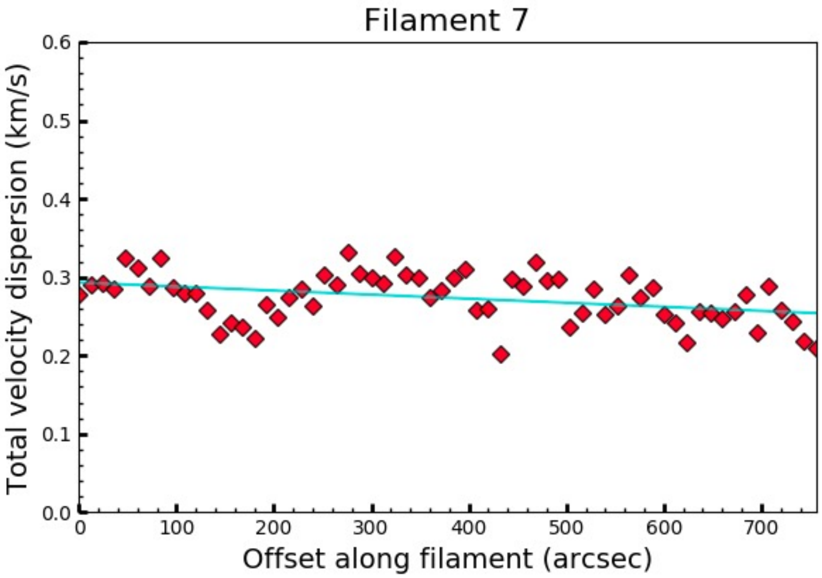

Figure 7.3: Variation of total velocity dispersion σ_{tot} as a function of the position offset along filament 7, in cyan color solid line is the linear regression of line-of-sight velocity dispersion in this case. The velocity dispersion was derived using the first moment where in the case of filament 7, we found a single centroid velocity component.

7.5 Power spectrum analysis

The normalized power spectrum of a given 1D signal is the square of the Fourier amplitude normalized by the interval's length. In the present case, the velocity power spectrum allows to characterize the amplitude of the fluctuation as a function of spatial-scale and can be expressed as follows :

$$P(k) = \frac{\left|\tilde{V}(k)\right|^2}{L} \tag{7.4}$$

where P(k) is the power spectrum at a given spatial frequency k, and $\tilde{V}(k) = \int V(l) e^{-2i\pi kl} dl$ is the Fourier transform of the observed line-of-sight velocities $V(l)$. In our analysis, we computed $\tilde{V}(k)$ for each observed filament in the Aquila region. To compute the velocity power spectrum we used the centroid velocity (described above) along the filament.

7.6 Velocity power spectrum

Figure 7.4 shows an example of the velocity power spectrum analysis applied to the super-critical filament 1 (which correspond to the well-documented Serpens-South filament). The fluctuations of the line-of-sight centroid velocity observed in $C^{18}O(1–0)$ along the crest of Filament 1 in Aquila is shown in the top right panel. We found that filament 1 exhibits a slight velocity gradient of 0.5 km/s /pc (see Fig. 7.4 top right panel). The corresponding velocity power spectrum is consistent with $P(k) \propto k^{\alpha}$, where $\alpha \simeq -1.75 \pm 0.30$ which is close to 1D Kolomogorov power spectrum of subsonic turbulence ($\alpha = -5/3 = -1.67$) and close to the power spectrum found by Roy et al. (2015) for column density fluctuations along filaments ($\alpha = -1.6$).

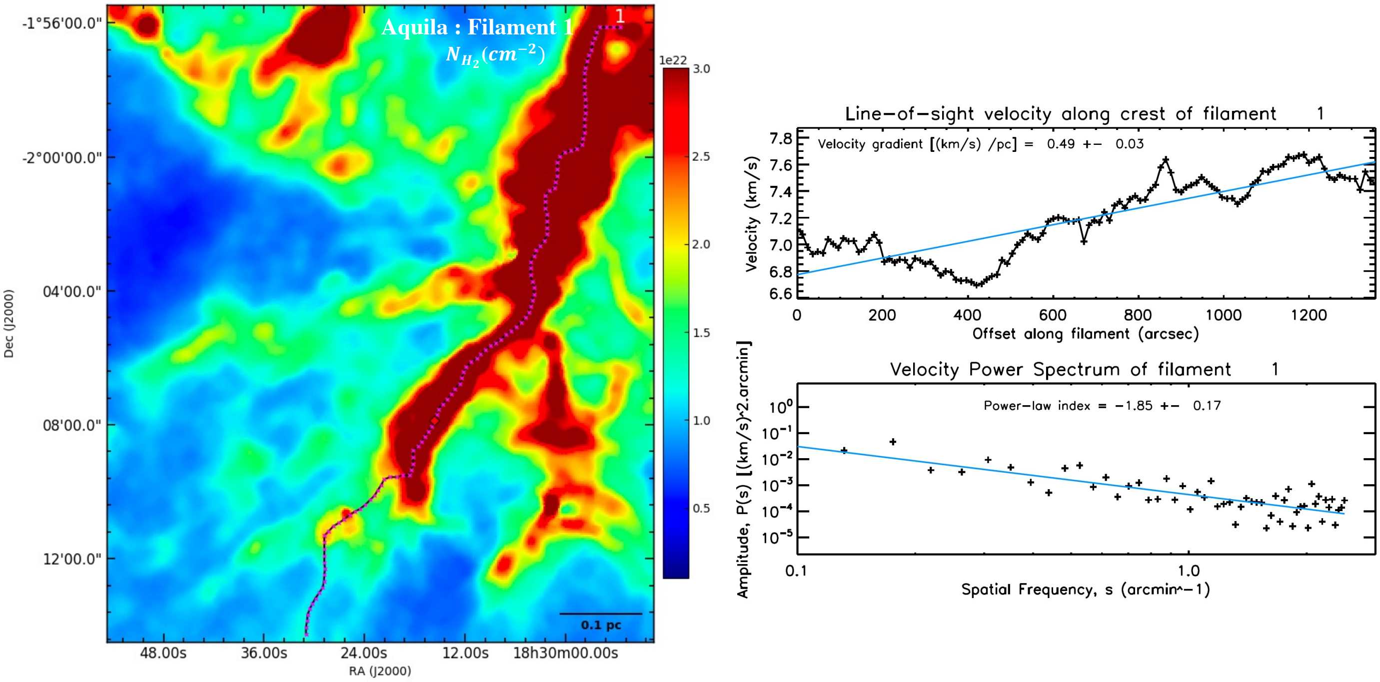

Figure 7.4: Left panel : Closeup view of the crest of filament 1 indicated as a black line and the observed positions in pink color overlaid on the column density N_{H_2} from HGBS (Könyves et al., 2015) in cm^{-2}. Top right panel: Fluctuations of the line-of-sight centroid velocity observed in $C^{18}O(1\text{–}0)$ along the crest of Filament 1 in Aquila. The sampling along the filament's crest is $12''$ (i.e., half a beam at 3mm). Apart from small-scale velocity fluctuations, this filament exhibits a weak linear velocity gradient of 0.5 km/s /pc. Bottom panel: Power spectrum of velocity fluctuations along the same filament (log-log plot). The black plus symbols show the observed power spectrum; the solid blue line is a power-law fit.

7.7 Concluding remarks

Herschel results on nearby star-forming molecular clouds support the filament paradigm for star formation in which the molecular filaments play a central role. At core scales (< 0.1 pc), Misugi et al. (2019) suggested that angular momentum of protostellar cores may be inherited from the large-scale turbulent motions which are responsible for filament formation and fragmentation. Constraining the dynamical state of star-forming filaments using observations of velocity fields is poorly understood. Whether filaments are quasi-equilibrium structures or out-of-equilibrium accretion flows is still under debate.

In an attempt to discriminate between these two models, we have observed a sample of filaments in the Aquila region to derive the power spectrum from the velocity fluctuations along these filaments. We investigated whether the velocity power spectrum is consistent with a 1D Kolmogorov spectrum. Recent results from column density power spectrum show consistency with 1D Kolmogorov (Roy et al., 2015). However, these column density fluctuations do not constraint the velocity power spectrum. In this project, we conducted power spectrum analysis for a sample of filaments (sub-critical, trans-critical, and super-critical), and we found consistency with the 1D Kolmogorov power spectrum. We used $C^{18}O$, ^{13}CO and N_2H^+ line observations to trace the line of sight velocity fluctuations in the selected filaments in the Aquila region. Our results suggest that the velocity power spectrum using velocity fluctuations along filaments is consistent with a power law $P(k) \propto k^{\alpha}$ with an index of $\alpha = -1.75 \pm 0.30$. This result is close to the 1D Kolmogorov power spectrum of subsonic turbulence ($\alpha = -1.67$) and to the power spectrum result of Roy et al. (2015) using density fluctuations along filaments ($\alpha = -1.6$).

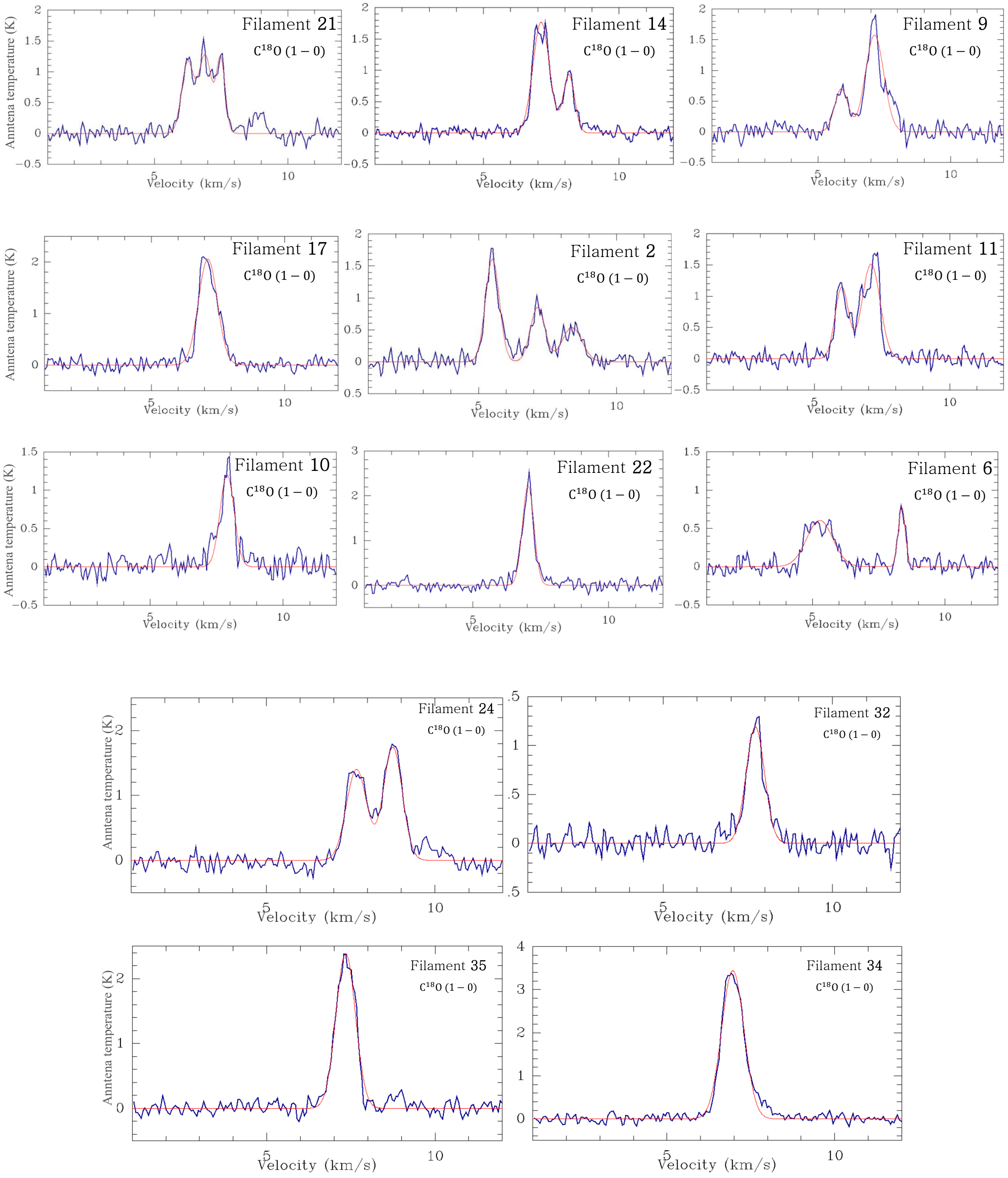

Figure 7.5: IRAM 30m $C^{18}O(1–0)$ molecular line observations of all *sub-critical* filaments observed in the Aquila region. The blue curve presents the spectrum while the solid red line is the applied Gaussian fit, which allowed a precise determination of the 1D centroid velocity and its dispersion. The upper number shown in each of the spectra corresponds to a filament number. The spectra were taken at the position marked by yellow circles in Fig. 7.1.

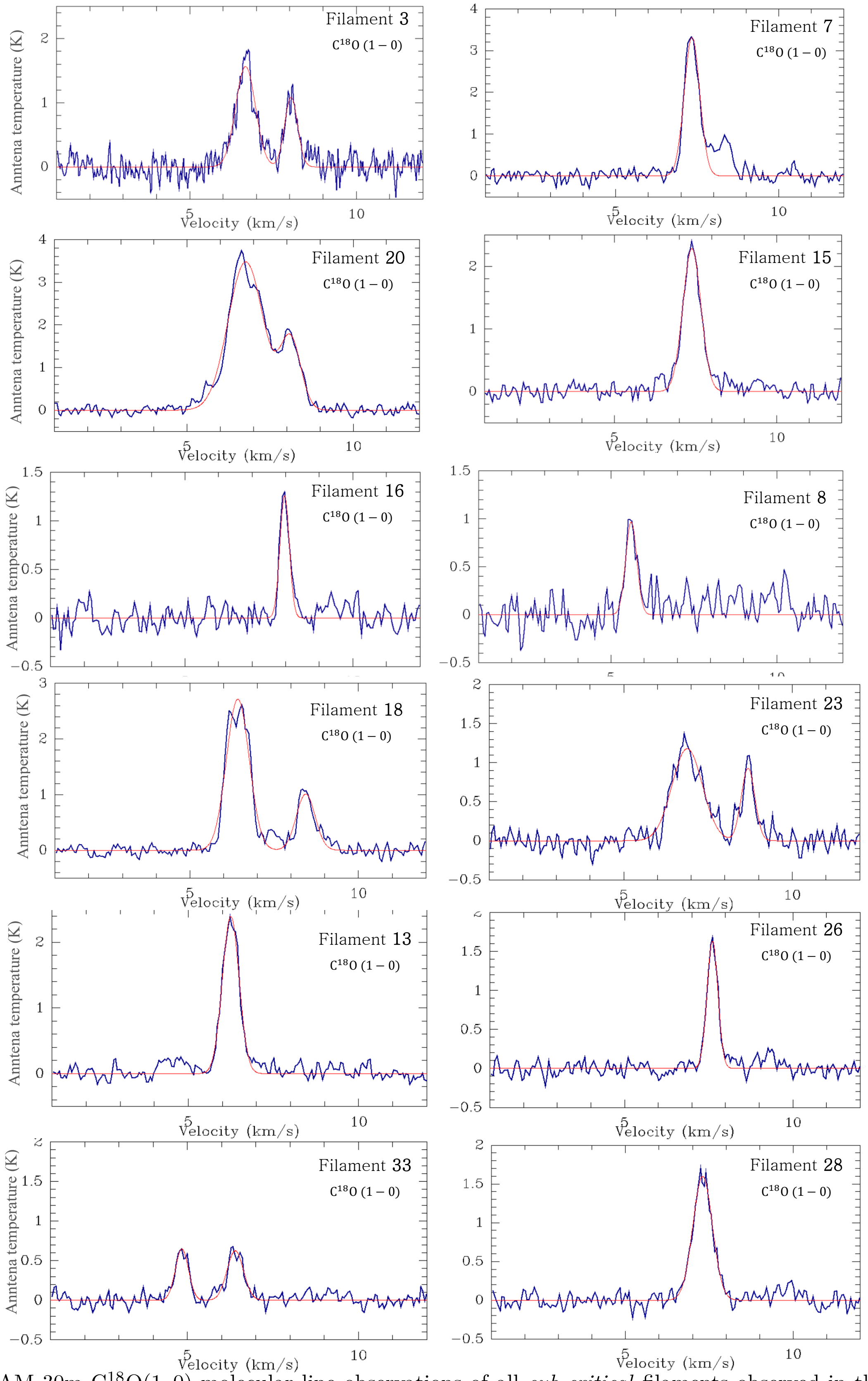

Figure 7.6: IRAM 30m C^{18}O(1–0) molecular line observations of all *sub-critical* filaments observed in the Aquila region. The blue curve presents the spectrum while the solid red line is the applied Gaussian fit, which allowed a precise determination of the 1D centroid velocity and its dispersion. The upper number shown in each of the spectra corresponds to a filament number. The spectra were taken at the position marked by yellow circles in Fig. 7.1.

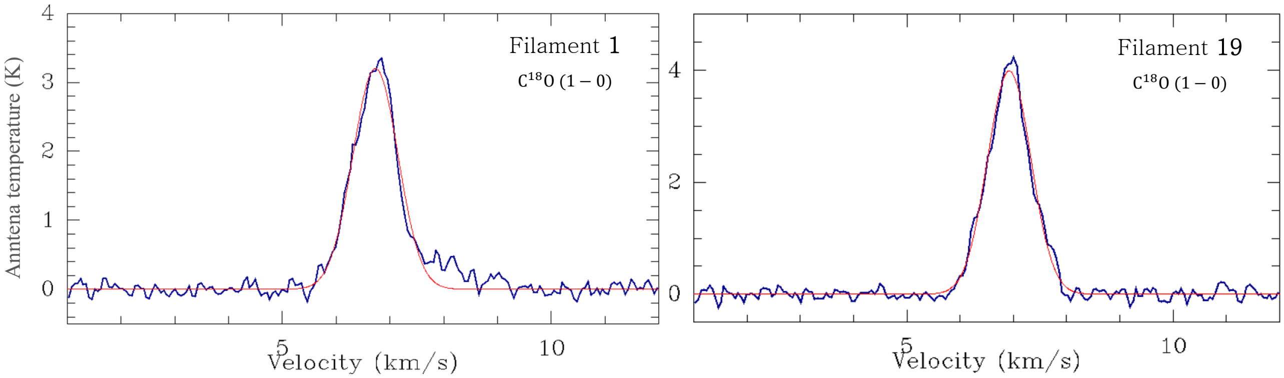

Figure 7.7: IRAM 30m $C^{18}O(1–0)$ molecular line observations of all *sub-critical* filaments observed in the Aquila region. The blue curve presents the spectrum while the solid red line is the applied Gaussian fit, which allowed a precise determination of the 1D centroid velocity and its dispersion. The upper number shown in each of the spectra corresponds to a filament number. The spectra were taken at the position marked by yellow circles in Fig. 7.1.

Chapter 8

Summary and perspectives

The star formation process has been under debate for decades. The detailed knowledge on how molecular clouds fragment to cores and then into stars is not yet well constrained. *Herschel* results have pointed out the crucial role played by molecular filaments in star formation (SF). Molecular filaments within the interstellar medium are considered the key to understand the star formation process. *Herschel* findings support a "filament paradigm " for SF in which : (1) Large-scale magnetohydrodynamic (MHD) supersonic turbulence compresses interstellar material to form a cobweb of filamentary structures with a common inner width of about $\sim$ 0.1 pc; (2) The densest filaments fragment to form prestellar cores due to gravitational instability when M_{line} is close to or exceeds the critical mass per unit length M_{line}^{crit}. However, the detailed process of how filaments fragment into cores remains actively debated. There are hints that the magnetic field may be the ignored ingredient toward understanding SF André et al.; André et al..

Planck dust polarization observations have made a big step toward understanding magnetic fields in star forming-regions. But, these observations were unable to provide a complete scenario of how the magnetic field is ordered at filament/core ($\sim$ 0.1 pc) and sub-core scales (<<0.1 pc). Several questions related to magnetic fields geometry in filamentary molecular clouds thus remained unanswered : (1) How do the magnetic field lines change in orientation from large scales to core scales ?, (2) How is the magnetic field strength is linked to B-field geometry? (3) How does the magnetic field strengths vary along the line-of-sight and in the plane-of-sky? (4) At which stage of SF, the magnetic field is dominating the process ?(5) How do isothermal cylindrical filaments fragment (if any) into cores spaced by $\sim$ 0.1 pc? (6) Why are most prestellar cores and protostars embedded in thermally trans-critical or super-critical filaments? (7) To resolve some of these issues, one needs sensitive and high angular polarization data.

This thesis aimed to answer some of the above questions, especially, the question of how the geometry/strength of magnetic fields change from the parent molecular cloud to its dense cores. The IRAM 30m large program "Probing the B-Field in star-forming Filaments Using NIKA2-Pol (B-FUN) " will provide high-quality polarization observations of nearby molecular clouds. B-FUN will help to understand the role of magnetic fields in filament evolution and fragmentation. It will provide a high angular resolution and sensitive polarization data to investigate the link between large-scale fields and protostellar magnetic fields. The NIKA2-Pol camera is under commissioning, which was essentially finalized during my thesis. I have been working with the NIKA2-Pol team to commission this new observing mode of the continuum camera operating with KIDs technology. During my thesis, three successful campaigns were carried out. I contributed to the observations, data reduction, and data analysis of these three campaigns. I mainly concentrated on the instrumental polarization seen with NIKA2-Pol and I showed how correcting for this effect can lead to reliable and high polarization data. The NIKA2-Pol commissioning data taken in Dec. 2018, Feb. 2020, and Nov. 2020 allowed me to characterize in detail how the instrumental polarization (IP) varies with different parameters. Hundreds of Uranus (unpolarized source) scans were used to analyze the instrumental polarization seen with NIKA2-Pol and investigate its origin (using data from all campaigns and all types of Uranus observations). The result of this analysis were presented in two international conferences and led to two refereed proceeding papers showing the NIKA2-Pol commissioning results (Ajeddig et al. (2020), **Ajeddig et al. submitted**) and a scientific paper using NIKA2-Pol data is in preparation (**Ajeddig et al. in prep**). A summary of my contribution to NIKA2-Pol commissioning in detail is presented in Chap. 4 and Chap. 5, and here I briefly summarize the most important results.

I used Uranus focused, defocused, short scans (5 minutes) and beam maps ($\sim$ 30 minutes) to characterize the IP leakage. We used the quasar 3C286, OMC-1 and the Crab nebula to check the absolute calibration of NIKA2-Pol angle on the sky. We also used OMC-1 to check the repeatability and stability of the polarization angles obtained with NIKA2-Pol from different campaigns.

For the **IP leakage** : (1) At stable weather conditions and optimal focus, the IP leakage pattern takes a form of a "cloverleaf" structure with a central positive spot surrounded by negative quadruple lobes, (2) It is sensitive to the focus position of the telescope (a change of ± 0.2 mm from the optimal focus will lead to a different leakage pattern), (3) It is dependent on elevation and also affected by the astigmatism of the telescope (deformed pattern at low elevation $< 30°$), (4) Its origin may come partially from the astigmatism of the telescope, NIKA2 camera itself (e.g, detectors). We proposed an analytical model allowing a precise representation of the observed leakage in different conditions (any type of leakage pattern). This model depends on 15 coefficients in Stokes Q and 15 coefficients in Stokes U, but we showed that the fourth order coefficients are more dominant than others. The IP correction was performed using Uranus data, quasars, and OMC-1. We showed how the scientific data (OMC-1 in this case) can be corrected for the IP using the current NIKA2 IDL pipeline down to 1 % of polarization fraction when appropriate Uranus maps are available. We suggest using the IP model to correct the polarization data when the Uranus map is not available.
For the **absolute calibration of polarization angles**: The polarization angles obtained during NIKA2-Pol commissioning toward OMC-1, 3C286, and the Crab nebula have an offset compared to XPOL and POL 2 polarization angles. We estimated this offset using these targets and found it to be about $\sim -5.5°$, which need to be subtracted from NIKA2-Pol polarization angles. This offset was determined using parallel XPOL observations of 3C286 and through comparison between NIKA2-Pol and POL2 polarization angles toward OMC-1 and Crab.
For the **reliability of NIKA2-Pol measurements** : We observed OMC-1 and Crab nebula during all three campaigns. We performed a series of OMC-1 observations to check the repeatability of the polarization data with NIKA2-Pol. We showed how the NIKA2-Pol instrument can deliver high-quality and reliable polarization data in a well-known extended source as OMC-1.
Our analysis led to new findings toward this region, especially at the Orion-KL position. We confirmed that the magnetic field distribution in OMC-1 forms an hourglass at a large scale. But, we also found evidence of new possible local hourglass centered at the Orion-KL position thanks to the high angular resolution provided by NIKA2-Pol. We analyzed the B-field geometry/strength using the NIKA2-Pol polarization data (see Chap. 5). These results show how polarization data with NIKA2-Pol can provide high angular and sensitive maps to infer magnetic fields in star-forming regions.

In addition, we used polarization observations obtained with SOFIA/HAWC+ toward the B211 filament in Taurus molecular cloud to study the geometry/strength of the magnetic field. We observed a pristine portion of the B211 filament to investigate how the magnetic field is organized in this region. We detected polarization at a level of $P/\sigma_P \geq 2$, for 282 independent positions in this region. We found high polarization angle dispersions toward this filament, which we divided in two distinct sub-regions (SR1 and SR2). The magnetic fields lines are regularly organized the SR2 but appear to be more chaotic in SR1. We estimated the B-field strength using IRAM 30m $C^{18}O$ (1-0) molecular line data and SOFIA/HAWC+ polarization angles in two sub-regions of B211 filament (see the paper in appendix).

To understand initial conditions of the fragmentation of filaments into cores, We conducted a power spectrum analysis using the line-of-sight velocity fluctuations along a sample of filaments in the Aquila region. Our analysis of the power spectrum using velocity fluctuations along the selected filaments is consistent with a power-law $P(k) \propto k^{\alpha}$ with an index of $\alpha = -1.75 \pm 0.30$. This result suggest a 1D Kolmogorov power spectrum of subsonic turbulence ($\alpha = -1.67$) and consistent with the power spectrum result of Roy et al. (2015) derived using column density fluctuations along filaments ($\alpha = -1.6$).

This thesis provides a detailed analysis of the instrumental polarization seen with NIKA2-Pol and shows the capability of this instrument to provide high-quality data. The next coming steps are : (1) Finalizing the introduced scientific papers, (2) starting BFUN large program and helping on data reduction and analysis of the NIKA2-Pol polarization data, (3) Analyzing the geometry/strength of the B-field in B-FUN targets. During this thesis, I contributed to the submission of two proposals : (1) Observing the B-field geometry in high mass star-forming region NGC6334 with SOFIA/HAWC+ (accepted, PI: Ph. André), (2): ALMA polarization observations toward NGC6334 in which we propose to search for new hourglass patterns in protostar cores detected previously (Shimajiri, 2019) with ALMA in this region (PI : Ph. André, accepted).

Bibliography

Adam, R., Comis, B., Macías-Pérez, J. F., et al. 2014, A&A, 569, A66

—. 2015, A&A, 576, A12

Adam, R., Adane, A., Ade, P. A. R., et al. 2018, A&A, 609, A115

Ajeddig, H., Adam, R., Ade, P., et al. 2020, in European Physical Journal Web of Conferences, Vol. 228, European Physical Journal Web of Conferences, 00002

Ajeddig, H., Adam, R., Ade, P., et al. 2021, arXiv e-prints, arXiv:2111.14533

Alina, D., Ristorcelli, I., Montier, L., et al. 2019, MNRAS, 485, 2825

Andersson, B. G., Lazarian, A., & Vaillancourt, J. E. 2015, ARA&A, 53, 501

André, P. 2002, in EAS Publications Series, Vol. 3, EAS Publications Series, ed. J. Bouvier & J.-P. Zahn, 1–38

André, P. 2017, Comptes Rendus Geoscience, 349, 187

André, P., Arzoumanian, D., Könyves, V., Shimajiri, Y., & Palmeirim, P. 2019, A&A, 629, L4

André, P., Di Francesco, J., Ward-Thompson, D., et al. 2014, in Protostars and Planets VI, ed. H. Beuther, R. S. Klessen, C. P. Dullemond, & T. Henning, 27

Andre, P., Ward-Thompson, D., & Barsony, M. 1993, ApJ, 406, 122

Andre, P., Ward-Thompson, D., & Barsony, M. 2000, in Protostars and Planets IV, ed. V. Mannings, A. P. Boss, & S. S. Russell, 59

André, P., Men'shchikov, A., Bontemps, S., et al. 2010, A&A, 518, L102

Andrianasolo, A. 2019, PhD thesis, thèse de doctorat dirigée par Ponthieu, Nicolas et Désert, François-Xavier Astrophysique et milieux dilues Université Grenoble Alpes (ComUE) 2019

Arzoumanian, D., André, P., Peretto, N., & Könyves, V. 2013, A&A, 553, A119

Arzoumanian, D., André, P., Didelon, P., et al. 2011, A&A, 529, L6

Arzoumanian, D., André, P., Könyves, V., et al. 2019, A&A, 621, A42

Arzoumanian, D., Furuya, R. S., Hasegawa, T., et al. 2021, A&A, 647, A78

Audit, E., & Hennebelle, P. 2005, A&A, 433, 1

Baars, J. W. M., Hooghoudt, B. G., Mezger, P. G., & de Jonge, M. J. 1987, A&A, 175, 319

Ballesteros-Paredes, J., Vázquez-Semadeni, E., & Scalo, J. 1999, ApJ, 515, 286

Ballesteros-Paredes, J., André, P., Hennebelle, P., et al. 2020, Space Sci. Rev., 216, 76

Bally, J. 2008, Overview of the Orion Complex, ed. B. Reipurth, Vol. 4, 459

Bally, J., Langer, W. D., Stark, A. A., & Wilson, R. W. 1987, ApJ, 312, L45

Barnard, E. E. 1907, ApJ, 25, 218

—. 1919, ApJ, 49, 1

Barvainis, R., Clemens, D. P., & Leach, R. 1988, AJ, 95, 510

Bastien, P., Bissonnette, E., Simon, A., et al. 2011, in Astronomical Society of the Pacific Conference Series, Vol. 449, Astronomical Polarimetry 2008: Science from Small to Large Telescopes, ed. P. Bastien, N. Manset, D. P. Clemens, & N. St-Louis, 68

Belitsky, V., Bylund, M., Desmaris, V., et al. 2018, A&A, 611, A98

Beltrán, M. T., Padovani, M., Girart, J. M., et al. 2019, A&A, 630, A54

Bino, G., & Basu, S. 2021, ApJ, 911, 15

Bino, G., Basu, S., Sharkawi, M., & Das, I. 2022, New A, 90, 101667

Blake, G. A., Keene, J., & Phillips, T. G. 1985, ApJ, 295, 501

Blitz, L. 1993, in Protostars and Planets III, ed. E. H. Levy & J. I. Lunine, 125

Bonnell, I. 1997, in Astronomical Society of the Pacific Conference Series, Vol. 130, The Third Pacific Rim Conference on Recent Development on Binary Star Research, ed. K.-C. Leung, 1

Bonnor, W. B. 1956, MNRAS, 116, 351

Born, M., & Wolf, E. 1980, Principles of Optics Electromagnetic Theory of Propagation, Interference and Diffraction of Light

Bourrion, O., Benoit, A., Bouly, J. L., et al. 2016, Journal of Instrumentation, 11, P11001

Bracco, A., Palmeirim, P., André, P., et al. 2017, A&A, 604, A52

Burton, M. G., Brand, P. W. J. L., Geballe, T. R., & Webster, A. S. 1989, MNRAS, 236, 409

Burton, M. G., Minchin, N. R., Hough, J. H., et al. 1991, ApJ, 375, 611

Calvo, M., Benoît, A., Catalano, A., et al. 2016, Journal of Low Temperature Physics, 184, 816

Carter, M., Lazareff, B., Maier, D., et al. 2012, A&A, 538, A89

Catalano, A., Calvo, M., Ponthieu, N., et al. 2014, A&A, 569, A9

Chandrasekhar, S., & Fermi, E. 1953, ApJ, 118, 113

Chapman, N. L., Goldsmith, P. F., Pineda, J. L., et al. 2011, ApJ, 741, 21

Chini, R., Reipurth, B., Ward-Thompson, D., et al. 1997, ApJ, 474, L135

Chuss, D. T., Andersson, B. G., Bally, J., et al. 2019, ApJ, 872, 187

Clark, F. O., Johnson, D. R., Heiles, C. E., & Troland, T. H. 1978, ApJ, 226, 824

Clemens, D. P., Leach, R. W., Barvainis, R., & Kane, B. D. 1990, PASP, 102, 1064

Clemens, D. P., Sarcia, D., Grabau, A., et al. 2007, PASP, 119, 1385

Coppin, K. E. K., Greaves, J. S., Jenness, T., & Holland, W. S. 2000, A&A, 356, 1031

Cortes, P. 2019, in ALMA2019: Science Results and Cross-Facility Synergies, 79

Cortes, P. C., Le Gouellec, V. J. M., Hull, C. L. H., et al. 2021, ApJ, 907, 94

Crutcher, R. M. 2004, in The Magnetized Interstellar Medium, ed. B. Uyaniker, W. Reich, & R. Wielebinski, 123–132

Crutcher, R. M. 2012, ARA&A, 50, 29

Crutcher, R. M., & Kemball, A. J. 2019, Frontiers in Astronomy and Space Sciences, 6, 66

Crutcher, R. M., Troland, T. H., Goodman, A. A., et al. 1993, ApJ, 407, 175

Crutcher, R. M., Troland, T. H., Lazareff, B., & Kazes, I. 1996, ApJ, 456, 217

Crutcher, R. M., Wandelt, B., Heiles, C., Falgarone, E., & Troland, T. H. 2010, ApJ, 725, 466

D'Addabbo, A., Adam, R., Adane, A., et al. 2013, arXiv e-prints, arXiv:1312.4801

Davis, Leverett, J., & Greenstein, J. L. 1951, ApJ, 114, 206

Davis, L. 1951, Physical Review, 81, 890

Di Francesco, J., Keown, J., Fallscheer, C., et al. 2020, ApJ, 904, 172

Didelon, P., Motte, F., Tremblin, P., et al. 2015, A&A, 584, A4

Dowell, C. D., Cook, B. T., Harper, D. A., et al. 2010, in Society of Photo-Optical Instrumentation Engineers (SPIE) Conference Series, Vol. 7735, Ground-based and Airborne Instrumentation for Astronomy III, ed. I. S. McLean, S. K. Ramsay, & H. Takami, 77356H

Draine, B. T. 2011, Physics of the Interstellar and Intergalactic Medium

Duvert, G., Cernicharo, J., & Baudry, A. 1986, A&A, 164, 349

Engel, C., Bernard, J.-P., Otrio, G., et al. 2017, in Society of Photo-Optical Instrumentation Engineers (SPIE) Conference Series, Vol. 10563, Society of Photo-Optical Instrumentation Engineers (SPIE) Conference Series, 105635T

Erickson, N. R., Snell, R. L., Loren, R. B., Mundy, L., & Plambeck, R. L. 1981, ApJ, 245, L83

Ewen, H. I., & Purcell, E. M. 1951, Nature, 168, 356

Ewertowski, B., & Basu, S. 2013, ApJ, 767, 33

Falceta-Gonçalves, D., Lazarian, A., & Kowal, G. 2008, ApJ, 679, 537

Fazio, G. G., Kleinmann, D. E., Noyes, R. W., et al. 1974, ApJ, 192, L23

Federrath, C. 2016, MNRAS, 457, 375

Ferrière, K. M. 2001, Reviews of Modern Physics, 73, 1031

Friberg, P., Berry, D., Savini, G., et al. 2018, in Society of Photo-Optical Instrumentation Engineers (SPIE) Conference Series, Vol. 10708, Millimeter, Submillimeter, and Far-Infrared Detectors and Instrumentation for Astronomy IX, ed. J. Zmuidzinas & J.-R. Gao, 107083M

Galitzki, N., Ade, P. A. R., Angilè, F. E., et al. 2014, Journal of Astronomical Instrumentation, 3, 1440001

Girart, J. M., Rao, R., & Marrone, D. P. 2006, Science, 313, 812

Goldsmith, P. F., Heyer, M., Narayanan, G., et al. 2008, ApJ, 680, 428

Goodman, A. A., Jones, T. J., Lada, E. A., & Myers, P. C. 1992, ApJ, 399, 108

Greaves, J. S., & Church, S. E. 1996, MNRAS, 283, 1179

Greaves, J. S., & White, G. J. 1991, A&A, 248, L27

Greve, A., Morris, D., Penalver, J., Thum, C., & Bremer, M. 2010, IEEE Transactions on Antennas and Propagation, 58, 959

Guerra, J. A., Chuss, D. T., Dowell, C. D., et al. 2021, ApJ, 908, 98

Hacar, A., & Tafalla, M. 2011, A&A, 533, A34

Hacar, A., Tafalla, M., Kauffmann, J., & Kovács, A. 2013, A&A, 554, A55

Harper, D. A., Runyan, M. C., Dowell, C. D., et al. 2018, Journal of Astronomical Instrumentation, 7, 1840008

Heiles, C., Goodman, A. A., McKee, C. F., & Zweibel, E. G. 1993, in Protostars and Planets III, ed. E. H. Levy & J. I. Lunine, 279

Heitsch, F., Zweibel, E. G., Mac Low, M.-M., Li, P., & Norman, M. L. 2001, ApJ, 561, 800

Hennebelle, P., & André, P. 2013, A&A, 560, A68

Hennebelle, P., Commerçon, B., Chabrier, G., & Marchand, P. 2016, ApJ, 830, L8

Hennebelle, P., & Fromang, S. 2008, A&A, 477, 9

Herrmann, F., Madden, S. C., Nikola, T., et al. 1997, ApJ, 481, 343

Herschel, W. 1785, Philosophical Transactions of the Royal Society of London Series I, 75, 213

Hildebrand, R. H., Dotson, J. L., Dowell, C. D., et al. 1995, in Astronomical Society of the Pacific Conference Series, Vol. 73, From Gas to Stars to Dust, ed. M. R. Haas, J. A. Davidson, & E. F. Erickson, 97–104

Hildebrand, R. H., Kirby, L., Dotson, J. L., Houde, M., & Vaillancourt, J. E. 2009, ApJ, 696, 567

Houde, M., Hull, C. L. H., Plambeck, R. L., Vaillancourt, J. E., & Hildebrand, R. H. 2016, ApJ, 820, 38

Houde, M., Vaillancourt, J. E., Hildebrand, R. H., Chitsazzadeh, S., & Kirby, L. 2009, ApJ, 706, 1504

Hubble, E. 1929, Proceedings of the National Academy of Science, 15, 168

Inutsuka, S.-i. 2001, ApJ, 559, L149

Inutsuka, S.-i., Inoue, T., Iwasaki, K., & Hosokawa, T. 2015, A&A, 580, A49

Inutsuka, S.-i., & Miyama, S. M. 1997, ApJ, 480, 681

Jeans, J. H. 1902, Philosophical Transactions of the Royal Society of London Series A, 199, 1

Johnstone, D., & Bally, J. 1999, ApJ, 510, L49

Juvela, M., Ristorcelli, I., Montier, L. A., et al. 2010, A&A, 518, L93

Keene, J., Hildebrand, R. H., & Whitcomb, S. E. 1982, ApJ, 252, L11

Kleinmann, D. E., & Low, F. J. 1967, ApJ, 149, L1

Koch, E. W., & Rosolowsky, E. W. 2015, MNRAS, 452, 3435

Koch, P. M., Tang, Y.-W., & Ho, P. T. P. 2012, ApJ, 747, 80

Kolmogorov, A. N. 1941, Akademiia Nauk SSSR Doklady, 32, 16

Könyves, V., André, P., Men'shchikov, A., et al. 2015, A&A, 584, A91

Könyves, V., André, P., Arzoumanian, D., et al. 2020, A&A, 635, A34

Lacy, J. H., Evans, Neal J., I., Achtermann, J. M., et al. 1989, ApJ, 342, L43

Lada, C. J. 1987, in Star Forming Regions, ed. M. Peimbert & J. Jugaku, Vol. 115, 1

Ladjelate, B., André, P., Könyves, V., et al. 2020, A&A, 638, A74

Larson, R. B. 1969, MNRAS, 145, 271

—. 1981, MNRAS, 194, 809

Lazarian, A., Andersson, B. G., & Hoang, T. 2015, Grain alignment: Role of radiative torques and paramagnetic relaxation, 81

Lazarian, A., & Hoang, T. 2007, ApJ, 669, L77

Lee, D., Berthoud, M., Chen, C.-Y., et al. 2021, ApJ, 918, 39

Li, D., & Goldsmith, P. F. 2012, ApJ, 756, 12

Li, P. S., Lopez-Rodriguez, E., Ajeddig, H., et al. 2021, MNRAS, arXiv:2111.12864

Li, P. S., McKee, C. F., & Klein, R. I. 2015, MNRAS, 452, 2500

Lopez-Rodriguez, E. 2021, Nature Astronomy, 5, 604

Lopez-Rodriguez, E., Fuller, L., Alonso-Herrero, A., et al. 2018, ApJ, 859, 99

Loren, R. B., Mundy, L., & Erickson, N. R. 1981, ApJ, 250, 573

Loren, R. B., & Wootten, A. 1986, ApJ, 310, 889

Mac Low, M.-M., & Klessen, R. S. 2004, Reviews of Modern Physics, 76, 125

Marsh, K. A., Kirk, J. M., André, P., et al. 2016, MNRAS, 459, 342

Masson, C. R., Lo, K. Y., Phillips, T. G., et al. 1987, ApJ, 319, 446

McKee, C. F., & Ostriker, E. C. 2007, ARA&A, 45, 565

McKee, C. F., & Ostriker, J. P. 1977, ApJ, 218, 148

Men'shchikov, A., André, P., Didelon, P., et al. 2012, A&A, 542, A81

Michail, J. M., Chuss, D., Dowell, C. D., et al. 2018, in American Astronomical Society Meeting Abstracts, Vol. 231, American Astronomical Society Meeting Abstracts #231, 152.21

Minh, Y. C., Ziurys, L. M., Irvine, W. M., & McGonagle, D. 1990, ApJ, 360, 136

Misugi, Y., Inutsuka, S.-i., & Arzoumanian, D. 2019, ApJ, 881, 11

Miville-Deschênes, M.-A., Murray, N., & Lee, E. J. 2017, ApJ, 834, 57

Molinari, S., Swinyard, B., Bally, J., et al. 2010, A&A, 518, L100

Moneti, A., Pipher, J. L., Helfer, H. L., McMillan, R. S., & Perry, M. L. 1984, ApJ, 282, 508

Motte, F., Zavagno, A., Bontemps, S., et al. 2010, A&A, 518, L77

Mouschovias, T. C. 1976, ApJ, 207, 141

—. 1991, ApJ, 373, 169

Mundy, L. G., Scoville, N. Z., Baath, L. B., Masson, C. R., & Woody, D. P. 1986, ApJ, 304, L51

Murata, Y., Kawabe, R., Ishiguro, M., et al. 1990, ApJ, 359, 125

Myers, P. C. 1983, ApJ, 270, 105

Myers, P. C., & Basu, S. 2021, ApJ, 917, 35

Myers, P. C., Dame, T. M., Thaddeus, P., et al. 1986, ApJ, 301, 398

Myers, P. C., & Goodman, A. A. 1991, ApJ, 373, 509

Nakano, T., & Nakamura, T. 1978, PASJ, 30, 671

Novak, G., Gonatas, D. P., Hildebrand, R. H., Platt, S. R., & Dragovan, M. 1989, ApJ, 345, 802

Ostriker, E. C., Stone, J. M., & Gammie, C. F. 2001, ApJ, 546, 980

Padoan, P., Goodman, A., Draine, B. T., et al. 2001, ApJ, 559, 1005

Palmeirim, P., André, P., Kirk, J., et al. 2013, A&A, 550, A38

Pardo, J. R., Cernicharo, J., & Serabyn, E. 2001, IEEE Transactions on Antennas and Propagation, 49, 1683

Pattle, K., & Fissel, L. 2019, Frontiers in Astronomy and Space Sciences, 6, 15

Pattle, K., Ward-Thompson, D., Berry, D., et al. 2017a, ApJ, 846, 122

—. 2017b, ApJ, 846, 122

Pattle, K., Lai, S.-P., Di Francesco, J., et al. 2021, ApJ, 907, 88

Penston, M. V. 1969a, MNRAS, 145, 457

—. 1969b, MNRAS, 144, 425

Perotto, L., Ponthieu, N., Macías-Pérez, J. F., et al. 2020, A&A, 637, A71

Pezzuto, S., Benedettini, M., Di Francesco, J., et al. 2021, A&A, 645, A55

Pilbratt, G. L., Riedinger, J. R., Passvogel, T., et al. 2010, A&A, 518, L1

Pisano, G., Maffei, B., Ng, M. W., et al. 2014, in Society of Photo-Optical Instrumentation Engineers (SPIE) Conference Series, Vol. 9153, Millimeter, Submillimeter, and Far-Infrared Detectors and Instrumentation for Astronomy VII, ed. W. S. Holland & J. Zmuidzinas, 915317

Pisano, G., Ritacco, A., Monfardini, A., et al. 2020, arXiv e-prints, arXiv:2006.12081

Planck Collaboration, Ade, P. A. R., Aghanim, N., et al. 2015, A&A, 576, A104

Planck Collaboration, Adam, R., Ade, P. A. R., et al. 2016a, A&A, 586, A135

Planck Collaboration, Ade, P. A. R., Aghanim, N., et al. 2016b, A&A, 586, A136

—. 2016c, A&A, 586, A138

Platt, S. R., Hildebrand, R. H., Pernic, R. J., Davidson, J. A., & Novak, G. 1991, PASP, 103, 1193

Ritacco, A. 2016, PhD thesis, thèse de doctorat dirigée par Macias-Pérez, Juan-Francisco et Monfardini, Alessandro Physique subatomique et astroparticules Université Grenoble Alpes (ComUE) 2016

Ritacco, A., Ponthieu, N., Catalano, A., et al. 2017, A&A, 599, A34

Rodriguez-Franco, A., Martin-Pintado, J., & Fuente, A. 1998, A&A, 329, 1097

Roy, A., André, P., Arzoumanian, D., et al. 2015, A&A, 584, A111

Salji, C. J., Richer, J. S., Buckle, J. V., et al. 2015, MNRAS, 449, 1782

Schleuning, D. A. 1998, ApJ, 493, 811

Schmalzl, M., Kainulainen, J., Quanz, S. P., et al. 2010, ApJ, 725, 1327

Schuller, F., André, P., Shimajiri, Y., et al. 2021, A&A, 651, A36

Seo, Y. M., Dowell, C. D., Goldsmith, P. F., Pineda, J. L., & Majumdar, L. 2021, ApJ, 917, 57

Shimajiri, Y. 2019, in ALMA2019: Science Results and Cross-Facility Synergies, 30

Shimajiri, Y., André, P., Palmeirim, P., et al. 2019, A&A, 623, A16

Shu, F. H. 1977, ApJ, 214, 488

Shu, F. H., Adams, F. C., & Lizano, S. 1987, ARA&A, 25, 23

Siringo, G., Kreysa, E., Reichertz, L. A., & Menten, K. M. 2004a, A&A, 422, 751

Siringo, G., Kreysa, E., Reichertz, L. A., & Menten, K. M. 2004b, in The Magnetized Interstellar Medium, ed. B. Uyaniker, W. Reich, & R. Wielebinski, 215–220

Smith, M. D. 1991, MNRAS, 253, 175

Smith, M. D., & Brand, P. W. J. L. 1990, MNRAS, 245, 108

Smith, N., Bally, J., Shuping, R. Y., Morris, M., & Hayward, T. L. 2004, ApJ, 610, L117

Soler, J. D. 2019, A&A, 629, A96

Soler, J. D., & Hennebelle, P. 2017, A&A, 607, A2

Soler, J. D., Alves, F., Boulanger, F., et al. 2016, A&A, 596, A93

Spoelstra, T. A. T. 1972, A&AS, 5, 205

Stolovy, S. R., Burton, M. G., Erickson, E. F., et al. 1998, ApJ, 492, L151

Tafalla, M., Myers, P. C., Caselli, P., Walmsley, C. M., & Comito, C. 2002, ApJ, 569, 815

Tanabe, Y., Nakamura, F., Tsukagoshi, T., et al. 2019, PASJ, 71, S8

Tielens, A. G. G. M., & Hollenbach, D. 1985, ApJ, 291, 747

Troland, T. H., Crutcher, R. M., & Kazes, I. 1986, ApJ, 304, L57

Troland, T. H., & Heiles, C. 1982, ApJ, 252, 179

Vaillancourt, J. E., Chuss, D. T., Crutcher, R. M., et al. 2007, in Society of Photo-Optical Instrumentation Engineers (SPIE) Conference Series, Vol. 6678, Infrared Spaceborne Remote Sensing and Instrumentation XV, ed. M. Strojnik-Scholl, 66780D

Vaillancourt, J. E., Dowell, C. D., Hildebrand, R. H., et al. 2008, ApJ, 679, L25

Vallée, J. P., & Fiege, J. D. 2007, AJ, 133, 1012

Verschuur, G. L. 1968, Phys. Rev. Lett., 21, 775

Wang, T. Y., Wouterloot, J. G. A., & Wilson, T. L. 1993, A&A, 277, 205

Ward-Thompson, D., Kirk, J. M., Crutcher, R. M., et al. 2000, ApJ, 537, L135

Wardle, J. F. C., & Kronberg, P. P. 1974, ApJ, 194, 249

Wiesemeyer, H., Hezareh, T., Kreysa, E., et al. 2014, PASP, 126, 1027

Williams, J. P., Blitz, L., & McKee, C. F. 2000, in Protostars and Planets IV, ed. V. Mannings, A. P. Boss, & S. S. Russell, 97

Wilson, R. W., Jefferts, K. B., & Penzias, A. A. 1970, ApJ, 161, L43

Wiseman, J. J., & Ho, P. T. P. 1998, ApJ, 502, 676

Wootten, A., Mangum, J. G., Turner, B. E., et al. 1991, ApJ, 380, L79

Ziurys, L. M., & Friberg, P. 1987, ApJ, 314, L49

Ziurys, L. M., Martin, R. N., Pauls, T. A., & Wilson, T. L. 1981, A&A, 104, 288

Ziurys, L. M., Wilson, T. L., & Mauersberger, R. 1990, ApJ, 356, L25

Zylka, R. 2013, MOPSIC: Extended Version of MOPSI, ascl:1303.011

Appendix A

Mapping the magnetic field in the Taurus/B211 filamentary cloud with SOFIA HAWC + and comparing with simulation

Li, Pak Shing search by orcid ; Lopez-Rodriguez, Enrique ; Ajeddig, Hamza ; André, Philippe ; McKee, Christopher F. search by orcid ; Rho, Jeonghee ; Klein, Richard I.

DOI: 10.1093/mnras/stab3448

Mapping the magnetic field in the Taurus/B211 filamentary cloud with SOFIA HAWC+ and comparing with simulation

Pak Shing Li[1]* (PSL), Enrique Lopez-Rodriguez[2], Hamza Ajeddig[3],
Philippe André[3], Christopher F. McKee[1], Jeonghee Rho[4], Richard I. Klein[1,5]
[1] *Astronomy Department, University of California, Berkeley, CA 94720*
[2] *Kavli Institute for Particle Astrophysics and Cosmology (KIPAC), Stanford University, Stanford, CA 94305, USA*
[3] *Laboratoire d'Astrophysique (AIM), CEA/DRF, CNRS, Université Paris-Saclay, Université Paris Diderot, Sorbonne Paris Cité, 91191 Gif-sur-Yvette, France*
[4] *SETI Institute, 189 N. Bernardo Ave., Ste. 200, Mountain View, CA 94043*
[5] *Lawrence Livermore National Laboratory,P.O.Box 808, L-23, Livermore, CA 94550*

ABSTRACT

Optical and infrared polarization mapping and recent Planck observations of the filametary cloud L1495 in Taurus show that the large-scale magnetic field is approximately perpendicular to the long axis of the cloud. We use the HAWC+ polarimeter on SOFIA to probe the complex magnetic field in the B211 part of the cloud. Our results reveal a dispersion of polarization angles of 36°, about five times that measured on a larger scale by Planck. Applying the Davis-Chandrasekhar-Fermi (DCF) method with velocity information obtained from IRAM 30m $C^{18}O(1\text{-}0)$ observations, we find two distinct sub-regions with magnetic field strengths differing by more than a factor 3. The quieter sub-region is magnetically critical and sub-Alfvénic; the field is comparable to the average field measured in molecular clumps based on Zeeman observations. The more chaotic, super-Alfvénic sub-region shows at least three velocity components, indicating interaction among multiple substructures. Its field is much less than the average Zeeman field in molecular clumps, suggesting that the DCF value of the field there may be an underestimate. Numerical simulation of filamentary cloud formation shows that filamentary substructures can strongly perturb the magnetic field. DCF and true field values in the simulation are compared. Pre-stellar cores are observed in B211 and are seen in our simulation. The appendices give a derivation of the standard DCF method that allows for a dispersion in polarization angles that is not small, present an alternate derivation of the structure function version of the DCF method, and treat fragmentation of filaments.

Key words: techniques: polarimetric, ISM:magnetic fields, ISM:clouds, ISM:kinematics and dynamics, ISM: structure, methods:numerical

1 INTRODUCTION

Filamentary structures have been found at almost all size scales in the Galaxy. Massive, long filamentary dark clouds are commonly found inside giant molecular clouds (GMCs; e.g. Bergin & Tafalla 2007; André et al. 2014, and references therein), such as the dark clouds L1495 in the Taurus cloud complex (e.g. Chapman et al. 2011) and the Serpens South cloud in the Serpens region (e.g. Dhabal et al. 2018). Filamentary clouds of 4 to 6 pc length are common, and possibly longer than 10 pc. Some of these clouds are dark at infrared wavelengths. The line-width size relation observed for molecular gas indicates that the thermal Mach number would exceed 10 at such size scales. The long-term survival of these filamentary structures requires a reinforcing mechanism. As shown in the ideal magnetohydrodynamical (MHD) simulations of Li & Klein (2019), a moderately strong, large-scale magnetic field (Alfvén Mach number, $\mathcal{M}_A \sim 1$) can provide such a mechanism. In the weak-field model with $\mathcal{M}_A = 10$, the appearance of molecular clouds is clumpy, rather than the long and slender filamentary clouds seen in moderately strong field models. High resolution images of massive molecular clouds from the *Herschel space telescope* reveal complex filamentary substructures (e.g. André et al. 2014). The characteristic inner width of molecular filaments found with *Herschel* is about ~ 0.1 pc (Arzoumanian 2011; Arzoumanian et al. 2019). Dense cores, where stars form, are located along or at the intersections of some of these fine substructures (e.g. Könyves et al. 2015; Tafalla & Hacar 2015). From these observations of molecular cloud structures at different size

---

* E-mail:psli@berkeley.edu

scales, one can visualize an evolutionary sequence of star formation starting from highly supersonic, magnetized GMCs, continuing on to filamentary dark clouds that form within them, and then on to finer filamentary substructures. Fragmentation of these filamentary structures and substructures leads to the clumps and dense cores that form protostellar clusters and protostars. Knowing the physical conditions inside filamentary clouds would provide crucial information on the formation of filamentary substructures and dense cores, and on the origin of the initial mass function (IMF) and the star formation rate. Particularly important is the characterization of the physical properties of transcritical filamentary structures whose mass per unit length is within a factor of $\sim$2 of the critical line mass $M_{\rm crit,\,th,\,\ell} = 2\,c_{\rm s}^2/G$ of nearly isothermal cylindrical filaments (e.g. Ostriker 1964; Inutsuka & Miyama 1997), where $c_{\rm s}$ is the isothermal sound speed. Indeed, *Herschel* observations suggest that transcritical filamentary structures dominate the mass function of star-forming filaments and that their fragmentation may set the peak of the prestellar core mass function and perhaps ultimately the peak of the IMF (André et al. 2019). In this paper, we report the results of polarimetric observations of the pristine section B211 of one such transcritical filament, the Taurus B211/B213 filament, using the High-resolution Airborne Wideband Campera plus (HAWC+) onboard Stratospheric Observatory For Infrared Astronomy (SOFIA). We determine the magnetic field structure inside a filamentary cloud with filamentary substructures.

The filamentary cloud L1495 is located in the Taurus molecular cloud at a distance of about 140 pc (Elias 1978). Using their H-band polarization observation and the Davis-Chandrasekhar-Fermi (DCF) method (Davis 1951; Chandrasekhar & Fermi 1953), Chapman et al. (2011) estimated the plane-of-sky (POS) magnetic field strength to be $10-17$ μG in the low density regions near the L1495 cloud, including the B211 region, and $25-28$ μG inside the cloud. From observations of ^{12}CO and ^{13}CO, they find that the velocity dispersion is $0.85-1.16$ km s^{-1}. Their observations have a resolution of 0.135 pc. The mean surface density is about $N(\mathrm{H}_2) \sim 1.45\times10^{22}$ cm^{-2} (Palmeirim et al. 2013). Using the density estimated by Hacar et al. (2013) and the measured velocity dispersion ~ 1 km s^{-1} cited above, the Alfvén Mach number of the long filamentary cloud is about 2.7. Combining the polarization observations of Heiles (2000), Heyer et al. (2008), and Chapman et al. (2011), Palmeirim et al. (2013) found that the large-scale mean field direction is almost orthogonal to the cloud axis in B211/B213 and roughly parallel to faint striations seen in both CO and *Herschel* data. There is also some kinematic evidence that the B211/B213 filament is embedded in a sheet- or shell-like ambient cloud and in the process of accreting mass from this ambient cloud (Shimajiri et al. 2019), perhaps through the magnetically-aligned striations. Is it possible that the magnetic field pierces straight through the cloud? If so, then the picture of the formation of filamentary clouds is simple: gas is simply gathered into the cloud along approximately straight field lines.

A portion of the Taurus/B213 filament was recently mapped with JCMT-POL2 as part of the BISTRO project (Eswaraiah et al. 2021), but the corresponding 850 μm polarization data only constrained the magnetic field toward the dense cores within the filament. Other recent high-resolution polarization observations of magnetic field structures within more massive molecular clouds, such as Vela C (Soler et al. 2013, 2017; Dall'Olio et al. 2019) and M17 SWex (Sugitani et al. 2019), show that magnetic fields inside dense filamentary clouds with complex substructures are not simple. Magnetic fields inside clouds can have large deviations from the large-scale field orientation. Within the $\sim$ 0.8 pc outer diameter measured on *Herschel* data, the B211/B213 filament system has a characteristic half-power width of $\sim$ 0.1 pc and exhibits complex filamentary substructures (Palmeirim et al. 2013; Hacar et al. 2013). Hacar et al. (2013) found that the B211 region has a mass of 138 M$_\odot$ and is roughly 2 pc long. From their C^{18}O intensity map, the width of the B211 region encompassed by the lowest C^{18}O contour is about 0.3 pc. Hacar et al. (2013) identified multiple velocity components in C^{18}O at different locations in B211-B213 with separations as large as about 2 km s^{-1}. Tafalla & Hacar (2015) find that the relative velocities between filamentary substructures in the filamentary cloud range over 2.2 km s^{-1}, possibly implying that the substructures are converging at high velocity. B211 is very bright in both C^{18}O and SO and has intense dust millimeter emission. The gas in B211 has an unusually young chemical composition and lack of young stellar objects, indicating that this region is at a very early state of evolution (Hacar et al. 2013). This region is therefore particularly suitable for the study of magnetic field structures in filamentary clouds without any confusion from protostellar activity.

In the high-resolution infrared dark cloud (IRDC) simulation by Li & Klein (2019) using the adaptive mesh refinement code ORION2, a long filamentary cloud is formed in a moderately strong magnetic field environment, even though the thermal Mach number was 10. The long filamentary cloud created in the simulation has filamentary substructures similar to those in L1495. The simulation may therefore provide unique information on the physical environment inside filamentary clouds and on how they form. In the simulation, the large scale magnetic field is approximately perpendicular to the cloud axis, similar to the case in L1495. However, the small-scale magnetic field inside the simulated cloud, which has a width similar to that of B211, has a chaotic structure. Until now, there has never been a polarimetric observation with a resolution and a sensitivity high enough to peer into a filamentary cloud with no star formation. This motivates us to map a portion of L1495 to determine the field morphology inside the cloud and thereby gain an understanding of the physical environment inside such a cloud.

We report in this paper our observations of the filamentary cloud L1495/B211 using the recently optimized HAWC+ polarimeter on SOFIA to probe the complex magnetic field inside a slender filamentary cloud with complex filamentary substructures. The observation using HAWC+ polarimeter, the data reduction method, and the results are presented in Section 2. In Section 3, we investigate the physical state of the B211 region from observation. Using the DCF method, we estimate the magnetic field strength in Section 3.1 with the aid of recent C^{18}O (1-0) line emission data from the IRAM 30m telescope. In Section 3.2, we study the relation between the inferred magnetic field from HAWC+ observation and the surface density contours. In Section 4, results of our numerical simulation of filamentary clouds is used to provide insights into the physical state of B211. Our conclusions are presented in Section 5.

2 OBSERVATIONS

2.1 SOFIA HAWC+ mapping observations and data reduction methods

L1495 was observed (ID: 07_0017, PI: Li, P.S.) at 214 μm ($\Delta\lambda = 44$ μm, full width at half maximum, FWHM) using HAWC+ (Vaillancourt et al. 2007; Dowell et al. 2010; Harper et al. 2018) on the 2.7-m SOFIA telescope. HAWC+ polarimetric observations simultaneously measure two orthogonal components of linear polarization arranged in two arrays of 32×40 pixels each, with a detector pixel scale of $9\farcs37$ pixel^{-1} and beam size (FWHM) of $18\farcs2$ at 214 μm. At 214 μm, HAWC+ suffers of vignetting where five columns cannot be used for scientific analysis (Harper et al. 2018), therefore the field-of-view (FOV) of the polarimetric mode is 4.2×6.2 sqarcmin. We performed observations using the on-the-fly-map (OTFMAP) polarimetric mode. This technique is an experimental observing mode performed during SOFIA Cycle 7 observations as part of the shared-risk time to optimize the polarimetric observations of HAWC+. Although we will focus on the scientific results of L1495, we here describe the high-level observational steps used in these these observations, where Sections 2.2 and 2.3 describe the details of the OTFMAP polarimetric mode.

We performed OTFMAP polarimetric observations in a sequence of four Lissajous scans, where each scan has a different halfwave plate (HWP) position angle in the following sequence: 5°, 50°, 27.5°, and 72.5°. This sequence is called ‘set’ hereafter (Table 1-column 9). In this new HAWC+ observing mode, the telescope is driven to follow a parametric curve at a nonrepeating period whose shape is characterized by the relative phases and frequency of the motion. Each scan is characterized by the scan angle, scan amplitude, scan rate, scan phase, and scan duration. The scan angle is the relative angle of the cross-elevation direction of the FOV of the scan with respect to north, where 0° is North and positive increase is in the east of north direction (Table 1-column 7). An example of the OTFMAP for total intensity observations of NGC 1068 using HAWC+/SOFIA is shown by Lopez-Rodriguez et al. (2018, fig. 1). The OTFMAP polarimetic mode using HAWC+/SOFIA at 89 μm has recently been successfully applied to the galaxy Centaurus A (Lopez-Rodriguez 2021). A summary of the observations at 214 μm are shown in Table 1. We performed square scans (Table 1-column 8) at three different positions as shown in Table 1 (column 5 and 6). After combining all scans, the full FOV is 20 × 20 sqarcmin. Although Table 1 lists all performed observations for this program with a total executed time of 6.37h, only a final executed time of 4.73h (with a total on-source time of 4.40h) was used for scientific analysis. The removed sets listed in Table 1 were not used due to loss of tracking during observations.

We reduced the data using the Comprehensive Reduction Utility for SHARP II v.2.42-1 (CRUSH; Kovács et al. 2006, 2008) and the HAWC_DRP_v2.3.2 pipeline developed by the data reduction pipeline group at the SOFIA Science Center. Each scan was reduced by CRUSH, which estimates and removes the correlated atmospheric and instrumental signals, solves for the relative detector gains, and determines the noise weighting of the time streams in an iterated pipeline scheme. Each reduced scan produces two images associated with each array. Both images are orthogonal components of linear polarization at a given HWP position angle. We estimated the Stokes I, Q, U parameters using the double difference method in the same manner as the standard chop-nod observations carried by HAWC+ described in Section 3.2 by Harper et al. (2018). The degree (P) and position angle of polarization were corrected by instrumental polarization (IP) estimated using OTFMAP polarization observations of planets. We estimated an IP of $Q/I = -1.0\%$ and $U/I = -1.4\%$ at 214 μm respectively, with an estimated uncertainty of $\sim 0.8\%$. The IP using OTFMAP observations are in agreement with the estimated IP using chop-nod observations. To ensure the correction of the position angle of polarization of the instrument with respect to the sky, we took each set with a fixed line-of-sight (LOS) of the telescope. For each set, we rotated the Stokes Q and U from the instrument to the sky coordinates. The polarization fraction was debiased (Wardle & Kronberg 1974) and corrected by a polarization efficiency of 97.8% at 214 μm. The final Stokes I and its associated errors were calculated and downsampled to the beam size ($18\farcs20$). The final Stokes Q, U, P, position angle, polarized intensity (PI), and their associated errors were calculated and re-sampled to a super-pixel of 3×3 detector pixel size, which corresponds to a re-sampled pixel size of $28\farcs1$ (or 0.019 pc at the distance of the cloud). This super-pixel was chosen to optimize the signal-to-noise ratio (SNR), obtain statistically independent measurements and significant polarization measurements without compromising spatial resolution for the data analysis.

2.2 HAWC+ OTFMAP polarization: advantages and limitations

Several advantages and limitations are found with the OTFMAP polarization mode. The advantages are the reduction of overheads and radiative offsets when compared with the chop-nod technique. The overheads of the OTFMAP are estimated to be 1.1 in comparison with the typical overheads of 2.7 by the chop-nod technique, which shows an improvement by a factor $\geqslant 2$. This improvement is due to OTFMAP constantly integrating with the source on the FOV while covering off-source regions to estimate the background levels, and observing overheads. For the OTFMAP method, the telescope is always on-axis, without chopping the secondary mirror as it is in the chop-nod technique. Thus, the radiative offset is not present and the sensitivity of the observations was estimated to improve by a factor of 1.6. The OTFMAP technique provides a larger map area when compared to the chop-nod technique. Our observations were taken at three different positions covering a FOV of 10 × 10 and 11 × 11 sqarcmin, yield a final FOV of 20 × 20 sqarcmin. Note the advantage of the large FOV by the OTFMAP when compared with the single 4.2 × 6.2 sqarcmin by the chop-nod technique.

The limitation of the OTFMAP technique lies in the recovering of large-scale diffuse and faint emission from the astrophysical objects. This is a result of the finite size of the array, variable atmosphere conditions, variable detector temperatures, and the applied filters in the reduction steps to recover extended emission. We applied several filters using CRUSH to recover large-scale emission structures of L1495 while paying close attention to any change that may compromise the intrinsic polarization pattern of the astrophysical

Table 1. Summary of OTFMAP polarimetric observations

Date (YYYYMMDD)	Flight Number	Altitude (ft)	RA (h)	DEC (°)	Scan Time (s)	Scan Angle (°)	Scan Amplitude (EL × XEL; $''$)	# Sets used (removed)
20190904	F605	41000	4.3036	27.5415	120	-30.0, 0.0, 23.7	300×300	1 (2)
					60	-23.7	300×300	1
20190905	F606	42000, 43000	4.3036	27.5415	60	-30.0, -26.8, 30, -20.5, -17.4, -14.2, -7.9, -4.7	300×300	8 (1)
20190907	F607	42000, 43000	4.3036	27.5415	120	-30.0, -26.7, -23.7, -20.5, -17.4, -14.2, -11.0	300×300	7
20190910	F608	42000, 43000	4.3075	27.4836	120	-30.0, -26.8, -23.7, -20.5, -17.4, -14.2, -11.0, -7.8, -4.7, -1.6	300×300	10
20190918	F611	42000, 43000	4.3036	27.5415	120	-30.0, -28.8, -23.7, -20.5, -17.4, -14.2, -11.0, -7.9	300×300	0 (8)
20191010	F621	43000	4.3075	27.4836	120	-30.0, -26.8, -23.7, 0.0, -7.1, -14.2, 30.0, 12.6, -4.7, 60.0	330×330	10

object. We conclude that the FAINT filter with a number of 30 iterations from CRUSH can recover large-scale emission structures larger than the Band E FOV from our observations of L1495. The FAINT option applies filtering to the timestreams and extended structures to recover fluxes with SNR < 10 in a single scan. In addition, the number of rounds are such as that the iterative pipeline is able to recover large-scale structures without introducing additional artificial structures not identified in the *Herschel* images. In general, the noise increases as a function of the length, L, of the extended emission as $\sim L^2$. We force each individual scan produced by CRUSH to have a pixel scale of 3×3 detector pixels ($28.''1$), which increase the SNR of each scan by a factor of 3 helping to recover larger and fainter structures.

2.3 HAWC+ OTFMAP polarization: zero-level background

An important step is the estimation of the zero-level background of the observations. We remind the reader that HAWC+ measures the power of the emissive and variable atmosphere and the astrophysical object. The data reduction scheme described above produces regions of negative fluxes in areas of extended and low surface brightness due to the similar levels of noise and astrophysical signal. Thus, it is of great importance to characterize and estimate the zero-level background across the observations of L1495, because there is a potential loss of flux that requires to be estimated and added to the full image.

We have determined and corrected the zero-level background of our observations as follows. Using *Herschel* images at 160 and 250 μm from the *Herschel* Archive[1], we identified a region in the sky where the fluxes of an individual pixel of size $28.''1$ are below the sensitivity of HAWC+ at 214 μm. This area is shown in Fig. 1, which is located in a common region for all scans across the multiple flights. The size of this region is chosen to be equal to the HAWC+ FOV at Band E, i.e. 4.2×6.2 sqarcmin. The size of the background region was chosen to be the same as if the observations were performed using the chop-nod observing mode. The size of this region does not influence the estimation of the zero-background level, rather the location and the surface brightness do. Then, for both arrays and each HWP position angle produced from the first step by CRUSH, we estimate the mean and standard deviation within the zero-level region. To remove negative values across the image, the mean is added to all pixels in each scan and HWP position angle. After this step, the same reduction procedures as described in Section 2.1 are followed. Using archival chop-nod and OTFMAP observations of well-known objects, e.g. 30 Doradus and OMC-1, and applied the same methodology, we reached similar conclusions and methodologies, while the polarization pattern was shown to be consistent between reduction schemes. Finally, we computed the SED of the source using $70 - 500$ μm *Herschel* images and estimated the expected flux at 214 μm. We estimated that the fluxes from the zero-level background corrected image are within 8% from the expected flux from the *Herschel* SED, which is within the flux calibration uncertainty of HAWC+ of $\leqslant 15\%$ provided by the SOFIA Science Center.

Although the zero-level background region has low surface

---

[1] *Herschel* archive: `http://archives.esac.esa.int/hsa/whsa/`

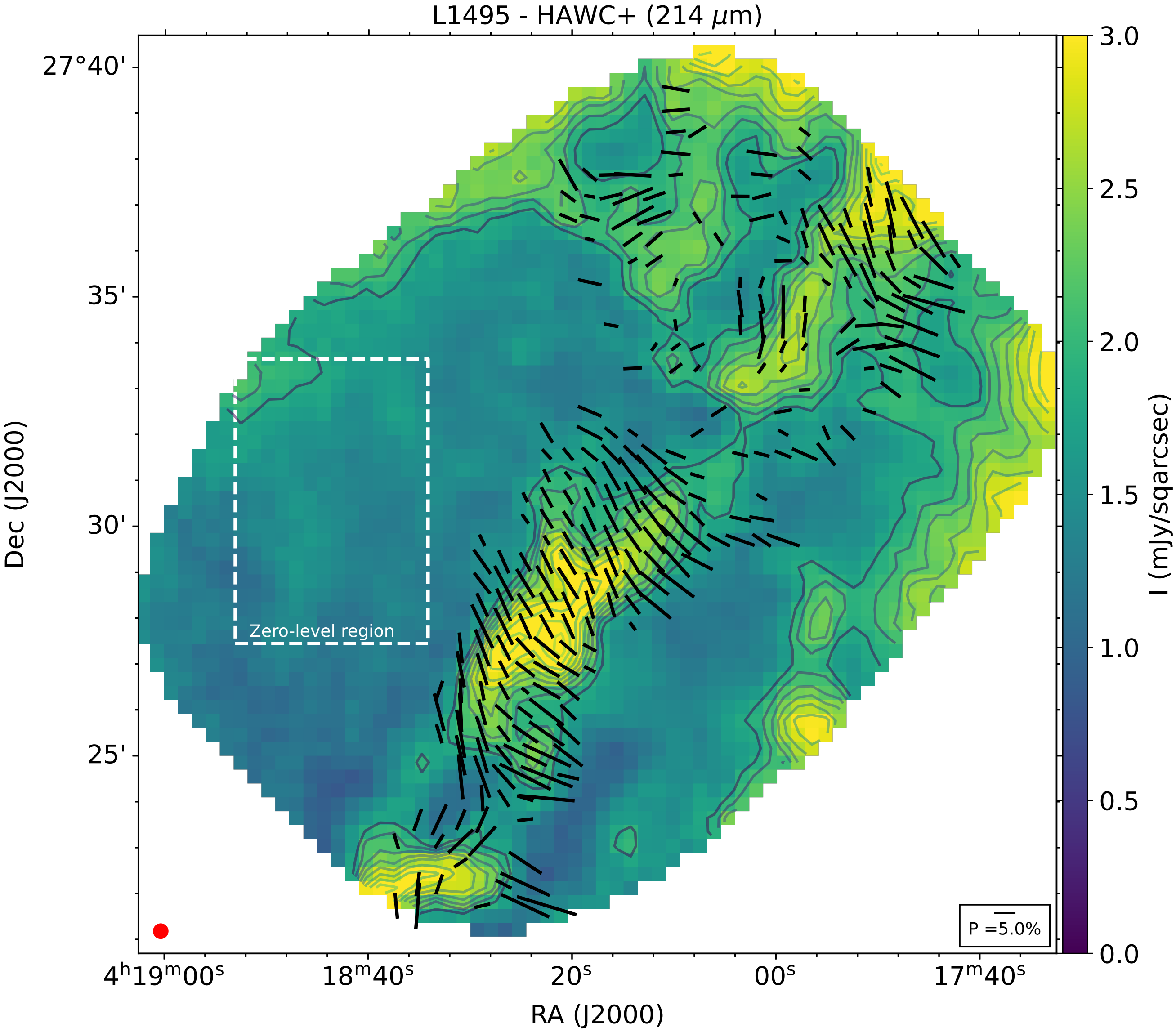

Figure 1. Total surface brightness at 214 μm of L1495 within a 1200×1200 sqarcsec region using the OTFMAP observations. Contours start at 45σ and increase in steps of 5σ, with $\sigma = 0.032$ mJy/sqarcsec. Although quality cuts have been performed to cut edge effects, there are still structural artifacts at the corners of the map (specially in the West region) due to the low coverage at the edges of the map. Polarization measurements (black lines) have been rotated by 90° to show the inferred magnetic field morphology. The length of the polarization vector is proportional to the degree of polarization. Only vectors with $P/\sigma_P \geqslant 2$ are shown. A legend with a 5% polarization and the beam size (18.″2) are shown. The zero-level background region (white dashed line) described in Section 2.3 is shown.

brightness, the polarization may be high and contaminate the astrophysical signal after the zero-level background correction. Here, we estimate the contribution of the zero-level background to the polarization measurements. As mentioned above, the mean and standard deviation within the zero-level background region was estimated for each array and HWP position angle. Using the double difference method (Section 3.2 by Harper et al. 2018), we estimate the Stokes Q and U and their uncertainties by spatial averaging within full FOV of the zero-level background region. Then, the Stokes Q and U were corrected by instrumental polarization, and P and position angle were estimated and corrected by bias and polarization efficiency. Finally, the P and position angle of the zero-level background region were estimated to be $8.5 \pm 3.5\%$

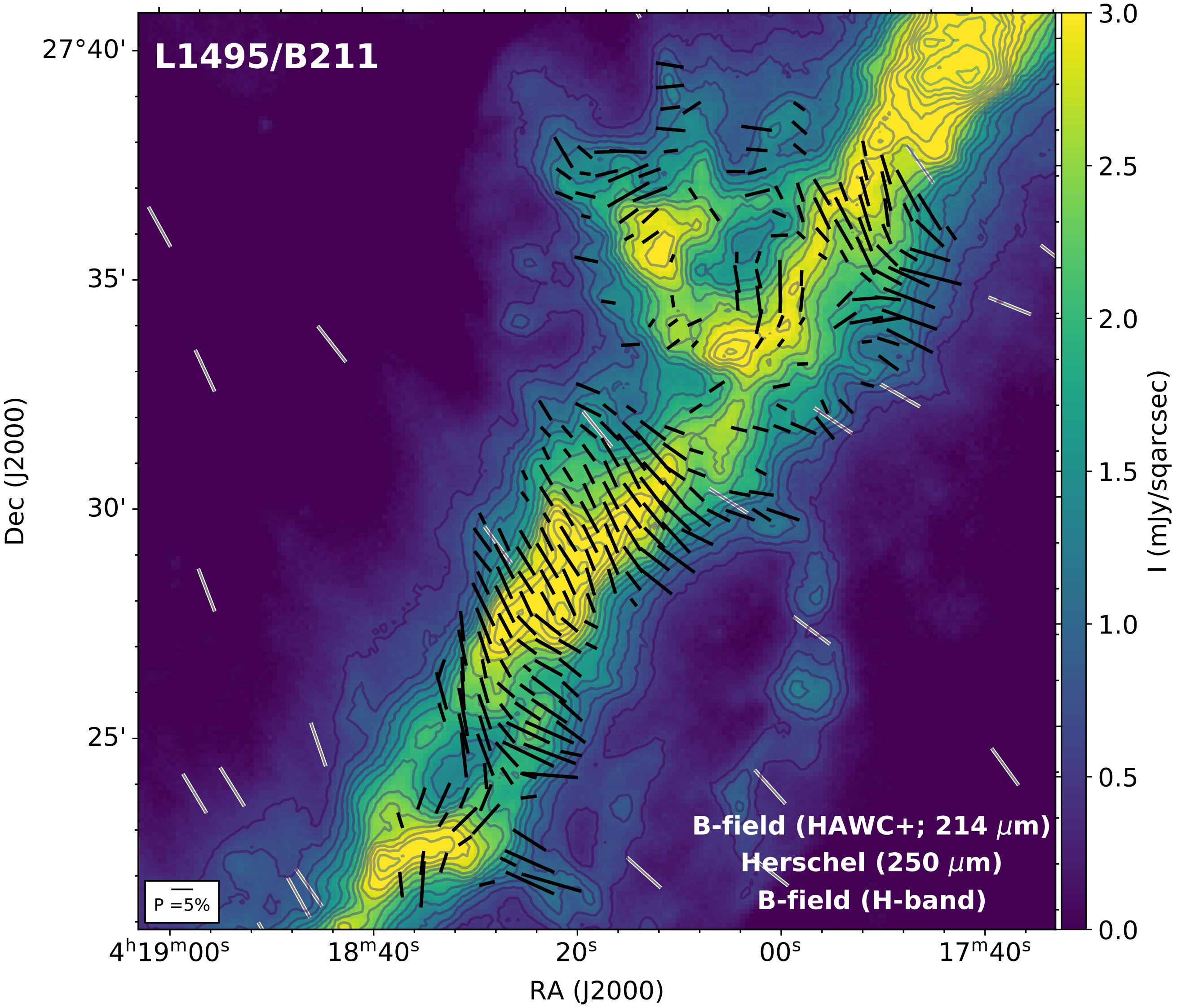

Figure 2. The 250 μm total surface brightness from *Herschel*/SPIRE (color scale) with the magnetic field morphology as inferred from the 214 μm HAWC+ (black lines) and H-band (grey lines; Chapman et al. 2011) observations. Contours start at 0.5 mJy/sqarcsec and increase in steps of 0.25 mJy/sqarcsec.

and $42 \pm 8^\circ$, respectively. The minimum detectable flux from Stokes I is estimated to be $3\sigma_I = 0.096$ mJy/sqarcsec, which corresponds to a polarized flux of $3\sigma_{PI} = 0.008$ mJy/sqarcsec using $P = 8.5\%$. From our polarization measurements with $P/\sigma_P \geqslant 2$, we estimate a median polarized flux of 0.055 mJy/sqarcsec. Thus, the zero-level background correction contributes a median of $\sim 14\%$ to the polarized flux in our measurements.

2.4 HAWC+ polarization map and orientation of magnetic fields

Fig. 1 shows polarization measurements projected onto the total surface brightness at 214 μm of the 1200×1200 sqarcsec region of L1495/B211 that we observed. The polarization measurements have been rotated by 90° to show the inferred magnetic field morphology. *All polarization angles (PAs) cited in this paper have been rotated in this manner.* Only polarization measurements with $P/\sigma_P \geqslant 2$ are shown

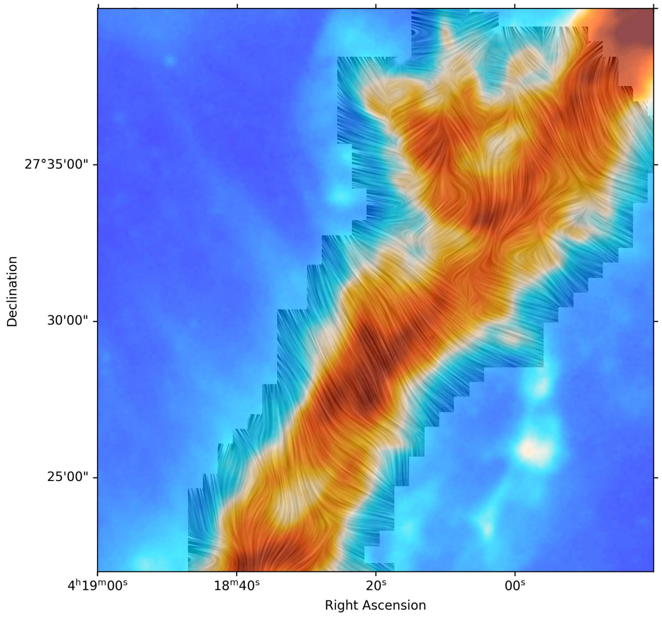

Figure 3. The inferred magnetic field orientation from HAWC+ polarization observations at 214 μm of the B211 filament is shown using the linear integral convolution algorithm (LIC; Cabral & Leedom 1993). Same polarization measurements as Figure 1, a resample scale of 20, and a contrast of 4 were used. The colorscale shows the 250μm total intensity image from the *Herschel* Gould Belt survey as shown in Figure 2.

(Wardle & Kronberg 1974). The length of the polarization lines are proportional to the degree of polarization, where a 5% polarization measurement is shown as reference. Images had edges artifacts due to the sharp changes in fluxes and limited number of pixels. The final 214 μm HAWC+ polarization measurements contain pixels with the following quality cuts: 1) pixels with a scan coverage $\geqslant$ 30% of all observations, 2) pixels which Stokes I measurements have an uncertainty $\geqslant 2.5\sigma_I$, where σ_I is the minimum uncertainty in Stokes I, 3) pixels with a surface brightness of $\geqslant$ 1 mJy/sqarcsec, 4) pixels with $P \leqslant 30\%$ given by the maximum polarized emission found by *Planck* observations (Planck Collaboration Int. XII 2013), and 5) polarization measurements with $P/\sigma_P \geqslant 2$. We find that 14% (40 out of 282) of the measurements are within $2 \leqslant P/\sigma_P \leqslant 3$.

In Fig. 2 we over-plotted the magnetic field orientations from near-infrared H-band observations obtained by Chapman et al. (2011). Note that the inferred magnetic field from the H-band arises from dichroic absorption, while our 214 μm measurements arise from dichroic emission. We detect many multiple structures of magnetic field over just 0.82 pc region inside the 2-pc-long B211 region from the HAWC+ polarization mapping at smaller scales $28\overset{''}{.}1$ compared to the lower resolution observation from the H-band and Planck observations (see Fig. 5). We note that the magnetic field of the lower half of the observed area is more uniform and close to the perpendicular direction of the filamentary cloud. From the *Herschel* intensity map, this part of B211 appears to have two filamentary substructures crossing each other in an x-shape appearance near RA of $4^{\rm h}18^{\rm m}20^{\rm s}$ and DEC of $27°29'$. The two structures may be spatially nearby and appeared

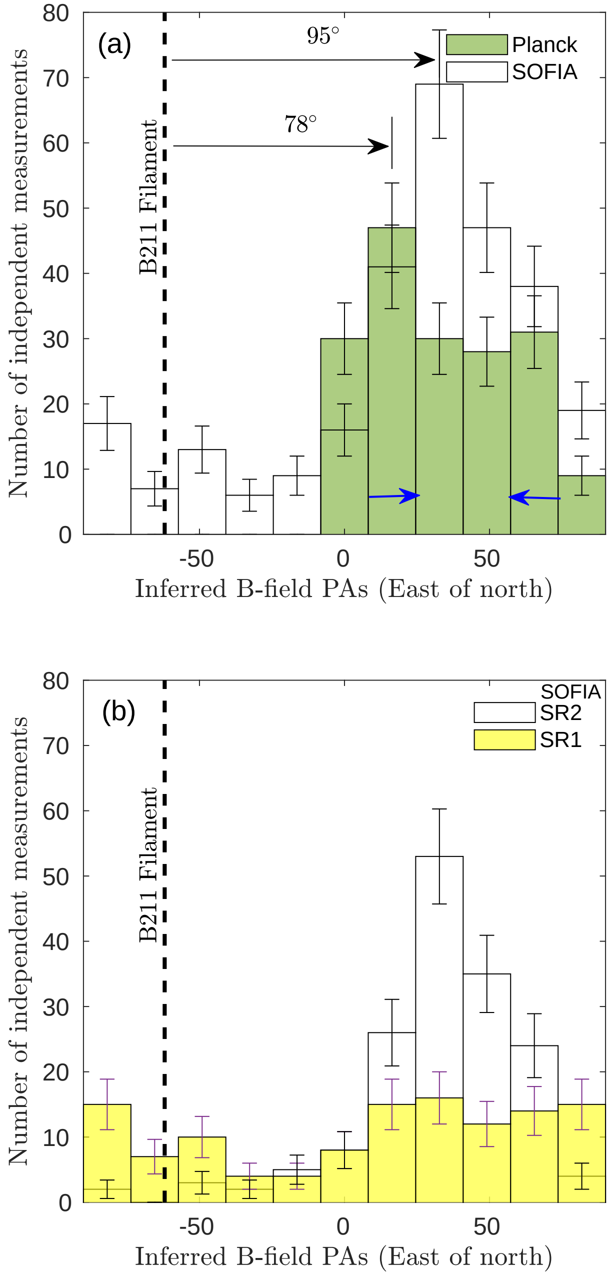

Figure 4. (a) The histograms of all the inferred magnetic field orientations from HAWC+ polarization observations of the B211 filament at resolution of 28.1 arcsec shown in Fig. 2 (empty) and from Planck polarization observations (green) of the entire Taurus/B211 region at resolution of 10 arcmin shown in Fig. 5. The six Planck polarization measurements within the FOV of our observations are inside the two bins 24° − 57° marked by the two blue arrows. The bin width of 16.4° is chosen to be larger than the measurement uncertainty of the PA. The vertical dashed line indicates the orientation of the B211 filament at PA = −62° equivalent to +118° (Palmeirim et al. (2013)). The angle differences of the peaks of the two sets of histograms from the PA of the B211 filament are shown. (b) The histograms of inferred magnetic field orientations from HAWC+ polarization observations of sub-regions SR1 (yellow) and SR2 (empty).

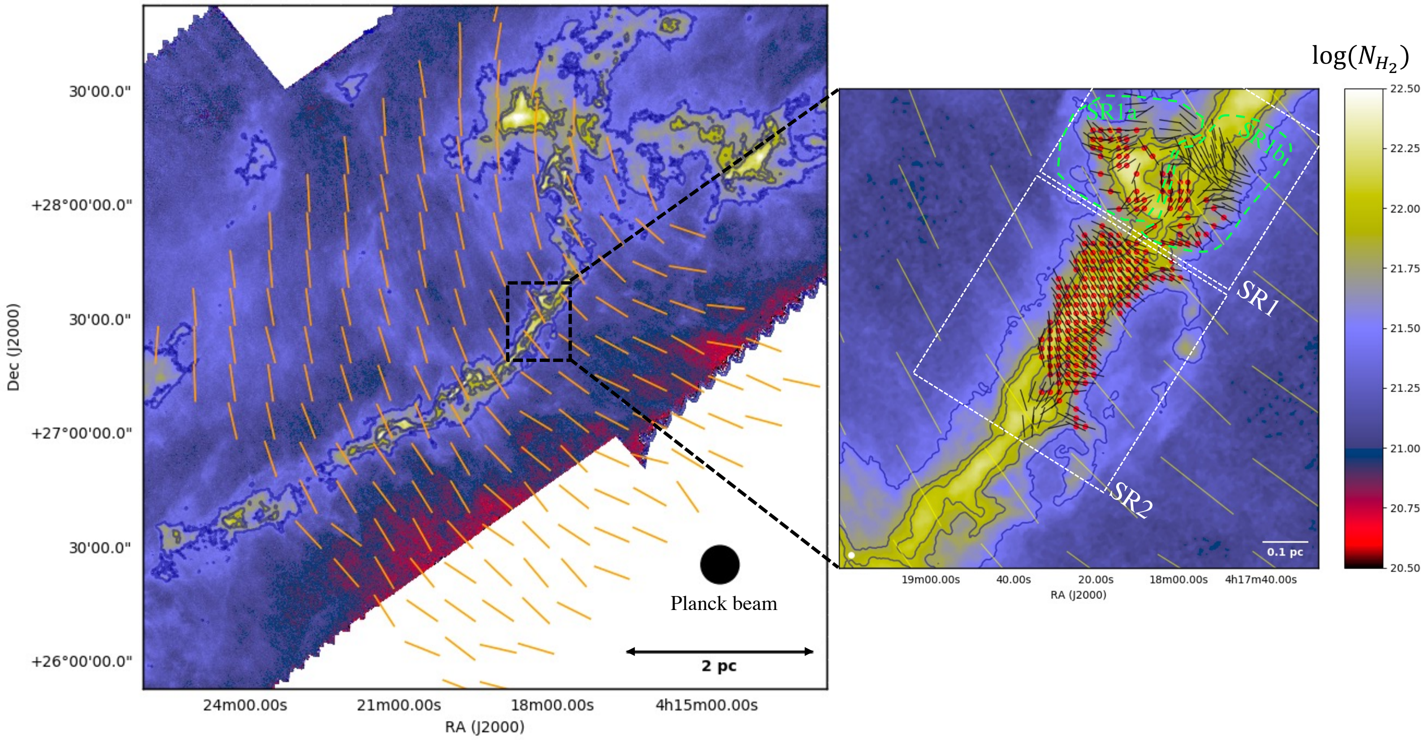

Figure 5. *Left:* Column density map from *Herschel* Gould Belt survey data at 18.2″ resolution (Palmeirim et al. 2013; André et al. 2010), with magnetic field vectors derived from *Planck* polarization data at 10′ resolution (Planck Collaboration Int. XII 2013) displayed in orange/yellow (and spaced every 10′). Contours are $N(\mathrm{H_2}) = 3 \times 10^{21}$, 6.7×10^{21}, and 10^{22} cm^{-2}. *Right:* Blow-up of the left image in the area mapped with SOFIA/HAWC+. Yellow vectors are from *Planck* and are here spaced by half a beam (5′). Smaller black segments show the magnetic field vectors derived from HAWC+ at 28″ resolution. The solid red circles mark positions where both significant HAWC+ polarization measurements and C^{18}O line data from the IRAM 30m telescope are available. The two sub-regions (SR1 and SR2) for which a DCF analysis has been carried out are marked by white dotted rectangles; the two components of SR1 (SR1a and SR1b) are outlined by green dashed contours.

to be overlapped along the LOS. The magnetic field could be a combined result of the overlapping projection. In the upper half, the magnetic field structure appears as a highly non-uniform chaotic state. It is consistent with the turbulent appearance of the underlining intensity map that there could be three tangling filamentary substructures at this location as identified by Hacar et al. (2013). The deviation of polarization angle is large from the uniform large scale field direction indicated by the near-infrared H-band and Planck observations. Fig. 3 is a line integral convolution (Cabral & Leedom 1993) plot of the inferred magnetic field from the HAWC+ polarization observations.

The histogram of the B-field PA distribution of all the polarization measurements detected with $P/\sigma_P > 2$ is shown in Fig. 4a. The peak is near 30°, which is very close to the large scale mean magnetic field orientation of 26° ± 18° and is nearly orthogonal to the L1495 filamentary cloud axis at 118°±20° (Palmeirim et al. 2013). If the PAs have a range approaching 180°, then the dispersion can depend on the choice of $\theta = 0°$ since PAs near +90° can be flipped to -90° by a change in the orientation of 0°. In this paper we evaluate the dispersion in PAs by choosing 0° to be consistent with the minimum dispersion in PAs. We find that the PAs in Fig. 4 have a dispersion of 36.1°, indicating that the small-scale magnetic field is strongly perturbed inside the cloud compared with the large scale field. Basically, the inferred B-field are pointing at all directions in the northwestern side region of 0.82 pc in size. The large-scale field PA distribution from Planck is also plotted in Fig. 4a for direct comparison. Note that most of the magnetic field orientations from Planck are located far from the B211 region (see Fig. 5) and have a dispersion of 37°. The several Planck polarization orientations inside the observed B211 region (indicated by a black dash-line box in Fig. 5) are all inside the two bins between 24°−57° at the peak of the Planck distribution and close to the peak of the mean magnetic field inside B211 from HAWC+. The resolution of the large-scale field from Planck is ∼ 0.4 pc, which is about 21 times the size of the super-pixel that we adopted for the HAWC+ results. In Section 4.3, we use a numerical simulation to discuss how the resolution of a polarization map can affect the interpretation of magnetic field structures.

2.5 IRAM 30m observations

C^{18}O(1–0) mapping observations of a portion of the B211 field imaged with HAWC+ were carried out with the Eight MIxer Receiver (EMIR) receiver on the IRAM-30m telescope at Pico Veleta (Spain) in April 2016, as part of another project (Palmeirim et al. in preparation). At 109.8 GHz, the

30 m telescope has a beam size of $\sim 23''$ (HPBW), a forward efficiency of 94%, and a main beam efficiency of 78% [1]. As backend, we used the VESPA autocorrelator providing a frequency resolution of 20 kHz, which corresponds to a velocity resolution of $\sim$0.05 km s^{-1} at 110 GHz. The standard chopper wheel method[2] was used to convert the observed signal to the antenna temperature $T_{\rm A}^*$ in units of K, corrected for atmospheric attenuation. During the observations, the system noise temperatures ranged from $\sim$85 K to $\sim$670 K. The telescope pointing was checked every hour and found to be better than $\sim 3''$ throughout the run.

3 PHYSICAL STATE OF B211 REGION INFERRED FROM OBSERVATIONS

3.1 Magnetic field strength in B211

We derive magnetic field strengths using the DCF method based on the observed velocity dispersion, surface density (which provides an estimate of the gas density), and the dispersion of polarization angles. We used IRAM 30m C^{18}O data to derive the velocity dispersion and a HAWC+ polarization map to derive the dispersion in polarization angles. The density is based on *Herschel* column density data published in the literature. We describe the detailed methods below. The observed and derived parameters are summarized in Table 2.

3.1.1 Davis-Chandrasekhar-Fermi Method

The Davis (1951)-Chandrasekhar & Fermi (1953) method (hereafter the DCF method) allows one to infer the strength of the POS magnetic field from observations of the fluctuations in the polarization angle (PA) and is discussed extensively in Appendix A. The mean POS field is denoted by B_0 and is related to the mean 3D field by

$$B_0 = B_{0,\rm 3D}\cos\gamma, \tag{1}$$

where γ is the angle between $\mathbf{B}_0$ and the plane of the sky. In the original DCF method, the mean POS magnetic field was determined over the entire field of view over which the PAs were measured. An expression for the value of this field that is valid for larger dispersions than the original DCF result and is related to a result obtained by Falceta-Gonçalves et al. (2008) is given in equation (A12):

$$\begin{aligned} B_0 &= f_{\rm DCF}\,\frac{(4\pi\rho)^{1/2}\sigma_V}{\tan\sigma_\theta}, & (2)\\ &= 0.383\sqrt{n(\rm H_2)}\,\frac{\sigma_V}{\tan\sigma_\theta}\quad \mu{\rm G}, & (3)\end{aligned}$$

where $n(\rm H_2)$ is the number density of H$_2$ molecules in cm^{-3}, σ_V is measured in km s^{-1}, and σ_θ is the dispersion in the orientation of the magnetic field orientations, and where we have set the factor $f_{\rm DCF}$, which corrects for the approximations made in deriving the DCF relation, to be 0.5 based on the results of Ostriker et al. (2001). Comparison with numerical simulations confirms that this formula (with $\tan\sigma_\theta$ replaced by σ_θ in radians under the assumption that σ_θ is small) is valid when $\sigma_\theta \leqslant 25°$ (Ostriker et al. 2001). The latter relation (with σ_θ) is often used for larger dispersions, however.

A key step in the DCF method is to infer the dispersion in the field, $\sigma_{\delta B_\perp}$, from the dispersion in PAs, σ_θ. A complication is that the field angles (FAs) can range over $-180°$ to $+180°$, whereas the PAs are restricted to the range $-90°$ to $+90°$. As a result, the direction of the implied field depends on the choice of zero angle for the PAs. A field angle of 60° if 0° is vertical becomes -30°if the coordinate system is rotated 90° counterclockwise. Since the magnitude of the PA depends on the choice of coordinate system, it follows that the value of σ_θ does also. In this paper, we adopt the convention that we choose the coordinate system that minimizes the dispersion, σ_θ, as recommended by Padoan et al. (2001). This becomes relevant only if some of the field angles differ by more than 180°, which generally occurs only if σ_θ is not small.

A second method of inferring the turbulent field strength from the spatial variation in the PAs is the structure function method introduced by Hildebrand et al. (2009) and extended by Houde et al. (2009) and Houde et al. (2016). This method is more general since it allows for a smooth variation in the orientation of the mean field. The structure function relates the PAs at different points and is defined as

$$\langle \Delta\Phi(\ell)^2\rangle \equiv \frac{1}{N(\ell)}\sum_{i=1}^{N(\ell)}[\Phi(\mathbf{x})-\Phi(\mathbf{x}+\boldsymbol{\ell})]^2, \tag{4}$$

where $\Phi(\mathbf{x})$ is the PA at position $\mathbf{x}$, $\boldsymbol{\ell}$ is the displacement, and $N(\ell)$ is the number of polarization angle pairs with separation ℓ. The structure function is related to the fluctuations in the magnetic field by equation (A21) in the small angle approximation. In order to infer the field dispersion, $\Delta\Phi(\ell)$ is extrapolated to $\ell = 0$, which gives $\Delta\Phi_0 = \sqrt{2}\sigma_{\delta B_\perp}/B_{\rm rms}$. Unlike Hildebrand et al. (2009), we insert a factor $f_{\rm DCF}$ into the result for B_0 and set $f_{\rm DCF} = 0.5$. Equation (A28) then gives

$$B_0 = 0.383\,n(\rm H_2)^{1/2}\sigma_V\,\frac{(2-\Delta\Phi_0^2)^{1/2}}{\Delta\Phi_0}. \tag{5}$$

The determination of σ_θ and $\Delta\Phi_0$ is discussed in section 3.1.3 below.

3.1.2 IRAM 30m C^{18}O data and Velocity Dispersion

Thanks to their high sensitivity, the IRAM 30m molecular line data highlight the kinematic complexity of the region mapped by HAWC+, with the presence of multiple velocity components. These multiple velocity components are consistent with the presence of filamentary substructures in this region as discussed by Hacar et al. (2013). The variety of observed C^{18}O(1–0) spectra is illustrated in Fig. 6, which shows clear changes in the number of velocity components and in overall centroid velocity as a function of position within and around the B211 filament.

C^{18}O(1–0) molecular line data trace the kinematics of the gas and can be used to estimate the level of non-thermal motions due to turbulence in the region. As the C^{18}O(1–0) transition is usually optically thin, multiple peaks in the spectra, when present, likely trace the presence of independent velocity components as opposed to self-absorption effects. For

---

[1] `http://www.iram.es/IRAMES/mainWiki/Iram30mEfficiencies`

[2] Chopper wheel method used in IRAM-30m can be found at `https://safe.nrao.edu/wiki/pub/KPAF/KfpaPipelineReview/kramer_1997_cali_rep.pdf`

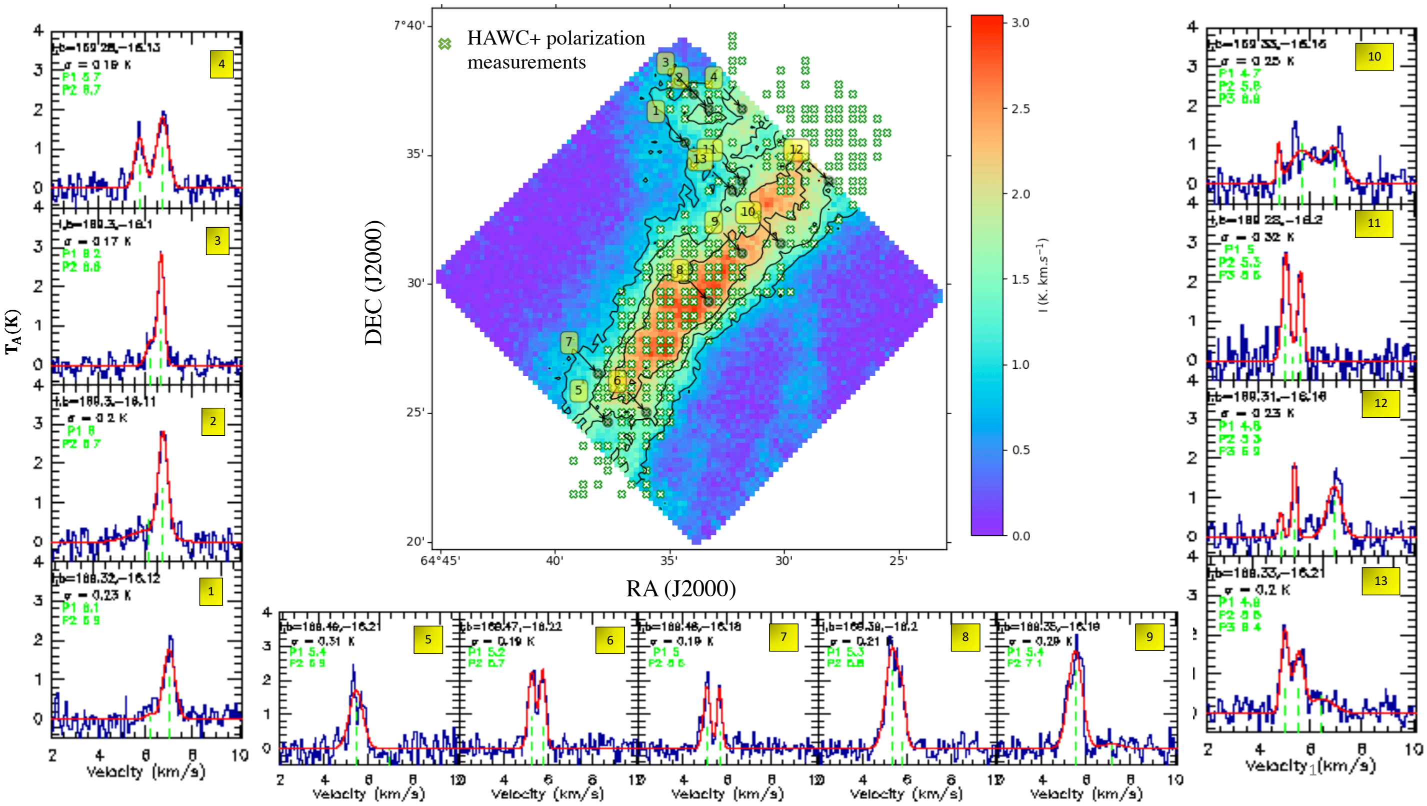

Figure 6. C^{18}O(1–0) integrated intensity map over all channel velocities from 4.5 to 7 km s^{-1}. The contours correspond to 30%, 50 %, and 70% of the maximum integrated intensity (3 K km s^{-1}). Markers (x) in green indicate positions where statistically significant polarization measurements were obtained with HAWC+. Representative C^{18}O(1–0) spectra observed with the IRAM 30m telescope at selected positions in the field are shown to the left, bottom, and right of the map.

better characterization of the different velocity peaks, we performed multiple Gaussian fits which allowed us to identify the centroid position of each velocity component where multiple components are observed. Comparing all of the C^{18}O(1–0) spectra observed in a given sub-region, it was possible to identify a dominant velocity component in each case. Table 2 provides the centroid velocity and velocity dispersion of the dominant and total velocity component in each sub-region for the significant HAWC+ detection where $P/\sigma_P \geqslant 2$, where P represents the polarization degree (first row for each sub-region in Table 2).

The centroid velocities of the relevant velocity components range from 5.4 km s^{-1} to 5.9 km s^{-1}, and the associated line-of-sight velocity dispersion range from ~0.2 to ~0.3 km s^{-1} for the dominant components and from ~0.4 to ~0.5 km s^{-1} if all velocity components are considered.

3.1.3 *Dispersion in polarization angles from HAWC+*

The SOFIA HAWC+ polarization data reveal a strongly perturbed structure of the magnetic field in the B211 region. In this work, we estimated the dispersion in polarization angles using independent polarization measurements in two sub-regions of B211, called SR1 and SR2 in Fig. 5. The motivation for this division is that the region with polarization detections (see Fig. 1) is clearly not homogeneous: the southeastern part (SR2) corresponds to a segment of the B211 main filament, while the northwestern part (SR1) is an interaction region where material associated with the striations seen in the *Herschel* data meet the main filament (cf. Palmeirim et al. 2013). Moreover, SR1 and SR2 correspond to different groups of C^{18}O velocity components, namely components #9, #12, #11 for SR1, and components #12, #14 for SR2, in the analysis presented by Hacar et al. (2013). It is also apparent from Fig. 1 that the dispersion of polarization angles is significantly higher in SR1 than in SR2. Taking into account measurement errors in our polarization data, we estimate σ_θ as the weighted standard deviation of polarization angles in each sub-region:

$$\sigma_\theta^2 = \frac{N}{N-1}\,\frac{1}{w}\sum_{i=1}^{N} w_i\,(\theta_i - \bar{\theta}_w)^2, \tag{6}$$

where N is number of independent measurements in each sub-region, $w_i = 1/\sigma_i^2$ the weight of measurement i given the measurement error in PA σ_i, $w = \sum_{i=1}^{N} w_i$, and $\bar{\theta}_w = (1/w)\sum_{i=1}^{N} w_i\,\theta_i$ is the weighted mean polarization angle in the sub-region. In sub-region 1 (SR1 from Fig. 5), where there are 120 independent HAWC+ measurements, the dispersion in polarization angles is $54^\circ \pm 5^\circ$, which is a rather large value considering the main regime of applicability of the DCF method ($\sigma_\theta \leqslant 25^\circ$ – see Ostriker et al. 2001). The error in the dispersion of polarization angles was estimated as $\sigma_\theta/\sqrt{N}$. In sub-region 2 (SR2), there are 162 independent HAWC+ measurements and the dispersion in polarization angles is 20° ± 2° (see Table 2).

While SR2 is dominated by one $C^{18}O$ velocity component (#12 with $V_{\rm LSR} = 5.6\,{\rm km\,s^{-1}}$ in Hacar et al. 2013), SR1 consists of two parts, SR1a to the north-east and SR1b to the south-west, where two distinct velocity components dominate (#11 with $V_{\rm LSR} = 6.7\,{\rm km\,s^{-1}}$ and #12 with $V_{\rm LSR} = 5.6\,{\rm km\,s^{-1}}$, respectively). These two components may be interacting with one another, increasing the dispersion in polarization angles. It may therefore seem justified to subdivide SR1 into these two parts (cf. SR1a and SR1b in Fig. 5) when estimating the field strength with the DCF method. Doing this results in a polarization angle dispersion of $65^\circ \pm 9^\circ$ in SR1a for 45 independent HAWC+ measurements and a dispersion of $42^\circ \pm 5^\circ$ in SR1b for 73 independent measurements. In both parts of SR1, the dispersion of polarization angles remains significantly higher than in SR2. For both SR1 and SR2, we also analyzed the data using the structure function (SF) variant of the DCF method (Hildebrand et al. 2009; section 3.1.1, Appendix A)[1]. In Fig. 7, we fit $\langle \Delta\Phi(\ell)^2 \rangle^{1/2}$ for the two sub-regions using the SF method after correcting for measurement error by computing the error-weighted $\Delta\Phi^2(\ell)$ as in equation (6). It is common practice to restrict $|\Delta\Phi|$ to be less than 90°; that is, whenever $|\Delta\Phi|$ is found to be larger than 90°, it is replaced by $|180^\circ - \Delta\Phi|$. As discussed in the Appendix, this often results in an underestimate of the dispersion in field angles and a corresponding overestimate of the field; in some cases, however, it can improve the accuracy of the field determination. We therefore provide both values. The intercepts of the fits at $\ell = 0$ in Fig. 7 are $\Delta\Phi_0 = 50.3 \pm 4.4^\circ$ and $\Delta\Phi_0 = 60.5 \pm 3.0^\circ$ for the restricted and unrestricted approaches, respectively. The difference is only 10°. The corresponding angular dispersions contributed from the turbulence ($\sigma_\theta \sim \Delta\Phi_0/\sqrt{2}$) (eq. A27) are about 36° and 43°, respectively. From the fitting, the turbulent correlation length scale of SR1 and SR2 is about 4 to 5 super-pixels, corresponding to 0.075 to 0.095 pc, about the size scale of the filamentary substructures. We divide the SR1 into four smaller portions, each with 30 polarization measurements. The root-mean-square of the angular dispersion in these four smaller portions is 30.3°, close to the angular dispersion of the turbulence from the SF analysis. The intercepts of fitting at $\ell = 0$ in Fig. 7 are $23.2 \pm 3.5^\circ$ and $24.0 \pm 3.6^\circ$ from the restricted and un-restricted approaches, almost the same. The summary of all the measured parameters, and the results of the DCF and SF analysis are listed in Table 2. The estimation for the ambient cloud around the entire L1495 is also provided in the table for comparison.

3.1.4 *Volume density from Herschel column density data*

The average volume density in each of the two portions of the B211 filament marked in Fig. 5 was estimated using the surface density map at 18.2″ resolution published by Palmeirim et al. (2013) and Marsh et al. (2016) from *Herschel* Gould Belt survey (HGBS) data[2]. To do so, we assumed that the depth of each sub-region along the LOS is the same as the mean projected outer width. This is a very reasonable assumption, especially for SR2 which corresponds to a segment of the filament, since there is good observational evidence that B211 is a true cylinder-like filament as opposed to a sheet seen edge-on (Li & Goldsmith 2012). The mean outer width was obtained using the projected area of pixels above the minimum surface density with a detected polarization signal [$\log N(H_2) = 21.59$], divided by the length of each sub-region. The average surface density $< N(H_2) >$ above $\log N(H_2) = 21.59$ in each sub-region was derived from the *Herschel* column density map, and the resulting value was divided by the mean outer width, namely $L \sim 0.15$ pc for SR2 and $L \sim 0.3$ pc for SR1. This provided the average density, $<n(H_2)> = <N(H_2)>/L$, given in Table 2.

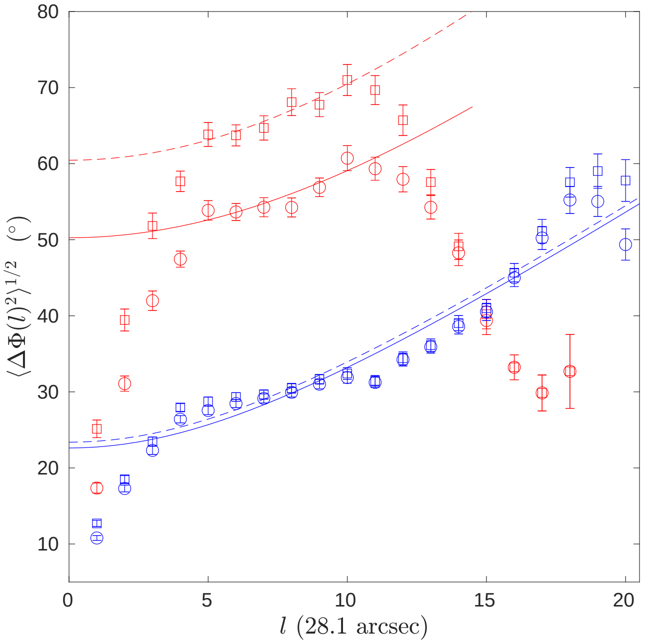

Figure 7. Structure functions and fits for sub-regions SR1 (red) and SR2 (blue) using $\Delta\Phi$ restricted to less than 90° (circles and solid curve) and no restriction on $\Delta\Phi$ (squares and dash curve) as functions of scale in units of HAWC+ superpixels. For SR1, the fitting is from $\ell = 5$ to 10. The fitted intercepts with restriction and no restriction are $50.9 \pm 4.3^\circ$ and $60.9 \pm 3.0^\circ$, respectively. Error bars are the standard deviations of angle differences at a given distance. For SR2, the fitting is from $\ell = 4$ to 18. The fitted intercepts with restriction and no restriction are $23.2 \pm 3.5^\circ$ and $24.0 \pm 3.6^\circ$, respectively.

3.1.5 *Magnetic field strength*

Using Equation (3) with the volume densities, velocity dispersions, and dispersions in polarization angles estimated in Sections 3.1.3 to 3.1.5, we can determine the field strengths for the two sub-regions marked by white dashed rectangles in Fig. 5. The results are summarized in Table 2. We begin with SR2, which has a relatively smooth field with a small dispersion, $\sigma_\theta = 20^\circ$. The field strength ranges between 43 μG and 66 μG from the standard DCF method and 79 μG to 82 μG with the SF variant. Knowing the magnetic field, it is possible

---

[1] We could not apply the SF technique to SR1a and SR1b separately, due to the low numbers of independent HAWC+ measurements in each of these smaller sub-regions.

[2] cf. `http://gouldbelt-herschel.cea.fr/archives`

Table 2. Summary of parameters and results of the DCF and SF analysis.

Region[1]	SR1	SR2	Taurus/B211[2]
N_i[3]	120	162	175
$V^d_{\rm LSR}$[4]- $V^m_{\rm LSR}$[5](km s^{-1})	5.4–5.9	5.5–5.5	6.6
σ^d_V[6]- σ^m_V[7](km s^{-1})	0.26–0.48	0.27–0.41	0.85 ± 0.01
σ_θ[8](°)	54 ± 5	20 ± 2	24 ± 2
$N(\mathrm{H_2})$[9](10^{21}cm^{-2})	8 ± 3	11 ± 4	1.5 ± 0.2
Depth[10](pc)	0.3	0.15	$0.5\ ^{+0.5}_{-0.25}$
$n(\mathrm{H_2})$[11](10^4cm^{-3})	1.0 ± 0.4	2.3 ± 1.0	$0.1^{+0.1}_{-0.05}$
DCF analysis			
B_0^d[12]- B_0^m[13](μG)	7–13	43–65	23^{+12}_{-6}
δB^d - δB^m[14](μG)	10–18	16–24	10^{+7}_{-5}
μ_Φ [15]	5.0–2.7	1.8–1.2	$0.5\ ^{+0.1}_{-0.1}$
$\mathcal{M}_{\rm A}/\cos\gamma$[16]	4.8	1.3	1.6
DCF/SF analysis			
$\Delta\Phi_{0,\rm res}$[17]$/\sqrt{2}$ (°)	35 ± 3	16 ± 3	14 ± 2
$\Delta\Phi_{0,\rm nores}$[18]$/\sqrt{2}$ (°)	42 ± 2	17 ± 3	14 ± 2
B_0^m[19](μG)	17–23	79–82	41^{+21}_{-11}
δB^m[20](μG)	18	24	10
μ_Φ	2.5–2.1	1.0	0.3
$\mathcal{M}_{\rm A}/\cos\gamma$[21]	2.6–3.5	1.0	0.9

[1] Sub-region of B211 in which the analysis was conducted.
[2] Estimation on a large scale covering the Taurus/B211 region using *Planck* polarization data (Planck Collaboration Int. XII 2013) and molecular line observations (Chapman et al. 2011).
[3] Number of independent SOFIA/HAWC+ polarization measurements for which $P/\sigma_P \geqslant 2$, where P is the polarized intensity.
[4] Average centroid velocity of the dominant velocity component in each sub-region.
[5] Average centroid velocity in each sub-region, including all velocity components.
[6] Average non-thermal velocity dispersion of the dominant component over each sub-region.
[7] Average value of the total non-thermal velocity dispersion over each sub-region.
[8] Dispersion of polarization angles with individual measurements weighted by $1/\sigma^2_{\theta_i}$). The uncertainty in this dispersion was was estimated as $\sigma_\theta/\sqrt{N}$, where N is the number of independent polarization measurements in each sub-region. (cf. Pattle et al. 2020)
[9] Weighted mean surface density derived from Herschel GBS data at the HAWC+ positions.
[10] Adopted depth of each subregion estimated from the width measured in the plane of sky.
[11] Average volume density estimated from $N(\mathrm{H_2})$ and Depth.
[12] Plane-of-sky mean field strength from the standard DCF method (eq. 3) using the dispersion of the dominant velocity component.
[13] Plane-of-sky mean field strength from the standard DCF method (eq. 3) using the total non-thermal velocity dispersion.
[14] The turbulent component of plane-of-sky B-field strength ($\delta B = B_0 \tan\sigma_\theta$, eq. A11).
[15] Estimated mass to flux ratio relative to the critical value based on the rms POS field, $B_{\rm tot} = (B_0^2 + \delta B^2)^{1/2}$ (eq. B5).
[16] $\mathcal{M}_{\rm A}$ is the 3D Alfvén Mach number ($\propto \sqrt{3}\sigma_V/B_{0,\rm 3D} = \sqrt{3}\sigma_V\cos\gamma/B_0$) with respect to the mean 3D field (eq. A13).
[17] Intercept of the fitted structure function at $\ell = 0$ with large-angle restriction.
[18] Intercept of the fitted structure function at $\ell = 0$ without large-angle restriction.
[19] The range of B_0 estimated from $\Delta\Phi_{0,\rm nores}$ and $\Delta\Phi_{0,\rm res}$, respectively, using the total non-thermal velocity dispersion (eq. 5).
[20] The turbulent component of plane-of-sky B-field strength $\delta B^m = \sigma_{\delta B_\perp} = f_{\rm DCF}(4\pi\rho)^{1/2}\sigma_V^m$ (eqs. A27 and A28).
[21] $\mathcal{M}_{\rm A}$ is the 3D Alfvén Mach number ($\propto \sqrt{3}\sigma_V/B_{0,\rm 3D} = \sqrt{3}\sigma_V\cos\gamma/B_0$) with respect to the mean 3D field for the DCF/SF method (eq. A26).

to determine the POS mass-to-flux ratio relative to the critical value, $\mu_{\Phi,\mathrm{POS}}$, and the Alfvén Mach number (Appendix B). SR2 is trans-Alfvénic, with $\mathcal{M}_\mathrm{A} \simeq 1.0 - 1.3$ and magnetically critical to mildly supercritical, $\mu_{\Phi,\mathrm{POS}} \simeq 0.9 - 1.7$, depending on the method of analysis that is adopted. The critical mass per unit length, $M_{\mathrm{crit},\ell}$, is that value of M_ℓ such that the pressure and magnetic forces are in balance with gravity (Appendix B). The SR2 filament segment is slightly subcritical, with $M_\ell \simeq 0.7 M_{\mathrm{crit},\ell}$–i.e., it is gravitationally stable against radial collapse. In the absence of perpendicular magnetic fields, filaments that are moderately subcritical ($0.9 \gtrsim M_\ell/M_{\mathrm{crit},\ell} \gtrsim 0.2$, with an optimum value of $M_\ell/M_{\mathrm{crit},\ell} \sim 0.5$) are subject to fragmentation into prestellar cores (i.e., starless cores with $M \geqslant M_\mathrm{BE}$) since gas can flow along the filament (Nagasawa 1987; Fischera & Martin 2012; see Appendix B). Perpendicular fields suppress fragmentation for $\mu_\Phi < 1$. SR2 contains at least 5 candidate prestellar cores (Marsh et al. 2016), which suggests that the lower estimates of the field in Table 2 are more accurate.

By contrast, SR1 has a chaotic field with a large dispersion in polarization angles, $\sigma_\theta = 54° \pm 5°$. This dispersion substantially exceeds the upper limit of applicability of the DCF method recommended by Ostriker et al. (2001), as well as the less stringent criterion in Appendix A1. We note that the same remains true even if we subdivide SR1 into the two parts SR1a and SR1b considered in Sect. 3.1.3. Nonetheless, the large dispersion implies a small, albeit uncertain, field: The standard method yields $B_0 \sim 7 - 13$ μG, depending on whether the velocity dispersion is estimated from the dominant velocity component (B_0^d) or the total line width (B_0^m). For the two sub-components of SR1, the DCF method gives $B_0 \sim 10-11$ μG for SR1a and $B_0 \sim 22-28$ μG for SR1b. The large dispersion in angles is due in part to large scale variations in the field structure that are allowed for in the DCF/SF analysis. Using that method with the total line width, the estimated magnetic field strength B_0^m is 23 or 16 μG, depending on whether $|\Delta\Phi|$ is restricted to be less than 90° or not (see Appendix A2.1). The turbulent magnetic field strength $\delta B_0^m = 18$ μG, comparable to B_0^m. We note that Marsh et al. (2016) found only one candidate prestellar core in the subregion SR1. Comparing the inset of figure 12 of Hacar et al. (2013) with the Herschel column density map suggests that SR1 may be the location where material from the ambient cloud is presently being accreted onto B211. In particular, the fiber #11 in Hacar et al. (2013) is not straight and part of it is parallel to the striations seen in CO and Herschel data; it matches a “spur” or “strand” (in the terminology of Cox et al. 2016) and may correspond to the tip of a striation where it meets and interacts with the main B211 filament (Shimajiri et al. 2019). This suggests that the flow velocities in the plane of the sky could be substantial, so that the observed LOS velocity is smaller than the POS velocities that determine σ_θ. In fact, Shimajiri et al. (2019) estimated that the inclination angle of the northeastern accretion flow to the line of sight is 70°, corresponding to a POS velocity 2.75 times larger than the LOS velocity. If so, the DCF value of the field there is an underestimate.

Myers & Goodman (1991) and Houde et al. (2009) have pointed out that if the turbulent correlation length, δ, is less than the thickness of the region being observed along the LOS, w, then the dispersion in PAs will be reduced. Houde et al. (2009) found that the reduction factor is $[w/(2\pi)^{1/2}\delta]^{-1/2}$ when δ is much larger than the beam width. From Fig. 7 we find that δ is about 3 super pixels in size for SR2 and 5 super pixels for SR1, significantly greater than the beam width, which is less than one super pixel. In both cases, the turbulent correlation length is about $w/3$, so the reduction factor is of order unity. This is to be expected in a filament that forms in a turbulent medium. Since this effect is small compared to the uncertainties in the observations and in the method, we ignore it.

It is instructive to compare DCF field measurements with Zeeman measurements. Myers & Basu (2021) have applied the DCF method to a carefully selected set of low-mass cores and have shown that the measured magnetic fields give a median normalized mass-to-flux ratio, $\mu_{\Phi,\mathrm{med}} = 1.7$, similar to that determined by the Zeeman method (Crutcher et al. 2010). As they note, there are very few cores with both DCF and Zeeman measurements. There are no Zeeman measurements of the field in B211, so we compare with the average Zeeman field in interstellar molecular clumps determined by Li et al. (2015) from the Zeeman data summarized by Crutcher et al. (2010). The average LOS field is $B_{\mathrm{Zeeman,\,LOS}} = 33 n_{\mathrm{H_2},4}^{0.65}$ μG. The median angle of inclination between a filament and the plane of the sky is $\gamma = 30°$, so the mean POS field inferred from the LOS field is $(\tan 30°/\tan\gamma) B_\mathrm{LOS}$. This is the mean field, not the total or rms field, since that is what Zeeman observations measure. The POS field corresponding to the average Zeeman field is thus

$$B_{0,\mathrm{Zeeman}} = 57 \left(\frac{\tan 30°}{\tan\gamma}\right) n_{\mathrm{H_2},4}^{0.65} \quad \mu\mathrm{G}. \qquad (7)$$

For SR1, with $n_{\mathrm{H_2},4} = 1$, this gives an inferred POS field (not a measured one) of 57 μG at the average inclination, much larger than the 13-23 μG from the DCF methods with the full line profile. This suggests that the DCF method indeed underestimates the field in this region. For SR2, with $n_{\mathrm{H_2},4} = 2.3$, the inferred Zeeman POS field is 98 μG, a little larger than the DCF estimates, 66-82 μG.

We also estimated the field strength of a larger area of Taurus/B211 using *Planck* polarization data from Planck Collaboration Int. XII (2013) (at an effective HPBW resolution of $10'$). The independent polarization measurements from *Planck* in this area (displayed as orange vectors in Fig. 5) indicate a dispersion in polarization angles of about 24° at $10'$ resolution. The average velocity dispersion in this extended environment around almost the entire L1495/B213 filament is $\sim$0.85 km s^{-1} as estimated by Chapman et al. (2011) from ^{13}CO(1–0) observations. We estimated the average volume density, $n_{\mathrm{H_2}} \simeq 10^3$ cm^{-3}, following the same approach as described in Section 3.1.5 but adopting a characteristic depth of $\sim$0.5 pc for the ambient cloud around Taurus/B211 (see Shimajiri et al. 2019). Applying the DCF formula of Equation (3) with these values lead to a field strength of $\sim 41\,\mu$G.

3.2 Polarization vectors and surface density contours

As discussed in Soler et al. (2017) and references therein, the gas that feeds a cloud appears to be gathered along the magnetic field direction. Physically, it is easier for gas to flow along the field than perpendicular to the field when the field is dynamically important. Furthermore, a long, slender filament can accrete gas much more easily on its sides than at its ends. This accounts for the observation that the dense regions in many molecular clouds show magnetic fields that tend to be perpendicular to contours of the surface density (Planck Collaboration Int. XXXV 2016).

Let ϕ be the magnitude of the angle between the field vector inferred from polarization (i.e., the PA) and the tangent to the surface density contour, so that $0^\circ \leqslant \phi \leqslant 90^\circ$. Soler et al. (2013) found that in many of the cases they considered the magnetic field tended to be parallel to the isodensity contours in 3D and column density contours in 2D ($\phi \sim 0^\circ$). For strong fields ($\beta = 8\pi\rho c_s^2/B^2 \lesssim 1$), the relative orientation became closer to perpendicular ($\phi \sim 90^\circ$) at high densities. Seifried et al. (2020) attributed the change in relative orientation at high density to the gravitational energy becoming comparable to the magnetic energy. An alternative description of the ϕ distribution was introduced by Soler et al. (2013, 2017), the histogram shape parameter:

$$\xi = \frac{A_0 - A_{90}}{A_0 + A_{90}}, \tag{8}$$

where A_0 is the area under the histogram of ϕ values for $0^\circ \leqslant \phi \leqslant 22.5^\circ$ and A_{90} is the area for $67.5^\circ \leqslant \phi \leqslant 90^\circ$. A negative value of ξ means that the PAs tend to be perpendicular rather than parallel to the surface contours. The ratio of perpendicular to parallel PAs is $A_{90}/A_0 = (1-\xi)/(1+\xi)$.

Gas flows near the cloud determine how gas is accreted onto the cloud and thus how the cloud forms (Shimajiri et al. 2019). However, observations provide only the LOS velocity information, which can be very different from the POS velocity and thereby give a misleading idea of the true spatial gas movement (Li & Klein 2019). As noted above, fields with a substantial component normal to a filament can facilitate accretion of gas onto the filament. To assess the importance of magnetic fields in B211, we present two complementary plots of the data. In Fig. 8a, we plot the orientations of the gradient of the surface density from *Herschel* data against the PAs from the HAWC+ observations. Note that the gradient of the surface density is normal to the contours of surface density, so that fields perpendicular to the filament are parallel to the gradient. In Fig. 8b, we plot a histogram of the ϕ distribution (i.e., the distribution of angles between the PAs and the tangents of the surface density contours). Because of the relatively small number of detected pixels and the limited dynamic range of the SOFIA polarization data in terms of column density, we cannot meaningfully apply a tool such as the histogram of relative orientations (HROs) as a function of surface density to the HAWC+ observations in B211. Therefore, we show only one HRO in Fig. 8b from all the detected pixels of the observed B211 region. The histogram shape parameter for B211 is $\xi = -0.28$. The negative value is primarily due to SR2, which has $\xi = -0.48$; the chaotic field in SR1 has $\xi \sim 0$. It is clear from Fig. 8b that there are more pixels at 90° than at 0°. The distribution of angles in this figure is similar to the high surface density Centre-Ridge region in the Vela C molecular complex. As noted above, a negative value of ξ is consistent with gas accretion along field lines that thread the cloud.

4 COMPARISON WITH SIMULATION

Above we used observational data from HAWC+ and the IRAM 30m telescope to obtain the LOS velocity, the magnetic field orientation, and an estimate of the field strength. In this section we shall compare these observations with a numerical simulation that was designed not to simulate L1495 in particular, but rather to simulate the formation of filamentary structures in a typical supersonically turbulent, magnetized interstellar molecular cloud (Li & Klein 2019). Although there are some differences between the simulated filamentary cloud and L1495, such as the mass per length and probably the overall magnetic field strength in the regions, the filamentary substructures in the simulated cloud are similar to those in L1495 (Hacar et al. 2013). In fact, the results of our simulation inspired this high-resolution polarization observation of the L1495/B211 region with the aim of understanding the three-dimensional structure of the magnetic field inside filamentary clouds.

To compare the HAWC+ observational results in Section 2.1 with simulation, we use our high-resolution simulation results of the formation of filamentary molecular clouds described in detail in Li & Klein (2019). This simulation used our multi-physics, adaptive mesh refinement (AMR) code ORION2 (Li et al. 2012a). Since the purpose of the simulation was to study the formation of filamentary structures prior to the onset of star formation, radiation transport and feedback physics were ignored. The ideal MHD simulation begins with turbulent driving but without gravity for two crossing times in order to reach a turbulent equilibrium state. The entire simulation region is 4.55 pc in size with a base grid of 512^3. Two levels of refinement were imposed to refine pressure jumps, density jumps, and shear flows to reach a maximum resolution of 2.2×10^{-3} pc, which was chosen to be sufficient to study filamentary substructures with a width of order 0.1 pc. Turbulence was driven throughout the simulation at a 3D thermal Mach number $\mathcal{M} = 10$ on the largest scales, with wave number $k = 1 - 2$. Gravity was turned on after two crossing times. After gravity was turned on, we included an additional refinement requirement, the Jeans condition (Truelove et al. 1997). We adopted a Jeans number of 1/8, which means that the Jeans length is resolved by at least 8 cells. We adopted periodic boundary conditions and assumed an isothermal equation of state for the entire simulation at a temperature of 10K. Using the turbulent line-width-size relation (McKee & Ostriker 2007), setting the Alfvén Mach number to be 1, and setting the virial parameter to be 1, implies that the total mass of the entire cloud is $M = 3110\,M_\odot$ and the initial magnetic field is 31.6 μG. A long, massive filamentary cloud formed after gravity was turned on, and at a time of 700,000 yr, it had a length of 4.42 pc and a mass of about $471\,M_\odot$. The moderately strong large-scale field was found to be crucial in maintaining the integrity of the long and slender filamentary cloud. Details of the physical properties of the filamentary cloud can be found in Li & Klein (2019).

4.1 Simulation parameters and methods

In our simulation, even the base grid has resolution of ~ 0.009 pc per cell, higher than HAWC+ superpixels. To produce the same resolution map for direct comparison with HAWC+

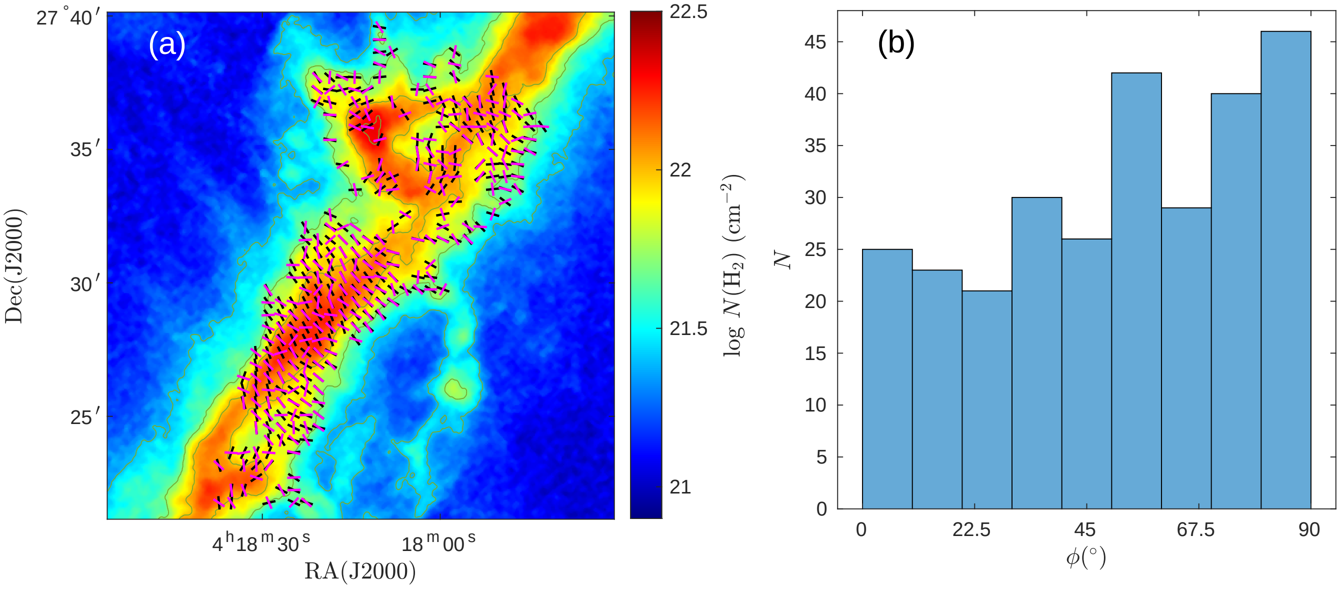

Figure 8. (a) Orientations of the inferred magnetic field (black) from HAWC+ and of the surface density gradient vectors (magenta) are plotted over the Herschel surface density. (b) Histogram of the distribution of angles between the inferred magnetic field directions and the tangents of the contours of surface density.

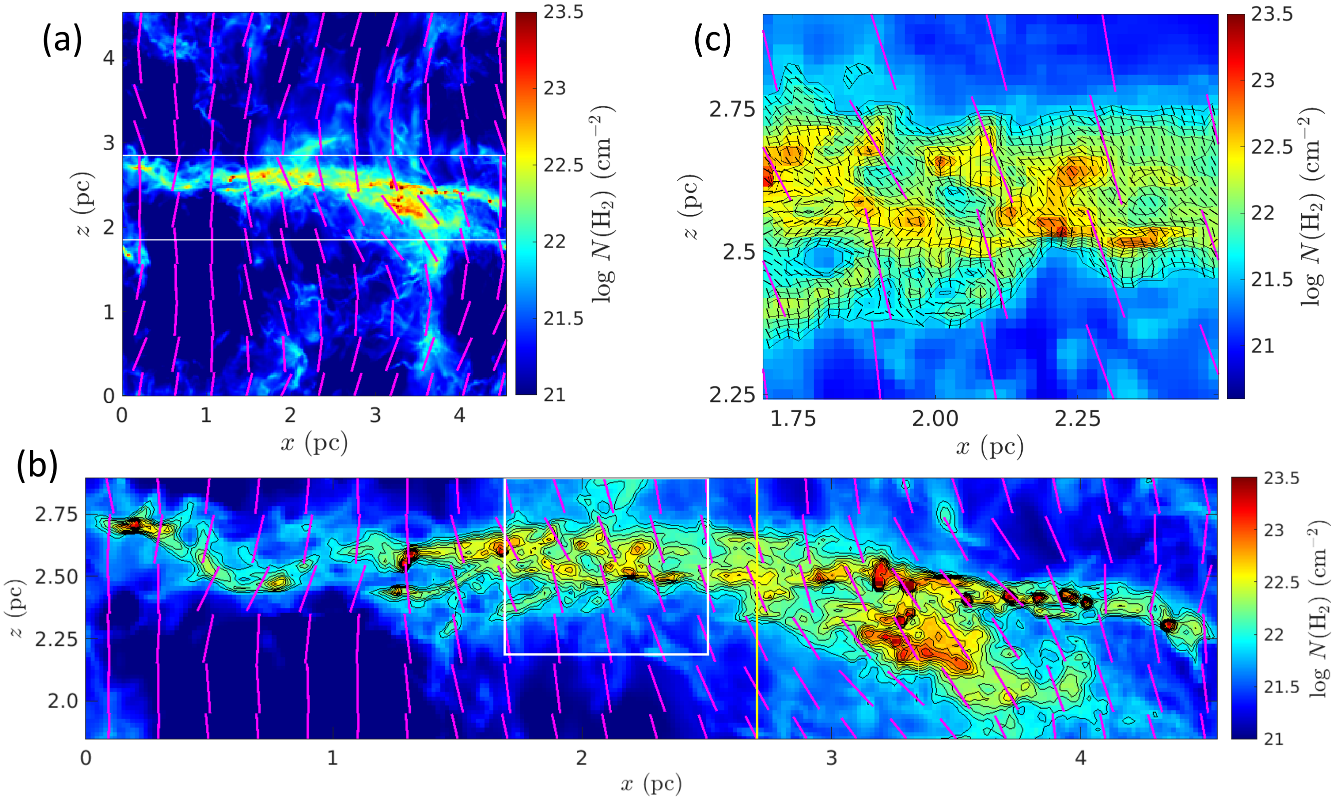

Figure 9. (a) Surface density map of the entire simulated region as viewed along the y-axis; the mean field is in the z direction. Magenta lines indicate the large-scale magnetic field at a resolution of 0.4 pc. The filamentary cloud lies between the two long white lines. (b) Enlargement of the surface density map of the filamentary cloud with contours of $\log_{10} N(\mathrm{H_2})$ ranging from 21.875 to 23, separated by $\Delta \log_{10} N(\mathrm{H_2}) = 0.125$. Due to a collision of two filamentary clouds near $x = 3.3$ pc, only the range $x = 0$ to 2.7 pc (up to the yellow vertical line) of the cloud is used for comparison with observation. Magenta lines indicate the large-scale magnetic field at 0.2 pc resolution. (c) Zoom in around the 0.82 pc × 0.69 pc FOV window in panel (b) showing the highly perturbed magnetic field at 28.″1 resolution (the same as the HAWC+ observation). The local orientation of the field is indicated by the short black lines (shown only at pixels with $\log_{10} N(\mathrm{H_2}) \geqslant 21.59$). As in (b), magenta lines indicate the large-scale magnetic field at 0.2 pc resolution. The surface density contours start from $\log_{10} N(\mathrm{H_2})$ of 21.59 and separated by $\Delta \log_{10} N(\mathrm{H_2}) = 0.125$.

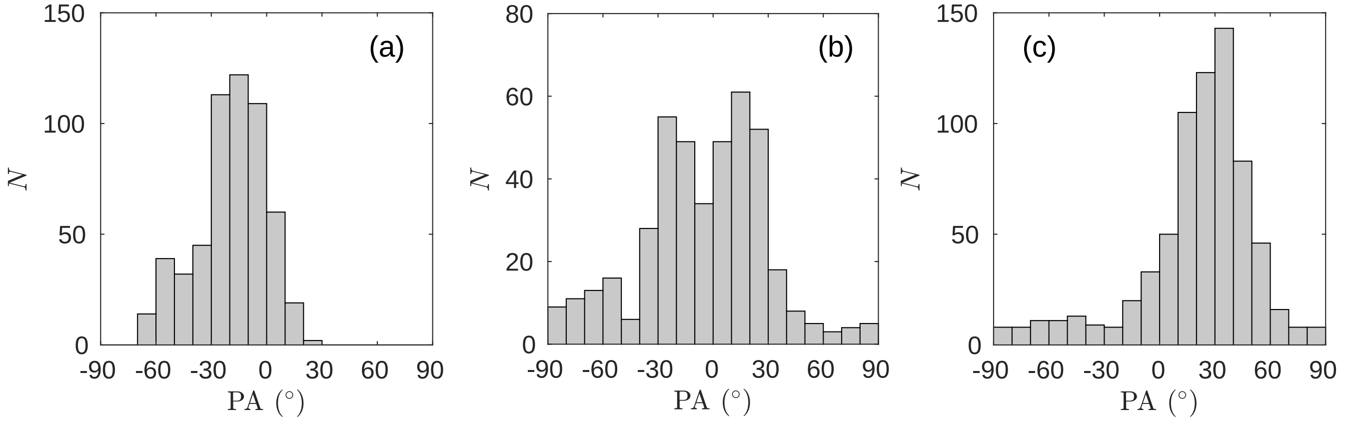

Figure 10. PA distributions of magnetic field of three 0.82 pc long FOVs of the simulated cloud. The angle θ is measured relative to the mean direction of the field in the simulation box. (a) Single group PA distribution from a FOV starting at $x = 0.16$ pc; the distribution peaks at $-25°$. (b) Double-hump PA distribution from a FOV starting at $x = 0.75$ pc. (c) A single group PA distribution from a FOV starting at $x = 1.69$ pc, with a peak at 35°, at the location of the FOV window in Figure 9b.

or Planck data, we first integrate LOS quantities, such as volume density to obtain the surface density, over the base grid to create a 2D map at 512^2 resolution. We compute the Stokes parameters following Zweibel (1996). Density weighting is used when computing the Stokes parameters and the LOS velocity dispersion. We then coarsen the 2D map to the resolution of a HAWC+ superpixel or of the Planck data by computing the mean of the corresponding number of pixels.

The surface density map of the entire simulated region is shown in Fig. 9a. The polarization field indicating the density-weighted large-scale magnetic field at a resolution of 0.4 pc, which is the best resolution that Planck can achieve at the distance of L1495, is superimposed on the map. In the other two panels of Fig. 9, the large-scale polarization field are shown at 0.2 pc resolution. The main filamentary cloud in between the two white lines is enlarged in Fig. 9b. The simulated filamentary cloud is composed of rich filamentary substructures along the entire length, similar to L1495 and other filamentary clouds. To study the magnetic field structures of filamentary clouds at the early stage of the formation, it is helpful to observe a cloud before the formation of protostars because powerful protostellar outflows can disrupt the magnetic field structures within filamentary substructures. The region B211 in L1495 has no protostars but contains filamentary substructures (Hacar et al. 2013) and prestellar cores (Marsh et al. 2016). Therefore, the simulated cloud is suitable for comparison with B211. Due to the collision of two filamentary clouds in our simulation at $x \sim 3.3$ pc, our comparison with observations will be in the range of $x = 0 - 2.7$ pc, i.e. up to the left of the vertical yellow line in Fig. 9b. The length of B211 with signal detected by HAWC+ is about 0.82 pc. We can create a projection of the cloud of the same length within this range for comparison. An example of a projected window, the white box in Fig. 9b, is shown in Fig. 9c. The small scale magnetic field structures at the resolution of 0.019 pc, corresponding to the super-pixel resolution in the HAWC+ observation, are shown together with the low resolution magnetic field. All the following comparisons between the simulation and HAWC+ observations will be at this resolution. For clarity, we show only vectors at pixels with surface density $\log_{10} N(\mathrm{H}_2) \geqslant 21.59$, corresponding to the minimum surface density with detected polarization signal in the observed B211 region by HAWC+. We can see the small-scale magnetic fields inside the cloud have large deviations from the low resolution large-scale fields surrounding the dense substructures, as shown in Li & Klein (2019).

4.2 PA distribution

The HAWC+ observations of B211 show a larger dispersion of PAs than the lower resolution Planck observations of the large-scale field as discussed in Section 2.4. The results indicate that small-scale perturbations of the magnetic field are present in B211. In Fig. 10, we show the PA distributions of three FOVs in the simulation. They have a length of 0.82 pc, which corresponds the HAWC+ map, and height of 0.69 pc, which is large enough to include the width of the filament. The distribution in Fig. 10a is a single group peaking at about $-15°$. In Fig. 10b, the distribution becomes double-humped, with peaks at $-25°$ and 15°. These two FOVs along the filamentary cloud have quite different PA distributions even though they are offset by only 0.6 pc. In Fig. 10c, which is the white colored FOV shown in Fig. 9b, the distribution returns to a single group again and peaks near 35°. We see that the PA distribution and the mean PA vary along the simulated cloud. In Palmeirim et al. (2013), the mean PA of the extended optical and infrared polarization vectors also changes along the filamentary cloud L1495. More polarization mapping in different parts of the filamentary cloud Taurus/B211 will be needed to find out if the PA distribution would change as in Fig. 10.

In Fig. 11, we compare two PA distributions in the simulation by viewing the simulated cloud at the same distance of L1495, one in a small region at the HAWC+ superpixel resolution of 28.1 arcsec and one in the whole simulated box at the Planck resolution of 10 arcmin. For the small region, we choose the FOV outlined in Fig. 9 since the PA distribution of this segment of the simulated cloud is similar to that of the observed B211 region. The other two FOV windows are quite different from B211, so we shall not discuss them fur-

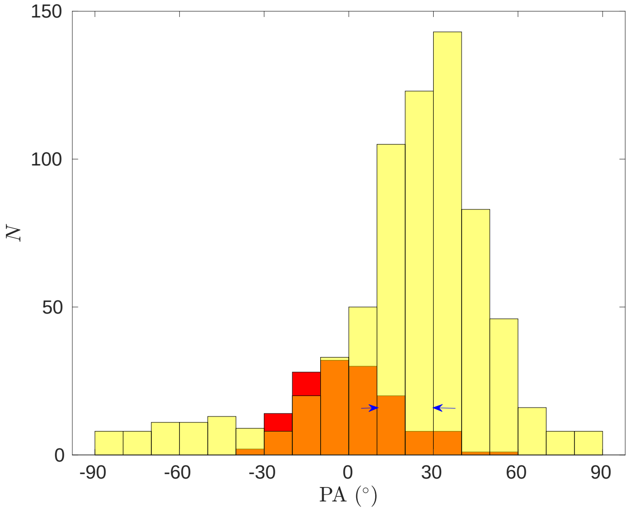

Figure 11. Comparison of the PA distributions of magnetic field in the simulation FOV window of Fig. 9b at HAWC+ 28.1 arcsec resolution (yellow histogram) and the entire simulation box (Fig. 9a) at Planck 10 arcmin resolution (red histogram; overlapping points are in orange). The 10 arcmin low resolution field vectors inside the simulation FOV window are all within the two bins between $10° - 30°$, marked by the blue arrows.

ther. The PA distribution at the Planck 10 arcmin resolution (red histogram in Fig. 11) is obtained from all the vectors in Fig. 9a. At this resolution the dispersion is only 6.6°, much smaller than the dispersion of 29.2° of the polarization at the HAWC+ superpixel scale (see Table 3). The resolution effect on the dispersion of PAs is clear both in simulation and observation (Fig. 4a). Some of this reduction in dispersion is likely due to a much lower dispersion in the low column-density gas that fills much of the Planck field: We found a dispersion of only 6.8° in a low-column region above the FOV window in the simulation. Since the polarization in the high-column LOSs is dominated by emission in the filament whereas that in the low-column LOSs is spread more uniformly over the entire LOS, the dispersion in the low-column directions is reduced by averaging along the LOS. In other words, the longer effective path length in the low-column directions leads to an LOS resolution effect.

In addition to this observational effect, the dispersion of PAs inside a molecular cloud is increased by the combined results of differential motions of dense substructures during cloud formation (Li & Klein 2019) and small-scale local gravity-driven motion as seen in numerical simulations of molecular cloud formation (e.g Chen et al. 2016; Li & Klein 2019; Seifried et al. 2020). These motions stretch the magnetic field locally, causing large changes in the direction of the magnetic field, as shown in figure 10 of Li & Klein (2019) and Fig. 9c in this paper.

4.3 DCF field estimates in the simulation

Here we apply the DCF and DCF/SF methods at HAWC+ super-pixel resolution to the FOV outlined in white in Fig. 9b. The velocity dispersion is density-weighted along the LOS. The mean width of the simulated filament, $w = 0.33$ pc, was computed by dividing the projected area of pixels above log $N(\mathrm{H_2}) = 21.59$ (the minimum surface density of the observed B211 region with a detected polarization signal) by the 0.82 pc length of the segment. Following the procedure used in analyzing the observations, we then estimated the density from the column density by assuming that the mean depth of the cloud is the same as the mean width, w.

Table 3. Comparison of physical properties of the simulated filamentary cloud estimated from DCF and DCF/SF methods at HAWC+ resolution

Method	DCF	DCF/SF
w (pc)	0.33	0.33
$n(\mathrm{H_2})$ ($\mathrm{cm^{-3}}$)	1.52×10^4	1.52×10^4
σ_θ (°)	29.2	-
$\Delta\Phi_{0,\mathrm{res}}$ (°)	-	35.4
$\Delta\Phi_{0,\mathrm{nores}}$ (°)	-	37.2
σ_V (km $\mathrm{s^{-1}}$)	0.45	0.45
$B_{0,\mathrm{DCF}}$ (μG)	38.0	41.0 - 43.6[1]
δB_{DCF} (μG)	21.2	21.2
$B_{0,\mathrm{true}}$ (μG)	55.9	55.9
δB_{true} (μG)	55.9	55.9

[1] The smaller value is obtained using $\Delta\Phi_{0,\mathrm{nores}}$, the value obtained without restricting $\Delta\Phi$ to be in the range $0° - 90°$.

In Table 3, we compare the results for the simulated cloud at HAWC+ super-pixel resolution using the DCF and the DCF/SF methods. The turbulent correlation length, δ, in the simulated cloud segment is about 5 to 6 super-pixels, similar to that in SR1 and SR2 (see Fig. A1). This length is resolved by more than 40 cells at the highest resolution, so the DCF/SF results should be reliable. The magnetic field strength estimated using the DCF/SF method is in the range $41.0 - 43.6$ μG, a little larger than the estimated value using DCF method and slightly closer to the true value.

The mean volume density, $n(\mathrm{H_2})$, LOS velocity dispersion, σ_V, and dispersion of polarization PA, σ_θ, are listed in Table 3, and the Alfvén Mach number based on the POS field in this window, $\mathcal{M}_\mathrm{A}/\cos\gamma$, is given in Table 4; all these values are intermediate between the values for SR1 and SR2 given in Table 2. The primary difference between the simulated and observed regions is that the simulation has a higher mass per unit length, M_ℓ, and correspondingly a smaller value of the filament virial parameter, $\alpha_{\mathrm{vir,f}} = 2\sigma_V^2/(GM_\ell)$ (Fiege & Pudritz 2000a) (Table 4); the magnetic properties are similar.

To determine the true mean POS magnetic field strength above the surface density threshold in the simulation, the volume-means of the two projected magnetic field vector components for each pixel above the threshold were computed first. These vector fields were then averaged along the line of sight to a depth of 0.8 pc to obtain the mean vector field, $\mathbf{B}_{0,\mathrm{true}}$. Since the value of the true field is volume weighted whereas the DCF field is based on the density-weighted polarization (which is quite different from a density-weighted field), we do not expect the true field to exactly agree with the DCF field. The true 3D field is 57.1 μG, which implies that the mean field is at an angle of 12° with respect to the plane of the sky. Table 3 shows that the DCF and DCF/SF estimates of the mean POS field are about 70 percent of the true value. The SF variant is slightly closer to the true value than the standard DCF method, and the restricted value for the SF variant is slightly closer than the unrestricted value, but given the uncertainty in $f_{\rm DCF}$ and the fact that the true field and the DCF field have different weightings, it is not clear that these differences are significant.

The turbulent field, $\delta B_{0,\rm true}$, is the root-mean-square of the vector difference of the field vectors from the volume-mean field vector in all the cells in the volume corresponding to the FOV. The true values of δB are significantly greater than the true values of $\delta B_\perp$ (the rms value of component $\delta \mathbf{B}$ perpendicular to the mean POS field) due to the substantial parallel component of $\delta \mathbf{B}$ in δB. The value of $\delta B_\perp$ is the same for the DCF and DCF/SF methods since both are based on equation (A2). The approximations made in the DCF/SF method imply that the value of δB calculated in this method is actually $\delta B_\perp$. The fact that the true value of $\delta B_\perp$ is about 1.7 times larger than the DCF value, $B_0 \tan \sigma_\theta$, accounts for most of the difference between the DCF value of B_0 and the true value.

The derived physical parameters of the observed sub-regions in B211 and the segment of the simulated cloud are summarized in Table 4. The values of $\alpha_{\rm vir,f}$ are based on the total velocity dispersions (including thermal motions) of SR1, SR2, and the segment of the simulated cloud. The normalized mass-to-flux ratio in the simulation based on the DCF field is $\mu_{\Phi,\rm POS} = 2.7$, comparable to the observed values in SR1. Since the true value of the total POS field is 79 μG, the true value of $\mu_{\Phi,\rm POS}$ is 1.5, intermediate between the values for SR1 and SR2 and comparable to the initial value of 1.62 of the entire box viewed normal to the initial field. It is this value that we have used in determining $\mu_{\Phi,\rm POS}$ in the simulation. (Note that the use of the POS field to estimate μ_Φ leads to a slight overestimate of $M_\ell/M_{{\rm crit},\ell}$–see eq. B6.) Including the effect of a perpendicular magnetic field, the ratio of the line mass to the critical line mass, $M_\ell/M_{{\rm crit},\ell}$ (eq. B8), is less than unity for both observed subregions and for the simulated cloud segment, as shown in the table. These structures are therefore gravitationally stable against radial collapse on the scale at which this ratio is determined. In the absence of perpendicular magnetic fields, the critical mass and the virial mass are the same, and the filaments would be subject to fragmentation (Nagasawa 1987; Fischera & Martin 2012; see Appendix B2). Perpendicular fields would stabilize the cloud against fragmentation if the normalized mass-to-flux ratio is $\mu_\Phi < 1$. The results in Table 4 show that SR1 and the simulated filament should be subject to fragmentation; since SR2 has $\mu_\Phi \sim 1$ it is marginally susceptible. There is some evidence that pre-stellar cores are forming in both SR1 and SR2 (e.g., Marsh et al. 2016); as noted above, the fact that pre-stellar cores are observed in SR2 favors a lower estimate for the field there than the value given in Table 4. Equation B16 shows that fragments that form in SR1 are near the critical mass and could collapse, whereas those in SR2 appear to be stable against collapse; however, given the uncertainty in the parameters in Table 4, these conclusions are tentative. The FOV window in the simulation is magnetically supercritical, and dense cores are forming along some filamentary substructures. On small scales, we expect the velocity dispersion to be primarily thermal. At a temperature of 10 K, the thermal values of the virial parameter are $\alpha_{\rm vir,f} = 0.30$, 0.46, and 0.15, respectively.

Table 4. Summary of physical properties of the observed B211 sub-regions and a segment of the simulated filamentary cloud.[1]

Region	SR1	SR2	simulation
$M_\ell (M_\odot \ {\rm pc}^{-1})$	54	36	111
$\alpha_{\rm vir,f}$[1]	2.0	2.2	0.85
$B_{0,\rm DCF}$ (μG)	13 - 23[2]	65 - 82	38 - 44
$B_{\rm tot,\,DCF}$ (μG)[3]	23 - 30	70 - 85	44 - 48
$\mu_{\Phi,\,\rm DCF}$[4]	2.7 - 2.1	1.2 - 1.0	2.7 - 2.4
$\mathcal{M}_{\rm A}/\cos\gamma$[5]	4.8 - 2.6	1.3 - 1.0	2.0 - 1.6
$M_\ell/M_{{\rm crit},\ell}$[6]	0.50-0.49	0.43 - 0.42	0.97[7]

[1] The virial parameter for a filament is $\alpha_{\rm vir,f} = 2\sigma_V^2/(GM_\ell)$.
[2] The two values quoted for parameters that depend on the magnetic field correspond to the DCF and the larger of the two DCF/SF estimates, respectively, of the field strength using the total non-thermal velocity dispersion.
[3] The total DCF field, $B_{\rm tot,\,DCF} = (B_{0,\rm DCF}^2 + \delta B_{\rm DCF}^2)^{1/2}$.
[4] Normalized mass-to-flux ratio based on the total DCF field, $B_{\rm tot,\,DCF}$. The value based on the true total field is $\mu_{\Phi,\,\rm true} = 1.5$.
[5] 3D Alfvén Mach number ($\propto \sqrt{3}\sigma_V$) based on the mean POS field, $B_{0,\rm DCF}$, and assuming isotropic turbulence (eq. A13).
[6] M_ℓ is the mass per unit length for $N({\rm H_2}) \geqslant 10^{21.59}$ cm^{-2}. The critical line mass, $M_{\ell,\,\rm crit}$, is given in equation (B8).
[7] Based on the true value of $\mu_{\Phi,\rm POS} = 1.5$.

5 CONCLUSIONS

In this work, we have used HAWC+ on-board SOFIA to observe the L1495/B211 region in Taurus to investigate the magnetic field morphology in thin filamentary clouds. This observation is challenging because of the low surface brightness of the filamentary cloud. We needed to re-sample 3 × 3 detector pixel data to a super-pixel of 28.″1 to optimize the SNR. We have total 282 independent measurements that have $P/\sigma_P \geqslant 2$. The morphology of the observed polarization map clearly reveals two sub-regions, designated SR1 and SR2, in the observed B211 region. With IRAM 30m C^{18}O (1-0) data, we estimate the magnetic field strengths using the standard DCF method and the alternative DCF method using a structure function. We then compared the physical states of the two sub-regions with a simulated filamentary cloud.

1. *Polarization morphology of the two sub-regions in B211.* The chaotic appearance of the polarization vectors in SR1 indicates a strongly perturbed region, in contrast to SR2, which has a well organized magnetic field structure mostly, but not entirely, perpendicular to the filamentary cloud axis. The organized field in SR2 matches the large-scale field from Planck observation very well. The dispersion of the PAs in SR1 is 54 deg, almost 3 times of that in SR2.
2. *Filamentary substructures in B211.* The IRAM 30m C^{18}O (1-0) data reveals multiple velocity components in the observed B211 region, similar to what has been reported in a previous study of L1495 (e.g. Hacar et al. 2013). There are at least 3 velocity components in SR1 and 2 velocity components in SR2. Multiple filamentary substructures are also clearly seen in the high resolution Herschel map. The chaotic appearance of substructures, polarization vectors, and the multiple-component line profiles in SR1 may indicate strong interaction among substructures.

3. *Magnetic fields of the two sub-regions and of the simulated filament.* Using the DCF and DCF/SF methods, the estimated field strength based on the total LOS velocity dispersion in SR1 is in the range 13 to 23 μG. Because of the very large dispersion of the polarization angles ($\sigma_\theta = 54°$), the field estimate in this region is very uncertain, but it is clear that the field is small. By contrast, the estimated field strength of SR2 is from 66 to 82 μG, significantly larger than that in SR1. These estimates are based on the assumption that the numerical coefficient introduced to correct for the approximations in the DCF method, $f_{\rm DCF}$, is 0.5 (Ostriker et al. 2001). In the part of the simulated filament that we analyzed in detail, the field strength is intermediate between that of SR1 and of SR2. The measured value of $f_{\rm DCF}$ was slightly larger than 0.5, but consistent with that value within the expected statistical uncertainties.

4. *Comparison with Zeeman field estimates.* Based on the Zeeman data summarized by Crutcher et al. (2010), Li et al. (2015) concluded that the average 3D magnetic field in molecular clumps in the ISM is $66 n_{\rm H_2,4}^{0.65}$ μG. For a typical inclination with respect to the plane of the sky of 30°, this corresponds to a POS field $B_0 = 57 n_{\rm H_2,4}^{0.65}$ μG. This is several times larger than the DCF estimate of the field in SR1, and we suggested that this could be due to the measured LOS velocity dispersion being less than the POS velocity dispersion. The POS field (for $\gamma = 30°$) corresponding to the average interstellar Zeeman field agrees reasonably well with the DCF field in SR2 and with the true POS field in the simulation.

5. *Resolution effect on the magnetic field dispersion.* The dispersion in polarization angles from the low resolution Planck data is significantly smaller than that of the high resolution HAWC+ data. Heitsch et al. (2001) and Falceta-Gonçalves et al. (2008) found this resolution effect in their simulations, and we do also. The simulation shows that the angle dispersion in low-column regions is less than in high-column regions, which contributes to the observed resolution effect.

6. *Polarization vectors and surface density gradients.* The relative distribution of the inferred magnetic field vectors and the tangent of surface density contours in the observed B211 region shows that the magnetic field has a tendency to be normal to the contours of surface density. This can be quantified by the histogram shape parameter, ξ, defined in equation (8). In B211, we find $\xi = -0.28$, meaning that the number of pixels with a magnetic field nearly normal to the contours of the surface density is about 1.8 times that with the magnetic field nearly parallel to the contours. The tendency for the field to be normal to the contours is primarily due to SR2, which has $\xi = -0.48$ and an average angle between the contours and the field of $\langle\phi\rangle = 55°$. The fact that there is some correlation between the orientation of the field and the column density contours of the gas indicates that the magnetic field is at least marginally dynamically important there. In the chaotic region SR1, the fact that $\xi = -0.03$ indicates that the magnetic field is dynamically sub-dominant, in agreement with the large value of the projected Alfvén Mach number there (Table 4).

7. *Physical states of the two subregions and of the simulated filament.* From the mass-to-flux ratios and Alfvén Mach numbers, SR1 is magnetically supercritical and slightly super-Alfvénic, although we have suggested that the DCF method underestimates the field in SR1. The magnetic field in SR2 is significantly greater than that in SR1. Both the standard DCF analysis and the DCF/SF method suggest that SR2 is approximately magnetically critical and that it is trans-Alfvénic. The segment of the simulated filament we have analyzed is magnetically supercritical like SR1, although it has a significantly smaller dispersion of PA angles; it has an Alfvén Mach number of about unity. The ratio of the line mass to the critical line mass is slightly less than unity for SR1, SR2, and the simulated filament if the full velocity widths of the filaments are used to estimate the virial parameters. Pre-stellar cores are suggested in both SR1 and SR2 (Marsh et al. 2016). There are two cores forming in the segment of the simulated filament that we have analyzed.

8. *The DCF method.* In Appendix A, we present derivations of both the standard DCF method and the structure function (SF) variant that are not restricted to small values of the polarization angles. We show that the standard DCF result often applies for the case of equipartition even if the perturbed field is not due to Alfvén waves. Our simulation confirms that δ, the correlation length of the turbulent magnetic field, is small, as assumed in the derivation of the DCF/SF method (Hildebrand et al. 2009). For SR1, SR2 and our simulation, we find that $\delta \sim$ FWHM of the filament ~ 0.1 pc, consistent with the formation of a filament in a turbulent medium. We discuss the restriction procedure often used in the DCF/SF method in which differences in angles that exceed 90° are converted to $|180 - 90°|$ and suggest that restriction provides a lower limit on the structure function and is significant only when the dispersion in PAs is large, so that the DCF method is of questionable accuracy.

9. *Different versions of the DCF method.* In Appendix A we also compare the standard DCF method with the DCF/SF version (Hildebrand et al. 2009) and the parallel-$\delta\mathbf{B}$ version (Skalidis & Tassis 2021a; Skalidis et al. 2021b). In most cases, the three methods agree within the uncertainties for both the observed regions, SR1 and SR2, and for the simulation. The exception is the standard DCF method, which gives a low value for the mean field in the highly tangled region SR1, probably because this method does not allow for spatial variation of $\mathbf{B}_0$.

10. *Equilibrium filaments and their fragmentation.* In Appendix B we give analytic estimates of the fragment mass and the condition for the formation of a pre-stellar core in an unmagnetized filament.

ACKNOWLEDGMENTS

Support for this research is based on observations made with the NASA/DLR Stratospheric Observatory for Infrared Astronomy (SOFIA) under the 07_0017 Program. SOFIA is jointly operated by the Universities Space Research Association, Inc. (USRA), under NASA contract NNA17BF53C, and the Deutsches SOFIA Institut (DSI) under DLR contract 50 OK 0901 to the University of Stuttgart. We thank Che-Yu Chen, Amitava Bhattacharjee, Martin Houde, Alex Lazarian, and Junhao Liu for a number of very helpful conversations. We also thank the two anonymous referees for their many helpful suggestions that greatly improve the paper. Support for this research was provided by NASA through a NASA ATP grant NNX17AK39G (RIK, CFM & PSL) and the US Department of Energy at the Lawrence

Livermore National Laboratory under contract DE-AC52-07NA 27344 (RIK). CFM acknowledges the hospitality of the Center for Computational Astronomy of the Flatiron Institute in New York, where he was a visiting scholar. JR thanks partial support from SOFIA program 07_0017 and support from the SOFIA program 07_0047 and NASA Astrophysics Data Analysis grant (80NSSC20K0449). PhA acknowledges support from "Ile de France" regional funding (DIM-ACAV+ Pro- gram) and from the French national programs of CNRS/INSU on stellar and ISM physics (PNPS and PCMI). This work is partly based on observations carried out under project number 129-15 with the IRAM 30m telescope. IRAM is supported by INSU/CNRS (France), MPG (Germany) and IGN (Spain). The present study also made use of data from the Herschel Gould Belt survey (HGBS) project (http://gouldbelt-herschel.cea.fr). This work used computing resources from an award from the Extreme Science and Engineering Discovery Environment (XSEDE), which is supported by the National Science Foundation grant number ACI-1548562, through the grant TG-MCA00N020, computing resources provided by an award from the NASA High-End Computing (HEC) Program through the NASA Advanced Supercomputing (NAS) Division at Ames Research Center, and an award of computing resources from the National Energy Research Scientific Computing Center (NERSC), a U.S. Department of Energy Office of Science User Facility located at Lawrence Berkeley National Laboratory, operated under Contract No. DE-AC02-05CH11231.

DATA AVAILABILITY

The processed HAWC+ data in FITS format is available at CDS via anonymous ftp to cdsarc.u-strasbg.fr (130.79.128.5) or via https://cdsarc.unistra.fr/viz-bin/cat/J/MNRAS.

REFERENCES

Andersson B.-G., Lazarian A., Vaillancourt J. E., 2015, ARA&A, 53, 501

André, P., Di Francesco, J., Ward-Thompson, D., et al. 2014, Protostars and Planets VI, ed. H. Beuther, R.S. Klessen, C.P. Dullemond, T. Henning (Tuscon, AZ: Univ. Arizona Press), 27

André, Ph., Arzoumanian, D., Könyves, V., Shimajiri, Y., Palmeirim, P. 2019, A&A, 629, L4

André, Ph., Men'shchikov, A., Bontemps, S., et al. 2010, A&A, 518, L102

Arzoumanian, D., André, P., Didelon, P. et al. 2011, A&A, 529, 6

Arzoumanian, D., André, P., Könyves, V. et al., 2019, A&A, 621, 42

Bergin, E.A., Tafalla, M., 2007, ARA&A, 45, 339

Bhattacharjee A., Ng C. S., Spangler S. R., 1998, ApJ, 494, 409

Cabral, B., Leedom, C., Proc. SIGGRAPH '93, 263

Chandrasekhar S., Fermi E., 1953, ApJ, 118, 113

Chapman, N.L., Goldsmith, P.F., Pineda, J.L., Clemens, D.P., Li, D., Krčo, M. 2011, ApJ, 741, 21

Chen, C.Y., King, P.K. and Li, Z.Y., ApJ, 829, 84

Cox, N.L.J., Arzoumanian, D., André, P., et al. 2016, A&A, 590, 110

Crutcher R. M., Wandelt B., Heiles C., Falgarone E., Troland T. H., 2010, ApJ, 725, 466

Dall'Olio, D., Vlemmings, W. H. T., Persson, M. V. et al., 2019, A&A, 626, 36

Davidson J. A., Novak G., Matthews T. G., Matthews B., Goldsmith P. F., Chapman N., Volgenau N. H., et al., 2011, ApJ, 732, 97

Davis, L. 1951, Phys. Rev., 81, 890

Dowell, C.D., Cook, B.T., Harper, D.A., et al. 2010, Proc. SPIE, 7735, 77356H

Dhabal, A., Mundy, L.G., Rizzo, M.J., Storm, S., & Teuben, P., 2018, ApJ, 853, 169

Elias, J. H., 1978, ApJ, 224, 857

Eswaraiah, C., Li, D., Furuya, R.S., et al. 2021, ApJ, in press (arXiv:2103.02219)

Falceta-Gonçalves, D., Lazarian, A., Kowal, G., 2008, ApJ, 639, 537

Fiege, J.D., Pudritz, R.E. 2000, MNRAS, 311, 85

Fiege, J.D., Pudritz R.E., 2000, ApJ, 544, 830

Fischera J., Martin P. G., 2012, A&A, 542, A77

Guerra J. A., Chuss D. T., Dowell C. D., Houde M., Michail J. M., Siah J., Wollack E. J., 2021, ApJ, 908, 98

Hacar, A., Tafalla, M., Kauffmann, J., Kovács, A., 2013, A&A, 554, 55

Harper, D.A., Runyan, M.C., Dowell, D.A., et al. 2018, JAI, 740008H

Heiles, C., 2000, AJ, 119, 923

Heitsch, F., Zweibel, E. G., Mac Low, M.-M., Li, P. S., Norman, M. L., 2001, ApJ, 561, 800

Hennebelle P., Commerçon B., Joos M., Klessen R. S., Krumholz M., Tan J. C., Teyssier R., 2011, A&A, 528, A72

Heyer, M., Gong, H., Ostriker, E., Brunt, C. 2008, ApJ, 680, 420

Hildebrand, R. H., Kirby, L., Dotson, J. L., Houde, M., Vaillancourt, J. E., 2009, ApJ, 696, 567

Houde, M., Vaillancourt, J. E., Hildebrand, R. H., and Chitsazzadeh, S., Kirby, L., 2009, ApJ, 706, 1504

Houde M., Hull C.L.H., Plambeck R.L., Vaillancourt J.E., Hildebrand R.H., 2016, ApJ, 820, 38

Inutsuka, S., & Miyama, S.M. 1997, ApJ, 480, 681

Kashiwagi R., Tomisaka K., 2021, ApJ, 911, 106

Kawachi T., Hanawa T., 1998, PASJ, 50, 577

Könyves, V., André, P., Men'shchikov, et al., 2015, A&A, 584, 91

Kovács, A. 2006, PhD thesis, CalTech.

Kovács, A. 2008, Proc. SPIE, 7020, 70201S

Li, D., Goldsmith, P.F., 2012, ApJ, 756, 12

Li P.S., Martin D.F., Klein R.I., McKee, C.F., 2012a, ApJ, 745, 139

Li P.S., McKee C.F., Klein R.I., 2015, MNRAS, 452, 2500

Li P.S., Klein R.I. 2019, MNRAS, 485, 4509

Lopez-Rodriguez, E., Fuller, L., Alonso-Herrero, A., et al., 2018, ApJ, 859, 99

Lopez-Rodriguez, E. 2021, Nat. Astron., 5, 604

Marsh K. A., Kirk J. M., André P., Griffin M. J., Könyves V., Palmeirim P., Men'shchikov A., et al., 2016, MNRAS, 459, 342

Martin, P.G., 1974, ApJ, 187, 461

McKee C. F., 1989, ApJ, 345, 782

McKee C.F., Ostriker E.C., 2007, ARA&A, 45, 565

Motiei M. M., Hosseinirad M., Abbassi S., 2021, MNRAS, 502, 6188

Myers P. C., Basu S., 2021, arXiv, arXiv:2104.02597

Myers P. C., Goodman A. A., 1991, ApJ, 373, 509

Myers A. T., McKee C. F., Cunningham A. J., Klein R. I., Krumholz M. R., 2013, ApJ, 766, 97

Nagasawa M., 1987, PThPh, 77, 635

Nakano T., Nakamura T., 1978, PASJ, 30, 671

Ostriker, E. C., Stone, J. M., & Gammie, C. F. 2001, ApJ, 546, 980

Ostriker J., 1964, ApJ, 140, 1056

Padoan P., Goodman A., Draine B. T., Juvela M., Nordlund Å., Rögnvaldsson Ö. E., 2001, ApJ, 559, 1005

Palmeirim, P., André, P., Kirk, J., Ward-Thompson, D., Arzoumanian, D., Könyves, V. et al., 2013, A&A, 550, 38

Pattle K., Lai S.-P., Di Francesco J., Sadavoy S., Ward-Thompson D., Johnstone D., Hoang T., et al., 2021, ApJ, 907, 88
Planck Collaboration 2013 results. XI, 2013, A&A, 571, A11
Planck Collaboration Int. XXXV, 2016, A&A, 586, 138
Seifried D., Walch S., Weis M., Reissl S., Soler J. D., Klessen R. S., Joshi P. R., 2020, MNRAS, 497, 4196
Shimajiri, Y., André, P., Palmeirim, P., et al. 2019, A&A, 623, A16
Shercliff J. A., 1960, JFM, 9, 481
Skalidis, R., Tassis, K., 2021, A&A, 647, 186
Skalidis R., Sternberg J., Beattie J. R., Pavlidou V., Tassis K., 2021, arXiv, arXiv:2109.10925
Soler, J.D., Hennebelle, P., Martin, P.G., Miville-Deschênes, M.A., Netterfield, C.B. et al., 2013, ApJ, 774, 128
Soler, J.D., Ade, P.A.R., Angiè, F.E., Ashton, P., Benton, S.J., Devlin, M.J. et al., 2017, A&A, 603, 64
Stodólkiewicz J. S., 1963, AcA, 13, 30
Sugitani, K., Nakamura, F., Shimoikura, T., et al., 2019, PASJ, 71, 7
Tafalla, M., Hacar, A., 2015, A&A, 574, 104
Tomisaka K., 2014, ApJ, 785, 24
Tomisaka K., Ikeuchi S., Nakamura T., 1988, ApJ, 335, 239
Truelove J.K., Klein R.I., McKee C.F., Holliman II J.H., Howell L.H., Greenough, J.A., 1997, ApJ, 489, 179
Vaillancourt, J.E., Chuss, D.T., Crutcher, R.M., et al., 2007, Proc. SPIE, 6678, 66780D
Viala Y. P., Horedt G., 1974, A&A, 33, 195
Wardle, J.F.C., Kronberg, P.P. 1974, ApJ, 194, 249
Zweibel E. G., 1990, ApJ, 362, 545
Zweibel, E.G., 1996, in ASP Conf. Ser. 97, Polarimetry of the Interstellar Medium, ed. W. G. Roberge & D. C. B. Whittet (San Francisco : ASP), 486
Zweibel E. G., McKee C. F., 1995, ApJ, 439, 779

APPENDIX A: THE DAVIS-CHANDRASEKHAR-FERMI METHOD

Davis (1951) and Chandrasekhar & Fermi (1953) proposed a method for estimating magnetic field strengths in the ISM based on the assumptions that the medium is isotropic and that variations in the orientation of the field are due to Alfvén waves. Hereafter, we refer to this as the DCF method. However, there are different approximations used and assumptions made in the literature, particularly in dealing with a large dispersion in the polarization angles (PAs). Therefore in this appendix we give a more rigorous derivation of the DCF result based on the method of Hildebrand et al. (2009). We then discuss two variants of the DCF method, the structure function method (DCF/SF) of Hildebrand et al. (2009) and the parallel-δB version of Skalidis & Tassis (2021a). In applications of the DCF/SF method, differences between the PAs at different points are often restricted to be less than 90°, and we show how that can be problematic.

Only fields in the plane of the sky (POS) can be inferred in this manner, and, as noted in equation (1), in this paper $\mathbf{B}$ (and $\mathbf{v}$) always refer to the components of the magnetic field and velocity in the POS. For Alfvén waves, which are transverse, the equation of motion implies

$$\delta\mathbf{v} = \pm\frac{\delta\mathbf{B}}{(4\pi\rho)^{1/2}}, \tag{A1}$$

where $\delta\mathbf{v}$ and $\delta\mathbf{B}$ represent the wave amplitude in the POS. For circularly polarized simple waves, this relation is valid for arbitrary wave amplitudes (Shercliff 1960); for linearly polarized waves, it is valid only in the linear regime, since the wave is affected by the magnetic pressure gradients. This relation implies equipartition between the turbulent kinetic energy of motions normal to the mean magnetic field in the POS, $\mathbf{B}_0$, and the corresponding field energy in the waves, $\rho\delta v_\perp^2/2 = \delta B_\perp^2/8\pi$, where the POS quantities $\delta\mathbf{v}_\perp$ and $\delta\mathbf{B}_\perp$ are perpendicular to the mean POS field. Under the assumption that the turbulent velocities are isotropic, the rms value of $\delta v_\perp$ is the same as the LOS velocity dispersion, σ_V. If the mean 3D field is at an angle γ with respect to the POS and this angle is small enough that $\cos\gamma \simeq 1$, the assumption of isotropic velocities can be relaxed to be that the turbulent velocities are isotropic in the plane perpendicular to the mean 3D field. Let $\sigma_{\delta B_\perp}$ be the rms value of $\delta B_\perp$. Equation (A1) then implies

$$\sigma_V \simeq \frac{\sigma_{\delta B_\perp}}{(4\pi\rho)^{1/2}}, \tag{A2}$$

where ρ is a suitably averaged mean density. As discussed below, it is possible to measure the ratio $\sigma_{\delta B_\perp}/B_0$. We can therefore obtain the value of B_0 by dividing both sides of this equation by B_0,

$$B_0 \simeq \frac{(4\pi\rho)^{1/2}\sigma_V}{\sigma_{\delta B_\perp}/B_0}. \tag{A3}$$

The same result holds under the more general assumption of equipartition of turbulent magnetic and kinetic energies in the POS, $\rho\delta v^2/2 \simeq \delta B^2/8\pi$, provided that the fluctuations in the velocity and in the field are isotropic. Isotropy implies $\delta v^2 = 2\sigma_V^2$ and $\delta B^2 = 2\delta B_\perp^2$ (recall that δv and δB are POS quantities and thus two dimensional). Equipartition then implies $\rho\sigma_V^2 = \sigma_{\delta B_\perp}^2/4\pi$, which is the same as equation (A3). Heitsch et al. (2001) found that the magnetic fluctuations were somewhat smaller than expected from equipartition, so that equation (A3) overestimates B_0; this is taken care of by the factor $f_{\rm DCF}$ in equation (A12) below.

Isotropy is an important assumption in the DCF method. Observations by Heyer et al. (2008) of the Taurus molecular cloud show that the turbulence there is anisotropic; it is not known if this is typical for molecular clouds. Their simulations for $\beta = 2c_{\rm s}^2/v_{\rm A}^2 = 0.02$ were strongly anisotropic, with 1D velocities perpendicular to the mean field 2-4 times greater than those along the field. As noted in the discussion of Alfvénic turbulence above, the DCF method can still be applied in the presence of such anisotropy if the mean 3D field is close to the POS. (The median value of the inclination γ is 30°, for which $\cos\gamma \simeq 0.87 \sim 1$.) For larger values of β, the simulations of Heyer et al. (2008) for $\beta \geqslant 0.2$ and those of Heitsch et al. (2001) for $\beta \geqslant 0.05$ showed approximately isotropic turbulence.

Another important assumption that went into the derivation of equation (A2) for Alfvén waves and equation (A3) for the case of equipartition is that a single turbulent region dominates the signal along the LOS; if there is one dominant object along the LOS, its depth must be smaller than, or at most comparable to, the turbulent correlation length. If there are multiple turbulent regions, then σ_V includes the differences in mean velocities of the regions and $\sigma_{\delta B_\perp}$ includes the differences in the mean field orientation along the LOS. Such effects have been analyzed by Zweibel (1990), Myers & Goodman (1991), and Houde et al. (2009). As discussed in Section 3.1.5, possible effects of this type of inhomogeneity in the region we have observed are small.

The ratio $\sigma_{\delta B_\perp}/B_0$ is estimated from fluctuations in the orientation of the field as revealed by polarization observations. We now discuss two methods of doing this, the standard method and the structure function method developed by Hildebrand et al. (2009). Bear in mind that a basic assumption of the DCF method is that the polarization traces an appropriately weighted (including by the density) integral of the direction of the magnetic field along the LOS. It must be borne in mind that the polarization angles (PAs), θ_i, are limited to the range $-90^\circ \leqslant \theta_i \leqslant 90^\circ$, whereas the field angles (FAs), $\theta_{\mathrm{FA},i}$, extend over the range $-180^\circ \leqslant \theta_{\mathrm{FA},i} \leqslant 180^\circ$, so that that there is a 180° ambiguity in the relation between the FAs and the PAs. Martin (1974) showed that the PA traces the mean FA in the simple case in which the FA is a linear function of position and the density is constant; for variable density, the conclusion holds if the FA is a linear function of surface density.

A1 The Standard DCF method

Let the total POS field be $\mathbf{B} = \mathbf{B}_0 + \delta\mathbf{B}$, where $\mathbf{B}_0 = \langle\mathbf{B}\rangle$ is the mean POS field in the region being studied and $\langle\delta\mathbf{B}\rangle = 0$. Let $\mathbf{B}_\parallel = \mathbf{B}_0 + \delta\mathbf{B}_\parallel$ be the component of the POS field parallel to $\mathbf{B}_0$ and $\delta\mathbf{B}_\perp$ be the POS component perpendicular to $\mathbf{B}_0$. Then the field angle (FA), θ_{FA}, at point i relative to $\hat{\mathbf{B}}_0$ is:

$$\cos\theta_{\mathrm{FA},i} = \hat{\mathbf{B}}_i \cdot \hat{\mathbf{B}}_0 = \frac{B_{\parallel,i}}{(B_{\parallel,i}^2 + \delta B_{\perp,i}^2)^{1/2}}. \tag{A4}$$

This is presumably the density-weighted mean along the LOS for optically thin emission so that the PA coincides with the FA to within a 180° ambiguity. We now evaluate this under the assumption that $\delta B_i \ll B_0$ and then extend it to larger values. With this assumption, equation (A4) becomes

$$\cos\theta_{\mathrm{FA},i} \simeq \frac{1}{\left(1 + \delta B_{\perp,i}^2/B_0^2\right)^{1/2}}, \tag{A5}$$

with an error of order $\delta B_{\perp,i}^2 \delta B_{\parallel,i}/B_0^3$. The average value of $\cos\theta_{\mathrm{FA},i}$ is then

$$\langle\cos\theta_{\mathrm{FA},i}\rangle \equiv \cos\Delta\theta_{\mathrm{FA}} = \left\langle \frac{1}{\left(1 + \delta B_{\perp,i}^2/B_0^2\right)^{1/2}} \right\rangle \tag{A6}$$

with an error of order $\langle\delta B_{\perp,i}^2 \delta B_{\parallel,i}^2\rangle/B_0^4$. Note that $\Delta\theta_{\mathrm{FA}}$ depends only on perturbations perpendicular to the mean field; uniform compressions or rarefactions have no effect. Since the sign of θ_{FA} is irrelevant, we choose it to be positive. For a random field, $\langle\cos\theta_{\mathrm{FA},i}\rangle = 0$ so that $\Delta\theta_{\mathrm{FA}} = \pi/2$. Equation (A6) shows that in this case $B_0 = 0$: Despite being derived under the assumption that $\delta B/B_0$ is small, this equation remains valid in the opposite limit. Note that while the average FA as measured by $\Delta\theta_{\mathrm{FA}}$ must be in the range $0 - \pi/2$, our analysis does not exclude the possibility that some individual FAs can exceed $\pi/2$. Defining $\sigma_{\delta B_\perp} = \langle\delta B_\perp^2\rangle^{1/2}$, we approximate equation (A6) as

$$\cos\Delta\theta_{\mathrm{FA}} \simeq \frac{1}{(1 + \sigma_{\delta B_\perp}^2/B_0^2)^{1/2}} \tag{A7}$$

with an error relative to that equation of order $(\sigma_{\delta B_\perp}/B_0)^4$. Relating the cosine to the tangent, we then obtain

$$\tan\Delta\theta_{\mathrm{FA}} \simeq \frac{\sigma_{\delta B_\perp}}{B_0}, \tag{A8}$$

so that (eq. A3)

$$B_0 \simeq \frac{(4\pi\rho)^{1/2}\sigma_V}{\tan\Delta\theta_{\mathrm{FA}}}. \tag{A9}$$

Despite the approximations made, this result remains valid in the limit of a random field, for which $B_0 = 0$: In that case, $\langle\cos\theta_{\mathrm{FA},i}\rangle = 0$ and $\Delta\theta_{\mathrm{FA}} = \pi/2$ as noted above and $\tan\Delta\theta_{\mathrm{FA}} = \infty$; equation (A9) then gives $B_0 = 0$, as required.

We now make two approximations. First, to express the mean field in terms of the dispersion in the PAs, $\sigma_\theta = \langle\theta_i^2\rangle^{1/2}$, we note that the standard approximation $1 - \cos\theta \simeq \frac{1}{2}\theta^2$ implies that $\Delta\theta \simeq \sigma_\theta$ from equation (A6). This approximation for $1 - \cos\theta$ is reasonably good even for relatively large values of θ: For $\theta = \pi/2 = 1.57$, the approximation gives $\theta = [2(1-\cos\theta)]^{1/2} = \sqrt{2}$, which is off by only 11 percent. The second approximation is central to the DCF method: We assume that for the most part the FAs are approximately equal to the PAs, so that $\cos\Delta\theta_{\mathrm{FA}} \equiv \langle\cos\theta_{\mathrm{FA},i}\rangle \simeq \langle\cos\theta_i\rangle \equiv \cos\Delta\theta$. We combine these approximations to set

$$\tan\Delta\theta_{\mathrm{FA}} \simeq \tan\sigma_\theta, \tag{A10}$$

which relates the average cosine of the FAs, which determines B_0, to the dispersion of the PAs, which is what can be observed. For a Gaussian distribution of FAs, one can show that this approximation is accurate to within 10 percent for $\sigma_\theta < 45^\circ$. The approximation is even more accurate for a uniform distribution of PAs (quite different from a Gaussian) with this dispersion; note that the distribution of FAs in the simulation of Padoan et al. (2001) is much closer to a uniform distribution than to a Gaussian.[1] Equations (A8) and (A10) then give the standard result for the dispersion of the component of the POS field perpendicular to the mean POS field,

$$\frac{\sigma_{\delta B_\perp}}{B_0} \simeq \tan\sigma_\theta, \tag{A11}$$

although this is less accurate than equation (A10). Correspondingly, the strength of the total POS field is $B = B_0 \sec\sigma_\theta$. The resulting value of the mean POS field is then (eq. A9)

$$B_0 = f_{\mathrm{DCF}} \frac{(4\pi\rho)^{1/2}\sigma_V}{\tan\sigma_\theta}, \tag{A12}$$

where f_{DCF} allows for inaccuracies in the approximations that led to this result. For $f_{\mathrm{DCF}} = 1$, the RHS of this equation is identical to the result of Falceta-Gonçalves et al. (2008). The factor f_{DCF} must be determined from simulations. Following Ostriker et al. (2001), we set $f_{\mathrm{DCF}} = 0.5$ in this work. Padoan et al. (2001) found $f_{\mathrm{DCF}} = 0.4 \pm 0.11$ in their analysis of the fields in three gravitationally bound cores in their simulation. In general, f_{DCF} depends on the physical conditions and possibly on the resolution (Houde, private communication).

The accuracy of the DCF method depends upon both the dispersion of the PAs, σ_θ, and on the angle between the mean

---

[1] A uniform distribution of PAs changes significantly for $\sigma_\theta > 52^\circ$. If the distribution of FAs extends over the range $\pm\theta_m$, then $\sigma_{\theta_{\mathrm{FA}}} = \theta_m/\sqrt{3}$, so that a dispersion of 52° corresponds to $\theta_m = \pi/2$. For $\theta_m \leqslant \pi/2$, the PAs are identical to the FAs (to within an overall sign ambiguity of 180°). For $\sigma_{\theta_{\mathrm{FA}}}$ between 90° and 180°, σ_θ is confined to the narrow range 52°-59°.

field and the plane of the sky, γ, through its effect on σ_θ. The method fails for $\gamma \simeq 90^\circ$, where $\sigma_{\delta B_\perp} \gg B_0$ and $\tan \sigma_\theta$ becomes large. Ostriker et al. (2001) found that a sufficient condition for the DCF method to be accurate is $\sigma_\theta \leqslant 25^\circ$ and $\gamma \leqslant 60^\circ$. The approximations that led to equation (A8) become increasingly inaccurate as $\sigma_{\delta B_\perp}/B_0$ increases, so it is best to keep $\sigma_{\delta B_\perp}/B_0 \simeq \tan \sigma_\theta < 1$, corresponding to $\sigma_\theta < 45^\circ$. A limit on σ_θ gives a limit on the 3D Alfvén Mach number, $\mathcal{M}_{\rm A}$. The value of $\mathcal{M}_{\rm A}$ for the mean 3D field, $B_{0,\,\rm 3D} = B_0/\cos\gamma$, for isotropic turbulence is (eq. A12)

$$\mathcal{M}_{\rm A} = \frac{\sqrt{3}\tan\sigma_\theta \cos\gamma}{f_{\rm DCF}} \rightarrow 3.5\tan\sigma_\theta\cos\gamma, \qquad \text{(A13)}$$

where the last step is for $f_{\rm DCF} = 1/2$. For $\sigma_\theta < (25^\circ, 45^\circ)$ this is $\mathcal{M}_{\rm A} < (1.6,\,3.5)\cos\gamma$.

Different assumptions lead to different approximations for $\sigma_{\delta B_\perp}$. For example, Zweibel (1996) assumed that the FAs are identical to the PAs at the outset. She therefore excluded the possibility that individual FAs could exceed 90°, in contrast to our approach. With $\delta B_i = B_0 \tan\theta_i$, averaging δB^2 over different lines of sight gives $\sigma^2_{\delta B_\perp}/B_0^2 = \langle \tan^2\theta\rangle$; she obtained the same result through an analysis using the Stokes parameters. Heitsch et al. (2001) recognized that this is problematic for flows with Alfvén Mach numbers $\gtrsim 1$ since the average of $\tan^2\theta$ is dominated by angles near 90°, and they suggested several approximations to overcome this. As noted above, Falceta-Gonçalves et al. (2008) suggested replacing the average of the tangent by the tangent of the average, which we derived above; this also overcomes this problem.

A2 The Structure Function Version of the DCF Method (DCF/SF)

Hildebrand et al. (2009) improved on the standard DCF approach by allowing the direction of the mean magnetic field to be a slowly varying function of position, $\mathbf{B}_0(\mathbf{x})$; the magnitude of the field was assumed to be constant, however. A strength of their method is that the unknown direction of the mean field is not needed in order to determine its magnitude. Furthermore, it is relatively independent of the dispersion of PAs on large scales and can therefore handle cases in which large dispersions on large scales cause the standard DCF method to break down. Houde et al. (2009) extended this method to allow for variations along the line of sight and across the telescope beam, but at the expense of adding an additional parameter that must be fit from the data. Here we follow the simpler approach of Hildebrand et al. (2009). We include possible effects of integration along the line of sight, in addition to the effects of other approximations made in the method, in a numerical factor $f_{\rm DCF}$, as in equation (A9).

The field is decomposed into a smooth part and a turbulent part,

$$\mathbf{B}(\mathbf{x}) = \mathbf{B}_0(\mathbf{x}) + \delta\mathbf{B}(\mathbf{x}) \qquad \text{(A14)}$$

with

$$\begin{aligned} \langle \delta\mathbf{B}(\mathbf{x})\rangle &= 0, && \text{(A15)}\\ \langle \delta\mathbf{B}(\mathbf{x})\cdot\mathbf{B}_0(\mathbf{x}+\boldsymbol{\ell})\rangle &= 0, && \text{(A16)} \end{aligned}$$

where the average is taken over the observed area and $\boldsymbol{\ell}$ is constant. Note that since $\mathbf{B}_0(\mathbf{x})$ is now a function of position, the value of $\sigma_{\delta B_\perp}$ differs from that in the standard method, in which $\mathbf{B}_0(\mathbf{x})$ is assumed to be constant. They then evaluate the two-point correlation function[1]

$$\langle \cos\Delta\Psi(\ell)\rangle = \left\langle \hat{\mathbf{B}}(\mathbf{x})\cdot\hat{\mathbf{B}}(\mathbf{x}+\boldsymbol{\ell})\right\rangle. \qquad \text{(A17)}$$

Making the approximation that the average of the ratio is the ratio of the averages yields

$$\langle \cos\Delta\Psi(\ell)\rangle = \frac{\langle \mathbf{B}_0(\mathbf{x})\cdot\mathbf{B}_0(\mathbf{x}+\boldsymbol{\ell})\rangle + \langle \delta\mathbf{B}(\mathbf{x})\cdot\delta\mathbf{B}(\mathbf{x}+\boldsymbol{\ell})\rangle}{\langle B^2\rangle}. \qquad \text{(A18)}$$

Since

$$\langle B^2\rangle = B^2_{\rm rms} = B_0^2 + \sigma^2_{\delta B}, \qquad \text{(A19)}$$

this approximation has eliminated the effect of non-zero values of $\delta\mathbf{B}\cdot\mathbf{B}_0$ on the analysis. We then have

$$\begin{aligned} 1 - \langle\cos\Delta\Psi(\ell)\rangle \quad &= \qquad\qquad \text{(A20)}\\ \frac{[B_0^2 - \langle\mathbf{B}_0(\mathbf{x})\cdot\mathbf{B}_0(\mathbf{x}+\boldsymbol{\ell})\rangle] + [\sigma^2_{\delta B} - \langle\delta\mathbf{B}(\mathbf{x})\cdot\delta\mathbf{B}(\mathbf{x}+\boldsymbol{\ell})\rangle]}{B^2_{\rm rms}}&. \end{aligned}$$

Hildebrand et al. (2009) assumed that $\mathbf{B}_0(\mathbf{x}+\boldsymbol{\ell})$ is slowly varying and expanded it in powers of ℓ. The linear term averages out, so the lowest order term varies as ℓ^2. Hildebrand et al. (2009) made the small angle approximation, but we follow Houde et al. (2009) in not doing that yet. This equation then becomes

$$\begin{aligned} 1 - \langle\cos\Delta\Psi(\ell)\rangle \quad &= \qquad\qquad \text{(A21)}\\ \frac{1}{2}m^2\ell^2 + \frac{\sigma^2_{\delta B}}{B^2_{\rm rms}} - \frac{\langle\delta\mathbf{B}(\mathbf{x})\cdot\delta\mathbf{B}(\mathbf{x}+\boldsymbol{\ell})\rangle}{B^2_{\rm rms}}&, \end{aligned}$$

where m is a constant that is determined by fitting the data. Note that this equation is the same as would have been obtained had we assumed that $\delta\mathbf{B}\cdot\mathbf{B}_0 = 0$, a result of the approximation made in equation (A18).

Hildebrand et al. (2009) further assumed that the last term vanishes for length scales ℓ exceeding the correlation length of the turbulent field, δ. Let $1-\cos\Delta\Psi_0$ be the value of $1-\langle\cos\Delta\Psi(\ell)\rangle$ obtained by extrapolating the first two terms of this equation from large ℓ, where the last term is negligible, to $\ell = 0$:

$$1 - \cos\Delta\Psi_0 = \frac{\sigma^2_{\delta B}}{B^2_{\rm rms}}, \qquad \text{(A22)}$$

so that with the aid of equation (A19)

$$\frac{\sigma_{\delta B}}{B_0} = \left(\frac{1}{\cos\Delta\Psi_0} - 1\right)^{1/2}. \qquad \text{(A23)}$$

The total POS field strength is $B = B_0/(\cos\Delta\Psi_0)^{1/2}$. The result for B_0 is then

$$B_0 = (4\pi\rho)^{1/2}\sigma_V \left(\frac{1}{\cos\Delta\Psi_0} - 1\right)^{-1/2} \qquad \text{(A24)}$$

from equation (A3). Note that in contrast to our derivation of the standard DCF method, it is the total dispersion in the POS field, $\sigma_{\delta B}$, that enters equation (A23) rather than the dispersion perpendicular to the mean field, $\sigma_{\delta B_\perp}$ (eq.

---

[1] Actually, they defined the correlation $\langle\cos\Delta\Psi(\ell)\rangle$ as $\langle \mathbf{B}(\mathbf{x})\cdot\mathbf{B}(\mathbf{x}+\boldsymbol{\ell})\rangle/\langle B^2(\mathbf{x})\rangle^{1/2}\langle B^2(\mathbf{x}+\boldsymbol{\ell})\rangle^{1/2}$, which agrees with the exact expression if $B(\mathbf{x})B(\mathbf{x}+\boldsymbol{\ell})$ is uncorrelated with $\cos\Delta\Psi(\ell)$ and if $\langle B(\mathbf{x})B(\mathbf{x}+\boldsymbol{\ell})\rangle = \langle B^2(\mathbf{x})\rangle^{1/2}\langle B^2(\mathbf{x}+\boldsymbol{\ell})\rangle^{1/2}$. In the end, their approximations and ours lead to the same result.

A7). They assumed that $\delta\mathbf{B}$ is isotropic, and in that case the difference is small.

As for the standard DCF method, one must then assume that the FAs are approximately equal to the PAs. Following Hildebrand et al. (2009) we label the PAs by Φ. The value of Φ is the same as that of θ in section A1 if angles are measured relative to the mean field direction. The value of B_0 in terms of measurable quantities is then

$$B_0 = f_{\rm DCF}(4\pi\rho)^{1/2}\sigma_V\left(\frac{1}{\cos\Delta\Phi_0}-1\right)^{-1/2}, \tag{A25}$$

where $f_{\rm DCF}$ allows for inaccuracies in the approximations that led to this result. Hildebrand et al. (2009) did not include such a factor. As noted above, Houde et al. (2009) explicitly allowed for variations along the line of sight, but did not correct for the effect of the approximations in the method. In the text, we set $f_{\rm DCF} = 0.5$. The 3D Alfvén Mach number with respect to the mean 3D field is

$$\mathcal{M}_{\rm A} = \frac{\sqrt{3}}{f_{\rm DCF}}\left(\frac{1}{\cos\Delta\Phi_0}-1\right)^{1/2}\cos\gamma. \tag{A26}$$

For small values of $\Delta\Phi_0$, this reduces to $\mathcal{M}_{\rm A} \simeq (\sqrt{3}\cos\gamma/f_{\rm DCF})\Delta\Phi_0/\sqrt{2}$, which agrees with the result for the standard DCF method (eq. A13) for small σ_θ if $\Delta\Phi_0/\sqrt{2}$ is replaced by σ_θ (see below eq. A28).

Hildebrand et al. (2009) made the small-angle approximation, retaining terms of order $\Delta\Phi_0^2$, and assumed $\Delta\Psi_0 = \Delta\Phi_0$, so that equation (A23) becomes

$$\frac{\sigma_{\delta B}}{B_0} = \frac{\Delta\Phi_0}{(2-\Delta\Phi_0^2)^{1/2}}, \tag{A27}$$

where $\Delta\Phi_0$ is inferred from $\Delta\Phi(\ell)$ in the same way that $\Delta\Psi_0$ is inferred from $\Delta\Psi(\ell)$ as described above. This approximation is accurate to within 10 percent for $\Delta\Phi_0 < 60^\circ$. For small angles, $\Delta\Phi(\ell)$ is given by equation (4). Equation (A25) for the mean magnetic field becomes

$$B_0 = f_{\rm DCF}(4\pi\rho)^{1/2}\sigma_V\,\frac{(2-\Delta\Phi_0^2)^{1/2}}{\Delta\Phi_0}. \tag{A28}$$

For $f_{\rm DCF} = 1$, this agrees with their result since their b is $\Delta\Phi_0$. The factor $(2-\Delta\Phi_0^2)^{1/2}$ arises because equation (A22) gives $\Delta\Phi_0$ in terms of $\langle B\rangle$ instead of B_0. For small $\Delta\Phi$, this result agrees with equation (A9) for the standard DCF method: $\Delta\Phi_0$ is an average of the difference of two random angles, so that $\Delta\Phi_0 = \sqrt{2}\sigma_\theta$ (Hildebrand et al. 2009). The agreement of the two expressions for B_0 implies that the value of the correction factor $f_{\rm DCF}$ is the same for the two methods.

Hildebrand et al. (2009) assumed that δ, the maximum scale of the turbulent velocity correlations, was of order 1 mpc, well below the resolution of the observations they were fitting. Subsequent work using the method of Houde et al. (2009) obtained larger values: for example, Guerra et al. (2021) found $\delta \sim 10 - 100$ mpc for OMC-1. Our analysis of SR1 and SR2 also gives $\delta \sim 100$ mpc, as does our simulation (see below). The observations we have analyzed and our simulation are consistent with the turbulent correlation length δ being of order the FWHM of the filament, which is plausible for a filament formed in a turbulent medium and consistent with the results of Palmeirim et al. (2013). Note that the value of δ does not enter; all that is required is that it be small enough that there is a range of ℓ over which $\Delta\Phi(\ell)^2$ is accurately fit by the first two terms in equation (A21).

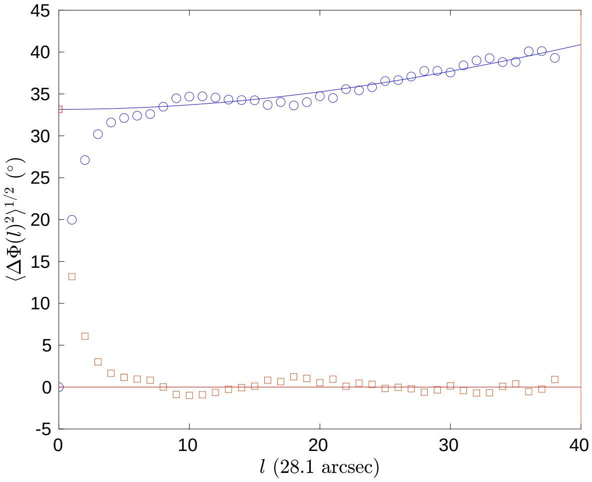

Figure A1. The structure function of magnetic field vectors in the simulation window (blue circles) as a function of scale in units of HAWC+ superpixels (28.1 arcsec), with the best fit (solid curve) and the negative of the last term of equation (A21) (red squares).

How well does our simulation agree with the SF variant of the DCF method? The actual values of the field strength are compared with the DCF/SF values in Table 3. Here we focus on the validity of the SF relation between the dispersion in field angles and the dispersion in field strength, equation (A21). For simplicity, we adopt the small angle approximation; had we not done that, the results would have changed by only 7%. Fig. A1 compares the dispersion in angle, $\Delta\Psi(\ell)$, measured in the FOV window of the simulation with values from equation (A21). The blue curve plots the first two terms in the equation, using the measured value of $\sigma_{\delta B_\perp}/B_{\rm rms}$ and treating m as a free parameter. It provides an excellent fit to the data for $\ell \gtrsim 5$ superpixels, or about 0.1 pc for the parameters we have adopted. This is the turbulent correlation length, δ, and is about 1/3 the width of the filament, as noted above. It is well resolved in the simulation, with more than 40 grid cells at the highest resolution. The red curve shows the last term in equation (A21). As assumed by Hildebrand et al. (2009), it is negligible except at small scales, $\ell < \delta \sim 0.1$ pc. The figure shows that the approximations made in deriving equation (A21) are reasonably good in this case, and that the turbulent velocity correlations extend to scales large enough that they must be taken into account.

A2.1 Restriction of $\Delta\Phi$

A fundamental problem with determining the field strength from polarization observations is that the field angles (FAs), Ψ, can range over 360 degrees whereas the PAs, Φ, are limited to a range of 180 degrees. For a given choice of the direction corresponding to 0°, let the orientation of the PAs lie in the range ±90°. FAs lying outside that range will have PAs in the opposite direction–i.e., such an FA will differ from the corresponding PA by 180°. As a result, the measured value of $\Delta\Phi$, based on the PAs, will differ from the actual value, which is based on the FAs. The error depends on the number of FAs that are flipped in direction, which in turn depends on the choice of the 0° direction; we choose that to be the direction that gives the minimum dispersion in the PA angles, Φ_i. In an attempt to reduce this error in the DCF/SF method, it is common to restrict the difference between angles, $\Delta\Phi$, to be less than 90° by replacing $|\Delta\Phi|$ with $|180^\circ - \Delta\Phi|$ when $|\Delta\Phi| > 90^\circ$ (e.g., Davidson et al. 2011). Under what conditions is this valid? If the angles are restricted when they should not be, then the dispersion will be underestimated and the field overestimated.

First assume that the PAs are an accurate reflection of the FAs, up to an ambiguity of 180°. If the FAs are confined to a range less than 180°, then the FAs and PAs can be in alignment and restricting $\Delta\Phi$ would lead to an error. If the FAs extend beyond that range, but the mean field has a constant direction, then the dispersion in the PAs will be less than that in the FAs and the the field strength will be overestimated. The error will only grow larger if $\Delta\Phi$ is restricted. It follows that restriction should never be used if the mean field has a constant direction.

If $\mathbf{B}_0$ changes direction as a function of position, the situation becomes more complicated. If the average angle differs significantly from the FAs in a local region, then it is possible that some of those FAs will be flipped by 180° when converted to PAs, thereby increasing the dispersion relative to neighboring PAs. Restriction corrects this by significantly reducing $\Delta\Phi$ for the PAs in that region. On the other hand, it also reduces $\Delta\Phi$ for the PAs that were initially quite different from the initial FA direction. This discussion suggests that restriction provides a lower limit on $\Delta\Phi_0$ and that it is significant only when the dispersion in angles is large, when the DCF method is of questionable accuracy. For SR2, with $\sigma_\theta = 20^\circ$, restriction reduced $\Delta\Phi_0$ by 4% and therefore increased B_0 by the same factor; for the simulation, with $\sigma_\theta = 29^\circ$, restriction increased the inferred field by 5%; and for SR1, with $\sigma_\theta = 54^\circ$, restriction increased B_0 by 20%. An approach that reduces the uncertainties due to restriction is to map the field locally (Guerra et al. 2021), so that there is less variation of the mean field in each region.

A3 The parallel-$\delta\mathbf{B}$ version of the DCF method

Skalidis & Tassis (2021a) and Skalidis et al. (2021b) adopt an alternative approach to inferring the mean field strength and assume that the turbulent motions are in approximate equipartition with the *parallel* component of the perturbed field, $0.5\rho\delta v^2 = B_0\delta B/4\pi$ for small δB. Setting $\sigma_\theta = \delta B/B_0$, they obtained

$$B_{0,\mathrm{ST}} = (2\pi\rho)^{1/2}\,\frac{\sigma_V}{\sigma_\theta^{1/2}}. \qquad (A29)$$

They did not find it necessary to introduce a correction factor f_{DCF} as is often done for the standard DCF method. They present the results of simulations showing that their result is more accurate than the standard one.

In our simulation, we find that $\langle|\delta\hat{\mathbf{B}}\cdot\hat{\mathbf{B}}_0|\rangle \simeq 0.8$, so the parallel component of $\delta\mathbf{B}$ is indeed significant. On the other hand, the positive and negative values nearly cancel so that $\langle\delta\hat{\mathbf{B}}\cdot\hat{\mathbf{B}}_0\rangle \simeq 0.06$–i.e., rarefactions, which have $\delta\hat{\mathbf{B}}\cdot\hat{\mathbf{B}}_0 < 0$, nearly cancel the effect of compressions, which have $\delta\hat{\mathbf{B}}\cdot\hat{\mathbf{B}}_0 > 0$. This effect is not included in the model of Skalidis & Tassis (2021a) since they assumed that $\langle\delta\mathbf{B}\cdot\mathbf{B}_0\rangle$ can vanish only for incompressible turbulence and proceeded to make the incorrect assumption that $\langle\delta\mathbf{B}\cdot\mathbf{B}_0\rangle = \langle|\delta\mathbf{B}|\rangle B_0$. They attempted to justify this step by appealing to Bhattacharjee, Ng, & Spangler (1998), although that work applies only to very subsonic turbulence and has $\langle\delta\mathbf{B}\rangle = 0$. Skalidis et al. (2021b) argued that the maximum kinetic energy in fluctuations, a second order quantity, is in equipartition with the maximum magnetic energy in the fluctuations, a first order quantity; as shown by Zweibel & McKee (1995), however, it is the second order energies that are in equipartition. In agreement with equation (A11), they note that a non-zero polarization angle is possible only in the presence of a perpendicular component of the field. As a result their method requires $\delta B_\parallel \simeq \delta B_\perp$, which they find to be satisfied to within a factor 2 in the simulations they analyze.

For $\tan\sigma_\theta \simeq \sigma_\theta$, the ratio of their result to the standard DCF one is $(\sigma_\theta/2)^{1/2}/f_{\mathrm{DCF}}$. For $f_{\mathrm{DCF}} = 0.5$, the two values of the field agree for $\sigma_\theta = 27^\circ$; since that is close to the values we find in our simulation, we are not able to determine whether their result is more accurate than the standard DCF method. It should be noted, however, that their result has no free parameters, whereas f_{DCF} is a free parameter for the standard method. In view of the questionable assumptions underlying their method, more work is needed to understand the physical basis for the method and the circumstances under which it works.

Applying their method to the observed fields in B211 with the full line width σ_V^m gives $B_0 = 27\ \mu$G for SR1, about twice the value with the standard DCF method but only slightly larger than the 23 μG with the DCF/SF method with restriction. If σ_θ is replaced by $\tan\sigma_\theta$ in their formula, their result would be 22 μG for this region, not that much larger than the DCF/SF value without restriction, 16 μG. For SR2 they find $B_0 = 57\ \mu$G, somewhat less than the 66 μG with the standard DCF method and $\sim 80\ \mu$G with the DCF/SF method. In most cases the three methods agree within the uncertainties for both observation and simulation. The exception is the standard DCF method, which gives a low value for the tangled-field SR1, most likely because it includes variation in $\mathbf{B}_0$ in its determination of σ_θ. The parallel-$\delta\mathbf{B}$ method includes such variation as well, but the result is less sensitive since it enters only as the square root.

APPENDIX B: EQUILIBRIUM AND FRAGMENTATION OF FILAMENTS

B1 Equilibria of Cylindrical Filaments

Under what conditions are the filaments that we have observed and simulated expected to be stable against gravitational collapse? Fiege & Pudritz (2000a) have shown that the maximum mass per unit length of an unmagnetized, equilibrium filamentary cloud is $M_{\mathrm{vir},\ell} = 2\langle\sigma_V^2\rangle/G$. The virial parameter for a filament, $\alpha_{\mathrm{vir,f}}$, is the ratio of twice the 2D kinetic energy to the magnitude of the potential energy and is given by

$$\alpha_{\mathrm{vir,f}} = \frac{M_{\mathrm{vir},\ell}}{M_\ell} = \frac{2\sigma_V^2}{GM_\ell}. \qquad (B1)$$

Equilibria require $\alpha_{\mathrm{vir,f}} > 1$. In contrast to the spherical case, the gravitational energy term in the virial theorem is independent of the internal structure of the filament, so long as the density is independent of azimuth and distance along the filament.

The stability of a cloud against gravitational collapse is also affected by magnetic fields, which are parameterized by the mass-to-flux ratio relative to the critical value, μ_Φ. Let M_Φ, the magnetic critical mass, be the maximum mass that can be supported by magnetic fields against gravity; then $\mu_\Phi = M/M_\Phi$. In general,

$$M_\Phi = \frac{c_\Phi \Phi}{G^{1/2}}, \tag{B2}$$

where Φ is the magnetic flux threading the cloud and $c_\Phi = 1/(2\pi) \simeq 0.16$ for a thin disk (Nakano & Nakamura 1978) and 0.17 for a spheroidal cloud with a constant mass-to-flux ratio (Tomisaka, Ikeuchi, & Nakamura 1988). The field in the ambient cloud is generally perpendicular to the filament when self-gravity is important (e.g., Planck Collaboration Int. XXXV 2016); the filament can then grow by flows along the field lines (Palmeirim et al. 2013). We shall focus on the case of a perpendicular field here; Nagasawa (1987); Fiege & Pudritz (2000a) and Motiei, Hosseinirad, & Abbassi (2021) have considered the case in which the field is parallel to the filament. We anticipate that the critical mass per unit length of a filament is obtained from equation (B2) by dividing both sides by the length, and indeed that is what Tomisaka (2014) found for the case of a filament with a mass-to-flux distribution corresponding to a constant-density filament threaded by a uniform field. Kashiwagi & Tomisaka (2021) generalized this analysis to polytropic filaments. For $\gamma \to 1$, where here γ is the adiabatic index, their result is within 1% of the result expected from the case of a thin disk,

$$M_{\Phi,\ell} = \frac{\Phi_\ell}{2\pi G^{1/2}}, \tag{B3}$$

where $\Phi_\ell = w B_{0,\,3\mathrm{D}}$ is the flux per unit length, $B_{0,\,3\mathrm{D}}$ is the mean 3D field in the filament, and w is the width of the filament. (They defined Φ_ℓ as half the flux per unit length, so their coefficient is twice as large.) Since the mean surface density is $\Sigma = M_\ell/w$, the mass-to-flux ratio relative to the critical value is

$$\mu_\Phi = \frac{M_\ell}{M_{\Phi,\ell}} = \frac{2\pi G^{1/2}\Sigma}{B_{0,\,3\mathrm{D}}}. \tag{B4}$$

The derivation of the magnetic critical mass neglects the presence of turbulent magnetic fields. Since it is the total field energy that counteracts the effect of gravity, we assume that it is the total 3D field, $B_{3\mathrm{D}} = (B_{0,\,3\mathrm{D}}^2 + \delta B_{3\mathrm{D}}^2)^{1/2}$, that enters equation (B4). The value of μ_Φ that we can measure depends on the POS values of the field and of the surface density (we have added the subscript "POS" to the total POS field for clarity):

$$\mu_{\Phi,\mathrm{POS}} = 7.6 \times 10^{-21} N(\mathrm{H}_2)_{\mathrm{Obs}}/B_{\mathrm{POS}}, \tag{B5}$$

where B_{POS} is measured in μG and $N(\mathrm{H}_2)_{\mathrm{Obs}}$ is the observed column density of the filament. The stability of the filament depends on the column density normal to the filament, which is smaller than that by $\cos\gamma_f$, where γ_f is the inclination angle of the filament relative to the POS. The actual value of μ_Φ is then related to $\mu_{\Phi,\mathrm{POS}}$ by

$$\mu_\Phi = \mu_{\Phi,\mathrm{POS}} \cos\gamma_f \left(\frac{B_{\mathrm{POS}}}{B_{3\mathrm{D}}}\right). \tag{B6}$$

We note that Li et al. (2015) showed that the volume-averaged field, which enters μ_Φ, is generally less than the mass-averaged field determined from Zeeman observations. If this same effect occurs for DCF determinations of the field, which are also mass-averaged, then the observed value of $\mu_{\Phi,\mathrm{POS}}$ is an underestimate of the true value.

When the filamentary cloud is supported by both a perpendicular magnetic field and thermal/turbulent motions, Kashiwagi & Tomisaka (2021) found that the maximum stable mass per unit length for $\gamma \to 1$ is

$$M_{\mathrm{crit},\ell} \simeq \left(M_{\Phi,\ell}^2 + M_{\mathrm{vir},\ell}^2\right)^{1/2}, \tag{B7}$$

with a factor 0.85 before $M_{\mathrm{vir},\ell}^2$; we have omitted that factor in order to make the result exact in the limit $\Phi_\ell = 0$. Equation (B7) implies

$$\frac{M_\ell}{M_{\mathrm{crit},\ell}} = \frac{1}{\left(\mu_\Phi^{-2} + \alpha_{\mathrm{vir,f}}^2\right)^{1/2}}. \tag{B8}$$

Equilibrium clouds must have $\mu_\Phi^{-2} + \alpha_{\mathrm{vir,f}}^2 > 1$ so that M_ℓ is less than the critical value.

B2 Fragmentation of Filaments Stable Against Radial Collapse

In the text, we find that the filaments SR1 and SR2 have $\alpha_{\mathrm{vir,f}} > 1$, so they are stable against radial collapse. Can they fragment? We begin with the case $B = 0$ since the effects of magnetic fields have been considered only for fields parallel to the filament. Self-gravitating, isothermal filaments are characterized by the ratio of the radius to the scale height, $H = c_s/(4\pi G\rho_c)^{1/2}$, where ρ_c is the central density. With the aid of the results of Fischera & Martin (2012), this ratio is

$$\frac{R}{H} = \left(\frac{8}{\alpha_{\mathrm{vir,f}} - 1}\right)^{1/2}. \tag{B9}$$

Note that Fischera & Martin 2012 express their results in terms of $f_{\mathrm{cyl}} = M_\ell/M_{\mathrm{vir},\ell} = 1/\alpha_{\mathrm{vir,f}}$. Nagasawa (1987) studied the stability of isothermal filaments and found two types of behavior. For large R/H, gas compresses along the filament with a maximum growth rate at a wavenumber $k_m = 0.284/H$ (the "compressible instability"). For small R/H, the gas flow is almost incompressible (the "deformation instability"), with a maximum growth rate at $k_m = 0.58/R$. Combining these results, we obtain the approximation

$$k_m H \simeq \left[0.284^2 + \frac{0.58^2}{(R/H)^2}\right]^{1/2}, \tag{B10}$$

$$\simeq 0.204(\alpha_{\mathrm{vir,f}} + 1)^{1/2}, \tag{B11}$$

where the second expression was obtained with the aid of equation (B9). The latter expression agrees with the results of Nagasawa (1987) to within a few percent. A more accurate approximation, a fourth-order polynomial, is given by Fischera & Martin (2012). It is convenient to express this in terms of the FWHM of the filament, F, which is observable. The results of Fischera & Martin (2012) can be fit to within 10% by the expression $F/H = 4.9/(\alpha_{\mathrm{vir,f}} + 0.28)^{1/2}$ so that

$$k_m F \simeq 1.00 \left(\frac{\alpha_{\mathrm{vir,f}} + 1}{\alpha_{\mathrm{vir,f}} + 0.28}\right)^{1/2}, \tag{B12}$$

which is within about 10% of the curve for λ_m in Fig. 11 of Fischera & Martin (2012). Observe that the ratio of the wavelength of the fastest growing mode to the FWHM of the filament is almost constant, with $k_m F$ varying from 1.25 to 1.00 as $\alpha_{\mathrm{vir,f}}$ increases from 1 to ∞.

The growth rate of the instability is within 25% of $0.3(4\pi G\rho_c)^{-1/2}$ for all R/H based on Fischera & Martin (2012)'s fit to the results of Nagasawa (1987). Thus, unmagnetized filaments that are stable against radial collapse always fragment, although the amplitude of the perturbation could be small, as we shall now see.

The fragment mass is

$$M_{\rm frag} = M_\ell\lambda = \frac{4\pi c_{\rm s}^2}{\alpha_{\rm vir,f}Gk}, \tag{B13}$$

where λ is the wavelength of the instability. An isolated fragment will settle into equilibrium for $M < M_{\rm BE}$, where $M_{\rm BE} = 1.182c_{\rm s}^3/(G^3\rho_s)^{1/2}$, the critical Bonnor-Ebert mass, is the maximum equlibrium mass for an isothermal sphere (Inutsuka & Miyama 1997). The ratio of the fragment mass to the Bonnor-Ebert mass is

$$\frac{M_{\rm frag}}{M_{\rm BE}} = \frac{(4\pi)^{1/2}}{1.182}\left(\frac{\alpha_{\rm vir,f}-1}{\alpha_{\rm vir,f}^2 kH}\right), \tag{B14}$$

which is equivalent to the result of Fischera & Martin (2012). In deriving this expression, one must keep in mind that H is defined in terms of the central density whereas $M_{\rm BE}$ is defined in terms of the density at the surface. We expect that the wavenumber k corresponds to the fastest growing mode, so equation (B11) implies

$$\frac{M_{\rm frag}}{M_{\rm BE}} = 14.7\,\frac{(\alpha_{\rm vir,f}-1)}{\alpha_{\rm vir,f}^2(\alpha_{\rm vir,f}+1)^{1/2}}. \tag{B15}$$

For $\alpha_{\rm vir,f} \gg 1$, this result shows that $M_{\rm frag} \ll M_{\rm BE}$; self-gravity is not important and the density in the fragment is not much larger than the mean density in the filament. The fragment mass exceeds $M_{\rm BE}$ for $1.12 < \alpha_{\rm vir,f} < 4.8$ ($0.89 > f_{\rm cyl} > 0.21$), and an isolated unmagnetized fragment would be expected to undergo gravitational collapse under these conditions. The optimum condition for fragmentation occurs when this ratio is a maximum, at $\alpha_{\rm vir,f} \sim 2$ ($f_{\rm cyl} \sim 0.5$). These results are consistent with the graphical results in Figure 11 of Fischera & Martin (2012). More generally, in the absence of magnetic fields pre-stellar cores (i.e., starless cores with $M \geqslant M_{\rm BE}$) would be expected to form for $1.1 \lesssim \alpha_{\rm vir,f} \lesssim 5$ ($0.9 \gtrsim f_{\rm cyl} \gtrsim 0.2$), although magnetic fields can inhibit their formation and collapse (see below). In their SPH simulations, Inutsuka & Miyama (1997) found that a filament with $f_{\rm cyl} = 0.2$ produced a stable core, consistent with our expectation; however, filaments with $f_{\rm cyl} = 0.9$ produced cores that collapsed, contrary to expectation from equation (B15). Their simulation had periodic boundary conditions, so the results are not expected to be identical to those for an isolated filament. They found that stable fragments could merge; gravitational collapse would ensue if the mass of the merged fragments exceeded $M_{\rm BE}$.

Motiei, Hosseinirad, & Abbassi (2021) studied the stability of polytropic filaments with a field parallel to the filament. For $B = 0$ and $\gamma = \frac{3}{4}$ (the case closest to $\gamma = 1$), they found that the most unstable wavelength and the critical wavelength are within about 30% of the values for an isothermal filament (eq. B11). This suggests that there is no significant difference between the unstable wavelengths of isothermal filaments and polytropic filaments with $\gamma \to 1$ despite the fact that isothermal filaments have a much steeper density gradient at large radii, $\rho \propto r^{-4}$ (e.g., Ostriker 1964), than polytropic filaments, $\rho \propto r^{-2/(2-\gamma)}$ (Viala & Horedt 1974). The results discussed above should therefore apply to both isothermal filaments and polytropic ones with $\gamma \to 1$. We note that observationally, the polytropic solution appears to be favored – for example, Palmeirim et al. (2013) found $\rho \propto r^{-2}$ with γ just below 1.

Simulations have shown that magnetic fields reduce fragmentation (e.g., Hennebelle et al. 2011; Myers et al. 2013). A magnetic field parallel to the filament reduces the growth rate of the fragmentation instability, particularly for large $\alpha_{\rm vir,f}$ (small $f_{\rm cyl}$), but it does not prevent instability (Nagasawa 1987). Fragmentation in the presence of a perpendicular field has not been analyzed to our knowledge, but we anticipate that fields with $\mu_\Phi < 1$ (magnetically subcritical) would be stable. Subcritical magnetic fields are rarely observed, however (Crutcher et al. 2010). Although a strong perpendicular magnetic field is required to suppress fragmentation, a weaker field can prevent gravitational collapse of an approximately spherical fragment: For such a clump, the critical mass is $M_{\rm crit} \simeq M_{\rm BE} + M_\Phi$ (McKee 1989): Both kinetic and magnetic energies contribute to stability, as in the case of stability against radial collapse. For a fragment, the relation analogous to equation (B8) for filaments is

$$\frac{M_{\rm frag}}{M_{\rm crit}} = \frac{1}{\dfrac{M_{\rm BE}}{M_{\rm frag}} + \mu_\Phi^{-1}}, \tag{B16}$$

where the first term is given in equation (B15). Fragments with $M_{\rm frag} > M_{\rm crit}$ are expected to undergo gravitational collapse.

université
PARIS-SACLAY

ÉCOLE DOCTORALE
Astronomie
et Astrophysique
d'Île-de-France (AAIF)

Titre: Champ magnétique et formation d'étoiles le long des filaments interstellaires : Observations avec NIKA2-Pol

Mots clés: formation d'étoiles, milieu interstellaire, champs magnétique

Résumé: La formation d'étoiles dans le milieu interstellaire est débattue depuis des décennies. Les observations récentes de la mission spatiale *Herschel* ont montré que les structures filamentaires sont présentes dans tout les nuages moléculaires observés et que ces filaments jouent un rôle crucial dans la formation d'étoiles. Ces observations ont montré que ces filaments ont une largeur commune de 0.1 pc et que la plupart (75 %) des cores pre-stellaires détectés sont dans des filaments trans-critiques ou super-critiques pour lequel la masse par unité de longueur excède le seuil critique de l'instabilité gravitationnelle d'un filament cylindrique de gaz isotherme dont $M_{line} \gtrsim M_{line}^{crit}$ ($M_{line}^{crit} = 2c_s/G \sim 16M_\odot$ est la la masse par unité de longueur). Les résultats d'Herschel favorisent le paradigme de formation d'étoiles dans les filaments dans lequel : (1) la turbulence supersonique magnéto-hydrodynamique (MHD) à grande échelle comprime la matière pour former des structures filamentaires avec une largeur interne commune $\sim$ 0.1 pc; (2) Les filaments les plus denses se fragmentent et s'effondrent pour former des noyaux préstellaires en raison de leur instabilité gravitationnelle lorsque M $_{line}$ est proche ou dépasse la masse critique par unité de longueur M $^{crit}_{line}$. Cependant, le processus détaillé de comment les filaments fragmentent en noyaux pre-stellaire resté activement débattu. Il y a des indices que le champ magnétique peut être l'ingrédient ignoré pour comprendre la formation d'étoiles. De plus, les données obtenues avec *Planck* en émission polarisée des poussières froides suggèrent que la formation et l'évolution des filaments moléculaires aient en grande partie contrôlées par le champ magnétique. Les observations polarisées avec Planck sont incapables de determiner la géométrie du champ magnétique à l'intérieur des filaments aux échelles auxquelles la fragmentation se produit. La compréhension du rôle du champ magnétique dans la formation d'étoiles n'est donc pas encore complete. Explorer la géométrie et l'intensité du champ magnetic dans les filaments moléculaires à différentes longueurs d'onde et à une résolution angulaire élevée aidera à comprendre son rôle dans le processus de formation d'étoiles dans le milieu interstellaire froid.

L'objectif de cette thèse est de clarifier le rôle de champ magnétique dans la formation d'étoiles en utilisant des polarimètres plus sensibles et à haute résolution angulaire. Le grand programme d'observations (B-FUN) garanti avec NIKA2-Pol et alloué par l'IRAM 30m va conduire des observations d'imagerie polarimétrique à 1.2 mm pour observer des filaments moléculaires proches formant des étoiles. Durant ma thèse, j'ai contribué aux tests et à la mise en service de l'instrument NIKA2-Pol. Cet instrument a dû faire face aux plusieurs problèmes, en particulier l'effet de la polarisation instrumentale ou la fuite de l'intensité total à la polarisation. J'ai caractérisé la variation de cet effet avec plusieurs paramètres (elevation, foyer et conditions d'observations). J'ai enquêté sur l'origine de cette polarisation instrumentale affectant les données de NIKA2-Pol comme toute aute polarimetre au monde. J'ai présenté un modèle analytique qui permet de reproduire cet effet. J'ai montré comment corrigé les données de NIKA2-Pol de la polarisation instrumentale et j'ai exploité ces données pour étudier le filament d'OMC-1 dans le nuage moléculaire d'Orion A. J'ai présenté une comparaison statistique entre les résultats obtenus par les polarimètres SCUBA-POL2 et NIKA2-Pol. Ces résultats ont permis de démontrer la capacité de NIKA2-Pol à fournir des données de polarisation de haute qualitées. Par ailleurs, j'ai étudié la géométrie/l'intensité du champ magnétique avec les données obtenu durant les compagnes de tests de l'instrument NIKA2-Pol. J'ai confirmé la présence du champ magnétique se forme d'une "hourglass" (sablier) à grande échelle dans le filament OMC-1 précédemment détecté par d'autre polarimetres. J'ai trouvé des preuves d'un possible nouvel "hourglass " centré à la position d'Orion-KL grâce à la sensibilité et la haute résolution angulaire de NIKA2-Pol. J'ai estimé l'intensité du champ magnétique dans cette région en utilisant la méthode Davis-Chandraskher-Fermi. En parallèle, j'ai utilisé les données de polarisation obtenu par le polarimetre SOFIA/HAWC+ pour étudier la géométrie/intensité du champ magnétique dans le filament B211/B213 du nuage moléculaire Taurus. Enfin, j'ai effectué une analyse du spectre de puissance des fluctuations de vitesse le long d'un échantillon de filaments dans la région de formation d'étoiles d'Aquila pour élucider les conditions initiales de la fragmentation des filaments en chaînes de noyaux denses.

ÉCOLE DOCTORALE
Astronomie
et Astrophysique
d'Île-de-France (AAIF)

Title: Probing the role of magnetic fields in star-forming filaments and protostellar cores : Observing with NIKA2-Pol

Keywords: star formation, magnetic field, ISM

Abstract: Star formation in the interstellar medium has been under debate for decades. The unprecedented high-quality images provided by *Herschel* have shown that filaments are ubiquitous in molecular clouds and play a key role in the star formation (SF) process. These filaments have been shown to exhibit a common inner width of about $\sim$ 0.1 pc, and more than 75 % of the detected prestellar cores are embedded in thermally trans-critical or super-critical filaments with masses per unit length $\mathrm{M}_{line} \gtrsim \mathrm{M}_{line}^{crit}$ (where $\mathrm{M}_{line}^{crit} = 2c_s/G \sim 16M_\odot$ is the critical mass per unit length of an isothermal filament). *Herschel* findings support a filament paradigm for SF in which : (1) Large-scale magnetohydrodynamic (MHD) supersonic turbulence compresses interstellar material to form a cobweb of filamentary structures with a common inner width of about $\sim$ 0.1 pc; (2) The densest filaments fragment to form prestellar cores due to gravitational instability when M_{line} is close to or exceeds the critical mass per unit length M_{line}^{crit}. However, the detailed process of how filaments fragment into cores remains actively debated. There are hints that the magnetic field may be the ignored ingredient toward understanding SF. *Planck* results suggest that the B-field lines tend to be parallel to low density filaments and perpendicular to the high-density filaments. Due to the low angular resolution of *Planck* polarization data (10 arcmin), these observations are, however, unable to probe the magnetic field inside filaments on scales at which fragmentation occurs. The detailed knowledge of the role of magnetic fields in the SF process has therefore not yet been achieved. Constraining the B-field geometry/strength at different wavelengths and high angular resolution will help understand how magnetic fields may regulate the SF in the cold interstellar medium (ISM).

This thesis aims to clarify the role of magnetic fields in SF using high-angular resolution, sensitive polarimetric instruments. The B-FUN large program with the NIKA2-Pol polarimeter on the IRAM 30m telescope will provide high angular resolution (11.7 arcsec) and sensitive polarization data toward nearby star-forming filaments. During my Ph.D., I contributed to the commissioning of NIKA2-Pol. The commissioning of NIKA2-Pol had to face several challenging issues, in particular, the instrumental polarization (IP) or intensity-to-polarization "leakage" effect. I characterized the variation of the leakage effect with several parameters (elevation, focus position, and observing conditions). I investigated the origin of the IP, and presented an analytical model for the IP leakage. I illustrated how this effect can be corrected for, leading to reliable exploitable data in a structured, extended field such as the OMC-1 filament in the Orion A molecular cloud. I presented a statistical comparison between NIKA2-Pol and SCUBA2-Pol2 results in the OMC-1 region. These results helped to demonstrate the ability of NIKA2-Pol to provide high-quality polarization data. Furthermore, I investigated the geometry/strength of the magnetic field toward the OMC-1 filament using NIKA2-Pol commissioning data. I confirmed the presence of a previously-detected large-scale hourglass pattern in the magnetic field distribution, and I found evidence of a possible new local hourglass centered at the position of Orion-KL detected thanks to the NIKA2-Pol high angular resolution data. I also made estimates of the magnetic field strength in this region using the Davis-Chandraskher-Fermi method. In parallel, I used SOFIA/HAWC+ polarization data to study the magnetic field geometry/strength in the B211/B213 filament of the Taurus molecular cloud. Finally, I performed a power spectrum analysis of velocity fluctuations along a sample of filaments in the Aquila star-forming region to elucidate the initial conditions for the fragmentation of filaments into chains of dense cores.